Imaging of osmiophilic excipients using electron microscopy approaches

Dissertation

zur

Erlangung des Doktorgrades (Dr. rer. nat.)

der

Mathematisch-Naturwissenschaftlichen Fakultät

der

Rheinischen Friedrich-Wilhelms-Universität Bonn

vorgelegt von

Thilo Faber

aus

Bitburg

Bonn 2025

Angefertigt mit Genehmigung der Mathematisch-Naturwissenschaftlichen Fakultät

der Rheinischen Friedrich-Wilhelms-Universität Bonn

Gutachter/Betreuer: Prof. Dr. Alf Lamprecht

Gutachter: Prof. Dr. Günther Weindl

Tag der Promotion: 25.06.25

Erscheinungsjahr: 2025

Diese Arbeit wurde unter der Aufsicht und Betreuung von Prof. Dr. Alf Lamprecht vom März 2019 bis Februar 2025 in der Abteilung für pharmazeutische Technologie und Biopharmazie des Pharmazeutischen Institutes der Rheinischen Friedrich-Wilhelms-Universität Bonn angefertigt.

Des Weiteren ist die vorliegende Arbeit an den nachstehenden Stellen auszugsweise veröffentlicht

Focused ion beam-scanning electron microscopy provides novel insights of drug delivery phenomena
T. Faber, J.T. McConville, A. Lamprecht, Journal of Controlled Release 366 (2024) 312–327. https://doi.org/10.1016/j.jconrel.2023.12.048.

Cellular Uptake and Trafficking of Lipid Nanocarriers Using High-Resolution Electron Microscopy
T. Faber, A. Lamprecht, AAPS PharmSciTech 26 (2025) 71.
https://doi.org/10.1208/s12249-025-03061-3.
Die in dieser Publikation enthaltene Abbildungen sind markiert mit (#)

Weitere Arbeiten, die während dieser Zeit publiziert wurden, befinden sich in der Publikationsliste

Diese Arbeit ist denen gewidmet die ihre Fertigstellung nicht mehr erleben

Für
Oma Brigitte

Für
Opa Jakob

Für
Mama Judith

Danksagung

Ich möchte mich als erstes bei meinem Doktorvater Prof. Alf Lamprecht bedanken, dass er mir die Möglichkeit zur Promotion gegeben hat. Die Elektronenmikroskopie als Hauptthema gab mir die Möglichkeit, eine Vielzahl von Proben zu untersuchen und so Einblicke in die Pharmazie und die Struktur von Arzneistoffträgern zu erhalten, wie sie nicht viele Wissenschaftler in diesem Ausmaß erhalten. Des Weiteren danke ich meinen Gutachtern Prof. Günther Weindl, Prof. Gerd Bendas und Prof. Alexander Blanke.

Während der Zeit meiner Promotion haben mich viele sehr geschätzte Kollegen und Freunde begleitet. Diesen möchte ich für die vielen gemeinsam verbrachten Stunden danken. Hier möchte ich besonders meine Bürokollegen aus Büro 2.040 und Büro 2.036 nennen, die mit mir die Hochs und Tiefs meiner Promotion erlebt haben.

Ich möchte meiner Familie danken, die mir immer die Gewissheit gab, dass ich auf ihre Unterstützung zählen kann. Hier möchte ich insbesondere meine Mutter Judith und meine Großeltern Jakob, Brigitte und Erika nennen. Leider hat das Schicksal entschieden, dass weder Opa Jakob, Oma Brigitte noch meine Mutter den Abschluss meiner Promotion erleben werden, da alle drei 2023 diese Welt verlassen mussten.

An dieser Stelle möchte ich erneut Prof. Lamprecht für sein Verständnis und seine Kooperationsbereitschaft während dieser Zeit danken. Ebenfalls möchte ich Annette, Bine, Helga, Carla, Alex, Konrad und allen anderen für ihre Unterstützung während der Krankheit meiner Mutter danken.

Zu guter Letzt möchte ich Charlotte meine tiefe Dankbarkeit aussprechen für all die Unterstützung während meiner Promotion und den Schicksalsschlägen in dieser Zeit.

Contents

Tables

Figures

List of abbreviations

Abbreviations	Meaning
AFM	Atomic force microscopy
API	Active pharmaceutical ingredient
ASD	Amorphous solid dispersions
ATP	Adenosine tri phosphate
BSE	Back scattered electrons
CBS	Concentric backscatter electron detector
CI	Confidence Interval
CLEM	correlative light and electron microscopy
CLSM	Confocal laser scanning microscopy
CQ	Chloroquine
CT	Computed tomography
DCM	Dichloromethane
DDS	Drug delivery System
DLS	Dynamic light scattering
DMEM	Dulbecco's modified eagles medium
DMSO	Dimethyl sulfoxide
DNA	Desoxyribonucleic acid
DPBS	Dulbecco′s Phosphate Buffered Saline
EDS	Energy-dispersive X-ray spectroscopy
EE	Ethyl ester
EM	Electron microscopy
FIB-SEM	Focused ion beam scanning electron microscopy/ Focused ion beam scanning electron microscope
HMDS	Hexamethyldisilazane
ICD	In column detector
LAL 2	Lalistat 2
LD	Lipid Droplet
LNC	lipid nano carrier
MCT	Medium chain triglycerides
MTT	3-(4,5-Dimethylthiazol-2-yl)-2,5-diphenyltetrazoliumbromid
MvB	Multivesicular body
NE	Nano Emulsion
NP	Nanoparticles
PCL	Polycaprolactone
PEG	Polyethylene glycol
PEO	Polyethylene oxide
PVP	Polyvinylpyrrolidone
RAB	Ras-related in brain
RNA	Ribonucleic acid
rO	reduced osmium tetroxide
rOTO	reduced Osmium-Thiocarbohydrazide-Osmium
RPM	rotations per minute
SE	Secondary Electrons

SEDDS	Self-emulsifying drug delivery systems
SEM	Scanning electron microscopy/ Scanning electron microscope
SMEDDS	Self-micro emulsifying drug delivery systems
STEM	Scanning transmission electron microscopy
TEM	Transmission electron microscopy
TG	Triglyceride
TGA	Thermo gravimetric analysis
VCM	Vacuum compression molding

Preface

Microscopy has been an essential part of most scientific fields for centuries. The first true light microscope was invented in the late 16th century. Over the years, microscopes have been constantly developed and their resolution improved. These improvements led to discoveries that humankind was unaware of, such as the existence of bacteria and cells. One of the greatest innovations in microscopy and imaging was the switch from light to electrons in 1931 by Ernst Ruska and Max Knoll, who built the first transmission electron microscope. Shortly afterwards Max Knoll introduced the first scanning electron microscope in 1935 [1]. The importance of this development was recognized in 1986 when Ernst Ruska was awarded the Nobel Prize in physics [2]. The continuous improvement of microscopes and their impact on research has recently been highlighted by two further Nobel Prizes. One was awarded in 2014 for the invention of super-resolution microscopy techniques such as stimulated emission depletion microscopy (STED) and single molecule microscopy [3], and the other in 2017 for the ability to image biomolecules at atomic resolution using cryo-electron microscopy [4].

Pharmaceutics and drug delivery science require a wide range of microscopic techniques, as the samples are heterogeneous in composition and size. Especially drug delivery is an interdisciplinary field that combines materials science with biological targets such as cells, tissues, organs or model organisms. This wide variety of samples is the basis for the application of numerous imaging techniques [5].

In pharmaceutics, SEM holds a significant position, with its own dedicated section in the European Pharmacopeia [6]. Given this importance, it is crucial to investigate and assess new developments in electron microscopy. The need for new electron microscopy techniques arises from the fact that new active pharmaceutical ingredients (APIs) are becoming increasingly complex and therefore require more advanced drug delivery strategies. These new drug delivery systems need to be characterized by suitable techniques to ensure that their structure and mode of action is addressed properly. Electron microscopy techniques can help to assess the quality characteristics of drug carriers and, in the case of nanomedicines, provide insights into their interactions with biological targets.

In recent years, focused ion beam scanning electron microscopy (FIB-SEM) has been introduced into drug delivery sciences [7]. Although its use is not yet widespread, its potential is promising. These emerging techniques including FIB-SEM provide new analytical capabilities but also benefit from advancements in sample preparation and contrast enhancement.

Aims and Scope

Drug delivery systems usually contain excipients composed of light elements such as carbon and nitrogen, oxygen. These elements in particular make up the majority of active ingredients and excipients resulting in no or minor differences in electron density. However, the materials can have different affinities towards contrast-enhancing agents, so that it is possible to differentiate between the various materials on the basis of the changes in electron density after contrasting. Cellular delivery of nanomedicines using drug delivery systems face similar challenges. Common excipients used for cellular delivery are composed of light elements and are thus nearly indistinguishable from the surrounding biological material.

Resulting from this, the main objective of this work is the visualization of pharmaceutical excipients in drug delivery systems and cells by electron microscopy using contrasting techniques. To achieve this contrast enhancement strategies using osmium tetroxide as well as ruthenium tetroxide are explored.

Neither contrast enhancement of drug delivery systems nor imaging of cellular ultrastructure after nanoparticle treatment by electron microscopy are commonly imaged in the field of pharmaceutics. These investigations will benefit our understanding of ultrastructural features of drug delivery systems and cellular trafficking of drug delivery systems.

Since the topics addressed are very different from one another, this work has two general introductions. One focuses on electron microscopy, sample preparation and contrast enhancement and another focusing on the underlying biological processes of nanoparticle uptake, trafficking and the organelles involved. Following this, each experimental section has its own chapter.

1. Basics of Electron microscopy

1.1. General principle

Electron microscopy is a technique in which a focused beam of electrons is used to produce images. When imaging with electrons, the resolution is not limited by the diffraction limit of the light, so that even smaller objects can be imaged. Although the traditional resolution limit of 0.2 µm set by Abbe for light microscopy has been surpassed by modern light microscopy techniques [8], electron microscopy exceeds even these super-resolution techniques in terms of resolution.

Since all electron microscopic images in this thesis were taken using scanning electron microscopes, the functionality of each technique will be explained based on SEMs as modern SEMs are also capable of transmission measurements. In short, an SEM consists of a sample chamber, usually under high vacuum, an electron gun generating a certain amount of electrons at a certain speed, an electron column focusing the electron beam and scanning it across the sample, and certain detectors to collect the electrons.

1.2. From source to sample

The electron source generates the electrons required for beam formation. The resolution is determined, among other things, by the electron source. Standard SEMs operate with thermionic electron sources from which the electrons are emitted into the vacuum by heating (approx. 2800 K). These emitted thermo-electrons are then accelerated to a desired energy by the anode. The typical thermionic electron sources are tungsten filaments or lanthanum hexaboride crystals. More expensive electron microscopes work with field emission sources in which the electrons are drawn out of the emitter by a magnetic field. These sources offer better resolution. Microscopes that use these sources are called field emission scanning electron microscopes (FE-SEM). Within FE-SEMs a distinction can be made between Schottky emitters and cold field emission. Schottky emission electron guns operate at higher temperatures (1800 K), yet the electrons are emitted from the source tip through the magnetic field. A cold-field emission gun emits electrons at room temperature [9–13] (Figure 1).

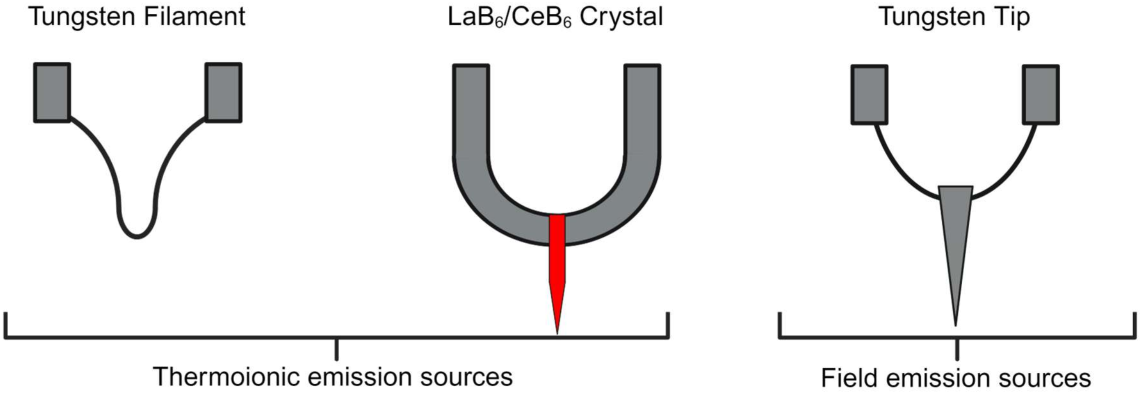

Figure 1: Electron emission sources.
Thermionic sources consist of tungsten filaments or lanthanum hexaboride/cerium hexaboride crystals. Field emission sources are nanometer sized tungsten tips. In case of Schottky emitters these tips are coated with zirconium oxide.

The released and accelerated electrons pass through the electron column through a series of apertures and electromagnetic lenses (Figure 2). The condenser lens together with the aperture control the current and diameter of the electron beam. Following the aperture, the scanning coils are used to scan the beam from point to point over the sample surface. Final focusing of the electron beam is performed using the objective lens. This process is similar for SEM and Scanning transmission electron microscopy (STEM). These techniques only differ in electron detection, which is explained in greater detail later. Generally, STEM is in most cases comparable to conventional transmission electron microscopy (TEM).

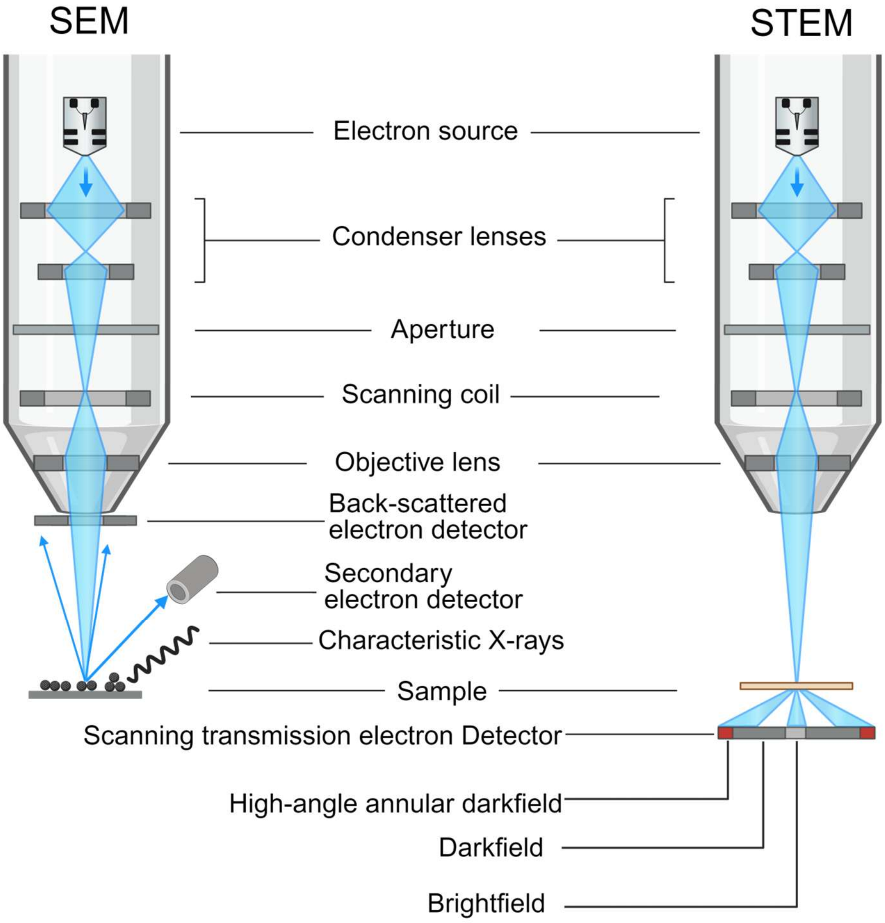

Figure 2: Essential components and detectors of SEM and STEM
SEM and STEM can be carried out in an SEM equipped with the appropriate detectors. Therefore, both techniques are identical in the structure of the electron column and differ only in electron detection.

1.3. Interaction of incident electrons with the sample

The energy of the incident electrons, measured in kilovolts (kV), determines the interaction volume created when electrons hit the sample. This interaction volume increases as the average atomic number of the material decreases. Additionally, the interaction volume increases with higher electron energies. Depending on the microscopy method used, various signals can be generated from this interaction (Figure 3). In bulk samples, interaction volumes can extend to several micrometers in size [14], which can negatively impact the quality of the obtained images.

The interaction between the primary electrons from the electron beam and the nucleus of a sample atom is elastic in nature. This scattering event is known as Rutherford scattering. Primary electrons are attracted by the positively charged nuclei and their trajectory path gets deflected. This deflection is further augmented with increasing atomic number. The primary beam electrons can change their trajectory path after one or numerous scattering events significantly. Such events can cause the electrons to leave the sample surface in the direction from which they came, retaining most of their energy. These electrons are called back scattered electrons (BSE) [15].

Inelastic scattering events from primary electrons with electrons from the electron clouds can result in the release of a valence electron. These electrons are low in energy and thus can only be released by the sample from the topmost layers. Such electrons are called secondary electrons (SE). SE generated in deeper layers cannot leave the sample and results in excited electron states. Ionized or excited atoms quickly convert back to their initial states accompanied by the release of characteristic X-rays or by the release of photons in case of cathodoluminescence [6,15]. The SE and BSE typically used for imaging in an SEM.

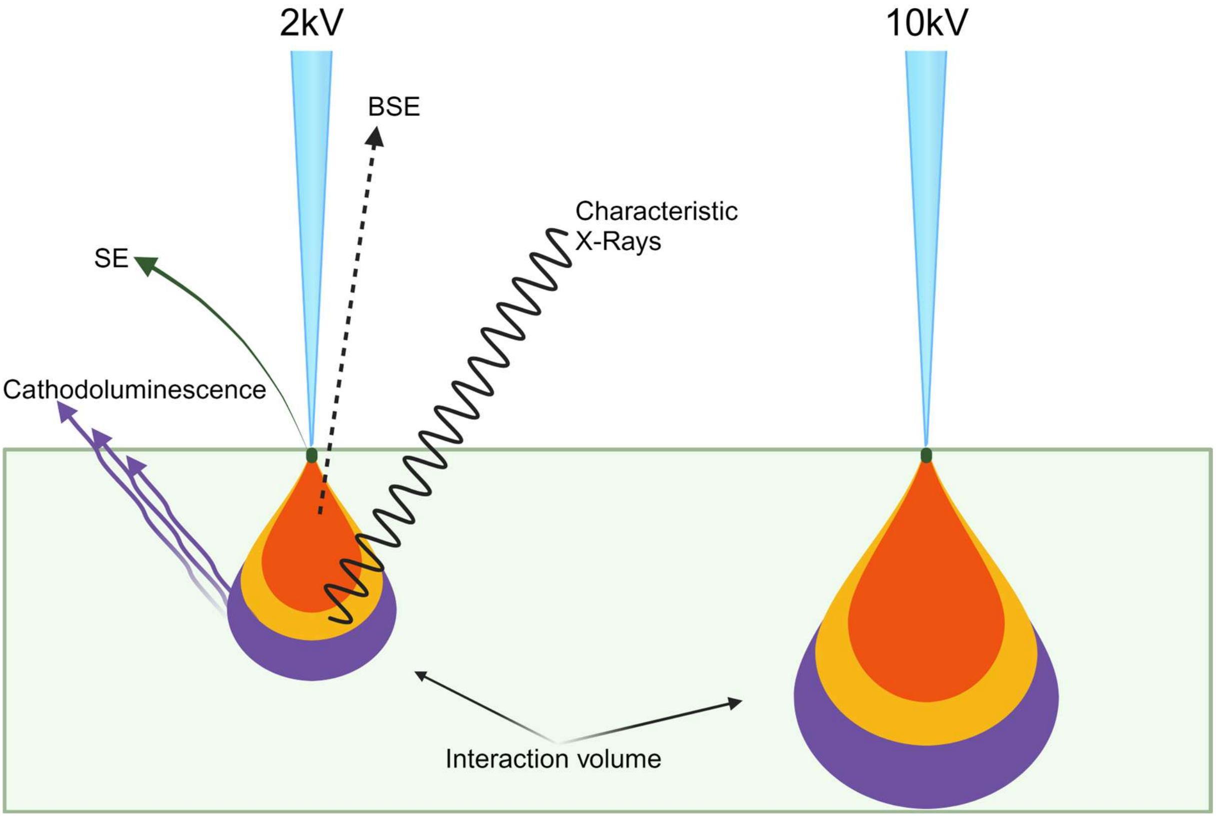

Figure 3: Interaction volumes at different incident electron beam energies and generated signals
The higher the incident electron energies the larger the respective interaction volumes. Resulting from the electron interaction several possible signals are generated which can be used for imaging. The dark green dot is the region where SE are generated from, as only the topmost sample layers release detectable SE. From deeper within the sample, resulting from several scattering events BSE can be collected. The volume from which characteristic X-Rays or cathodoluminescence can be collected is even larger. The larger the interaction volume the higher the negative impact on possible resolution.

Samples that are sufficiently thinned as they are needed for transmission electron microscopy do not show scattering events similar to imaging of bulk samples in SEM. Still electrons are deflected at the samples atom nuclei with deflection dependent on the atomic number resulting in similar processes of image generation. This results in increased resolution due to the high acceleration voltages as well as smaller interaction volumes, due to the limited sample volume. The lower the atomic number more electrons pass through the sample with minimal change in trajectory path and the higher the atomic number the higher the scattering (Figure 4) [9,16].

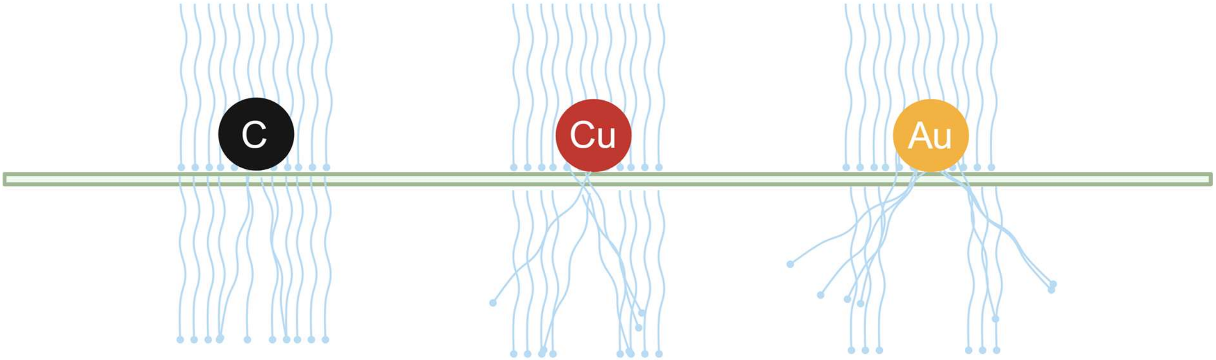

Figure 4: Schematic of 3 different materials with different atomic numbers.
The respective Atomic number increases from left to right from carbon (C) to copper (Cu) to gold (Au). Change in trajectory paths of electrons (blue waves) is depending on different material compositions. The higher the atomic number the higher the amount of scattered electrons as well as increase in scattering angle.

1.4. Scanning electron microscopy

As stated earlier scanning electron microscopy is a techniques in which a surface of a sample is scanned with an electron beam which allows to image morphological features of a sample like surface structure or compositional features. Secondary electrons are used for surface imaging, as they are generated directly at the sample's surface. For compositional analysis, backscattered electrons are employed, as the amount of back scattered electrons generated from a sample region correlates with the local average atomic number [14,15].

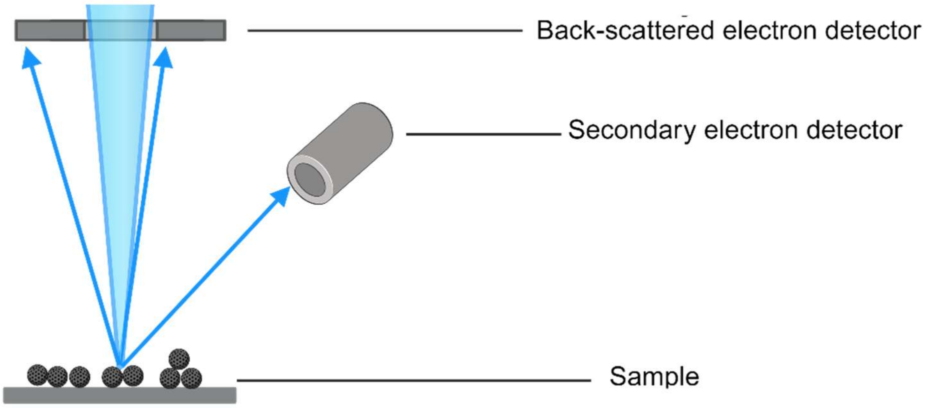

Figure 5:Schematic representation of SEM imaging and detector positions.
The beam of incident electrons hits the sample surface generating secondary and backscattered electrons. SE are used for depicting sample morphology while BSE are used for imaging of composition. The higher the average atomic number of the area scanned, the more BSE are generated. BSE detectors often come in circular form and can be inserted above the sample. Some detectors can activate only certain ring segments, the closer the BSE to the inner rings e.g. closer to the incident beam the higher their compositional information.

Sample size for SEM imaging is primarily limited by the microscope chamber and the holders used. In pharmaceutics, typical sample sizes range from the nanoscale to a few centimeters. Sample preparation involves fitting the sample conductively onto a holder. For non-conductive samples, the surfaces are sputter-coated with a thin metal layer, commonly gold, gold/palladium, or platinum to render them conducting. The type of coating depends on the resolution of the microscope; for field emission scanning electron microscopy platinum is often used due to its small grain size, which typically remains unresolved under normal imaging conditions [17].

Electron microscopes operate in high vacuum conditions, requiring the removal of all volatile substances from the sample. Specialized instruments like Cryo-SEM function at cryogenic temperatures, preventing the evaporation of most volatile substances. When biological samples are imaged by conventional techniques under ambient conditions, they must be fixed and dehydrated. Surface morphology of biological specimens can be analyzed by SEM after critical point drying or the hexamethyldisilazane (HMDS) drying method [18,19]. The sample processing of biological materials for SEM or EM in general will be discussed later in detail.

1.5. Scanning transmission electron microscopy (STEM)

Scanning transmission electron microscopy (STEM) is similar in many ways to conventional transmission electron microscopy (TEM), particularly in its application to samples in pharmaceutics and drug delivery. However, differences can emerge when observing thicker samples. One additional advantage of the STEM technique is that it can also be used within scanning electron microscopes. For STEM to function in an SEM, the microscope must be equipped with a suitable sample holder and a STEM detector. Normally for STEM investigations within a SEM the microscope is operated at 30 kV as it is usually the kV limit within SEMs. In dedicated STEM microscopes higher kV of 200 or 300 are common. To differentiate classical high kV STEM from STEM performed within a SEM the technique can be further defined as STEM in SEM.

The STEM detector (Figure 6) enables different imaging modes. Usually differentiated into bright-field (BF) imaging, dark-field (DF) imaging and high-angle annular dark-field (HAADF) imaging. In transmission electron microscopy, electrons that pass through the sample are used for imaging. These are primary beam electrons. Bright-field imaging uses nearly undeflected electrons, while dark-field imaging utilizes deflected or scattered electrons. A dark spot in a bright-field (BF) image will appear bright in a dark-field (DF) image, as both DF and high-angle annular dark-field (HAADF) imaging primarily collect deflected electrons. Electron penetration is dependent on electron energy, sample composition e.g. average atomic number and sample thickness. Sample thickness is usually below 100 nm. Typical samples within pharmaceutics and drug delivery suitable for STEM/TEM imaging would be nanosized particulates such as nanomedicines, viruses or ultra-thin sections from resin embedded biological materials or polymers. Nanoparticle samples can be dispersed onto TEM mesh grids covered with an electron-lucent polymer film. Bulk samples need to be cut by ultramicrotomy if their physical state allows it. These prepared ultrathin sections of around 70 nm are then placed onto TEM grids. Such bulk samples include epoxy resin embedded biological samples or sections from polymers.

Thus, the requirements of sample size are limiting especially when restricted to 30 kV, as accelerating voltage and sample thickness are intertwined. A certain electron energy is needed to be able to pass through a sample of a certain size. These requirements only apply to a limited number of samples within pharmaceutics.

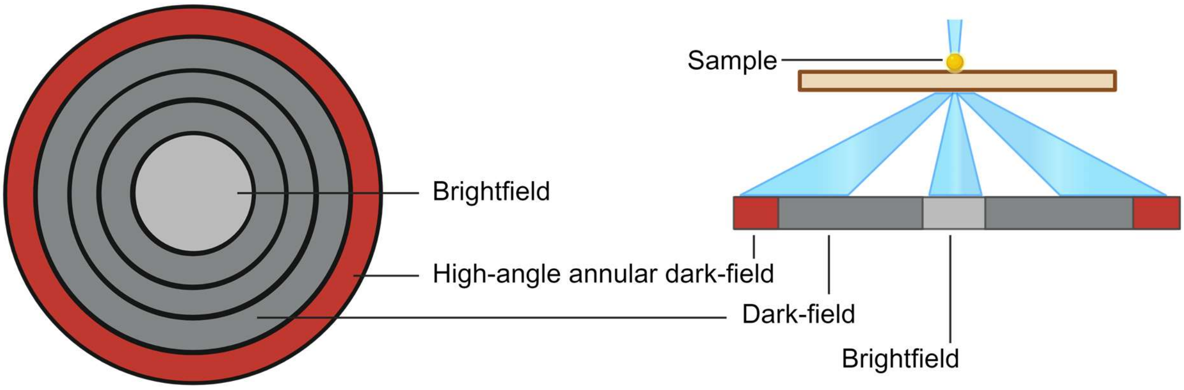

Figure 6: Schematic of a STEM detector and detector regions used for certain imaging approaches.
The left-hand side shows a schematic top view of a STEM detector with the respective detector sections used in different imaging modes. The right-hand side of the figure shows a schematic representation of the STEM detector and how an electron beam (blue) can interact with different detector sections.

1.6. Focused Ion Beam- Scanning Electron Microscopy (FIB-SEM)

The distinguishing feature of the FIB-SEM technique, compared to standard SEM, is its dual-beam configuration. This device uses an electron beam for imaging and a focused ion beam (FIB) for sample manipulation. Standard FIB-SEMs use a liquid metal ion source (LIMS) made from gallium, but other sources are applicable as well [20–22]. Gallium ions are significantly heavier than electrons, and thus their main purpose within such a microscope is for the most part not imaging but sputtering of sample material as they are accelerated onto the sample surface. Since the beam is finely focused this sputtering e.g. FIB-milling, could be performed with high precision and at the exact point of interest. This enables the user to remove sample material, creating local cross sections almost independent of sample composition. Besides this the FIB-milling could be alternated with electron imaging as a tomography tool. Sample material can be removed as thin as 5-10 nm, with each section revealing a new “slice” image which is captured by the electron beam. Since the slice thickness is known, the images can be aligned, segmented and reconstructed into a 3D-Model, which can be analyzed by quantitative means. To prepare cross sections or perform FIB-SEM tomography the region of interest is placed at the eucentric point, which is the point of the microscope were electron beam and focused ion beam image the same point. Usually this involves the tilting of the stage to a certain degree depending on manufacturer (52° for Dualbeam® devices by Thermo Fisher) or sample pretilt at a specific working distance. If the sample is sensitive to ion beam damage, a protective platinum pad can be applied. This pad is created through FIB-assisted chemical vapor deposition (CVD) of an organo-platinum compound (e.g., trimethyl-methylcyclopentadienyl-platinum). Under the high-vacuum conditions of the microscope chamber, this compound is volatilized by heat and introduced to the region of interest via a gas injection system. The ion beam then decomposes the organic framework of the compound, depositing platinum locally in the selected area [23].

In terms of sample preparation, the FIB-SEM technique requires only the standard steps for SEM preparation, and in terms of imaging, it offers the functionality of an SEM. When biological samples are about to be investigated by FIB-SEM, the samples need to be processed like TEM samples, except that the resin block could be imaged without the immediate need for microtomy. In terms of contrasting and staining of biological samples, they usually need more intense staining's compared to transmission based electron microscopy techniques but similar to other SEM based techniques for volume imaging like serial block face imaging [7,24–26].

Depending on the sample dimensions or the imaging goal, certain preparatory steps may be required.

1.6.1. Small or particulate samples

If the structure is directly exposed and visible, it can be milled directly as it is not obscured by the embedding resin or the sample material itself, which could be the case when examining an area within a bulky sample such as a tablet. This direct accessibility is often the case when dealing with particulates in a suitable size range or biological samples prepared using a minimal resin embedding process [27]. Producing a cross-section for qualitative analysis, cross sections of around 100 µm might still be acceptable. However, smaller volumes are preferred for FIB-SEM tomography (Figure 7). For the tomography function usually lower ion doses are needed resulting in increased milling time for each section to be cut resulting in imaging times which can easily exceed 24 hours.

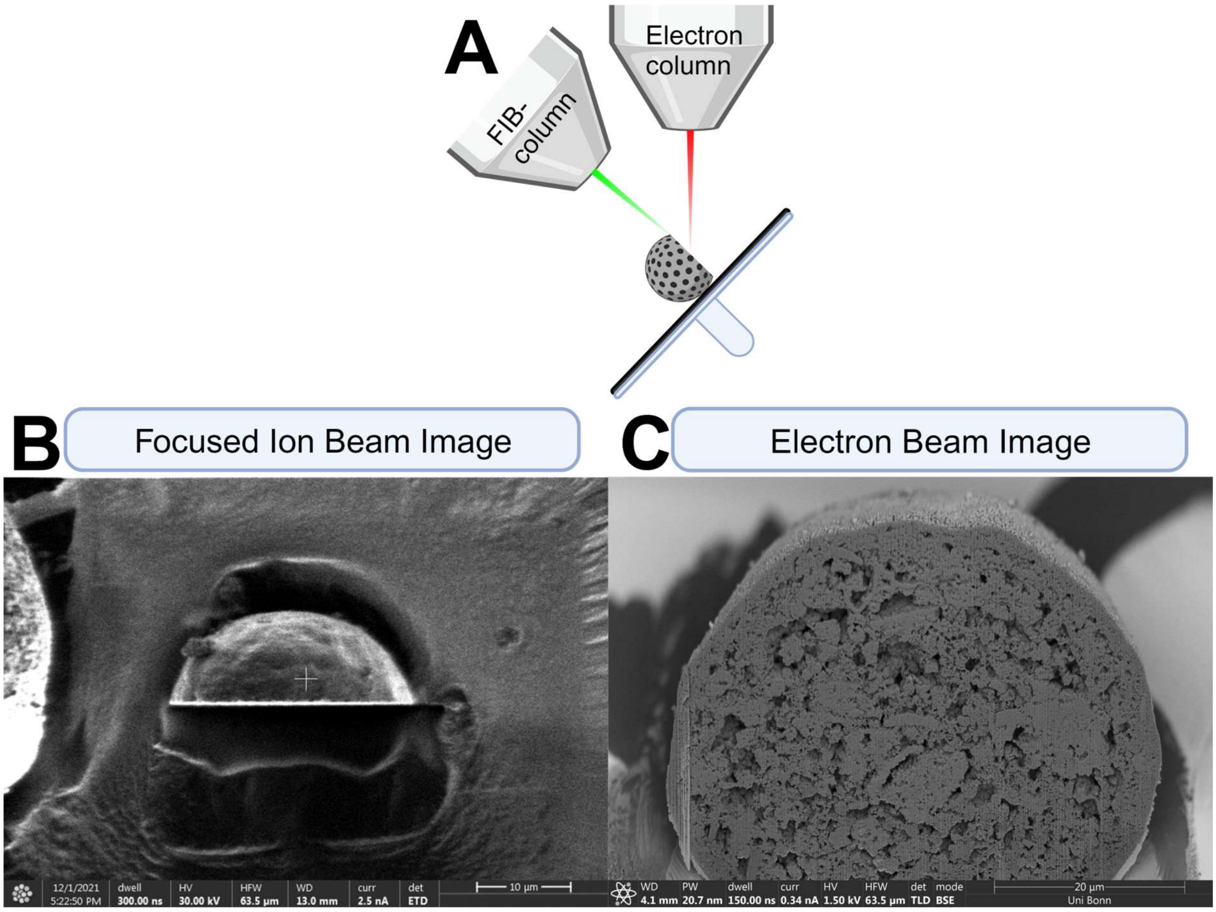

Figure 7: Schematic of FIB-SEM imaging of a particle.
Section A is showcasing the alignment of the sample stage, the sample and the corresponding columns for the FIB and the SEM. Micrograph (B) is displaying the image formed by the ion-beam and section C is the cross-section imaged by the SEM. Modified from [7] with permission from Elsevier.

1.6.2. Large or bulky samples

Large samples such as tablets, implants, resin-embedded cells or tissue require additional preparation steps with the ion beam. These samples usually require a trench, e.g. milling of the surrounding material, to facilitate visualization of the internal structures of interest. The front trench allows the electron beam to access the sample cross-section and ensures unhindered signal acquisition. The side trenches ensure that milled material does not redeposit on the cross-section, which is particularly important for FIB-SEM tomography. The preparation of cross-sections, especially for FIB-SEM tomography, in a bulky sample is inherently more time consuming as the size of the trench correlates with the size of the area of interest (Figure 8).

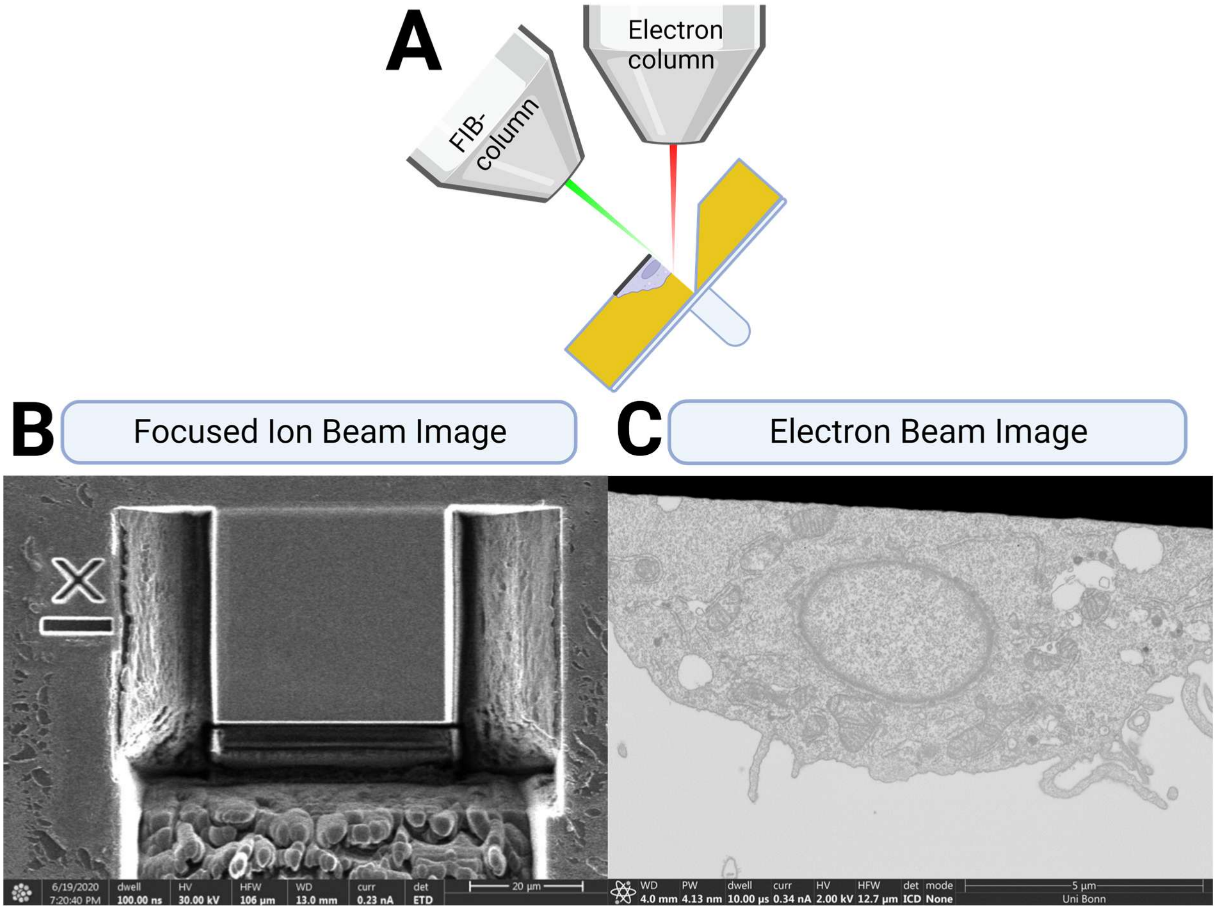

Figure 8: Schematic of FIB-SEM imaging of a bulky sample, in this case resin embedded cells.
Section A shows the alignment of the sample stage, the sample and the corresponding columns for the FIB and the SEM. Displayed is a resin block (yellow) with embedded cells (blue) and a protective platinum pad (black). Section B shows the FIB image with all necessary steps before the beginning of a FIB-SEM tomography run in a bulky sample. The square shaped block contains the volume of interest surrounded by front and side trenches. The underlined X is the fiducial marker used to align itself on. SEM micrograph C showcases the reveled cross-section of the embedded cell. Modified from [7] with permission from Elsevier.

1.6.3. FIB-SEM lift-outs

An additional option of the technique is the preparation of lamellas. Here a section is cut out of the region of interest using the ion beam. This section is then connected to a micromanipulator, a high precision maneuvering devise in a needle shape. This lift-out is then thinned to an electron lucent thickness suitable for transmission electron microscopy. The resulting section can be imaged within the FIB-SEM using STEM or can be transferred to any suitable microscope.

1.7. Energy dispersive X-ray spectroscopy

Energy dispersive X-ray spectroscopy or EDS / EDX is a technique that can be carried out in the SEM or TEM. It uses the release of characteristic X-rays that can occur after the impact of electrons striking the sample material. For characteristic X-rays to be generated, the energy of the electron beam must exceed the critical ionization energy. This ionization energy is linked to an element and its electron shells. As a result, this method can be used to determine which elements are present at the respective point of electron impact, e.g. at the beam position. Based on this, it is possible to analyze the elemental composition either at a specific point or in the entire area under investigation in the form of an element distribution map using the EDS technique.

1.8. Contrast enhancement in Electron microscopy

1.8.1. General Principle

In soft matter materials science and biomaterials research, most substances consist of light elements such as hydrogen, carbon, oxygen, nitrogen or perhaps traces of sulfur or phosphorus. This fact is transferable for materials used in pharmaceuticals, where excipients or APIs are also composed of these atoms. Some polymers or APIs may contain halogens such as fluorine, chlorine, bromine or iodine, but in most cases in quantities too small to be easily identified by contrast, especially using SEM. When structures of interest cannot be distinguished from other materials, it may be possible to enhance the contrast by reacting them with electron-dense compounds improving their visibility in the electron microscope.

In general, there are two different strategies for contrast enhancement, similar to light microscopy, e.g. positive and negative staining techniques. In positive staining, the structure of interest is directly stained due to an innate affinity of the contrasting agent for a particular structure. This can be an ionic interaction, a complex formation or a direct covalent reaction with the structure of interest. “Staining” or contrast enhancement in electron microscopy uses various heavy metal compounds. This is possible because heavy metals or their various salts and compounds have a high atomic number and therefore increase the scattering of electrons.

In the SEM, stained areas will appear brighter in micrographs generated by BSE or obtained by HAADF-STEM. A positively stained structure will appear darker in bright-field STEM. If it is not possible to stain a structure directly, the surrounding structures can be stained negatively. Negative staining creates a darker contrast in the surrounding space around the structure and thus makes it visible through a greater difference in electron scattering/deflection, as the sample itself is not stained. Negative staining is a very common technique in TEM as the resulting images are usually a 2D image (Figure 9). When working with biological samples uranyl acetate, lead citrate, phosphotungstic acid or osmium tetroxide are commonly used. Electron microscopy in materials science, especially for polymers, uses mostly osmium tetroxide and ruthenium tetroxide [16,28–32]. In general, all high atomic number compounds are suitable to generate contrast but require a certain affinity towards the structure of interest.

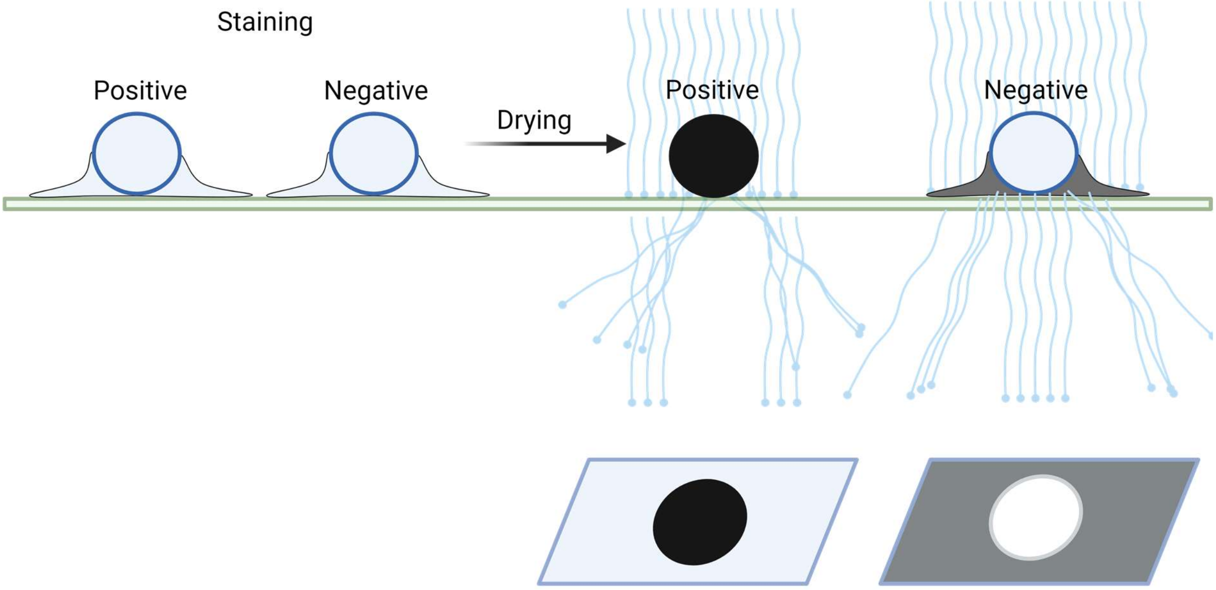

Figure 9: Schematic representation of positive and negative staining. *Schematic illustration of the difference between positive and negative staining in STEM/TEM imaging. Starting from indistinguishable particles, positive staining makes the structure itself visible by introducing electrodense features into it, resulting in the creation of a "shadow" in the schematic bright field image below. Negative staining produces a bright spot in the schematic bright field image. This is due to the presence of the electron-permeable structure of interest at the site, which allows higher electron penetration at that location. For successful negative staining the structure of interests needs to be unaffected by the contrasting agent. The light blue waves resemble electrons. The images below represent the generated brightfield images.*

1.8.2. Osmium Tetroxide Staining:

1.8.2.1. Biological samples

Osmium tetroxide primarily targets cell membranes and other lipid-rich structures due to its affinity towards unsaturated carbon double bonds. Additionally, caused by its reactivity with hydroxyl, amino and thiol groups, it also interacts to some extent with proteins [33–35]. Osmification of tissues reduces lipid extraction during dehydration [33] since many lipids are at least partly soluble in the organic solvents used. The contrast produced by osmium can be enhanced by several osmification steps. This is achieved when bound osmium reacts with bifunctional compounds such as thiocarbohydrazide [35–38]. Other suitable linkers include pyrogallol and tannic acid. Cells and tissues are usually stained by submerging the sample in the staining solution.

1.8.2.2. Material science

When osmium tetroxide is used to stain drug carriers, contact with water can alter the structure of the carrier system. This challenge appears also in soft matter materials science, which is why many staining protocols developed for electron microscopy of polymers use osmium tetroxide vapor [39–42]. The vapor pressure of osmium tetroxide crystals is reported to be 7 mm Hg (0.92 kPa) at room temperature. Using osmium tetroxide crystals for generation of vapor allows for contrast enhancement in the absence of any solvent. Since osmium tetroxide vapor is denser than air, it tends to remain at the bottom of containers [43]. Osmium tetroxide vapor has a remarkable penetration depth into materials and is highly lipophilic. Therefore, it is capable of staining bulk material samples. It is expected that osmium tetroxide reacts faster with amorphous materials than with crystalline ones, as it is the case with ruthenium tetroxide. As shown by Bahr (1954) [34], the reactivity of osmium tetroxide is not limited to carbon double bonds, but extends to various structural moieties, indicating a broader potential application as a contrast agent in drug delivery.

1.8.3. Ruthenium Tetroxide:

Ruthenium tetroxide is similar to osmium tetroxide in terms of its physical properties, has a high vapor pressure and thus enables samples to be stained with this vapor. Due to its high reactivity, there is no commercially available material as it has to be produced in situ [44]. It has only a niche application in contrasting biological samples, but vapor staining is an established method for polymers [28,31,39,40,45–47]. Due to its high reactivity, it can even stain aliphatic hydrocarbon chains. This allows most polymers and polymer blends to be analyzed. Amorphous regions of semi-crystalline polymers show a higher reactivity towards ruthenium tetroxide than crystalline regions, making spherulites and crystallites visible. Ruthenium tetroxide can stain bulk samples, but only reacts with surfaces, which is why it is mostly used to stain ultra-thin polymer sections prepared by ultramicrotomy [39].

1.9. Processing of biological samples for EM

Biological samples can be prepared by several methods for EM depending on the sample processing these samples can be suitable for different EM techniques. The first steps usually include fixation. Fixation is used to stop biological functions in place while maintaining structural integrity. The most common method is chemical fixation with aldehydes, routinely using glutaraldehyde, formaldehyde or combinations of them in buffered solutions. Even though chemical fixation is very common, the gold standard of fixation is high-pressure freezing with subsequent freeze substitution. For the most advanced techniques, electron microscopy under cryogenic conditions is also applicable [48–50]. In the context of this thesis only conventional chemical fixation was used. Following the fixation, the samples are contrast enhanced by electron dense stains. These compounds are commonly heavy metals such as osmium- tetroxide, uranium acetate, lead citrate or phosphotungstic acid. While the contrast agents mentioned are among the most commonly used, there are many others that are used for more specialized applications. Frequently contrasting agents are also combined with one another. Contrast enhancement might need several staining steps, depending on the sample, research question or species. Following contrast enhancement, samples need to be dehydrated using organic solvents mixable with water such as ethanol, acetone or acetonitrile [33,51,52]. Up to this point most preparation protocols are largely similar.

1.9.1. Preparation for morphological investigations by SEM

Starting from the beforementioned point, if cells are to be analyzed morphologically by SEM, the organic solvents need to be removed by a solvent with no or low surface tension. This can be done by critical point drying in a dedicated preparation system. This critical point dryer uses critical carbon dioxide to remove the residual solvent [53]. Alternatively, it is possible to use hexamethyldisilazane (HMDS) for this purpose, which does not require a dedicated device [18,19,54]. The sample can be simply immersed in it, incubated for a few minutes and then the HMDS can be removed and airdried. Following this step, the sample can be prepared as normal for

SEM investigations e.g. glueing the sample onto a sample holder and sputter coating it if necessary (Figure 10) [19,55,56].

1.9.2. Preparation for ultrastructural imaging by STEM, TEM, FIB-SEM

Starting with a fixed, contrast-enhanced and dehydrated sample, the next step is to replace the organic solvent with an embedding resin. The hardness of the resins can be tailored. Typical resins include epoxy, acrylic or various polyester resins [57,58]. Once the sample is fully penetrated by the resin, it is cured. These resin-embedded samples have either been prepared directly within molds or capsules suitable for further sample processing, or they need to be cut into suitable pieces. If the area of interest is already accessible, the sample can be used for FIB-SEM. For STEM and TEM examinations or for samples where excess material needs to be removed beforehand, microtomy is required. A sharp razor blade is used to remove coarse material before the sample is transferred to a microtome or ultramicrotome. Microtomes are devices used for precise cutting, while ultramicrotomes are capable of cutting sections from a sample smaller than 100 nm. Ultramicrotomes work with diamond knives equipped with a boat filled with water. The thin sections cut by the knife edge float on the surface of the water due to the surface tension. With the help of a loop and the surface tension of the water, these ultra-thin sections can be transferred and mounted on grids. These grids can then be used from imaging by STEM or TEM (Figure 10).

1.10. Workflow used in this work

1. Normal cell culture routine. Cells prepared for morphological observations need to be grown on a removable substrate such as a glass coverslip. J774A.1 cells used in this work readily attach to uncoated glass, other cell lines might need a surface coating using polylysin or fibronectin beforehand [59]. Cells for TEM or FIB-SEM can directly be grown inside the plate (Figure 10 I).
2. After applying the cell culture routine/treatment, the sample needs to be washed with buffer such as DPBS or cacodylate (Figure 10 II, III). Phosphate based buffers can form precipitates with many heavy metals and contrast agents [33,60].
3. Chemical fixation by buffered glutaraldehyde,
4. Buffer washing step (Figure 10 IV)
5. Contrast enhancement using osmium tetroxide or osmium tetroxide/ferricyanide (Figure 10 V). Osmium tetroxide will stain unsaturated lipids in the membranes or other unsaturated lipids present in organelles.
6. Buffer washing step (Figure 10 V) Samples for SEM investigation using the HMDS technique were stopped at this point for dehydration but can potentially be further processed if additional contrast enhancement is needed.
7. Incubation with further contrast enhancing substances. In Case of rOTO staining thiocarbohydrazide is added to further enhances osmium contrast by adding a bifunctional linker. Cells turn dark immediately after incubation due to reduction of bound osmium tetroxide.
8. Buffer washing step.
9. Adding osmium tetroxide to react with bound thiocarbohydrazide further enhancing contrast of already osmium enriched areas (Figure 10 VII). If residual amounts of thiocarbohydrazide are present precipitation is likely to occur.
10. Buffer washing step.
11. Start of gradual dehydration by organic solvents (absolute ethanol in this work) (Figure 10 VIII)
12. Further sample processing for either SEM, FIB-SEM or STEM. In the case of SEM by HMDS drying and in the case of STEM or FIB-SEM by epoxy resin embedding (Figure 11).

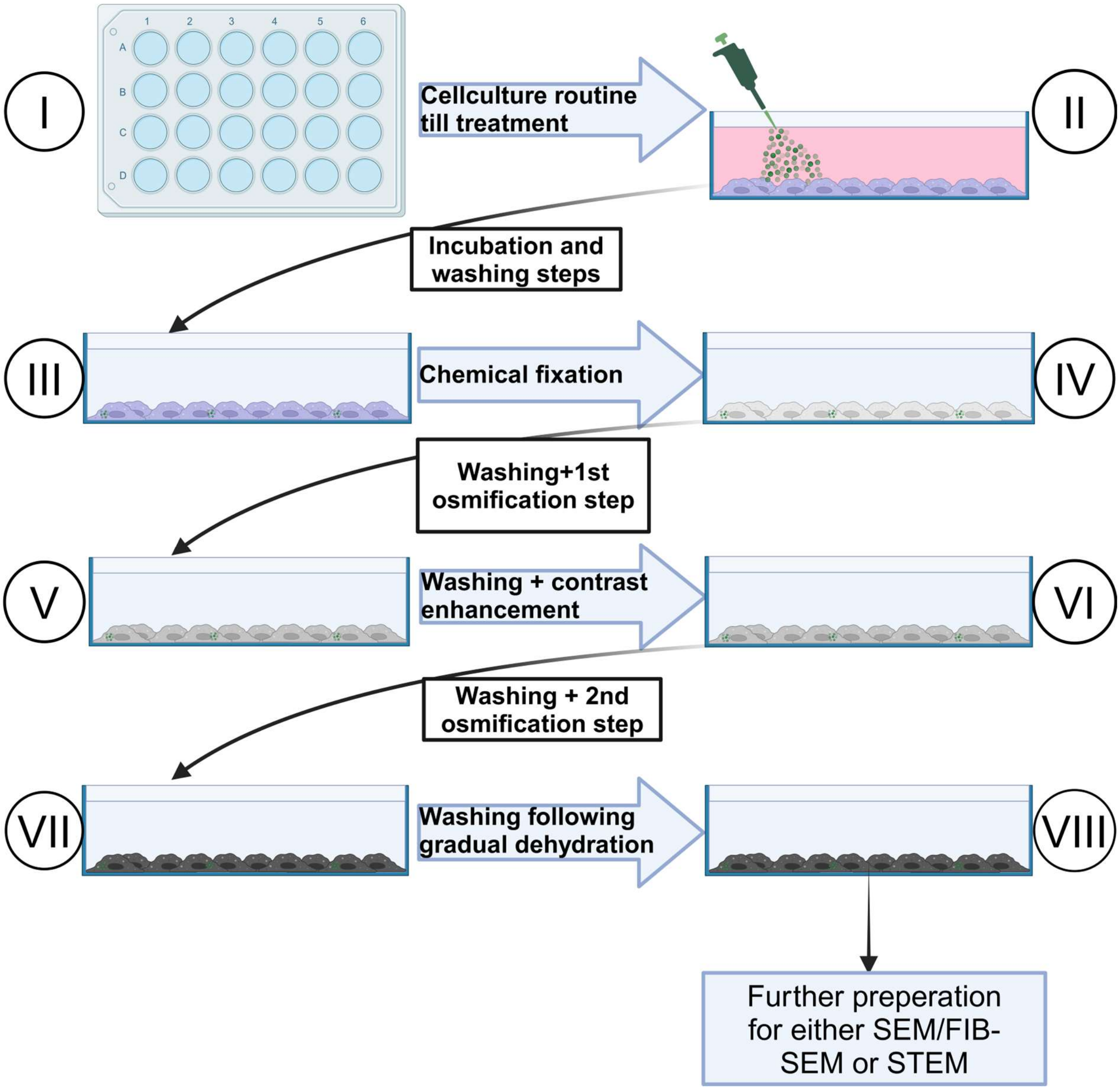

Figure10: Cell culture protocol for EM sample preparation used in this work. *Schematic representation of the sample preparation workflow beginning with cell culture routine to fixation, contrast enhancement and dehydration.*

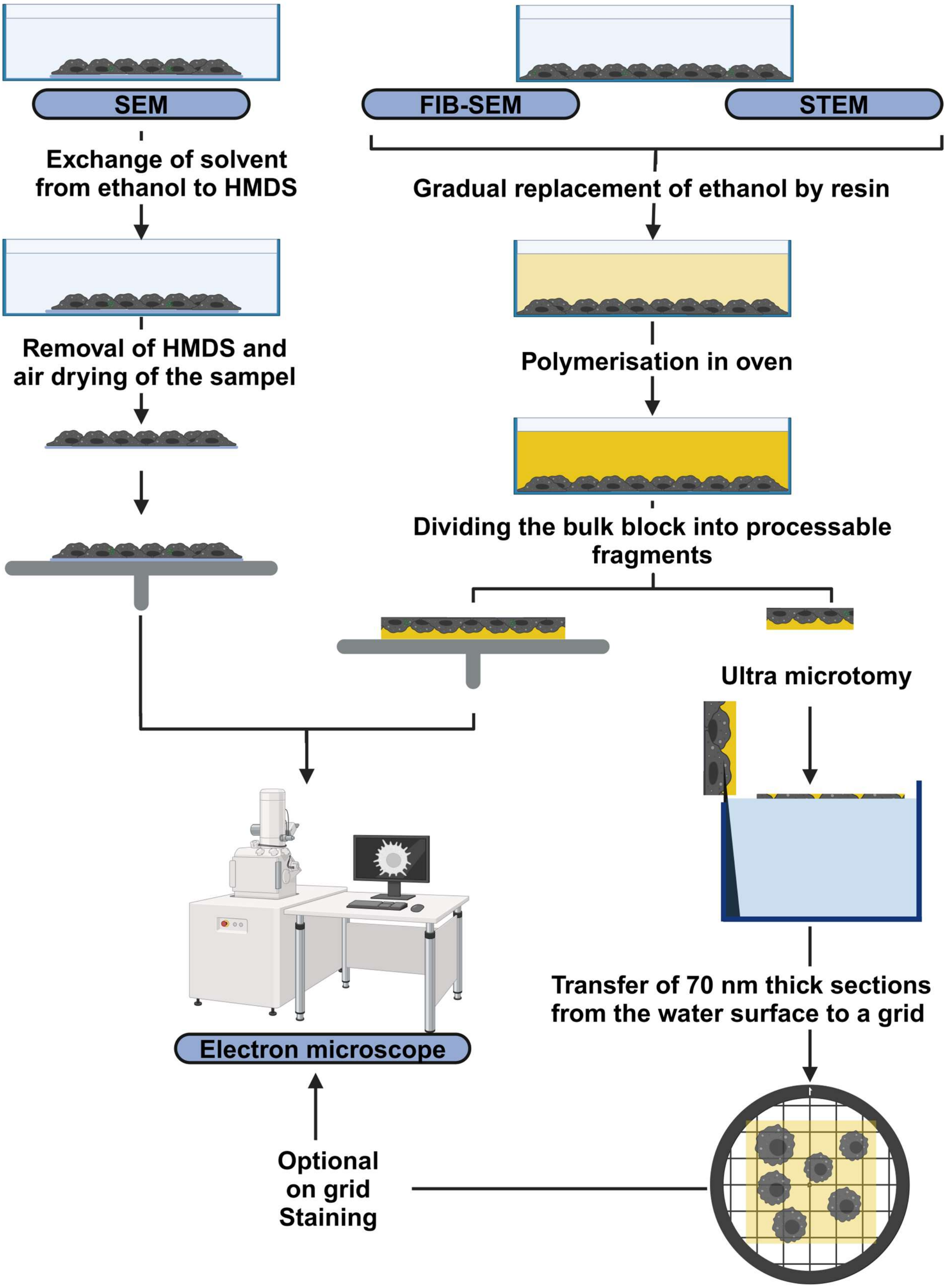

Figure 11: Sample processing of biological samples for different electron microscopic techniques
Schematic representation of the steps needed to transform biological samples from dehydrated cells to samples suitable for EM.

2. Basics of cellular nanomaterial uptake and sample preparation for electron microscopy

2.1. Endogenous uptake routes: Endocytosis

The uptake of active ingredients, such as drug molecules, can be achieved through various mechanisms [61]. These uptake routes are particularly significant for nanomedicines, as they can dictate the intracellular trafficking pathways. In general, the internalization of most nanomedicines occurs via endocytic pathways. The major types of endocytosis are clathrin coated pit mediated endocytosis (clathrin dependent endocytosis), fast endophilin mediated endocytosis (clathrin independent but dynamin dependent endocytosis), caveolin based endocytosis and clathrin independent and dynamin independent endocytosis [62] (Figure 12). Further internalization routes capable of bulk uptake are macropinocytosis and phagocytosis (Figure 13).

Of all potential endocytic pathways, the caveolin based is the most unlikely and less understood and will thus only be mentioned. The pathways displayed (Figure 12) have in common that their first step after internalization is trafficking to the early endosome. From there the receptors and cargo can be recycled back to the cell surface or passed on along the endocytic pathway. A clear distinction between these pathways is challenging and not always possible as the processes can be intertwined. Additionally, a blockade of a presumed pathway can lead to upregulation of other pathways or inhibitors can have many off target effects [62–64] . Nevertheless, the typical endogenous internalization mechanisms will be briefly outlined.

2.1.1. Clathrin dependent endocytosis

This pathway occurs within all mammalian cells and is involved in the uptake of nutrients e.g. iron via transferrin or cholesterol via lipoproteins such as low density lipoprotein. After binding, receptor phosphorylation triggers recruitment of adapter proteins (AP2) which recruit clathrin and form a clathrin coated pit. Following the invagination of the pit, the sphere is laced off by dynamin. A clathrin coated vesicle is within the size range of 100 nm. The clathrin coat of such vesicles can be displayed within an electron microscope [62,65].

2.1.2. Clathrin independent, dynamin dependent endocytosis

The clathrin independent, dynamin dependent endocytosis pathway is also named fast endophilin-mediated endocytosis (FEME) pathway. It is an established endocytic pathway for receptors such as the adrenergic-, dopaminergic receptors and muscarinic receptor 4, some receptor tyrosine kinases of growth factors as well as the interleukin-2 receptor [64]. It is a rapid process which forms invaginated vesicular structures of 60 to 80 nm in widths and up to several 100 nm in depth. Formation is triggered up on activation of the receptors following recruitment of endophilin. Dynamin is involved in lacing off the structure from the membrane.

2.1.3. Clathrin-independent/dynamin-independent endocytosis

This process was shown to exist in drosophila and fibroblast cell-lines [62,66]. It is involved in the uptake of abundant surface receptors, such as hyaluronic acid receptors. Endocytosis is independent from ligand binding to the receptor. Internalization is triggered by lectins e.g. galectins of glycosylated proteins which cause clustering of proteins before internalization. Actin is involved in the process of internalization.

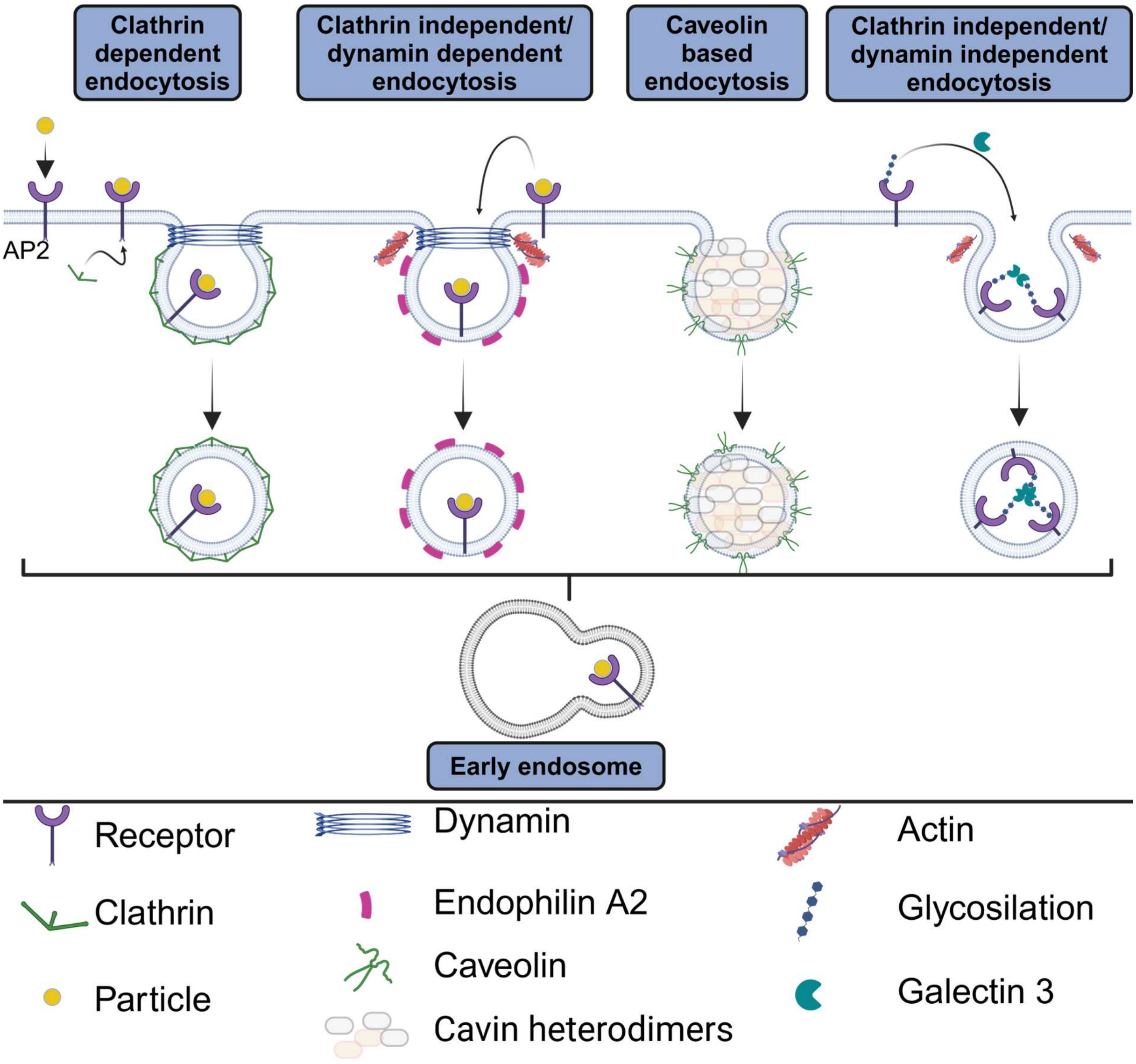

Figure 12: Overview of different types of endocytosis.
Schematic representation of endocytosis pathways and the involved protein machinery. All the endocytosed cargo is transported to the early endosome / sorting endosome for further processing. Modified from [62].

2.1.4. Phagocytosis

Phagocytosis is a specialized process only present in a limited number of cell types, for example macrophages and monocytes. It is an internalization mechanism focused on clearing larger material of endogenous or exogeneous origin such as cell debris after cell death or pathogens like viruses or bacteria but also particulate matter. Large volumes can be internalized depending on size and shape of the material to be phagocytosed [62,67]. Phagocytosis is triggered by receptor activation of scavenger receptors sensitive to a wide range of materials or can be triggered by more specialized receptors. Receptor activation triggers formation of a phagocytotic cup under actin involvement following the phagocytosis of the material/structure. The vesicle formed after this process is called phagosome and destined for further degradation by lysosomes [62] (Figure 13).

2.1.5. Macropinocytosis

Macropinocytosis is a process driven by actin polymerization and the generation of large membrane sheets [68]. These sheets fold back into the cell incorporating extracellular lumen containing solutes and other particular matter, thus it is an efficient way of fluid phase uptake [69]. This process is often referred to as membrane ruffling [70]. Macropinocytosis is not triggered by receptor binding but can be facilitated by certain substances that enhance the activity of this process, such as growth factors or lipopolysaccharide (LPS) [71]. All cells are capable of macropinocytosis to a certain level, as it is an evolutionary conserved form of endocytosis [72]. Depending on the cell type, macropinocytosis activity can vary largely. Macrophages show a high activity of macropinocytosis as these cells permanently screen for potential pathogens [70]. Not every membrane ruffle leads to the formation of a macropinosome, but when it does, a macropinosomal cup is formed, which closes as the membrane ruffle seals with the cell membrane, isolating it from the extracellular space and generating a macropinosome. Macropinosomes can reach sizes up to 10 μm. The size of macropinosomes is quickly reduced as they undergo recycling, fission and remodeling events [73,74]. If internalized cargo is not recycled, the lumen of the macropinosome will be acidified by V-type H+-ATPase and gradually acquire more late endosomal and lysosomal features [75]. This could happen via fusion with the organelles directly or the constituents are being delivered within vesicles (Figure 13).

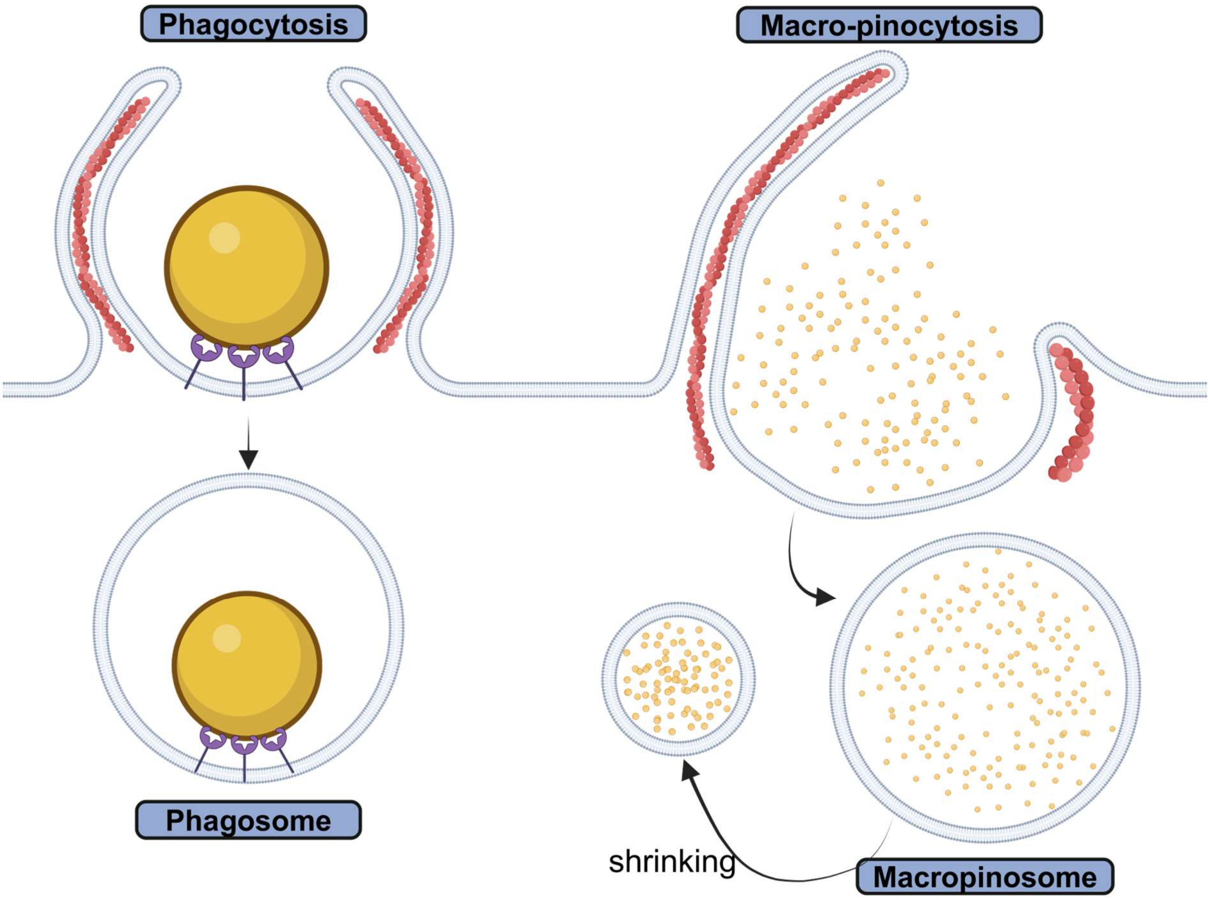

Figure 13: Bulk Uptake mechanisms: Phagocytosis and macropinocytosis. *Schematic representation of phagocytosis and macropinocytosis. Both mechanisms serve as uptake routes for larger particles. In the case of phagocytosis even several micrometers in size can be ingested whereas micropinocytosis internalizes large quantities of nano particulate matter or*

solutes. Particles are displayed in yellow. Both processes require actin filaments (Red) and are thus energy dependent.

2.2. Bypassing the cell membrane by other means

Direct cytoplasmic delivery of APIs or particles can be achieved by various techniques. Either due to chemical properties of a compound/drug delivery vehicle or by means of physical disruption (Figure 14). If a small molecular compound has sufficient low molecular weight while also maintaining a favorable lipophilicity the API can pass the double lipid membrane directly by passive diffusion [61,76]. It is also reported that certain nanoparticles can directly translocate through the cell membrane by diffusion, electrostatic interaction or the use of cell penetrating peptides. Cell membranes can also be physically altered by poration techniques such as electroporation, sono-poration or photoporation. Electroporation treats cells by generating high electromagnetic fields, leading to formation of pores through which nano particles or other actives can enter the cell plasma. Sono-poration uses ultrasound to generate cavitation forces of microbubbles to generate pores through which actives can enter [77]. Photoporation induces transient pores in the cell membrane by laser pulses directly or indirectly under the aid of certain nanomaterials. A comparable approach is micro injection. Using microinjection, the actives or nanoparticles are directly injected by a needle into a target cell. This could be achieved by direct injection or by needle scaffolds used as substrates for cell growth [61,78]. Further techniques harness the possibility of membrane fusion with targeted cells for example using fusiogenic liposomes [79,80].

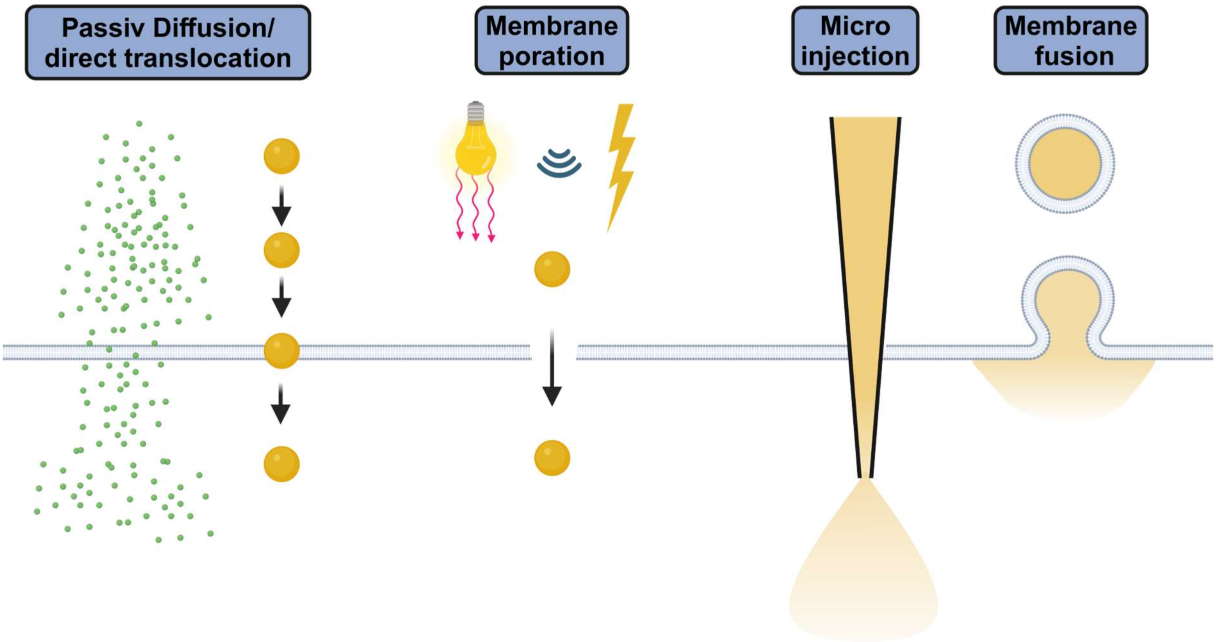

Figure 14: Various options to bypass the cell membrane and endocytosis pathways.
Different techniques to bypass the cell membrane are displayed. Such techniques include passive diffusion/direct translocation, photo-, sono- and electroporation, microinjection or membrane fusion. Modified from [61].

2.3. Characteristics of the endo-lysosomal system

After uptake of cargo via endocytosis, the resulting vesicle will be transported towards early endosomes/sorting endosomes except for cargo internalized by phagocytosis, which is destined for immediate degradation. Following the sorting events, this cargo is either directly recycled back to the cellular surface or passed further along the endolysosomal system reaching late endosomes and lysosomes for final degradation steps. The endosomal vesicles change drastically with the different maturation steps in their acidity and degradative capability (Figure 15). The detailed mechanisms and organelle properties of the endolysosomal system are still the subject of current research. Generally the endosomal system is termed heterogeneously within research and often lacks precise description and understanding [81]. Endosomal maturation involves a multitude of fission and fusion processes. Vesicles receive their modification either by direct delivery from the trans-Golgi network, so that they mature into the corresponding organelle, or vesicles receive the required biological properties from an already existing organelle. Some key features change during the maturation of endosomes. In particular, changes are observed regarding Rab GTPases, the intracellular pH value, the capacity for hydrolytic degradation and in the ultrastructural properties [82]. Rab-GTPases regulate intracellular membrane trafficking [83,84]. The endosomal steps can be roughly subdivided into early endosomes/sorting endosomes, late endosomes/multivesicular bodies and lysosomes (Figure 15).

2.3.1. Early endosomes/sorting endosomes

Under normal circumstances, early endosomes are the first endosomal vesicle after uptake via endocytosis routes. The early endosome regulates the first steps from which cargo is further processed. They are mostly associated with Rab5 [82,85]. Currently the literature is contradictory if the early endosome and sorting endosome are the same organelle or whether the sorting endosome is an independent subspecies [81,86]. Endosomal domains associated with sorting or sorting endosomes are characterized by Rab11. Degradative enzymes can already be found at the early endosomal stage even though early endosomes are not a main degradative organelle. This is backed up by the fact that not all degradative enzymes located in the endolysosomal pool of hydrolases have their pH optimum at lysosomal pH levels but rather at the pH associated with early endosomes e.g. Cathepsin S [87–90]. Early endosomes have a slightly acidic pH within the range of 6.0 to 6.5 [87,91]. Ultrastructural wise are early endosome characterized by sizes of up to 500 nm. The organelle is surrounded by a single lipid membrane, while often spherical elongated structures may exist. Only seldom visible cargo exists. It is possible to depict clathrin coats after fusion with a clathrin coated vesicle with EM [92].

2.3.2. Late endosomes/ multivesicular bodies

Late endosomes are characterized by an increased size normally ranging from 250 nm to 1000 nm [92]. They are characterized by a GTPase switch from Rab5 towards Rab7 and gradual acidification to a pH of around 5.5 by V-ATPase [81,93,94]. This switch is also characterized by an increase of digestive / hydrolytic function [87,90]. The late endosomes is a multifunctional organelle which serves multiple purposes amongst others further degradation by acquiring more degradative functions, excreting contents back towards the cell membrane or function as an intermediate step within autophagic processes [95–97]. In general, the organelle ultrastructure is composed of a single surrounding lipid layer containing vesicles and spheres of varying amount [92,98]. Except for the cargo, the organelle lumen is electron lucent. In terms of ultrastructure, multivesicular bodies (Mvb) contain vesicular structures, among others, but are not limited to such features, as they may contain exogenous material such as particles, viruses or nutrients, but also endogenous material, e.g. autophagosomes from autophagy. Late endosomes containing autophagosomes are called amphisomes (Figure 16), as their appearance differs from normal late endosomes. The late endosome/Mvb is a single membrane organelle but after fusion with an autophagosome, the membrane organization can have similarities with a double lipid membrane as the membrane of the autophagosome will be visible. Since the autophagosome inner membrane is decomposed over time this feature is dependent on the time point of fusion. Often fragments of the membrane will be visible [96].

2.3.3. Lysosomes

Lysosomes are heterogenic organelles with varying structure and sizes. They can be tracked or identified by their most abundant surface proteins the LAMP1 (lysosomal-associated membrane protein 1) and LAMP2 [99]. Endosomal structures can either directly fuse with a lysosome, acquire lysosomal contents by a "kiss and run" process or acquire the constituents from the trans Golgi network [100,101]. Besides the surface proteins, lysosomes contain over 50 hydrolases at an acidic pH of around 4.5 -5.0 [102]. The hydrolases enable the organelle to degrade most biological materials, repurposing it for cellular metabolism. When speaking of lysosomes the name is often used as an overall term but lysosomes could further be defined, depending on structure or cargo they obtained [96]. The inner membrane of lysosomes is negatively charged due to an abundance of bis(monoacylglycero)phosphate (BMP) [103–105].

Unfused lysosomes, without much cargo to degrade, are relatively small and often electron dense in stain and can contain membrane whirls. Lysosomes degrading endocytosed material can be much larger in size up to several μm and contain heterogeneous content and thus are called endolysosomes [106]. If lysosomes were to fuse with amphisomes or autophagosomes the resulting organelle would be an autophagolysosome (Figure 16).

The exact origin of these organelles can be challenging to identify. Due to the multitude of variable cargos and sizes their ultrastructure is also heterogeneous. They are limited by a single membrane, often being electron-densely stained [92,96,98].

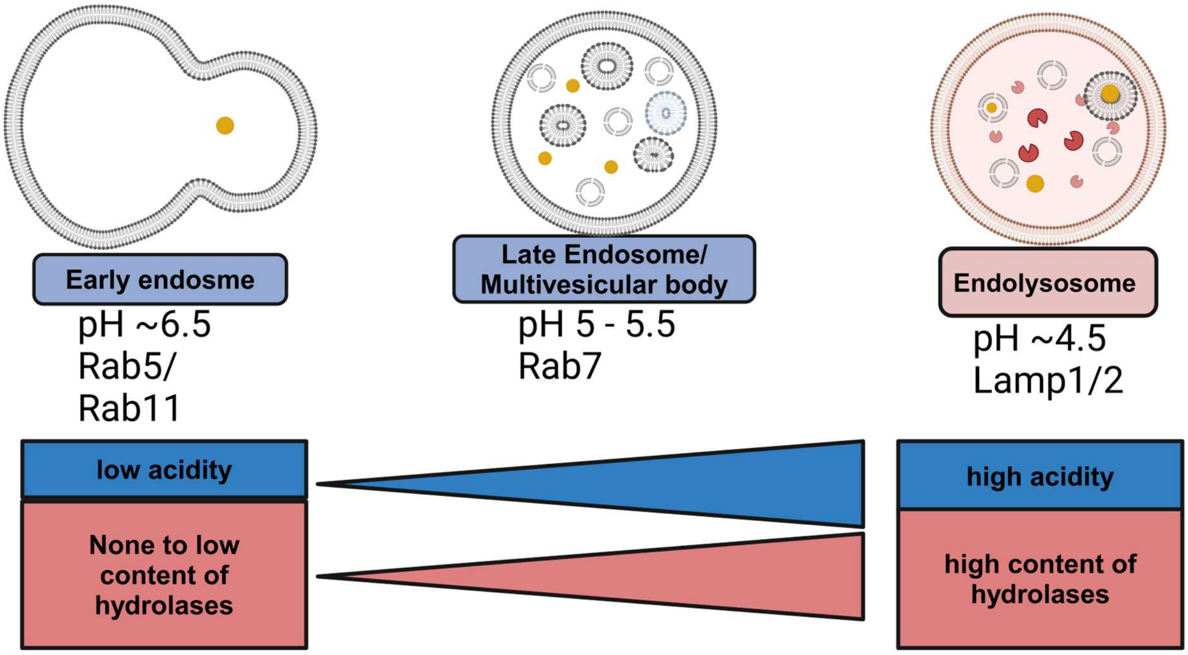

Figure 15: Characteristic changes during endo-lysosomal maturation
Schematic representation of Endosomes and lysosomes and their key characteristics.

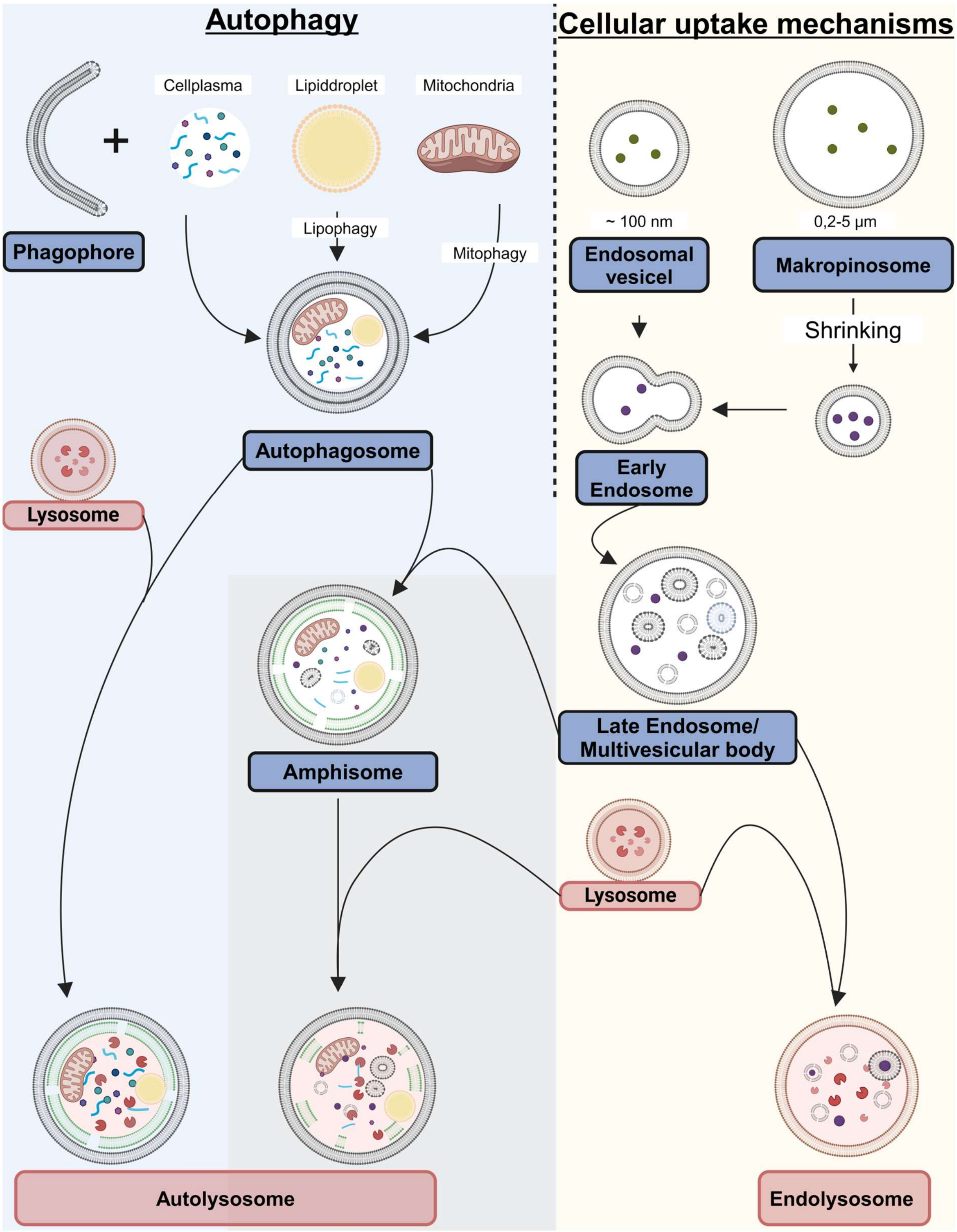

Figure 16: Interconnection of the endolysosomal system with autophagy.
Schematic representation of the endolysosomal and autophagosomal systems. This illustration shows the complexity and interdependence of the two systems. The lipid layers depicted show the actual structures. Most organelles are enveloped by a single membrane, except for the autophagosome and the phagophore itself. As shown by the deteriorating membrane in green, the inner cell membrane is destined for degradation but may still be visible at various stages of degradation. The cargo of endocytosis and autophagy can possibly meet at the amphisome stage or merge after lysosomal fusion.

2.4. Fate of drug delivery systems within the endolysosomal system

Endocytosed DDS are usually degraded quickly within the endolysosomal system. Nevertheless, drug delivery strategies exist to facilitate endosomal escape. Endosomal escape is important for the delivery of cargo which would otherwise be degraded for example when delivering biomolecules such as RNA, DNA or proteins to a cell. These substances are readily degradable by the lysosomal hydrolases. Proposed tactics which facilitate effective delivery of biomolecules are for example lipid nano particles with specific lipid combinations, delivery of ionizable (bio)-polymers or by cotreatment of lysosomotrophic substances [107–112]. The exact processes are still not very well understood and controversy discussed. Nevertheless, many studies could show successful delivery of the corresponding APIs. Especially the mRNA loaded lipid nano particle (LNP) technology attracted recent interest due to the commercial success of the COVID-19 vaccines and its future potential. Some studies have been published showing incorporation of the cargo mRNA from LNPs into exosomal vesicles which originated from exocytosis of multivesicular body content. They could also show that treatment with the resulting exosomes could lead to successful delivery [110]. Another research showed that extracellular vesicles also played a crucial role as a resistance mechanism in cancer cells. They found that LNPs attached themselves to extracellular vesicles, and the released extracellular vesicles were transported into the bloodstream and internalized by Kupffer cells leading to degradation [113].

Another often proposed way of escape is the proton sponge effect. Larger molecules, for example lipofectamine or polyethyleneimine, are substances with large amounts of basic amine motives. These functional groups can potentially bind many protons within the acidifying organelles of the endolysosomal system thus buffering or elevating the pH value. It is proposed that the pH value of the lysosomes increases and therefore leads to protection of the cargo and escape. The pH elevation is currently discussed contradictory within research. With findings supporting the theory, while others proving it false [111,112]. Additionally, it is proposed that lysosomes may swell when the V-ATPase is permanently pumping protons into the lumen to reach the desired pH. The swelling is said to be caused by an increase of osmotic pressure due to accumulation of chloride ions leading even to a bursting of lysosomes. Additional proposed mechanisms how the payload of such carriers is released and successful delivered involve membrane permeabilization or fusion processes of the lysosomal membrane [112].

A third option which can be used to successfully enhance delivery is the use of lysosomotrophic substances. Lysosomotropic substances include all substances which alter the lysosomal system. Although the term lysosomotropism is not frequently used in drug delivery science, it can be assumed that many active substances or excipients affect the endolysosomal system. Many of the substances are small molecules with weak basic properties who can diffuse passively into the cell and alter its function. Especially weak bases can accumulate within acidic organelles such as the lysosome or multivesicular bodies. Other routes of uptake use endocytosis to reach the endolysosomal system. Frequently used lysosomotropic substances used within research are for example chloroquine or bafilomycin [108]. Lysosomotrophic substances for example are used to influence for example the endolysosomal degradative function, fusion processes or acidification of the corresponding organelles [114–116]. A study could show that chloroquine co treatment resulted in improved mRNA delivery [117].

2.5. Imaging of nanoparticle uptake

To study the endo-lysosomal system and drug carrier internalization routes many microscopy-based methods can be used. Especially prominent are confocal laser scanning microscopy-based techniques using fluorescent dyes. This is especially true within the drug delivery context. Usually, a fluorescently labeled DDS is used to track its localization within the cell to prove uptake or subcellular localization. To further elucidate the cellular localization organelles can be stained by different dyes to prove colocalization. But as displayed in figure 16 colocalization should also be viewed in ultrastructural context, as not only the colocalization matters but also the surrounding ultrastructure. If target and drug delivery system meet within the lysosome, both are destined to be degraded. Electron microscopy-based techniques are capable of imaging cellular ultrastructure. Interestingly the capabilities of EM are mostly neglected within the drug delivery context leading to large knowledge gaps in terms of sample preparation of biological samples, how cellular ultrastructure changes or how to “stain” certain features of drug delivery systems rendering them visible in the EM.

The most sophisticated and powerful approach suitable to tackle the questions of nanoparticle trafficking would be the combination of both techniques in the correlative light and electron microscopy (CLEM) method [118–120].

3. Visualization of excipients using ruthenium tetroxide

3.1. Introduction

Polymers are a frequently used class of excipients with a multitude of possible functions in drug delivery. They are used as binders, tablet disintegrants, coatings for controlled or delayed drug release or as drug carriers themselves. These functions can be achieved by using various polymers or blends of polymers [121,122]. The compounding of active ingredients, excipients and polymer could be achieved by physical mixing and compaction, dissolving and drying or by melting the compounds together [123,124]. During the design process of a DDS multiple process steps may be needed. Often polymer and API are processed together for example to achieve controlled drug delivery or dissolution enhancement [125,126]. If compounding of API and polymer is performed by melting or dissolving, the mixture will solidify after removal of the solvent or after cooling down.

This solidified product can have various physical appearances. The API could be completely recrystallized within the surrounding polymer matrix on one hand whilst on the other it is possible that the API is molecularly dissolved in amorphous state within the polymer, such a system is called an amorphous solid dispersion [127]. Such ASD systems are of interest as they can enhance drug dissolution and are an ongoing longstanding research topic within pharmaceutics. Additionally, intermediate states between these two extremes exist, as a solid dispersion could recrystallize over a certain time period. The characterization of such systems is usually performed by X-ray diffraction (XRD), calorimetric techniques such as dynamic scanning calorimetry (DSC), Fourier transform infrared spectroscopy (FTIR) or polarized light microscopy (PLM) [128,129], but crystalline structures can also be visualized by EM [130].

Electron microscopy of polymers is challenging due to their beam sensitivity, their weak contrast differences and their often-amorphous structure and appearance. This applies both to classical polymer science and to polymer excipients used in drug delivery. Polymers can generally be amorphous or semi-crystalline. Amorphous polymers can still show ultrastructure, for example a phase separation between the different building blocks of a block polymer. Similar observations can be made when imaging polymer blends especially between immiscible polymers [28]. Semicrystalline polymers have distinct structural properties such as crystallites and spherulites [131]. These structures show a higher degree of order and are often organized in lamellae growing from the nucleation point in the center in cone shapes. Crystalline regions are separated by amorphous regions. It is possible to analyze these structures with EM. These structures can be imaged directly using certain techniques such as cryo-EM or specialized atomic force microscopy techniques. Depending on the microscopes available, contrast enhancement is required before imaging. A contrast agent used to visualize different polymer phases of polymer blends, block polymers and semi-crystalline polymers is ruthenium tetroxide. Ruthenium tetroxide is a highly reactive volatile compound. Due to its high reactivity and volatility, its vapor can be used for contrast enhancement thus avoiding structural alterations by solvents [28,31,39,40,45–47].

Since ruthenium tetroxide is used to stain semicrystalline polymers, it is suggested that crystalline regions caused by API crystallization may be displayed by EM techniques after ruthenium tetroxide staining. Additionally, it should be possible to display drug rich phases within polymers if there is a difference in reactivity of the different phases towards ruthenium tetroxide. It is expected that most organic substances used in the field of pharmaceutics obtain a certain reactivity towards ruthenium tetroxide as even aliphatic hydrocarbons show a strong reaction. Since ruthenium tetroxide only stains the surfaces of samples without deeper penetration into the sample flat samples are easier to interpret. Consequently, artificial formulations and polymer mixtures were prepared by dip coating glass coverslips and stained by ruthenium tetroxide vapor. These samples were then imaged by SEM.

3.2. Material and Methods

3.2.1. Material

Table 1: Material Section for contrast enhancement using ruthenium tetroxide

Material	Brand name	Vendor
Celecoxib		Swapnroop Drugs&Pharmaceuticals
Copovidon (copolymer of 1-vinyl-2-pyrrolidone and vinyl acetate 6:4)	Kollidon VA 64	BASF
Dichloromethane (DCM)		Sigma Aldrich
Ethanol absolute		Sigma Aldrich
Ethyl acetate		Sigma Aldrich
Ethylcellulose 45	Ethocel standard 45 Premium	Sigma Aldrich
Glass-coverslips (9 mm)		VWR
Hydroxypropylcellulose		Carl Roth
Methacrylic-acid-ethyl-acrylate copolymer	Eudragit L100 55	Evonik
Methanol		VWR
Polivinylpyrolidone K90	Kollidon K90F	BASF
Poly(ethylacrylate-co-methyl-methacrylate-co-trimethyl-ammonioethyl methacrylate chloride) 1:2:0.1	Eudragit RS	Evonik
Poly(ethylacrylate-co-methyl-methacrylate-co-trimethyl-ammonioethyl methacrylate chloride) 1:2:0.2	Eudragit RL	Evonik
Poly(lactic-co-glycolic acid)	Resomer 502H	Evonik
Polycaprolactone (PCL) 45k		Sigma Aldrich
Polyethylenoxide 200k (PEO)		Carl Roth
Polyvinyl caprolactam-polyvinyl acetate-polyethylene glycol graft copolymer	Soluplus	BASF
Ruthenium (IV) oxide hydrate		Sigma Aldrich
Sodium periodate		Sigma Aldrich
Sodium thiosulfate		Sigma Aldrich

3.2.2. Dip coating:

Coverslips were dip coated by immersion of coverslip within 2 ml of the coating mixture. Coating and stock solutions contained 10% solid content. Final polymer mixtures were prepared from stock solutions. After dip coating, samples were airdried and cured over a hotplate to form an homogeneous film. Film formation was confirmed by visual change from a turbid to a homogeneous clear coating.

Table 2: Solvent and polymers used for dip coating

Substance	Solvent
Celecoxib	Ethyl acetate
Ethylcellulose	DCM
Eudragit L100 55	50/50 Ethanol absolute, Ethyl acetate
Eudragit RS	DCM
Kollidon VA 64	DCM
PLGA	Ethyl acetate
Polycaprolactone	DCM
Polyethylenoxide 200k (PEO)	DCM
PVP K90	Methanol
Soluplus	DCM
Mixtures	
50/50 Celecoxib/Polycaprolactone	50/50 Ethyl acetate, DCM
10/90 Celecoxib/ Polycaprolactone	10/90 Ethyl acetate, DCM
50/50 Celecoxib/Eudragit 100 55	75/25 Ethyl acetate, Absolute ethanol
50/50 Celecoxib/PLGA	Ethyl acetate
75/25 Ethylcellulose/ Eudragit RL	DCM

3.2.3. In-situ preparation of ruthenium tetroxide and contrast enhancement

Ruthenium tetroxide needs to be prepared in- situ under the fume-hood due to its high reactivity. A small glass exicator was used as a vessel for the staining and the preparation of the ruthenium tetroxide solution. 3.2 g of sodium periodate were dissolved within MilliQ water. Following this step, the solution was placed in an ice bath and cooled before adding the ruthenium-(IV)-oxide. When all ruthenium-(IV)-oxide was dissolved the glassware was removed from ice bath to enhance ruthenium tetroxide evaporation. A glass mech with the samples e.g. coated coverslips was placed within the exicator and closed with a lid but still aerated by a glass faucet. Samples were exposed to the ruthenium tetroxide vapor released by the solution for 20 to 25 minutes. Incubation time within the vapor might vary depending on the sample. Samples turn gradually darker due to reaction with ruthenium tetroxide. Depending on the visual appearance the reactivity was estimated. Solution was discarded after reduction of all reactive compounds using sodium thiosulfate. Occurrence of ruthenium trumpets was used as an indicator of overstaining [39,44].

3.2.4. Electron microscopy

Coverslips were glued onto SEM stubs using silver conductive paint and sputter coated with platinum using the Q150T S (Quorum Technologies, Judges House, Lewes Road, Laughton, East Sussex, United Kingdom) at 30 mA for 20 seconds. Samples were imaged at 5kV using BSE collected with the concentric backscattered detector using a Helios G4 CX FIB-SEM microscope (former FEI Company now Thermo Fisher Scientific Inc, Eindhoven, Netherlands).

3.2.5. Energy dispersive X-ray spectroscopy

Samples used for EDS analysis were the same samples prepared for standard SEM imaging. Imaging was performed using a Hitachi SU-3500 SEM (Hitachi Ltd., Tokyo, Japan) at 10 kV acceleration voltage and 80% spot intensity. Elemental analysis was performed using a EDAX Element system (Ametek, Berwyn, Pennsylvania, United States of America). At least 30 EDS maps were collected per region of interest.

3.3. Results

As expected, most samples showed some kind of reaction after ruthenium vapor staining. Affinity towards ruthenium tetroxide was classified just qualitatively by the degree of blackening in three groups. Weak affinity for barely visible changes, medium and high for intense darkening during incubation (Table 3).

Table 3: Visual change of sample during ruthenium tetroxide staining

Amorphous polymers	
Sample	Degree of blackening
Ethylcellulose	Strong
Eudragit L100 55	Medium
Eudragit RS	Weak
Kollidon VA 64	Medium
PLGA (Resomer 502H)	Weak
PVP K90	Medium
Soluplus	Medium
Semi crystalline polymers	
Polyethylenoxide 200k (PEO)	Strong
Polycaprolactone (PCL) 45k	Medium

The ruthenium treatment on polymer covered coverslips prepared by dip coating resulted in various structural features. Only the polymers depicted showed structural features, whereas others couldn't be imaged due to either beam sensitivity or no observable structures.

The amorphous polymers PVP K90 (Figure. 17 A) and Soluplus (Figure 17 B) displayed a veiny structure of alternating electron density without a directly recognizable order. Semicrystalline polymers like polycaprolactone 45k (Figure 17 C, D) and or polyethylene 200k (Figure 17 E, F) show spherulite structure with crystalline and amorphous regions (Figure 17 C, E). Crystalline structures are better visible within the higher magnification sections (Figure 17 D, F). These crystalline structures in sections C-F are visible as darker regions with amorphous regions in bright.

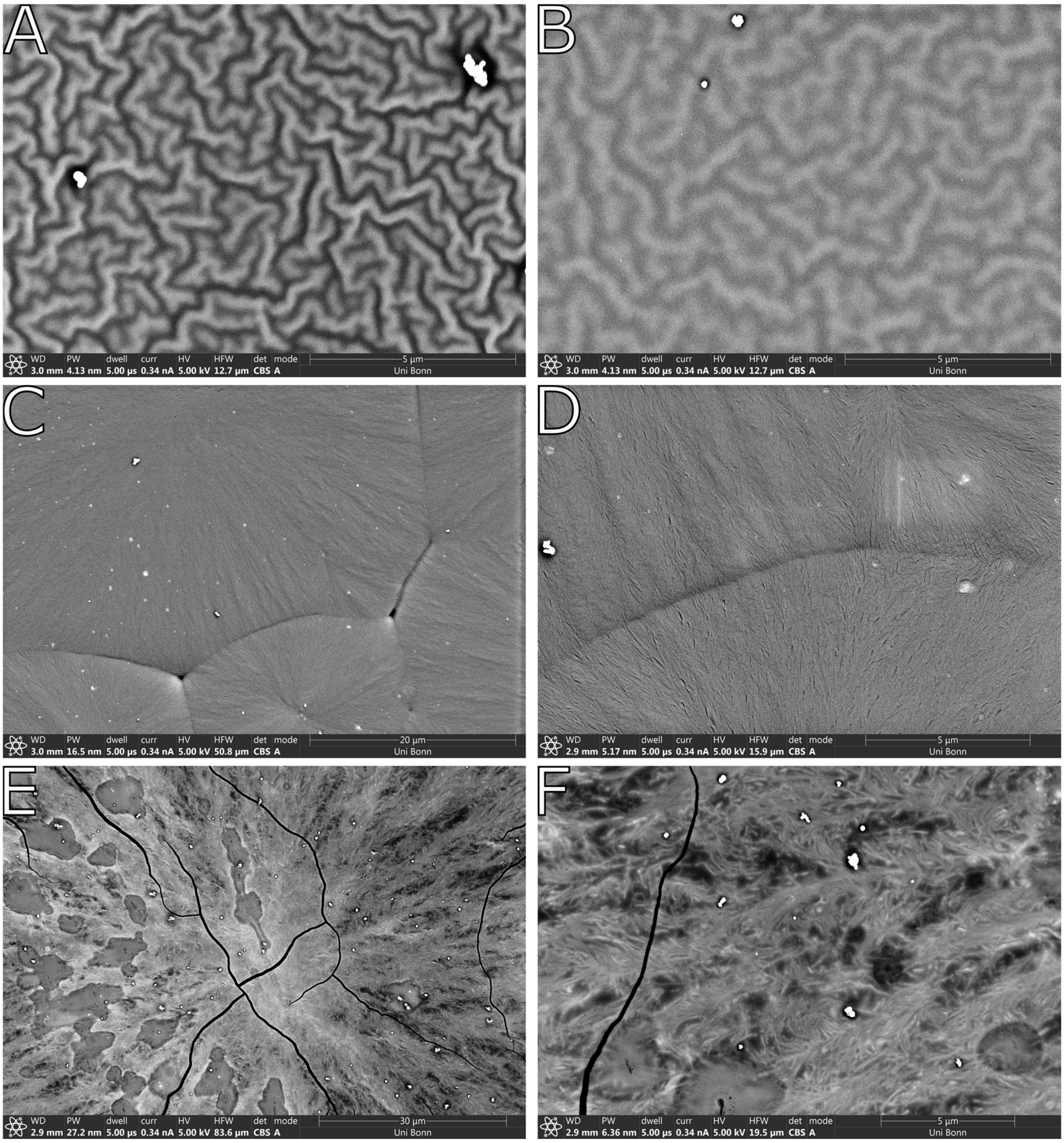

Figure17: Polymers after ruthenium tetroxide exposure.
Ruthenium rich phases are displayed in bright. BSE micrograph section (A) show PVP K90, Soluplus (B), PCL 45k (C, D) and PEO 200K (E, F). The spherulites (C, D) and crystalline regions (C -F) are well visible.

The polymer mixture composed 75% ethylcellulose and 25%Eudragit RL was successfully stained and imaged using BSE (Figure 18). This 75/25 ratio was chosen for the system to ensure that a clear identifiable outer phase exists. Three different phases are visible differentiated by contrast (Figure 18 A-C). Micrograph section A and B showed a bright electron dense surrounding polymer containing cracks displayed in in black. Embedded within this structure are dark, less electron dense circular phases (Figure 18 A-D). Additionally, a third phase is visible with intermediate contrast (Figure 18 C).

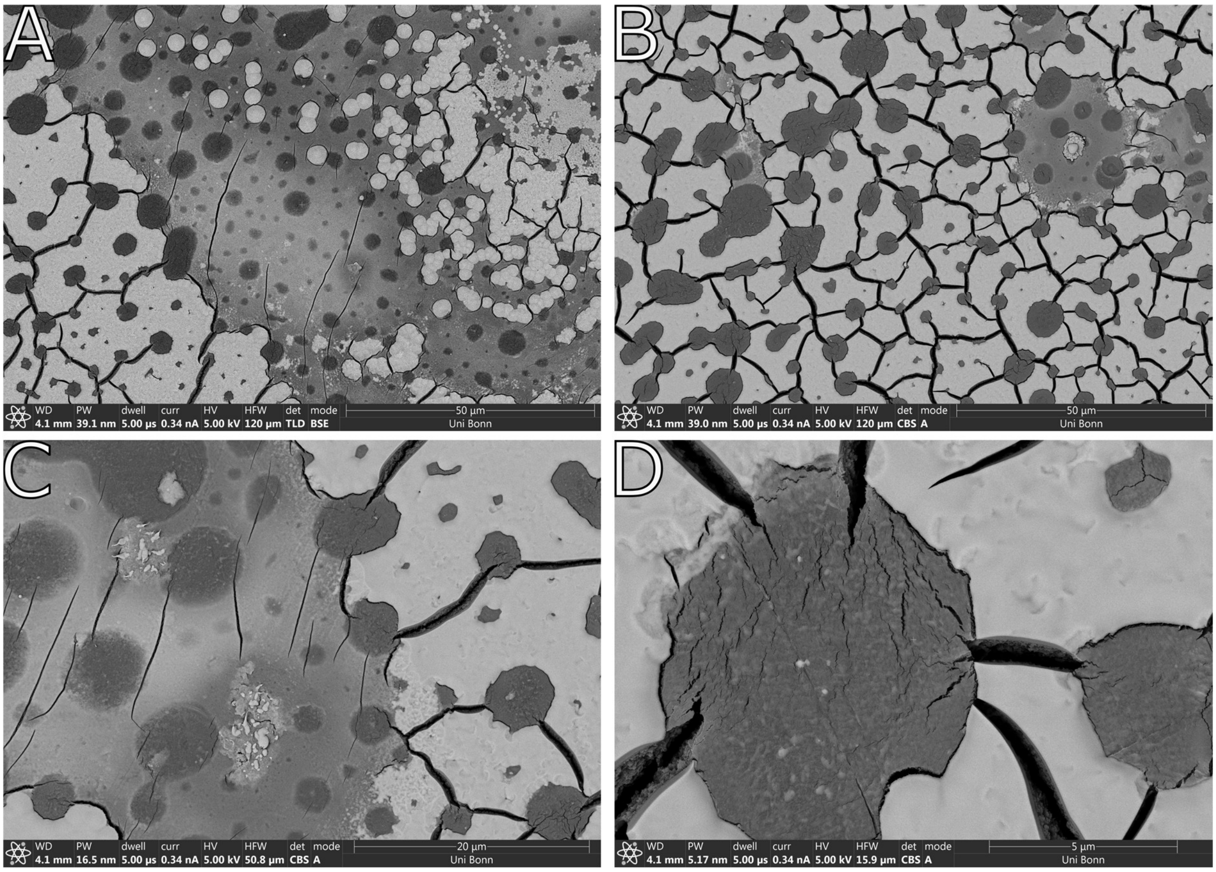

Figure 18: Polymer blends after ruthenium tetroxide exposure.
BSE micrograph sections from stained 75% ethylcellulose and 25% Eudragit RL polymer blends. Sections (A) and (B) show overview images displaying different phases corresponding to different degrees of ruthenium accumulation. A very bright outer phase, a dark spherical phase and an intermediate phase with cracks in black. Section (C) and (D) display the same sample with higher magnification.

When coverslips were dip-coated with celecoxib-polymer solutions the resulting micrographs display structures which were absent in controls (Figure 19 A-B). Additionally, celecoxib containing samples displayed a higher beam stability and were visually darker than coverslips coated with pure polymer. The two amorphous celecoxib containing polymers showed spherical phases embedded in a less electron dense polymer matrix. The phase contrast difference between the Celecoxib-PLGA blend (Figure 19 A) is less pronounced compared to the Eudragit L100 55/Celecoxib sample (Figure 19 B).

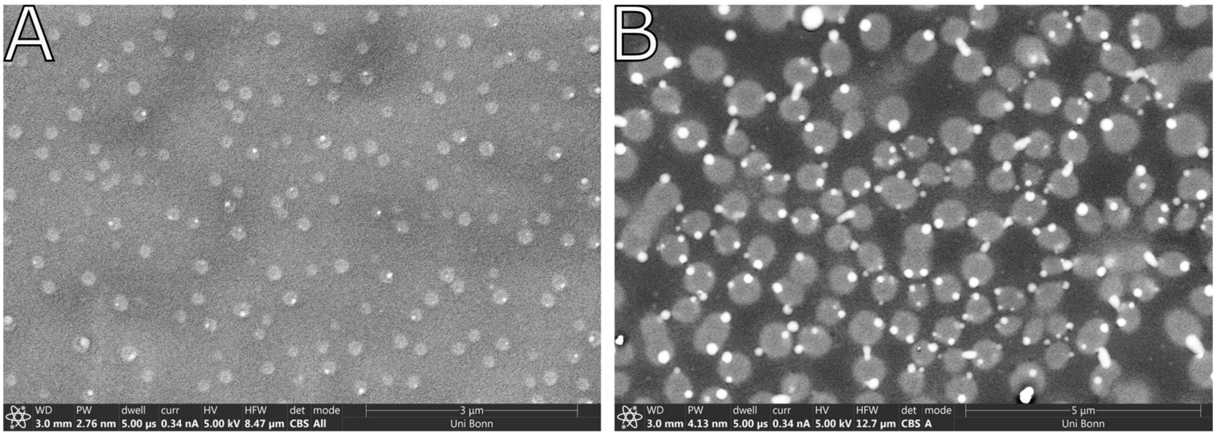

Figure 19: PLGA/Celecoxib (A) and Eudragit L100 films
BSE micrographs obtained by SEM imaging display films obtained by dip coating of PLGA/celecoxib (A) and Eudragit L100/celecoxib (B). Both sections display a darker surrounding matrix with brighter electron dense inclusions. This structure is more apparent in the Eudragit L100/celecoxib film (B) than in the PLGA/celecoxib film(A).

Similar investigations were conducted using a semicrystalline polymer API mixture composed of 50%/50% (w/w) polycaprolactone 45K and celecoxib. The overview images (Figure 20 A-C) reveal various structures. Visible features were elongated crystalline structures displaying a dark contrast. These features were often surrounded by a grayish phase extending over several hundred micrometers and embedded within a bright electron-dense matrix (Figure 20 A, B) containing black cracks. Besides these larger structures, smaller structures (Figure 20 C) with comparable morphological features existed. Closer investigation of Section B is displayed in section D, showing darker regions with greyish sheaf-like structures originating from the central dark crystals. The smaller structures lack the dark contrast of the crystalline central structures. Within this greyish phase alternating elongated feature existed showing thread like structures in lighter grey accompanied by darker less defined features. Additionally hexagonal structures were visible (Figure 20 E, F). These features were comparable contrast wise and displayed also 3 phases comparable to the larger features.

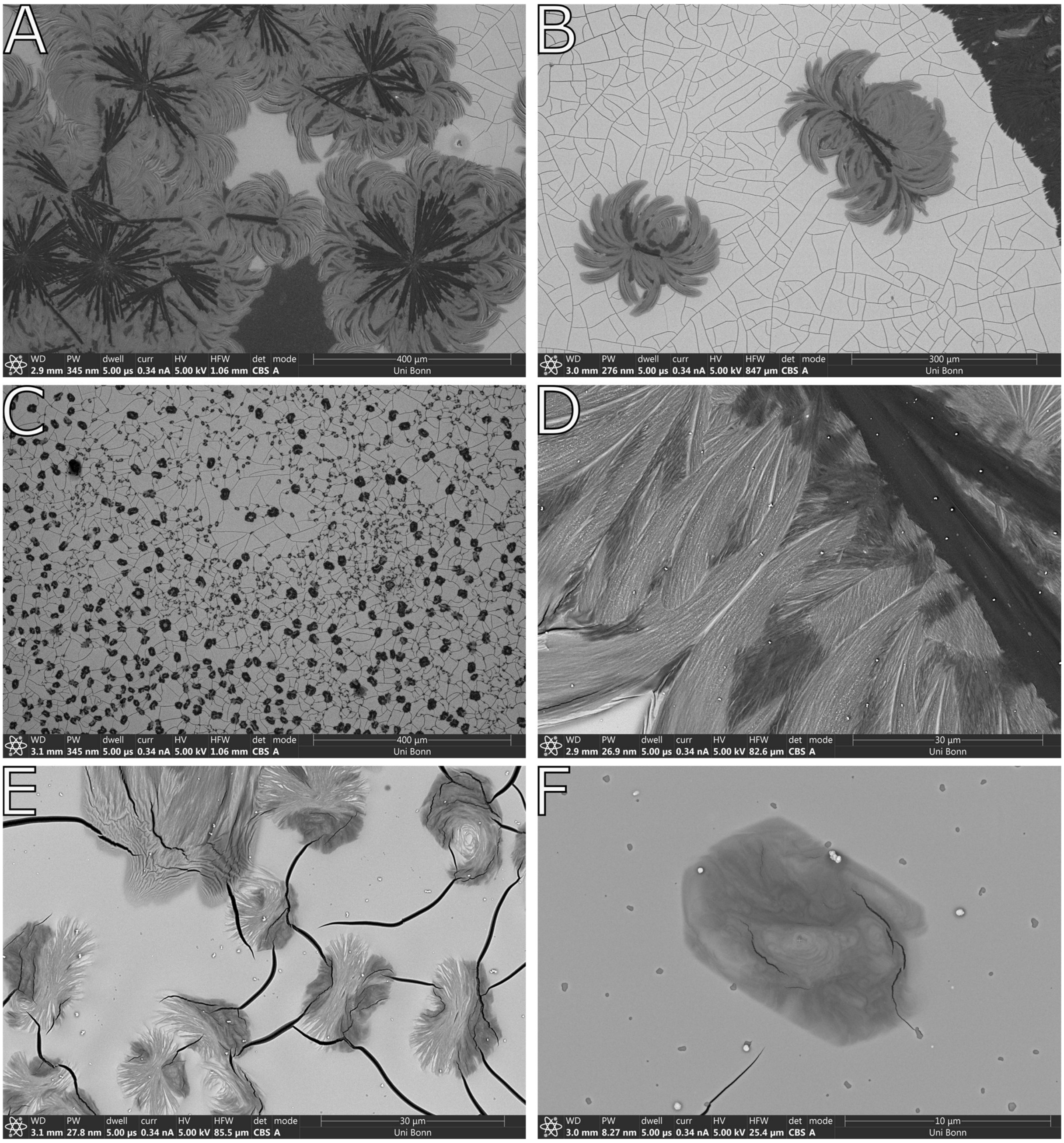

Figure 20: BSE micrographs of ruthenium tetroxide stained celecoxib/PCL dip coatings.
Overview images of 3 sample regions are displayed in section (A-C) All regions show generally 3 phases. A bright electron dense matrix, with greyish amorphous looking phases which contain dark structures with crystalline features. These features are either large as seen in the sections (A, B, D) or smaller in the lower micrometer range as seen in sections (C, E, F).

EDS investigations of the ruthenium tetroxide-treated celecoxib/PCL coverslips produced maps displaying the elemental distribution of the stained sample. The darker, unstained region (Figure 21 A) contained carbon (Figure 21 B), nitrogen (Figure 21 C), fluorine (Figure 21 D), and sulfur (Figure 21 E), with no trace of ruthenium (Figure 21 F). In contrast, the bright, electron-dense phase contains a high concentration of ruthenium, while the grayish areas show only trace amounts (Figure 21 F).

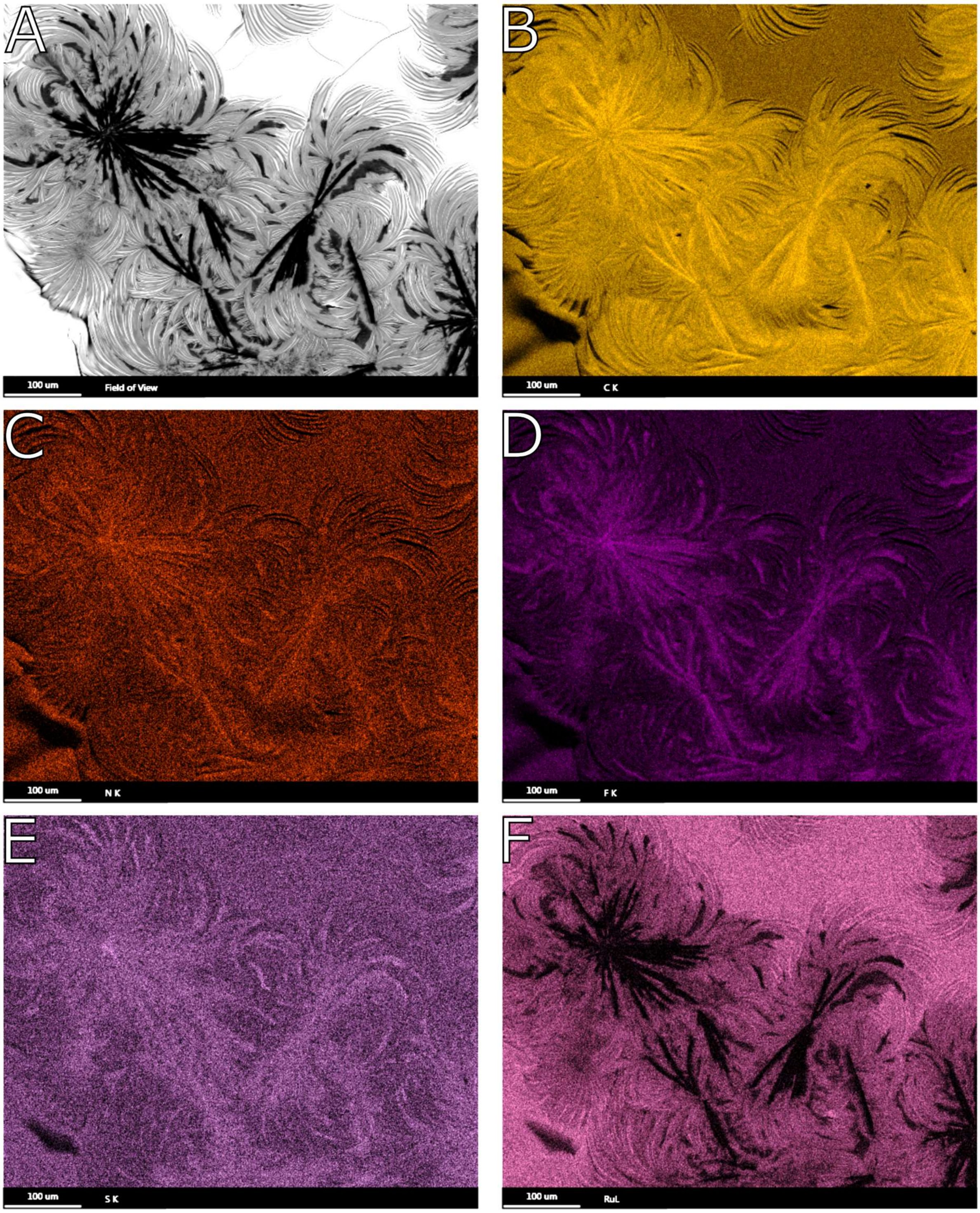

Figure 21: BSE micrograph and EDS elemental maps of ruthenium tetroxide stained celecoxib/PCL films.
Image section (A) displays the BSE micrograph obtained by SEM imaging. The other sections display EDS elemental maps (B-F). Each EDS element map stands for a specific element, whereby the elements shown are carbon (B), nitrogen (C), fluorine (D), sulfur (E) and ruthenium (F).

3.4. Discussion

The results show that most of the excipients tested are at least reasonably stained by ruthenium tetroxide. Using the dip coated coverslips it was demonstrated that the established application for staining polymeric ultrastructural features is possible also on polymers typically used as excipients. Polycaprolactone and polyethylene oxide spherulites were successfully displayed by ruthenium tetroxide staining due to the higher reactivity of the amorphous regions. All polymers containing at least polyvinylpyrrolidone as building blocks showed the irregular meandering structure. The nature of the structures could not be resolved. Nevertheless, the displayed structure fits morphologically to already imaged structures of block polymers [132,133] indicating a possibly higher structural alignment.

The polymer blend of Eudragit RL in ethylcellulose should phase separate due to the lipophilicity of ethylcellulose and the hydrophilicity of Eudragit RL caused by the permanent cationic charge of Eudragit RL [134]. This phase separation should be visualized in distinct phases of Eudragit RL enclosed by ethylcellulose. Due to the ratio of 75% of ethylcellulose, it should form the outer phase with inclusions of Eudragit RL. This structure could be displayed even though three different phases were visible instead of two. Eudragit RL was identified as the dark phase as its reactivity determined by darkening was much lower than that of ethylcellulose. The structure visualized proves this, only the intermediate contrast region cannot be fully explained. One explanation could be that during the heat curing a very thin covering ethylcellulose layer was created. These two layers generate an intermediate BSE signal. Nevertheless, the structure depicted is in line with investigations of other immiscible polymer composites or blends [134–136].

The investigations conducted on dip coated celecoxib containing polymer films resulted in the case of PLGA and Eudragit L100 55 in homogenous films with bright circular phases, which were absent in the pure films. These structures could indicate drug rich phases of amorphous celecoxib. This could be the case if the reactivity of ruthenium tetroxide towards the API is higher than towards the surrounding polymer. Formation of drug rich phases has been imaged before by various other imaging techniques such as Raman microscopy or Atomic force microscopy (AFM)-techniques [137,138]. Raman microscopy is a light microscopy-based approach and is thus limited in its resolution. AFM-based techniques achieve comparable results to that of electron microscopy while simultaneously don’t require contrast enhancement [139–141].

Since other nanoscale chemical imaging methods were not accessible, the nature of these structures could not be further determined. Techniques suitable for characterizing these features would include TEM based imaging coupled with higher resolution EDS mapping or AFM coupled with infrared spectroscopy or Raman spectroscopy.

In the case of the celecoxib polycaprolactone films, large dark structures occurred with elongated shapes typical of crystals. The nature of the crystals was proven by EDS mapping. The dark structures contain all elements specific for celecoxib e.g. fluorine, sulfur, nitrogen while lacking ruthenium. As stated earlier amorphous regions react faster with ruthenium tetroxide, this indicates that the surrounding bright electron dense phase is still amorphous as no spherulitic, or crystalline structures are visible. except for the phase with intermediate contrast. This phase still contains celecoxib as proven by EDS. It is possible that the bright phase contains celecoxib which could act as a plasticizer, affecting the crystallization of the PCL. The concentration of celecoxib in the bright phase could not be suitable displayed due to the high accumulation of ruthenium tetroxide. The large buildup of ruthenium blocked the collection of X-rays, especially the low energy ones emitted by light elements [142]. Nevertheless, the absence of ruthenium buildup proves that crystalline drug is not stained by ruthenium tetroxide and thus it is possible to distinguish amorphous from crystalline regions. In general, the ruthenium tetroxide contrast enhancement approach is more suitable for TEM based techniques as these require less contrast enhancement. Additionally, due to the smaller sample volumes the resolution and signal will be better.

3.5. Concluding remarks

These investigations demonstrate a certain potential of ruthenium tetroxide based contrast enhancement of polymeric systems. The experimental setup was limited by the use of highly artificial samples. Additionally, the study was limited by the reliance on SEM based imaging techniques. While SEM imaging is feasible, as shown in this research and in literature, it is not favorable.

In this work only flat films were imaged which are far from being relevant pharmaceutical films or even formulations. Moreover, some observed features may be influenced by drying kinetics or surface-associated artifacts. Bulky samples were too uneven and thus too noisy for image interpretation by SEM. To mitigate these issues, ultramicrotomy would have been necessary to flatten the surfaces before SEM imaging. If a material science-grade ultramicrotome had been available, the investigation could have been extended to STEM imaging of ultrathin sections, offering more precise insights.

Nevertheless, from the conducted experiments it can be concluded that polymeric excipients can be discerned when the excipients have different reactivity towards ruthenium tetroxide. Additionally, the staining of API containing polymeric excipients results in different contrasted structures. In the case of the PLGA / Eudragit L 100 55 based films further analysis by EDS was not possible due to the limitations of the available EDS system's resolution and low beam stability of the sample. This investigation was possible using the Celecoxib/PCL sample proving that recrystallized API is not stained by ruthenium tetroxide. Due to the absorption of X-rays, it was not possible to quantify the API in the electron dense surrounding areas. This is to be expected but could not be proven by EDS. Nevertheless, PCL without celecoxib showed spherulitic semi crystalline morphology which was absent in the sample containing celecoxib.

Further experiments should be conducted to further prove the hypothesis. Additional investigations would best be conducted on ultrathin sections from polymeric samples obtained by (cryo)-ultramicrotomy with an electrostatic transfer system to mount the samples on the grids. Conventional wet mounting will dissolve most excipients and API and thus risk solvent induced changes. Imaging would best be performed using TEM/STEM imaging with nanoscale EDS capabilities. The approach using ruthenium tetroxide vapor as a contrast enhacer generally appears to be promising, as it has a high reactivity and can therefore generate a contrast in many excipients. However, ruthenium tetroxide staining is highly reliant on a flat sample morphology, as only the uppermost layers are stained. This results in the necessity of ultramicrotomy as small topological deviations strongly influence the interpretation of the images.

4. Imaging of osmiophilic excipients within drug delivery systems

4.1. Introduction

New drugs often exhibit poor aqueous solubility or limited membrane permeability. Consequently, drug delivery scientists need to address these challenges by developing appropriate DDS to ensure adequate bioavailability, stability or release kinetics [143–145]. These innovative drug delivery systems often come at an increased complexity in structure, composition and manufacturing [146–148]. To characterize these DDS, various properties need to be characterized using a variety of techniques. These properties include pores or pore networks, the localization and distribution of excipients and active ingredients and their physical state. Furthermore, it must be ensured that both the components and the DDS have the required sizes[121]. Standard techniques to address the physico-chemical attributes of DDS include mercury intrusion porosimetry, gas adsorption measurements, X-ray diffractometry, dynamic scanning calorimetry or laser diffractometry [126,149,150].

Often these methods are backed by a multitude of microscopical or other imaging techniques. Amongst these, electron microscopy based techniques are of paramount importance as most microstructural features are too small to be addressed by light microscopy based techniques [7,151].

Regarding the type of electron microscopy technique used in pharmaceutics, SEM is far more common than TEM, except for the fields of nanomedicine, where TEM is regularly applied. Nevertheless, SEM possess often the necessary resolution to image typical nanoparticles. Due to the high resolution of FE-SEMs nanosized features can be imaged even on bulky samples unsuitable for TEM investigations. These already potent microscopes can be further enhanced by adding a focused ion beam column. This new variety of SEM, the FIB-SEM is getting more attention in the field of pharmaceutics [7,152–155]. The focused ion beam (FIB) is used to manipulate the sample, usually to sputter material away at a desired location with nanometer precision [7].

Since most excipients and APIs consist of light elements their visualization by BSE imaging is challenging. EDS in an SEM can help to identify structures of interest, especially APIs if containing halogen atoms such as fluorine, chlorine, bromine or iodine. Nevertheless, EDS will increase the imaging times and will not always be applicable. An alternative way to identify structures of interest, not only regarding the FIB-SEM technique but for EM in general as well, are contrast enhancement strategies. Contrast enhancement in scanning electron microscopy introduces electron dense compounds into a sample, increasing the yield of BSE and thus generating more signal from a stained area. Often the staining agents are dissolved in water or organic solvents, which is especially common in EM of biological samples [33,36,156,157]. In the case of DDS, these solvents bear the risk of changing the structure. Consequently, additional staining methods were developed not relying on contrast enhancement by immersion but rather using evaporating substances, especially in polymer science. The most common stains for polymers are ruthenium tetroxide and osmium tetroxide [28,39,40,46,158]. The benefits and disadvantages of ruthenium tetroxide were already discussed in the previous chapter.

In the case of osmium tetroxide, vapor from an osmium tetroxide crystal will be generated by sublimation [34]. For detailed information please refer to the introduction.

Consequently, this part of the thesis aims to investigate the suitability of osmium tetroxide as a contrast agent for the characterization of DDS using SEM, FIB-SEM and μ-CT. The μ-CT was included because similar principles that generate contrast in EM also generate contrast in μ-CT [159–161]. Denser material becomes less permeable to X-rays (radiopaque), so that material which previously could not be distinguished becomes visible after osmification. To examine this, various samples were prepared. Initially, omega-3 ethyl esters (Ω-3-EE) were loaded at different concentrations into a porous silicate carrier (Florite R). The Ω-3-EE were chosen as an example excipient due to its very high affinity to osmium tetroxide caused by the numerous unsaturated carbon double bonds. Additionally, a self-emulsifying drug delivery system (SEDDS) composed of Ω-3-EE and PS 80 was formulated and loaded into Florite R. SEDDS are of interest for drug delivery purposes as they can excel in delivery of lipophilic API. A huge drawback of them is that the liquid components need to be delivered either as liquids or liquid-filled capsules. A possibility to circumvent this delivery approach is the incorporation of SEDDS into porous silica transforming the liquid excipients/API mixtures into solid powdered SEDDS suitable for processing by other means e.g. tablets. Tablets are not only suitable for EM but for μ-CT as well. Therefore, tablets consisting of polyethylene glycol 6000 (PEG 6K) and Florite R, loaded with SEDDS, were prepared by standard compression and vacuum compression molding (VCM). All samples were analyzed by SEM and FIB-SEM, with additional CT scans of the larger drug delivery systems.

4.2. Material and Methods

4.2.1. Materials

Table 4: Materials Osmium Vapor staining

Material	Brand name	Vendor
Calcium Silicate	Florite R	Tomita Pharmaceuticals
Double sided conductive carbon tabs		Plano
Omega-3-ethylesters (Ω-3-EE)	K85EE	BASF
Osmium tetroxide 4% solution		Electron Microscopy Sciences
Osmium Tetroxide 100 mg		
Polyethylene glycol 6000		Carl Roth
Polysorbate 80	Tween 80	Croda
Silver conductive paint		Plano

4.2.2. Production of an osmiophilic SEDDS formulation

Surfactant and oil were mixed in snap cap vials for at least 30 minutes using a magnetic stirrer at 400 RPM. Weight ratios of Ω-3-EE and polysorbate 80 were 0.6 g / 1.4 g, 0.8 g / 1.2 g, 0.9 g / 1.1 g, 1.0 g / 1.0 g, 1.1 g / 0.9 g, 1.2 g / 0.8 g, 1.4 g / 0.6 g.

4.2.3. Particle size via Laser diffraction

4.2.3.1. Particle size Florite R

Placebo compacts were dissolved in 40 ml MilliQ water and briefly sonicated in a sonic bath. Sonication showed no influence on primary Florite R particle size. Only fully disintegrated compacts were analyzed by laser diffraction using a LA960 (Horiba, Kyoto, Japan). Prior each sampling from the supernatant, the dispersed particles were vortexed, added to the liquid measuring cell and measured in triplicate.

4.2.3.2. Particle size emulsion droplets

Particle size of the SEDDS formulation was performed using the LA960. 500 mg of each sample was released in 100 ml beakers and water was gently added. Samples were Stirred for 30 minutes using a magnetic stirring bar at 200 RPM. Samples containing silica were centrifuged prior to sampling. Measurements were performed in triplicate. Modified from [162]

4.2.4. Silica Loading:

Each batch was formulated with 5 g neat Florite R (silica) and loaded. Cargo was either an SEDDS system consisting of a 50/50 weight fraction of polysorbate 80 / Ω-3-EE or plain Ω-3-EE as described in table 5. Loading was done via pipetting the liquid cargo from a container onto the silica continuously stirred within a beaker by a propeller stirrer at 400 UPM.

Table 5: Silica loading and composition

Silica Amount [g]	Plain Oil [g]	Total [g]	Silica loading [%]
5	2.5	7,5	50
5	5	10	100
5	7.5	12,5	150
5	10	15	200
5	12.5	17,5	250
5	15	20	300
5	16	21	320
5	17.5	22.5	350
Silica Amount [g]	SEDDS [g]	Total [g]	Silica loading
5	7.5	12.5	150
5	12.5	17.5	250
5	17.5	22.5	350

4.2.5. Thermogravimetry (TGA)

TGA analysis was performed using TGA/SDTA851^e (Mettler Toledo). Samples were placed into 70 µl aluminum oxide crucibles and analyzed under oxidative conditions with Gas composition of 40 ml/min nitrogen and 40 ml/min air controlled by TSO800GC gas control system (Mettler Toledo). Temperature program was programmed for 5 minutes at 25°C isothermal, heating with 5 °C per minute from 25 °C to 120 °C and keeping 120 °C for 20 minutes followed by heating from 120°C to 600°C with 5°C /min. Quantification of silica loading was done with the weight loss from the 4th section using the tangential analysis tool from the STARe software. Modified from [163].

4.2.6. Compact production

4.2.6.1. Powder blending

Powder blending of the loaded silica PEG mixtures was performed using a 3D shaker mixer (Turbula T2A, Willy A. Bachofen, Muttenz Switzerland) at 50 RPM for 10 minutes with 20 g of powder.

4.2.6.2. Tableting

Tablets were produced using compaction pressures of 50, 100, 150, 200, 250 MPa using a Style One Classic 105 ML tablet press (Medelpharm, Beynost, France/Romaco Kilian, Cologne, Germany). Different weight ratios of Silica/PEG mixtures were used for tablet production with the silica being loaded with a self-emulsifying Ω-EE mixture or without. Compacts were produced if possible from following weight ratios. The tablet mass was adjusted to 140 mg per tablet, tablets with 50% Florite R were adjusted to 70 mg per tablet.

Table 6: Relative compositions of tablets produced

	Silica [%]	Cargo [%]	Silica + Cargo [%]	PEG [%]
Control	10	0	10	90
	20	0	20	80
	30	0	30	70
	50	0	50	50
SEDDS loaded	2.22	7.78	10	90
	4.44	15.56	20	80
	6.66	23.34	30	70
	11.1	38.9	50	50

4.2.7. Compacts analytics

4.2.7.1. Breaking force and tensile strength

Breaking force and diameter of the tablets were measured using an Erweka TBH 210 (Erweka GmbH, Langen, Germany).Tablet height was measured by a dial gauge (Mitutoyo Europe GmbH, Neuss, Germany).

4.2.7.2. Helium pycnometry

Pycnometric density was determined by a Belpycno L helium pycnometer (Microtrac MRB GmbH, Haan, Germany) after weighing the raw materials into the sample chamber. Repeated measuring cycles of 25 measurements were conducted to reach a 0.3% standard deviation. True density was used to calculate solid fraction of the tablets depending on their respective raw material weight fraction.

4.2.8. Vacuum compression molding

Vacuum compression molded biplanar 8 mm tablets were produced at 62°C for 10 minutes using the Meltprep device (MeltPrep GmbH, Graz, Österreich) with the low pressure lid. Vacuum setting was reduced to a minimum to press the piston into the mold and then completely removed. Mass per tablet was kept at the same magnitude for the molded tablets as for the compressed tablets. Molded tablets were prepared with a 10/90 composition, with 10% being SEDDS loaded silica and 90% PEG 6000 at a mass of 140 mg.

4.2.9. Contrast Enhancement

4.2.9.1. Osmium tetroxide vapor staining

Omega-3-ethylester and SEDDS loaded silica composites were glued on SEM sample holders using carbon conductive tape. The holders were placed into a glass desiccator lacking desiccant. After all samples were loaded into the desiccator three 100 mg osmium tetroxide crystals were added and the desiccator was sealed. Samples were incubated for 2 weeks with osmium tetroxide vapors. Afterwards, the samples were sputter coated with platinum using a Q150T S (Quorum Technologies, Judges House, Lewes Road, Laughton, East Sussex, United Kingdom) at 30 mA for 20 seconds.

Compacted or vacuum compression molded tablets were glued to SEM stubs using conductive silver paint. Reaction with osmium tetroxide vapor was performed under comparable conditions. The sputter coating conditions were kept identical.

4.2.10. Microscopy SEM

4.2.10.1. SEM of native Florite R silica carrier

Powdered sample was glued on SEM stubs using double sided carbon tabs and sputter coated with platinum using a Q150T S (Quorum Technologies, Judges House, Lewes Road, Laughton, East Sussex, United Kingdom) at 30 mA for 60 seconds and imaged by SE-imaging using a Helios G4 CX FIB-SEM microscope (former FEI Company now Thermo Fisher Scientific Inc, Eindhoven, Netherlands)

4.2.10.2. SEM of contrast enhanced loaded Florite R and Florite R Compacts

Contrast enhanced samples were prepared as described above by vapor staining and BSE images were taken using the CBD of a Helios G4 CX FIB-SEM microscope (former FEI Company now Thermo Fisher Scientific Inc, Eindhoven, Netherlands).

4.2.10.3. SEM of native compacted Florite-R fragments after disintegration

The resulting suspension of the disintegrated compacts with the 10/90 Florite R/PEG ratio used for particle size analysis by laser diffraction was sampled from the suspension for SEM imaging. 200 µl was sampled and placed in a Nanosep omega 300 kD (Pall Corporation, New York, USA) centrifugal filter and centrifuged at 5000 RCF for 2 min. Sample was washed by using 500 µl MilliQ water following an additional centrifugation step. After airdrying at room temperature the filters were removed from the inserts. Membranes were glued to SEM stubs by using silver conductive paint and airdried overnight. Dried samples were coated with platinum using a Q150T S (Quorum Technologies, Judges House, Lewes Road, Laughton, East Sussex, United Kingdom) at 30 mA for 60 seconds and imaged by a Helios G4 CX FIB-SEM microscope (former FEI Company now Thermo Fisher Scientific Inc, Eindhoven, Netherlands) using secondary electrons at a working distance of 3 mm.

4.2.11. Microscopy FIB-SEM

The contrast enhanced samples were imaged directly after fixation on SEM stubs and sputter coated with platinum using the sputter conditions mentioned above. For FIB-SEM investigations the sample had to be positioned at the eucentric point at 4 mm working distance and 52° stage tilt. Trench formation in the case of the tablets was performed using 30 kV and 21 nA for the rough milling. Polishing steps were conducted using 9.3 nA and 2.4 nA. The ion beam milling was operated at a dwell time of 25 ns in all cases. In the case of the pure silica particles milling was conducted similarly except for the 21 nA current which was omitted. Electron imaging was performed using the TLD and ICD collecting BSE. With the E-beam operating at 2 kV and 43pA for the carriers and at 2 kV and 0.34 nA for the tablets and compacts. All FIB and electron imaging related aspects were conducted using a Helios G4 CX FIB-SEM microscope (former FEI Company now Thermo Fisher Scientific Inc, Eindhoven, Netherlands).

4.2.12. Micro computed tomography (µ-CT)

The samples were placed on the sample holder and scanned using a Skyscan 1272 (Bruker Corporation, Billerica, Massachusetts, USA). Due to differences in composition after contrasting, scanning conditions needed to be adjusted for each sample type.

Table 7: Scanning conditions for CT

Sample	Voltage [kV]	Current [mA]	Rotation [°]	Exposure [ms]	Voxel size [µm]
Tablet 10/90 150 MPa-Control	40	200	0.1	1400	4.0
Tablet 10/90 150 MPa-Osmified	70	142	0.1	5500	4.0
VCM formed tablet-Osmified	100	100	0,1	4500	3.5

4.3. Results

4.3.1. Characterization Florite R particles by EM

SEM and FIB-SEM imaging results of unprocessed Florite R revealed fine powder particles ranging from 10 to 80 µm (Figure 22 A). The porous particles showed a pellatoide structure with occasional smaller clusters with a more spherical shape (Figure 22 B, C). High resolution surface imaging showed that the flakes are only a few nm in thickness and interconnected. FIB-SEM cross sectioning resulted in 2D slice images allowing a glimpse into internal particle morphology showing a continuous porous structure with small pores in the submicron range with occasional larger voids (Figure 22 D-F).

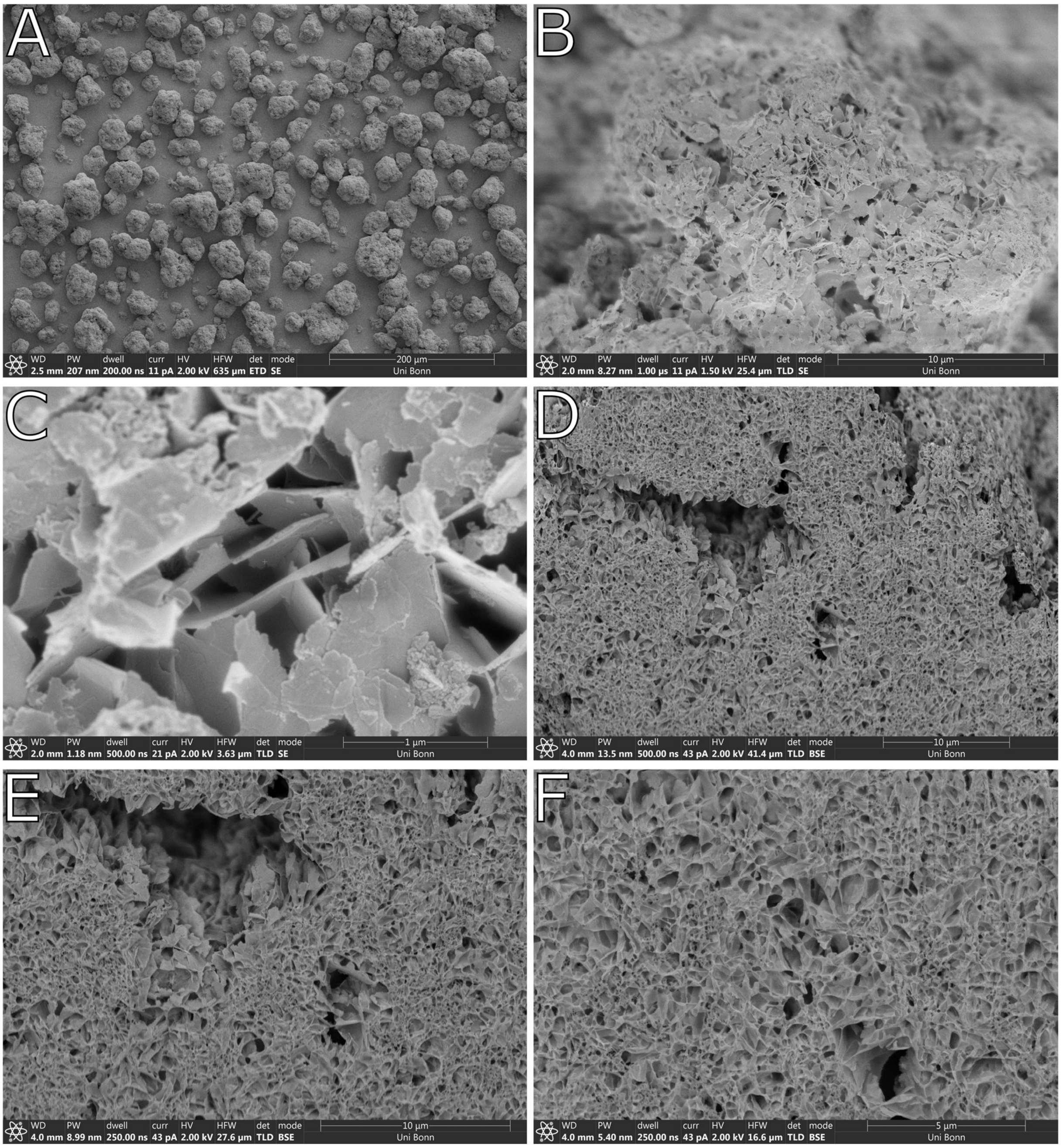

Figure 22: SE and BSE images from native, unprocessed Florite R carrier particles.
The imageds obtained by SEM (A-C) and FIB-SEM show particles in a size range below 100 µm. Higher magnifications (B, C) clearly show the composition of leaf like interconnected sheets. The sheets themselves only are a few nm in thickness (C). Cross section images show the interconnection of the leaves with pores in sub micrometer range (F) but also larger interparticular voids exist (D, E)

Fluoride R loaded with variable amounts of Ω-3-EE could successfully be stained by osmium tetroxide vapor. Accumulation of bright greyish electron dense material could be observed which increased with cargo incorporation ranging from 50% silica loading over 200% towards 300% and 350% cargo (Figure 23 A-D). Greyish cargo seemed to be mostly located within narrower pores bevor filling larger pores. Pores within the low micrometer range are not filled at all. Osmiophilic material within particles containing higher amounts of cargo seemed to be higher concentrated at the edges of the cross section. Especially within the 300% and 350% sample the brighter greyish signal is interspersed with darker less electron dense “vein” like structures (Figure 23 C, D).

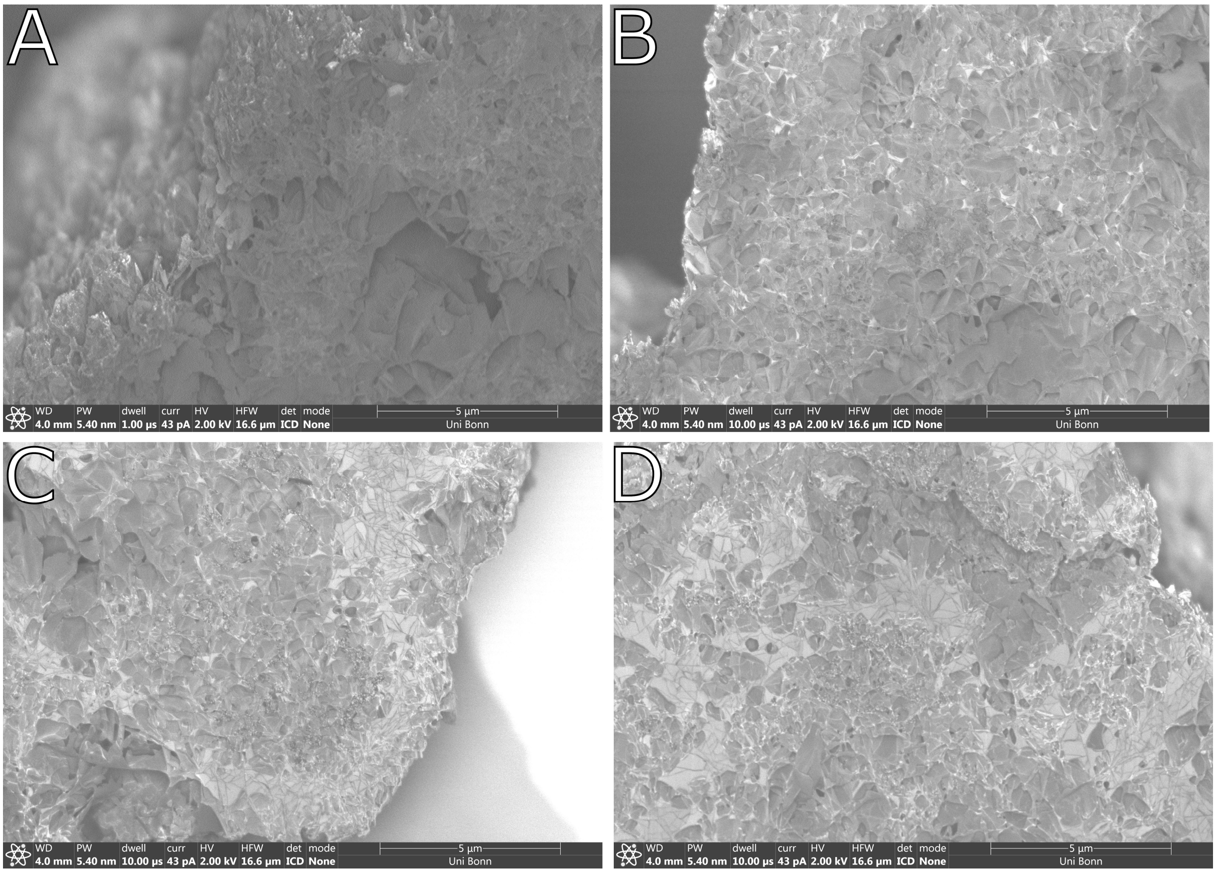

Figure 23: BSE micrograph of FIB-SEM cross sections of Ω-3-EE loaded Florite R.
Micrographs were taken by FIB-SEM imaging using BSE collected by the in-column detector of samples loaded with 50 % (A), 200 % (B), 300 % (C) and 350 % (D) of Ω-3-EE. Light greyish content was the stained cargo wish was marbled with darker, fine straight lines, from the leaf like structures. These structures appeared as lines within the regions of filled pores since the topology is mostly 2 dimensional.

Similar studies were conducted on Florite R particles, which contained 350% silica loading of a SEDDS formulation composed of polysorbate 80 and Ω-3-EE as cargo. In this case, the cargo was stained more electron-dense, improving the visibility of both the cargo and internal structures. The localization of the SEDDS was comparable to the sample containing only Ω-3-EE, being mainly confined to the smaller pores and not penetrating the larger intraparticular voids (Figure 24 A-D). The structural features are comparable in terms of the observation of interspersed fine lines in the samples, although they are better visible in the SEDDS sample

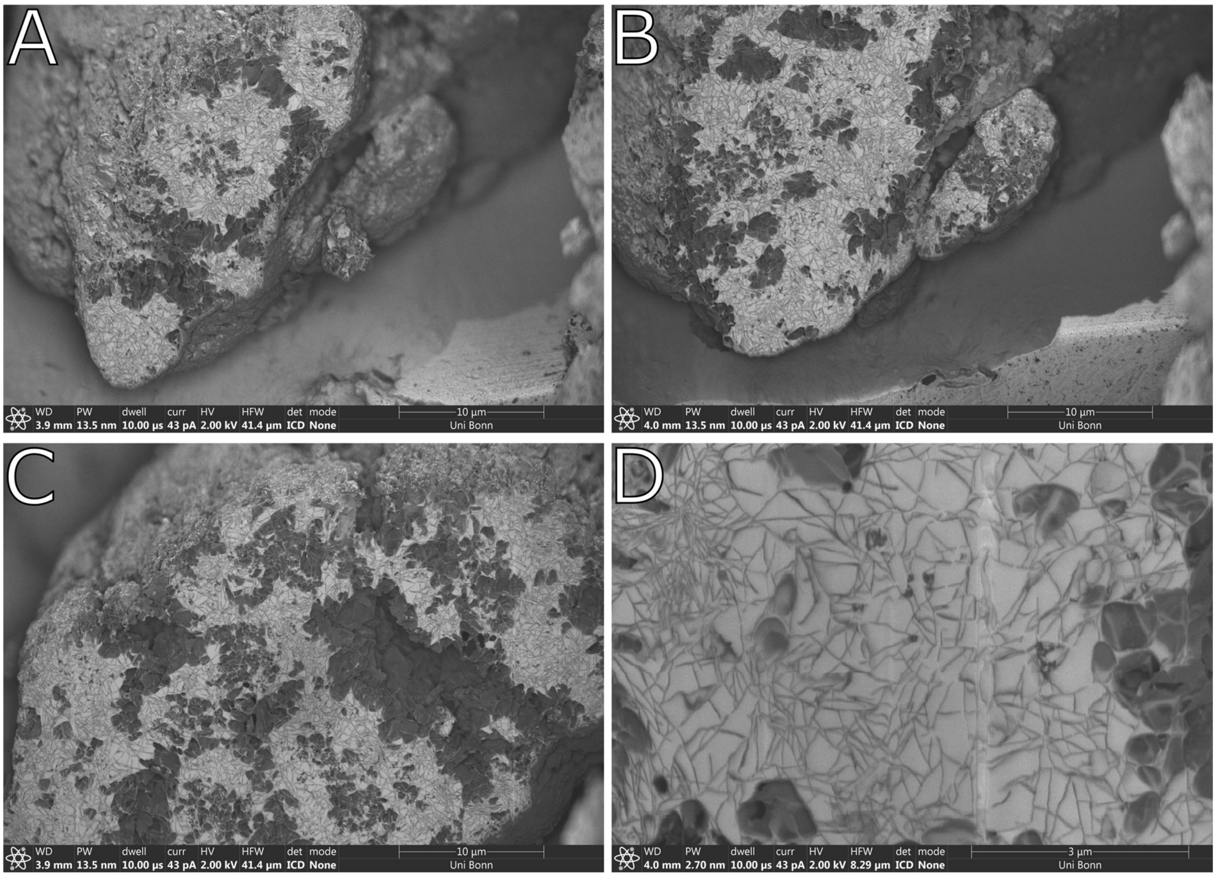

Figure 24: BSE micrograph of FIB-SEM cross sections of SEDDS loaded Florite R. *The micrographs were taken by FIB-SEM imaging using BSE collected by the in-column detector of Florite-R particles containing the 50/50 polysorbate 80-Ω-3-EE SEDDS formulation at a 350%silica loading (A-D). Sections A-C show overview images of 3 progressive cross sections from outer regions with each cross section getting deeper into the particle. A close up is depicted in section D showing the interspersed fine lines from the leaf like Florite-R structures within the brightly stained cargo.*

4.3.2. Characterization of tablets by EM

The SEDDS-loaded particles were compressed into tablets using a tablet press. However, none of the resulting tablets, which contained 10 %, 20 %, 30 % or 50 % (w/w) SEDDS-loaded silica and PEG 6000, exhibited sufficient hardness, with only one batch achieving measurable tablet hardness. Nevertheless, the samples remained structurally stable so that subsequent analysis by electron microscopy was possible. Prior to imaging, the tablets were successfully stained with osmium tetroxide vapor, which penetrated evenly throughout the tablet (3 mm height and 8 mm diameter), resulting in a clear color change to a deep black. SEM imaging with BSE revealed a heterogeneous surface with bright electron dense areas mixed with less electron dense gray areas (Figure 25 A, B). At higher magnifications, electron dense structures were observed, releasing a electron dense liquid-like substance that filled the interstices (Figure 25 C, D).

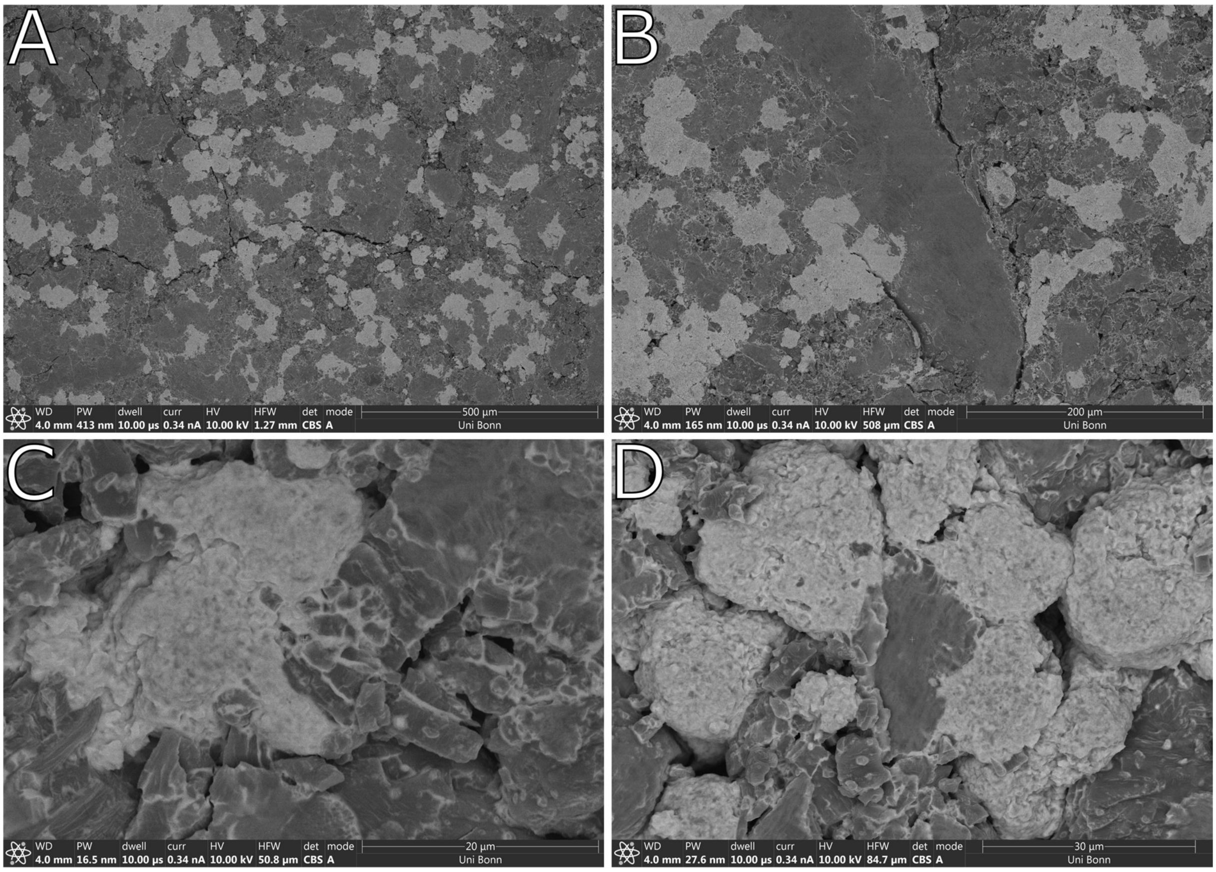

Figure 25: BSE micrographs of the surface of the 10/90 tablet compressed at 150 MPa.
Overview images (A, B) show a patchy surface of alternating bright electron dense spots and darker less dense spots. Higher magnification images show that the bright regions have some kind of structure and electron dense bright streams of contrasted material are located in the vicinity occupying interparticular voids (C, D)

Matching observations regarding the structure of the tablet were obtained by imaging cross section after FIB-milling a trench into the tablet (Figure 26 A-F). The rectangular feature displays the removed material after FIB-milling (Figure 26 A). The SEM image obtained using SE displayed the revealed cross section showing larger greyish particles coated with a bright electron dense material (Figure 26 B). Higher magnification BSE imaging confirmed the structure, displaying the contrast differences stronger than in the SE micrograph (Figure 26 C,E). Located within this bright electron dense structure are regions of less electron dense thin veins closely stacked up (Figure 26 D, F). These structures were already imaged when investigating the Florite R particles loaded with SEDDS (Figure 24). Within the tablet these structures seemed to be closer together as in the uncompressed sample.

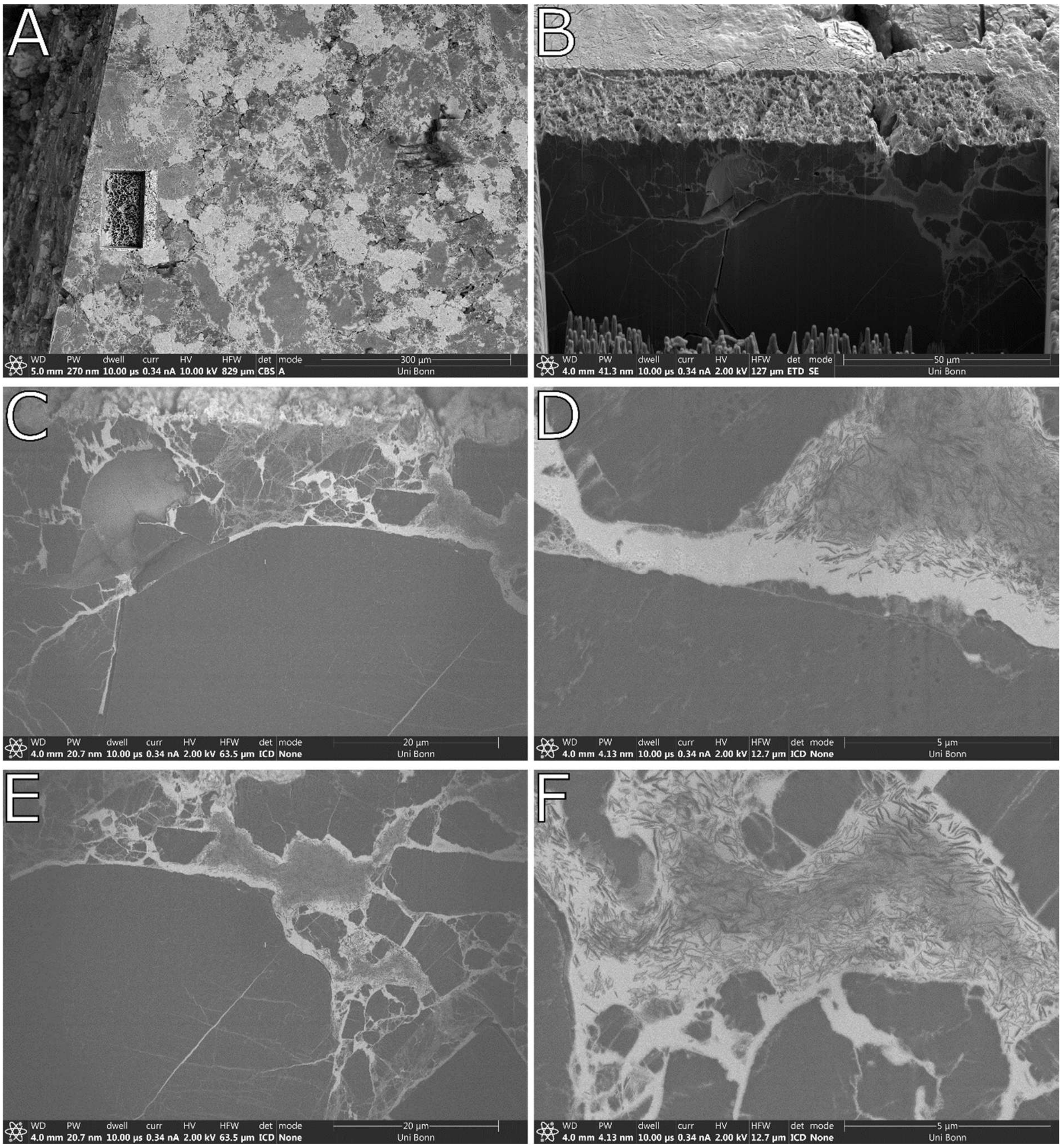

Figure 26: Electron micrographs obtained after FIB- milling into the osmified tablet.
Section (A) depicts the tablet surface with the square shaped region caused by FIB-milling. The overview of the cross section revealed by FIB-SEM as SE micrograph shows large particles and bright veiny structures (B). Higher magnification BSE images (C-F) show increased contrast differences and confirm the electron dense nature of the bright material covering the particles.

Osmification of the VCM tablets resulted in blackening throughout the whole tablet, comparable to the compressed tablets. Surface imaging using BSE electrons resulted in a homogeneous structure with very few small electron dense accumulations (Figure 27 A). The FIB- prepared cross section enabled visualization of the local internal structure (Figure 27 B). The Florite R particles are embedded within the polymer containing electron dense features comparable to the ones observed earlier (Figure 27 C). Higher magnification of the polymeric regions around the particle displays a polymer matrix finely marbled with elongated electron dense features (Figure 27 D).

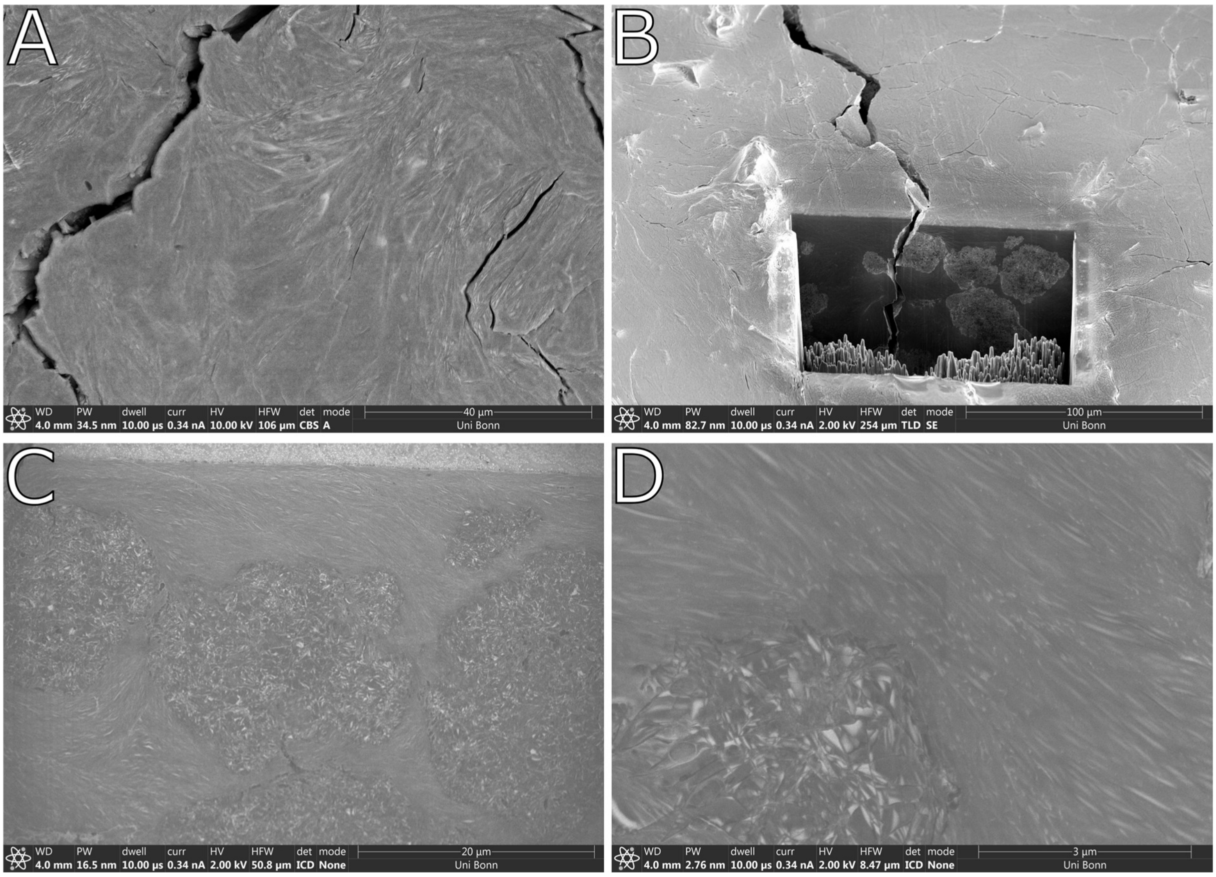

Figure 27: Electron micrographs of vacuum compression molded tablets.
The surface of the VCM-tablet showed no strong contrast differences except for the dark cracks on the surface and a slight marbling (A). The overview of the milled region displays a crack in black, a grayish matrix and some brighter roundish features. The pillar like formations are an artifact typically for FIB prepared trenches (B). Sections (C, D) display higher magnification images showing the Florite R particles and the fine marbling of bright electron dense material within more greyish content.

4.3.3. Characterization of tablets by µ-CT

Additionally, the structural features of the tablets were analyzed using micro-computed tomography (µ-CT). The sub volume of an unstained tablet (Figure 28 A-C) shows less dense particles surrounded by denser material, which appeared lighter on the image. Pores and cracks were visible as black areas. After osmification of the tablet, the µ-CT scan showed overall a comparable structure with the unstained tablet. The main difference between the osmified and the unstained samples was that the osmified samples displayed X-ray opaque material surrounding the particles (Fig. 29 A-C). When scanning the entire osmified tablet, there is considerable scattering in the central area (Figure 30 A-B). Similar artifacts can be observed when scanning the

VCM tablet. The VCM tablet appeared as a homogeneous mass with no noteworthy recognizable structural features, apart from a few slightly lighter areas (Fig. 24 A-C).

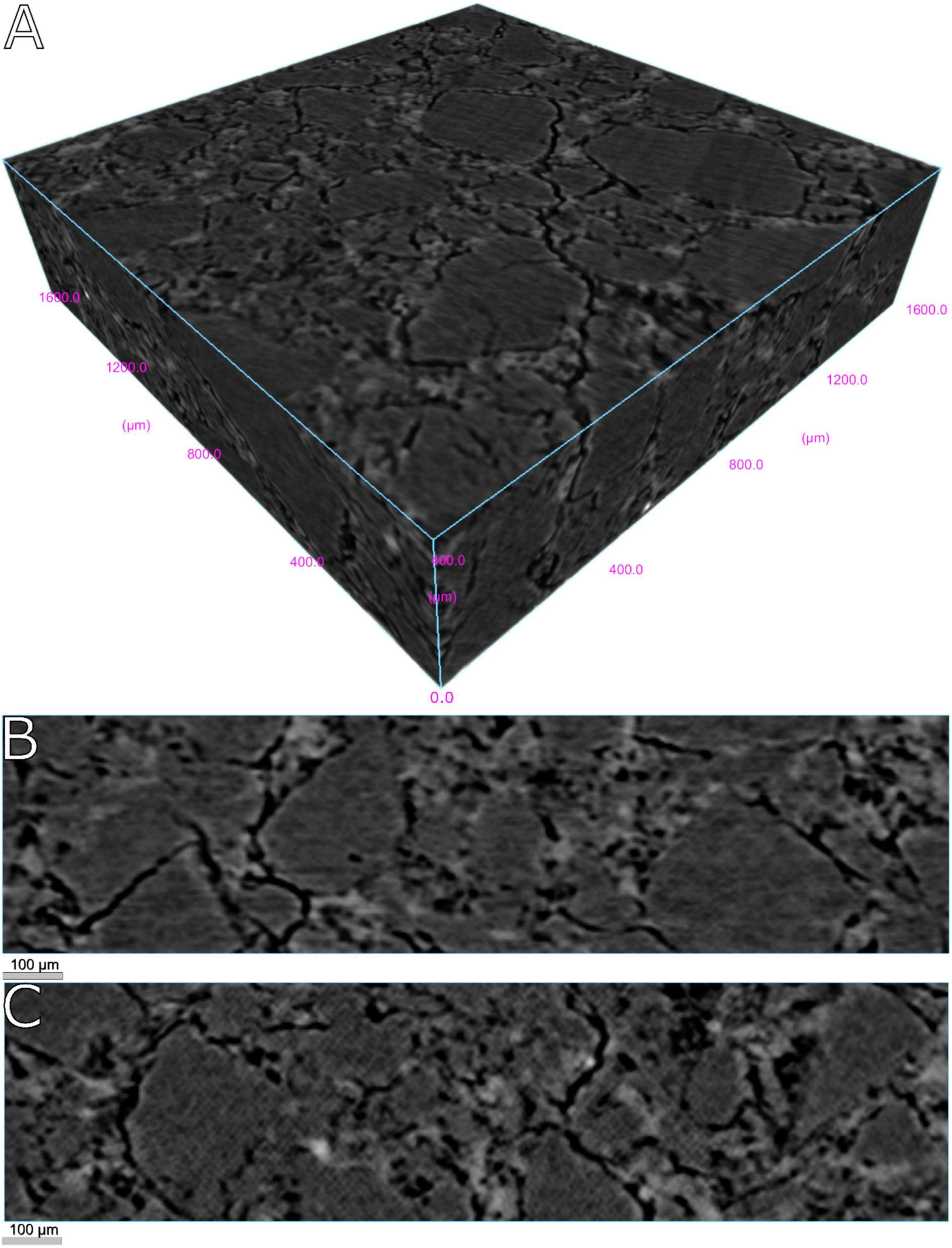

Figure 28: µ-CT-Scan sub volume of a 10/90 tablet loaded with SEDDS compressed at 150 MPa.
Displayed in section A is the sub volume of the tablet and sections B and C display slice images of that sub volume. The black elongated features are pores, with the darker material being PEG particles. Florite-R particles are displayed in grey.

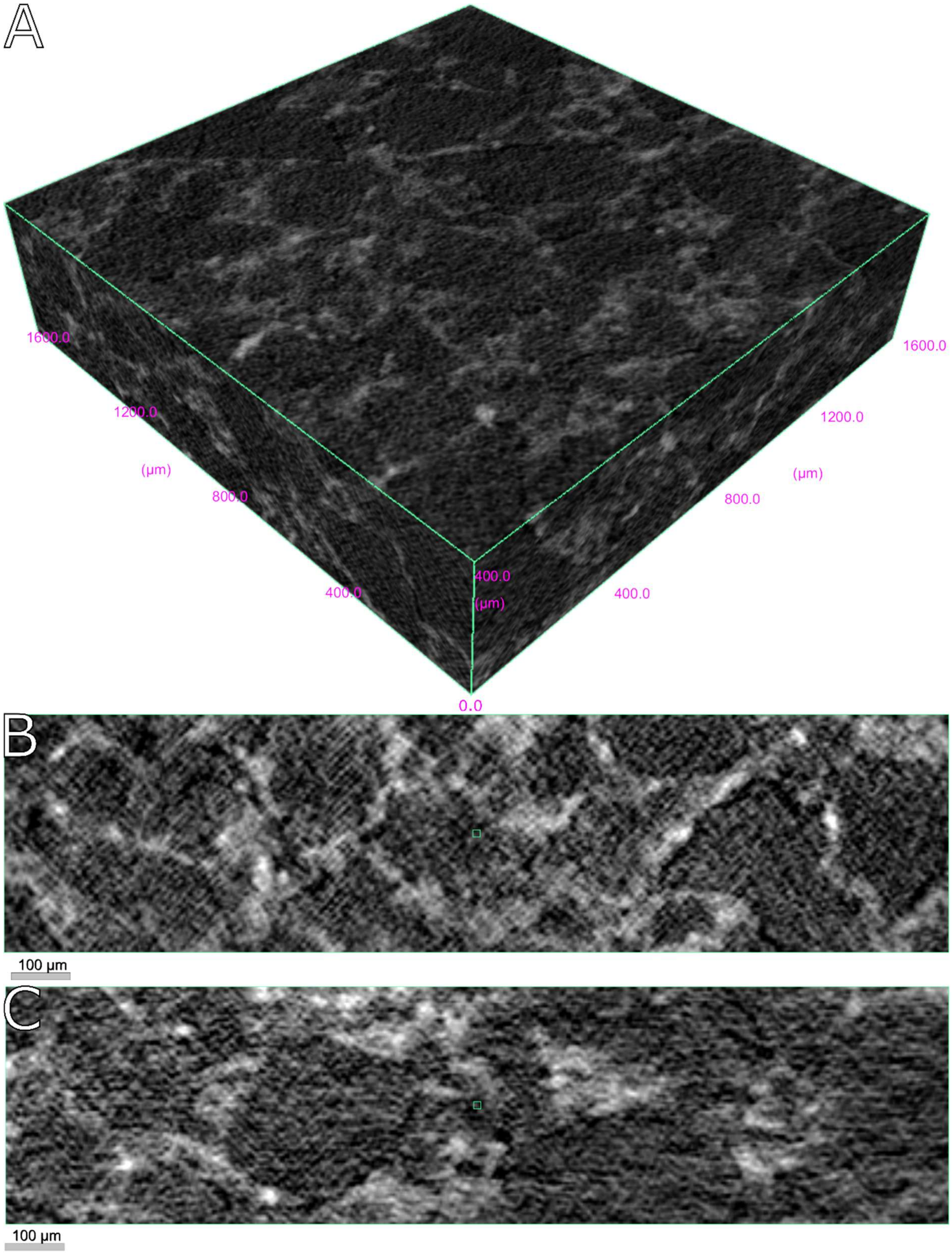

Figure 29: µ-CT-Scan sub volume of a 10/90 tablet loaded with SEDDS compressed at 150 MPa after osmification.
Displayed in section A is the sub volume of the tablet and sections B and C display slice images of that sub volume. The black elongated features are pores, with the darker material being PEG particles. Florite-R particles are displayed in grey.

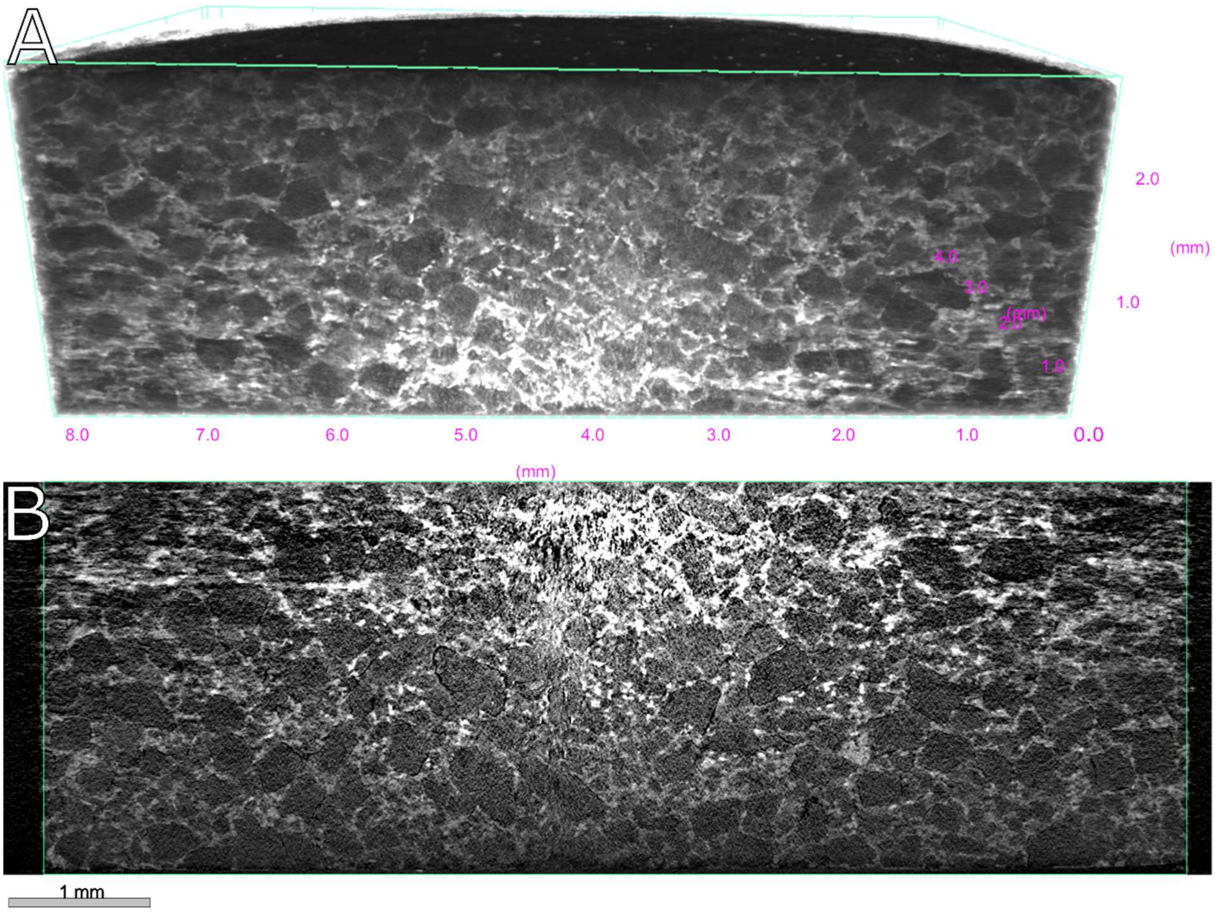

Figure 30: µ-CT-Scan cross section through a whole osmified tablet
Displayed in section A is a cross section through the tablet and section B is a representative slice image. Both sections display the scanning artefact in the center visible as bright structures.

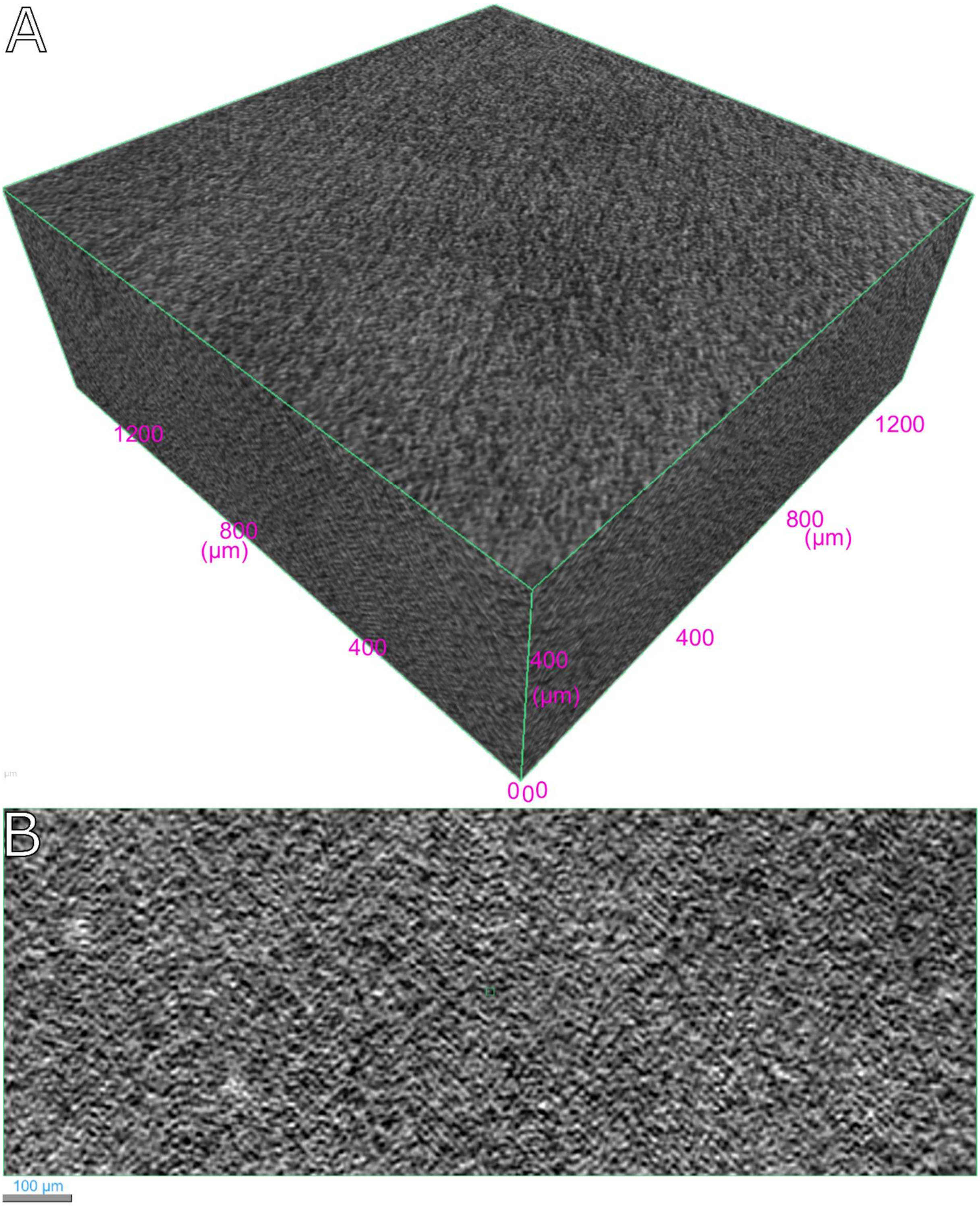

Figure 31: µ-CT-Scan of a sub volume of an osmified VCM-tablet.
Displayed in section A is the sub volume of the tablet and in section B displays a slice image of that sub volume. No significant structural features are visible.

4.3.4. Thermogravimetric results Ω-3-EE loaded Florite R

The experiments were conducted on the Ω-3-EE loaded Florite R particles. In order to assess the amount of cargo located within the particles the cargo was burnt away by TGA. The mass loss was in line with the amount of cargo. (Figure 32 A). The higher the silica loading of the particles the higher the respective mass loss. The onset of decomposition was around 60 minutes and at 200 °C (Figure 32 B). Pure Florite R also showed a certain amount of mass loss over the time but with the most significant decline below 120 °C, which was due to water loss (Quantified by Karl-Fischer-titration, Data not shown). Polysorbate 80 begins to rapidly decompose after 100 minutes at a temperature of around 380 °C (Figure 32 B).

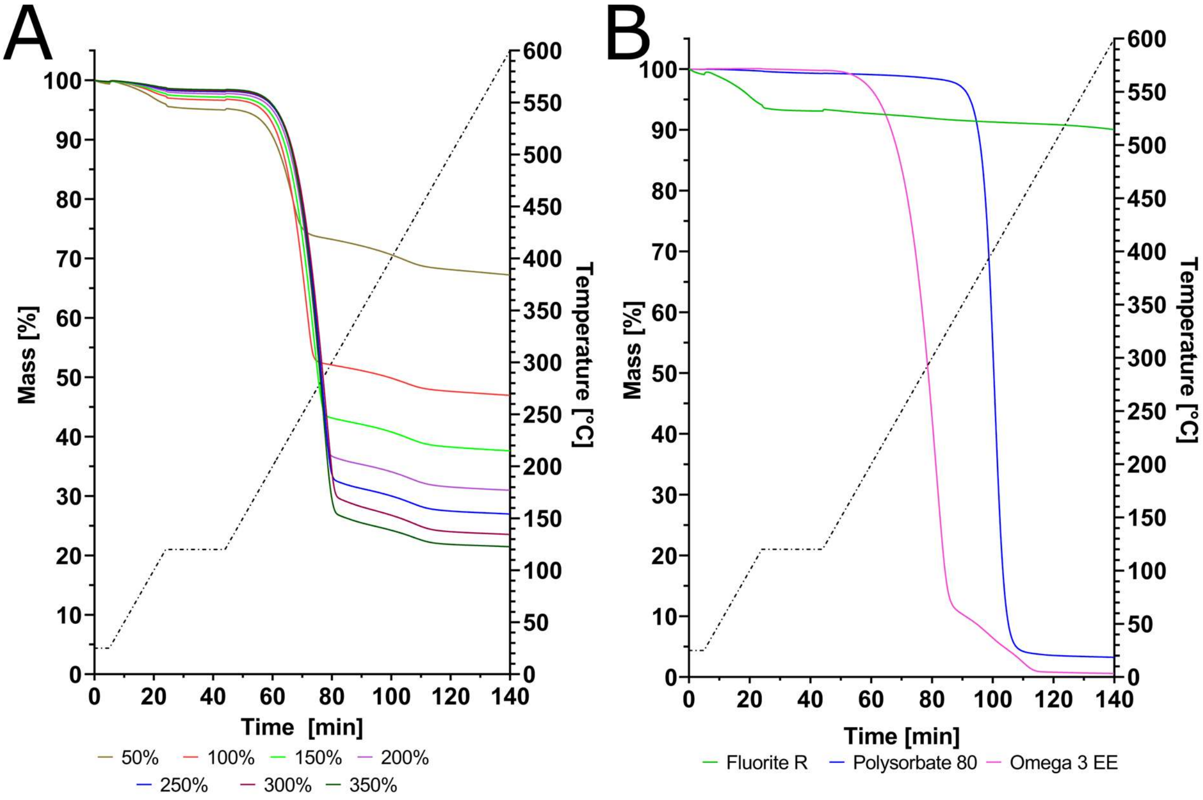

Figure 32: Thermograms of Ω-3-EE loaded Florite R particles and pure substances
The thermograms display Florite R loaded with Ω-3-EE (A) or thermograms of the pure substances (B) The colored lines refer to the respective mass losses (left), while the dashed line corresponds to the temperature(right) to which the sample is exposed at the respective time. Data is presented as means (n=3)

The theoretical loading of the respective carriers calculated from the mass loss is in good correlation with the measured ones obtained by TGA (Figure 33 A, B).

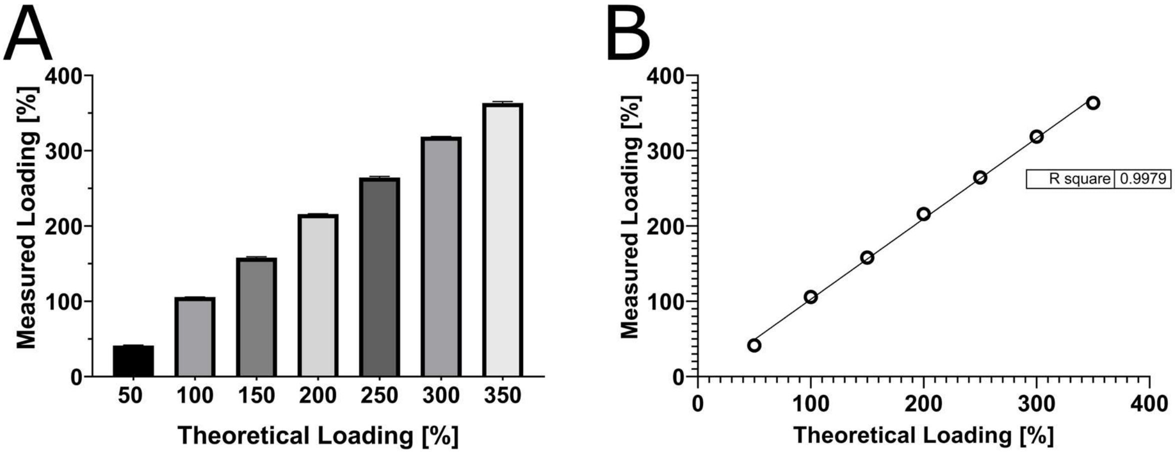

Figure 33: Correlation of expected and measured mass loss of Ω-3-EE loaded Florite R particles.
Displayed in A are the respective columns comparing theoretical and measured loading and in B the linear regression of the calculated loading values obtained by TGA.

4.3.5. Preparation and analysis of the SEDDS

The Ω-3-EE oil was transformed into a self-emulsifying drug delivery system by the addition of polysorbate 80 as surfactant. Various surfactant ratios were tested for their resulting particle size and distribution by laser diffraction. The desired particle size with most of the particles within 100 and 200 nm was the ratio of 50/50 (w/w) (Figure 34 A, B). This formulation was loaded onto Florite R at 3 different amounts 150%, 250% and 350% (Figure 34 A, B). The 350% loaded Florite R particles released the formulation with a larger particle size. (Figure 34 B)

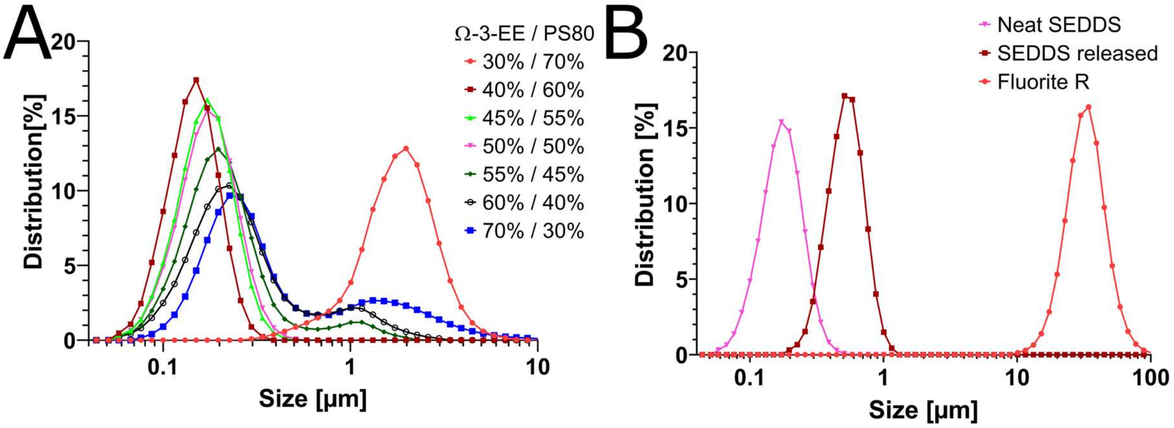

Figure 34: Particle size distributions from various SEDDS by composition and comparison of SEDDS released from Florite R
Displayed in figure section (A) are the corresponding particles size distributions of different SEDDS compositions obtained by laser diffraction. Section (B) displays the particle size distribution of Florite R, the particle size distribution of particles released from 350% loaded Florite R and the neat SEDDS before incorporation by Florite R. Particle size distribution are obtained by laser diffraction and displayed as volume distribution.

Loading of the SEDDS containing Florite R was calculated by the mass loss obtained by TGA (Figure 35 A).

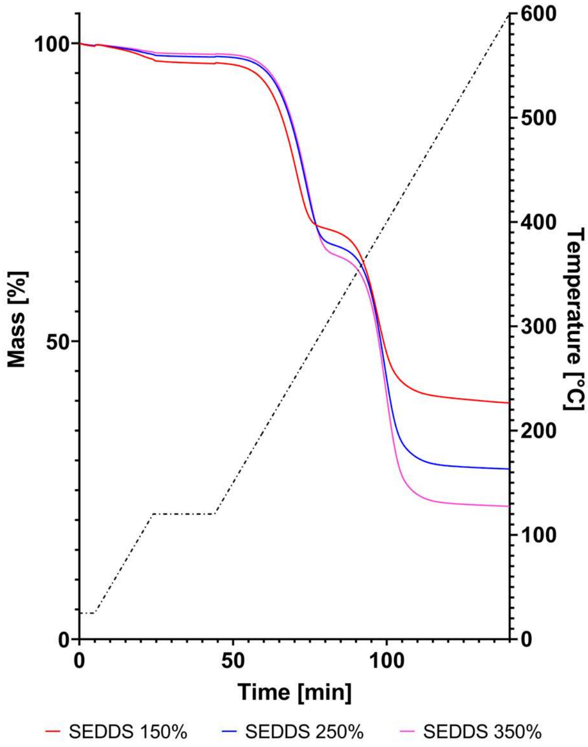

Figure 35: Thermograms obtained from SEDDS loaded Florite R
The thermograms display Florite R loaded with SEDDS containing 50% PS80 and 50% Ω-3-EE. Florite R particles were loaded with 150%, 250% and 350%. The colored lines refer to the respective mass losses (left), while the dashed line corresponds to the temperature(right) to which the sample is exposed at the respective time. Data is presented as means (n=3)

The measured loading fitted the theoretical loading of the SEDDS loaded Florite R well (Figure 36). Nevertheless, the measured values were underpredicting the theoretical values. The 350% loading containing sample was the sample with the highest amount of loading still showing acceptable flowability. Thus, these particles were incorporated into tablets.

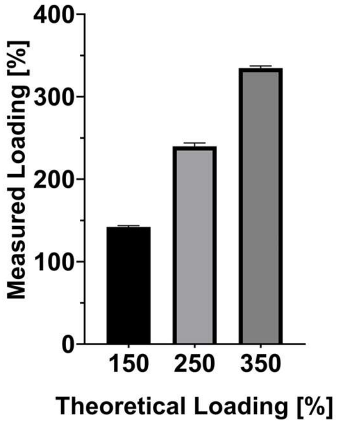

Figure 36: Comparison of theoretical and measured loading
Displayed are the theoretical loading with the measured ones. Data are presented as mean ±SD (n=3)

Following the blending of the mixtures, tablets were formed from unloaded and loaded Florite R particles and PEG 6000. Tablets composed of unloaded Florite R and PEG could successfully be compacted into stable tablets with each composition achieving at least a tensile strength of 1.5 N/mm^2 or higher. Solid fraction of the tablets was lower with increased amount of Florite R content and was reduced with increased compaction pressure. Tensile strength benefitted greatly from higher weight fractions of Florite R (Figure 37 A). With increased Florite R content only lower solid fractions could be achieved while maintaining sufficient tensile strength (Figure 37 B, C). None of the prepared SEDDS containing tablets had measurable breaking forces except for the batch of 10/90 compressed at 150 MPa, thus it was not possible to analyze the tablet properties further. Tablet shaped compacts could be prepared especially for the lower weight fractions (10 and 20%). These compacts had at least enough strength to be handled e.g. to be picked up and prepared for the imaging experiments. Thus, the experiments were conducted using the 10/90 150 MPa prepared tablets as from these their average breaking force and tensile strength was known. Tablets had an average breaking force of 5.2 N and tensile strength of 0.144 N/mm$^{2.}$

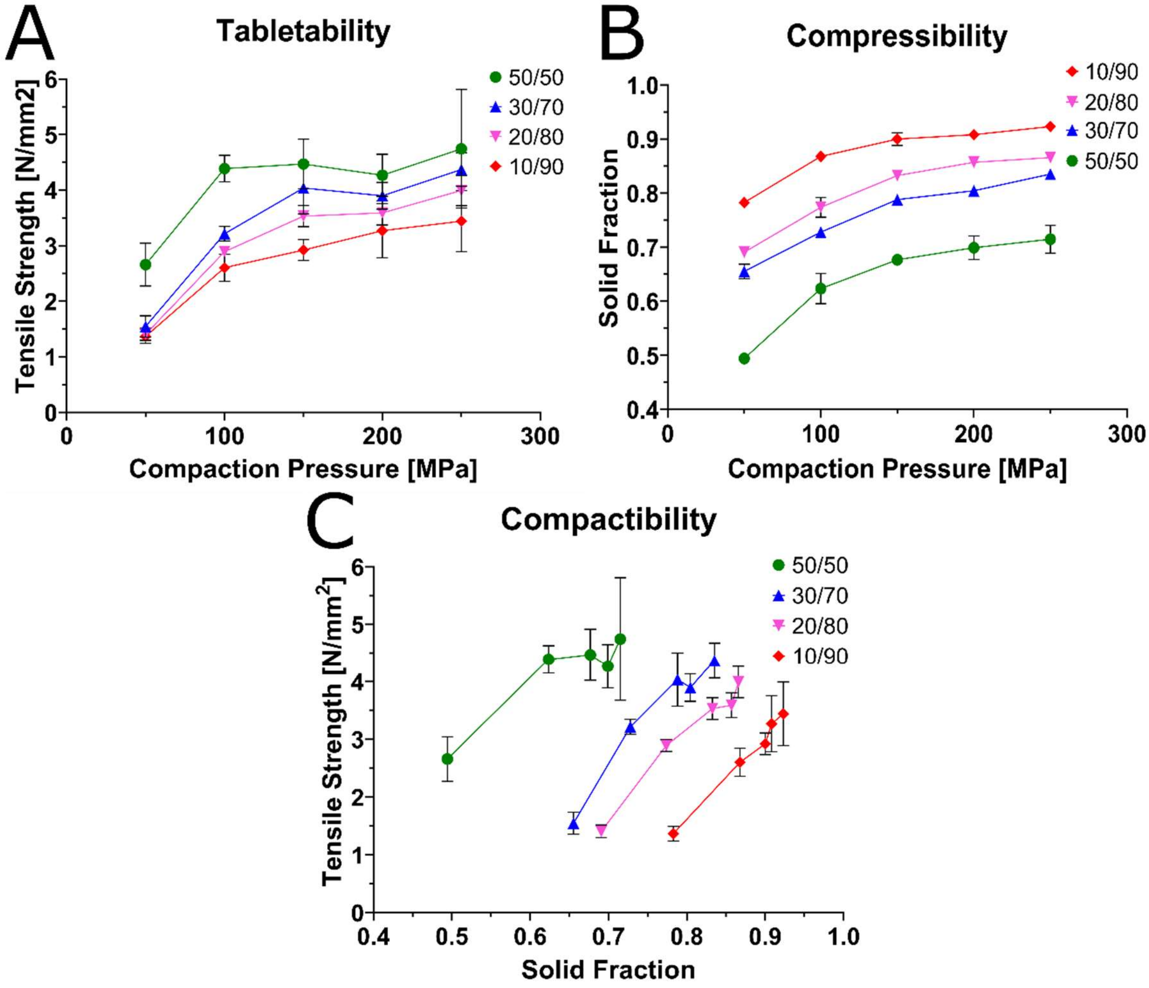

Figure 37: Tablet properties of control tablets

Displayed are tablet characteristics of 10/90 control tablets without the addition of SEDDS. Section A displays tabletability, section B displays compressibility and section C the compactability. Data is presented as mean ± SD (n=5)

The particle size of the Florite R compaction cycle could successfully be addressed after dissolving the PEG fraction of the tablet. Florite R particle distribution shifted from the uncompressed particles leftwards to smaller particles for compaction pressures of 50 MPa and 100 MPa. Particle distribution shifted towards larger particles and changed into a broader bimodal distribution which was more pronounced at 150 MPa and higher (Figure 38). These observations were only possible for the weight ratio of the control tablets 10/90 as the higher ratios did not disintegrate.

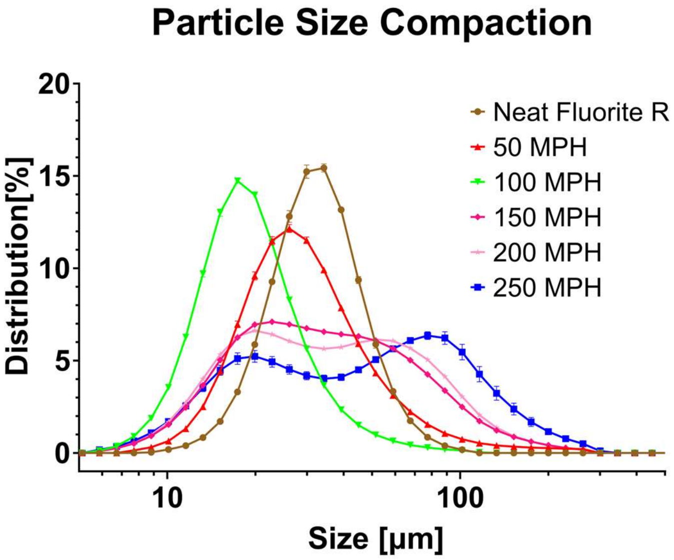

Figure 38: Particle sizes of Florite R particles after compaction.
Particle sizes are displayed after disintegration of 10/90 placebo tablets. Distributions are displayed as volume distributions obtained by liquid cell laser diffraction. Data is displayed as mean ± SD (n=3)

The findings regarding the particle size were additionally confirmed by SEM imaging. Uncompressed Florite R particles contain a very small amount of fine particles with petaloid shapes. Filtration and collection on centrifugal filters did not alter particle morphology overall. Florite R particles used as a control maintained their structure (Figure 39 A, B). After compression of 100 MPa the fine particle fraction visible on the centrifugal filter largely increased and some main particles lost their original shape. Particle morphology shifted towards flattened structures from the more spherical shapes observed before (Figure 39 C, D). This phenomenon was more pronounced at higher compression (Figure 39 E, F). Micrographs obtained from samples compacted at 250 MPa show a shift towards a bimodal particle size distribution with larger deformed particles and a large fine particle fraction

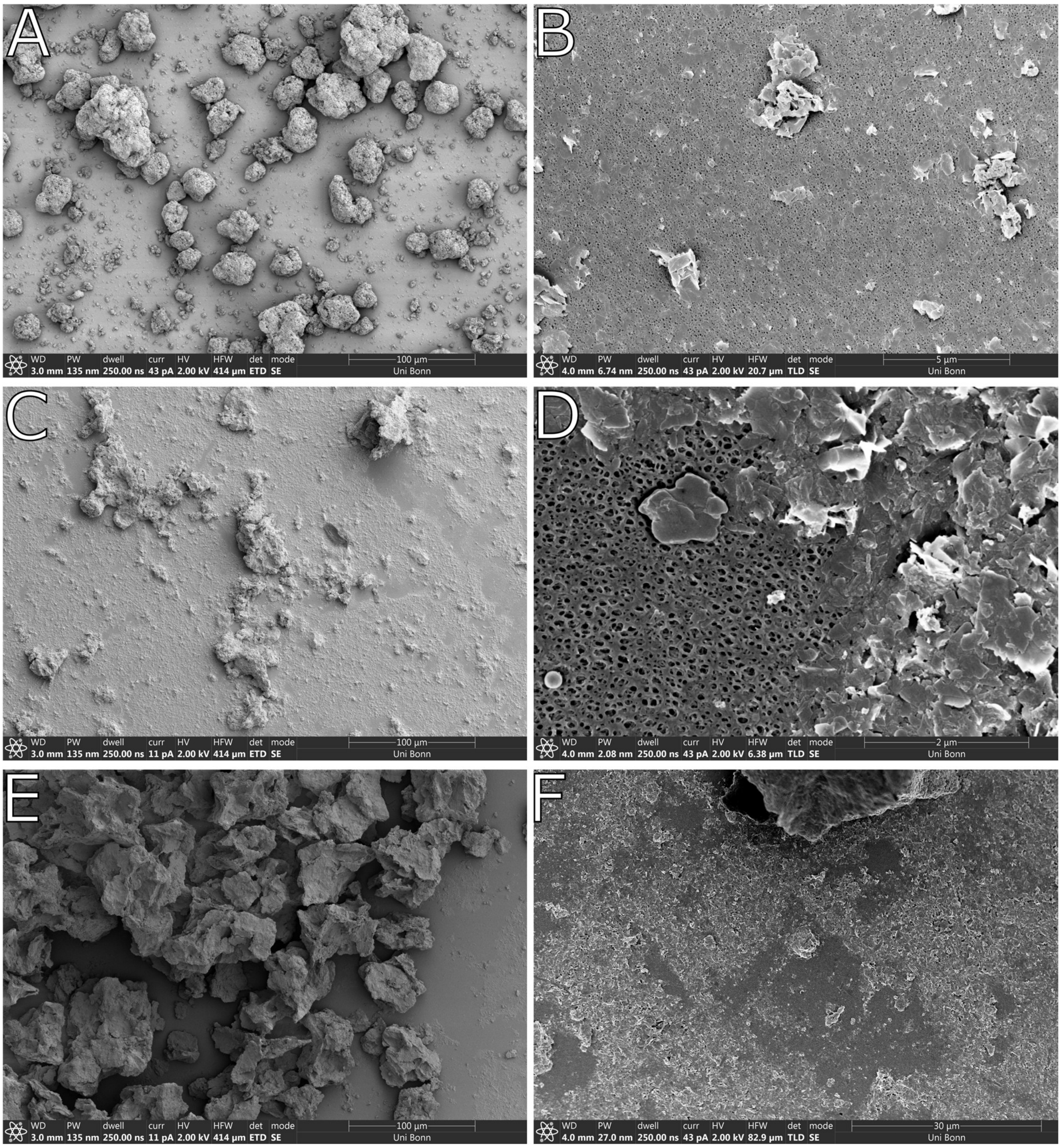

Figure 39: Florite R particles uncompressed after compression
The SEM micrographs were obtained after filtration of the disintegrated placebo tablets. Tablets contained a ratio of 10/90 silica to PEG and were compressed at 100 MPa (C, D) or 250 MPa (E, F). Uncompressed particles are displayed in A and B. The fine porous mech visible (B, D) is the filter surface.

4.4. Discussion

Ω-3-EE or other liquid or semisolid samples cannot be imaged directly by conventional high vacuum room temperature SEM or TEM. The osmification turned the Ω-3-EE into solid electron dense compounds suitable for EM. This was possible using only the osmium tetroxide vapors released from an osmium tetroxide crystal. Using this approach, it is now possible to image materials such as Ω-3-EE or Ω-3-EE based SEDDS inside porous carriers such as Florite R which is interesting as the incorporation of such formulations into porous carrier particles is a common strategy to transform liquid samples into solids [164–166].

The Florite-R particles loaded with Ω-3-EE exhibited a greater amount of grayish electron-dense material with increased loading. Since imaging was performed on individual particles, significant differences were only visible in the cross-sectional images after FIB milling between significantly different loading levels.
Nevertheless, the images showed that when lipids were incorporated as cargo, smaller intraparticle cavities were filled before the larger submicron cavities. Some particles contained micrometer-sized internal pores that were never filled. At higher loading levels, most of the cargo appeared to be localized near surface voids. Particles containing SEDDS were more intensely stained than those loaded exclusively with Ω-3-EE Florite R, probably due to insufficient staining. This inadequacy might be due to either an underestimation of the amount of osmium tetroxide required relative to the amount of Ω-3-EE or improper positioning of the sample in the desiccator-like device. Since the vapor of osmium tetroxide is denser than air, it tends to remain near the bottom of the beaker. Nevertheless, the Ω-3-EE is clearly visible in the silica and exhibits the desired properties, such as electron density and solid-state formation. Although the loading of Ω-3-EE and SEDDS was of a similar order of magnitude as quantified by TGA, the imaged silica particles with SEDDS contained more cargo. It is plausible that variations in particle loading at the single particle are possible, due to the dropwise addition of the cargo with constant agitation, which may have resulted in localized exposure to high amounts of cargo. However, the ultrastructural details of the particles are well resolved on the images. In addition, the beam stability of the samples was significantly improved. Silica particles, especially in the unloaded state, are notoriously difficult to image with the SEM due to their susceptibility to charging artifacts. Additionally, loading such particles with volatile organic components such as lipid based excipients can negatively impact image quality due to carbon deposition in the imaged areas [165]. The Osmification of such substances largely reduced artifacts associated with carbon contamination. The fine dark lines visible in the cross-sections correspond to the petal-like structures visible in the unloaded controls. Accumulation of osmium tetroxide in the cargo made the SEDDS, which originally consisted only of light elements, more electron dense than the silica matrix. Filling of the pores and the increased contrast in the images made them easier to interpret, as the images now largely represent 2D slice images. The unloaded Florite R particles were more challenging to interpret as they display more grey values due to topological effects of the pores. In the SEDDS loaded samples the larger micrometer sized voids remained unfilled. Generally the characterization of porous silica particles by FIB-SEM has not been conducted very frequently, but seems to be a promising approach for validating the carrier structure and cargo distribution [7,163,167].

In the next step, it was successfully demonstrated that contrast enhancement by osmium tetroxide is feasible when applied to larger drug delivery systems. Osmium tetroxide vapor is well-known for its ability to penetrate deeply into a wide range of organic materials. Tablets composed of the 350% SEDDS loaded silica particles and PEG 6K were produced to further address this topic. These tablets, however, failed to exhibit adequate mechanical properties, particularly in terms of tensile strength which was observed before [165]. In contrast, the control batches produced under similar conditions without SEDDS loading exhibited satisfactory properties. Despite this, the SEDDS-loaded tablets were stable enough to be processed for electron microscopy.

Contrasting was performed on intact tablets with a diameter of 8 mm and a height of 3 mm. The tablets were cut in half for imaging. The uniform black coloration of the entire sample indicates an accumulation of osmium tetroxide in the entire tablet volume. The SEM surface image showed a patchy surface consisting of bright, electron-dense silica particles next to grayish PEG 6K particles. Higher magnification images showed that lipids leaked from the particles and covered both the surface and the inter-particle gaps. The FIB-SEM images confirmed these observations and showed grayish PEG particles surrounded by bright, electron-dense material. In addition, fine lines corresponding to silica-petaloid structures were visible, appearing in a medium greyish color. In general, the structure appeared more compressed, with horizontally aligned silica sheets and indentations caused by PEG particles. This structural change during compression of the Florite R particles is also supported by the observation that the particle size in the unloaded control showed an increased proportion of fine particles. With increasing compaction pressure, the particle size distribution shifted towards a bimodal distribution, with one fraction consisting of fine particles and the other larger than the pure particles. The change in morphology was also visible in the SEM images after disintegration caused by dissolution of the PEG. However, the disintegration was only possible for samples with 10 % unloaded silica. Tablets with a silica content of 20 % or more did not disintegrate. Disintegration of tablets can be a critical attribute for drug release and thus is often required. To reach acceptable disintegration times for the placebo tablets, a disintegrant such as cross povidone might be needed [168].

As an alternative production method for creating a monolithic, tablet-shaped drug delivery system, vacuum compression molding was employed, resulting in molten, disc-shaped tablets. These systems were uniformly stained by osmium tetroxide vapor. BSE micrographs taken from the surface of the VCM tablets revealed a homogeneous structure. Under high magnification, fine, bright, electron-dense features were visible. Cross-sectional imaging, prepared via FIB-milling, showed finely distributed, bright electron-dense "veins" running through the PEG matrix. The electron density of the matrix appeared higher than in tablets prepared by compaction, possibly indicating a molecular distribution of osmiophilic material within the PEG 6K. The bright veins correspond to osmiophilic material, which is distributed in a colloidal state throughout the sample. This electron-dense material is also observed within the embedded Florite R particles. These findings suggest that the SEDDS self-emulsified into the molten PEG 6K matrix during production, forming a solid SEDDS system. The embedding of pegylated surfactants into PEG 6K was already investigated as a drug delivery tool [169].

The introduction of electron-dense substances benefits not only electron microscopy but also μ-CT imaging. The incorporation of contrast-enhancing materials alters the X-ray opacity of the stained material, allowing previously indistinguishable structures to become visible. Introduction of heavy metals or other x ray opaque substances for structural identification is a standard approach in many fields of biology but unexplored in the field of pharmaceutics [159,160,170,171].
The obtained μ-CT scans show that this approach is also applicable for drug carriers such as tablets. In the study, both the PEG-6K particles and silica particles were already distinguishable, along with the pores. The intraparticular spaces were at the edge of the resolution limit but were often large enough to be visible. The addition of osmium tetroxide to the tablet created radio-opaque regions surrounding many of the PEG-6K particles, whereas these regions were radiolucent in the control

sample. However, the osmium tetroxide also obscured most of the Florite R particles that were visible in the control sample. While contrast enhancement improved the visibility of certain features, it also presented challenges. The high enrichment of osmium tetroxide in the SEDDS formulation significantly altered the sample in terms of X-ray lucidity, so both the dwell times and the X-ray energy (kV) had to be adjusted. The increased kV was necessary to penetrate the osmified tablet. Unfortunately, this led to scattering and streaking artifacts, especially in the center of the tablet, due to the large density differences. Nevertheless, the CT scans showed comparable results as the FIB-SEM imaging. In the case of the VCM-tablet no structures or phase differences could be imaged except for some more radio-opaque spots or cracks. This is due to the small size of the features which were below the resolution of the μ-CT [170].

4.5. Concluding remarks

The experiments conducted could demonstrate the usefulness of contrast enhancement of drug delivery vehicles for SEM and FIB-SEM imaging as well as for μ-CT. Osmium tetroxide is an especially suitable contrasting agent as it can be used in vapor form nihilating effects of possible solvents which most likely will affect the structure of most delivery systems. The samples investigated in this study were expected to react with osmium tetroxide but since carbon double bonds are not the only chemical moiety known to react with osmium tetroxide this approach could be transferred to many other excipients. This method will help formulation scientists assess the distribution or localization of a substance of interest, even in large drug delivery systems. For this approach to work the only prerequisite is a certain osmiophilicity of the material or structure of interest.

5. Cellular uptake and fate of lipid nano carriers imaged by electron microscopy

5.1. Introduction

Facilitated by the success of RNA based therapies in research resulted in a renaissance of nanoparticle research [172]. Nevertheless, it is still poorly understood how drug carriers enter the cell, witch pathways they traffic on, how they deliver their cargo and where they are ultimately be degraded. The characteristics that influence particle uptake and the uptake pathways are initially dependent on the cells which are used for uptake investigation. In addition to the characteristics of the specific cells, particle properties such as charge, particle rigidity, core material or various surface modifications influence the uptake of nanoparticles [61,173,174]. RNAs can be delivered via multiple delivery systems ranging from polymeric to lipid-based systems. Especially the lipid-based systems are of great interest and include for example solid lipid nanoparticles, liposomes, nanostructured lipid carriers or nanoemulsions. Nanomedicine itself is not a new topic with the first marketed product being Doxil® in 1995, a liposomal formulation used to encapsulate doxorubicin [175,176] and the discovery of liposomes in general in the 1960 [172]. Nanotherapeutics can be composed of a variety of excipients and contain a multitude of different structures. Lipid nano carriers (LNCs) for example are solid lipid nanoparticles, liposomes, nanoemulsions, or nanostructured lipid carriers [177]. In addition to lipid-based excipients, nanomedicines can be composed of a variety of different polymers of natural or synthetic origin [178]. Nano particles for drug delivery can also consist of inorganic materials such as mesoporous silica nanoparticles, gold or iron oxide. The inorganic particles are mostly investigated in academic research [179].

One of the simplest forms of lipid nanocarriers are nanoemulsions. Such carriers can be manufactured from 2 excipients, a core lipid, usually oil, and a surfactant. The most sophisticated approach to investigate nanoparticle uptake by electron microscopy would be the visualization of the carriers directly within the cell without addition of further substances or tracers. Especially in the case of nanoemulsions or other lipidic compounds osmium tetroxide seems promising as it is generally used within electron microscopy as a secondary fixative and contrasting agent for lipid membranes. Based on this assumption It should be possible to visualize LNCs composed of osmiophilic excipients. Osmiophilic excipients are excipients with an innate reactivity towards osmium tetroxide leading to a direct binding of osmium tetroxide to the excipients. This will fix the material, blocking dissolution during the preparation with organic solvents while simultaneously rendering it visible.

Before the actual uptake investigations were performed, several excipients were screened for their ability to form reaction products with osmium tetroxide. From this screening 3 lipid excipients e.g. mono-, di- and triglycerides of linoleic acid [Maisine CC™], omega-3 ethyl esters [Incromex E 7010™] and omega-3 triglycerides [Incromex TG 4030™] were chosen for further investigation. They were screened over a wide range for their ability to form LNCs using polysorbate 80 as surfactant

These LNCs were incubated with J774A.1 cell-line which is regularly used in uptake experiments. The J774A.1´s are a monocyte derived macrophage cell originated from Balb/c mice. Uptake of the LNC´s was imaged by EM using the HMDS technique and by STEM imaging. Additionally, as lysosomal degradation was expected, the lysosomal function was disrupted by cotreatment of chloroquine or lalistat 2. Chloroquine is an established model substance for disrupting several lysosomal properties due to its accumulation in acidic organelles by ion trapping. Thus, chloroquine could mimic the effects of ionizable DDSs used for example in RNA delivery. It is known for disruption of lysosomal function by lysosomal swelling, pH elevation and inhibition of fusion processes. Additionally, the lysosomal acid lipase was inhibited by lalistat-2. Lysosomal acid lipase is the only known lysosomal lipase to mainly degrade acylglycerols and cholesterol esters.

5.2. Material and Methods

5.2.1. Materials

Table 8: excipients used in screening and LNC formulation

Material	Brand name	Vendor
Omega-3 fatty acid ethyl esters	Incromex E 7010™	Croda
Corn oil	Super refined corn oil	Croda
Cotton seed oil	Super refined cottonseed oil	Croda
Glyceryl linoleate mono-, di- and tri-ester mixture from corn oil	Maisine CC™	Gattefossé
Linoleoyl Polyoxyl-6 glycerides	Labrafil M2125	Gattefossé
Oleic acid	Super refined oleic acid	Croda
Olive oil	Olive oil Ph.Eur. grade	Carl Roth
Omega-3 fatty acid ethyl esters	K85EE omega-3-acid ethyl esters	BASF
Omega-3 triglycerides	Incromex TG 4030™	Croda
Sorbitan monooleate	Span 80 Ph.Eur. grade	Croda
Sorbitan trioleate	Span 85 Ph.Eur. grade	Croda
Squalene	Squalene	Tokyo Chemical Industry
Polysorbate 80	Tween 80	Croda

Table 9: Materials Electron microscopy

Material	Brand name	Vendor
Double sided conductive carbon tabs		Carl Roth
DPM-30 Accelerator ([2,4,6-Tris(dimethylaminomethyl)phenol)	Epon 812 substitute epoxy-embedding kit	Sigma Aldrich
Epoxy embedding medium	Epon 812 substitute epoxy-embedding kit	Sigma Aldrich
Ferricyanide		Sigma Aldrich
Glutaraldehyde 25% EM grade	Epon 812 substitute epoxy- embedding kit	Carl Roth
Hexamethyldisilazane (HMDS)		Sigma Aldrich
Methylnadic anhydride (MNA)	Epon 812 substitute epoxy- embedding kit	Sigma Aldrich

Osmium tetroxide 4% solution		Electron Microscopy Sciences
Silver conductive paint		Plano
Thiocarbohydrazide		Sigma Aldrich

5.2.2. Screening of suitable osmiophilic excipients

Unsaturated lipids were dispersed at 10% (w/w) in a water phase containing 1% polyvinyl alcohol 13000. The total weight of the mixture was 10 g. Emulsions were homogenized using Ultrathurax IKA T18 Basic (IKA®-Werke GmbH & Co. KG, Staufen, Germany) at 13000 rpm for 2 minutes. Afterwards, this pre-emulsion was then homogenized by ultrasound homogenization using a Bandelin Sonopuls HD 2200 homogenizer (BANDELIN electronic GmbH & Co. KG, Berlin, Germany) equipped with an SH 213 G booster horn and a TT13 titanium tip operated at 50% power in continuous mode for 2 minutes.

Samples were diluted 1:1000 and stained using 4% unbuffered osmium tetroxide reaching a final concentration of osmium tetroxide of 1%. Samples were pipetted after 12 hours onto glass coverslips and analyzed by SEM after sputter coating.

5.2.3. Preparation of nanocarriers:

The inner oil phases were premixed with the respective surfactants at 400 rpm for 30 min under magnetic stirring in 20 ml snap cap vials. MilliQ water was added proportionally to reach 10 g of total formulation weight and stirred again for 30 minutes. The resulting pre-emulsion was further processed by an Ultrathurax IKA T18 Basic (IKA®-Werke GmbH & Co. KG, Staufen, Germany) at 13000 rpm for 2 minutes followed by ultrasound homogenization using a Bandelin Sonopuls HD 2200 (BANDELIN electronic GmbH & Co. KG, Berlin, Germany) homogenizer equipped with a SH 213 G booster horn and a TT13 titanium tip operated at 50% power in continuous mode for 2 minutes.

5.2.4. Particle size analysis by laser diffraction

Particle sizes for the lipid nanocarriers were analyzed directly after production using a LA 960 laser diffraction (Horiba, Kyoto, Japan). Particle concentration was adjusted using the red laser light transmission for larger particles or blue laser light transmission for smaller particles to 85% transmittances. The real refractive index was set to 1.450 and imaginary refractive index was set to 0.000 with the refractive index of the dispersing medium at 1.333 for water. Particle size distributions were calculated as volumetric distribution.

5.2.5. Particle size analysis by dynamic light scattering (DLS)

Dynamic light scattering measurements were conducted using a nanoPartica SZ-100 (Horiba, Kyoto, Japan). Samples were diluted accordingly and analyzed at a 173° angle through single use cuvettes. The real refractive index was set to 1.450 and imaginary refractive index was set to 0.000 with the refractive index of the dispersing medium at 1.333 for water. Particle size distributions were calculated as volumetric distribution. Only particles used for further experiments were characterized by DLS

5.2.6. SEM imaging of nanocarriers

LNCs were further analyzed by SEM after osmification. Osmified particles were treated as described under 5.2.2 and dispersed on glass coverslips and airdried. After drying, the coverslips were glued on SEM stubs using silver conductive paint and sputter coated with platinum using a Q150T S (Quorum Technologies, Judges House, Lewes Road, Laughton, East Sussex, UK) at 30 mA for 20 seconds. Samples were imaged using 10 kV accelerating voltage and 0.34 nA current at a working distance of 4 mm using BSE for imaging via the concentric backscatter electron detector.

5.2.7. J774A.1 cell culture

5.2.7.1. Cell culture routine

J774A.1 mouse BALB/c monocyte macrophage cells (Sigma Aldrich, St. Louis, Missouri, USA) were kept in 75ml cell culture flask (VWR, Radnor, Pennsylvania, USA) and grown adherend in Dulbecco`s modified eagles medium (DMEM, PAN-Biotech GmbH, Aidenbach, Germany), complemented with 10% fetal bovine serum, 1% penicillin and streptomycin (Sigma Aldrich, St. Louis, Missouri, USA). Passaging of was done by scrapping. Each new cell batch was analyzed for mycoplasma contamination using MycoStrip® a mycoplasma detection kit (InvivoGen Europe, 5, rue Jean Rodier F-31400 Toulouse France).

5.2.7.2. Viability by MTT assay of LNCs

40.000 cells were seeded per well in 96 well plates using cell concentration of 400.000 cell/ml and incubated for 16 h at 37°C and 5% carbon dioxide using the beforementioned DMEM. Cells were treated over 24h with the various nanocarriers at respective concentrations. Viability was analyzed after 3 washing steps with Dulbecco’s phosphate buffered saline (DPBS) using a 3-(4,5-dimethylthiazol-2-yl)-2,5-diphenyltetrazolium bromide as formazan forming compound [180] incubating for 90 minutes. The formazan was dissolved in 100 µl DMSO and quantified at 560 nm using a Perkin Elmer Enspire plate reader (Perkin Elmer, Waltham, Massachusetts, United States of America).

The effect of lalistat 2 and chloroquine on viability was analyzed after 24 hours. Additionally, the viability influence of the co-treatments was analyzed. Cells were pretreated 90 minutes before LNC incubation with 10 µM lalistat 2 (Sigma Aldrich, St. Louis, Missouri, USA) and 20 µM chloroquine diphosphate (Sigma Aldrich, St. Louis, Missouri, USA). The resulting viability was addressed as mentioned above.

5.2.8. Confocal laser scanning microscopy (CLSM)

Cells were seeded into 4 well glass bottom imaging cell culture dishes (µ-Slide 4 Well, ibidi GmbH, Gräfelfing, Germany) under the same conditions as described under 5.2.7.2. Following the 16 hours incubation, the cells were washed 3 times with DPBS and then incubated using Hoechst 33342 (20 µg/ml) for 10 minutes to stain the nuclei. Unbound dye was removed and cells were 5 times washed with DPBS. Cells were treated afterwards with Lino-LNC (0,1 mg/ml) for 1 h. Lipid phase was stained with 1,1'-Dioctadecyl-3,3,3',3'-tetramethylindocarbocyanine perchlorate (DiI) at a DiI ratio of 0,013 mg per mg lipid. Imaging was performed after 1h of incubation using a Nikon A1 confocal laser scanning microscope (Nikon, Tokyo, Japan) equipped with an Eclipse Ti-E inverted microscope (Nikon, Japan) and an LU-NV laser unit (Nikon, Japan). Excitation wavelength for Höchst was 405 nm and for DiI 535.5 nm. Micrographs were taken using 60x objective with immersion oil [181]

5.2.9. Preparation of J774A.1 macrophages for SEM and SEM imaging

Cells were seeded over 16 hours at a density of 200.000 cells per well with a concentration of 400.000 cells/ml in 24 well plates containing sterile glass coverslips. Cells were treated with 0.1 mg/ml Lino LNCs or treated with 0.01 mg/ml in case of Ω-3 based LNCs. Following treatment, cells were washed 3 times with DPBS and fixed in 3 % glutaraldehyde buffered with 0.1 molar cacodylate pH 7.4 for 30 minutes at room temperature. Fixed cells were washed by DPBS in triplicate and stained in 1 % osmium tetroxide for 120 min. After contrast enhancement the cells were washed again and gradually dehydrated in a ethanol series 35 %, 50 %, 70 %, 80 %, 90 % v/v)) with the last step being 3 times absolute ethanol. As a last step the ethanol was removed and replaced by HMDS. HMDS was removed after 10 minutes, and the sample was airdried. Dried samples on coverslips were glued onto SEM stubs using conductive silver and sputter coated with platinum using a Q150T S (Quorum Technologies, Judges House, Lewes Road, Laughton, East Sussex, UK) at 30 mA for 20 seconds. Samples were imaged using the FE-SEM function of the Helios G4 CX FIB-SEM (former FEI Company now Thermo Fisher Scientific Inc, Eindhoven, Netherlands) at 10 kV to ensure sufficient electron penetration into the cells to collect subsurface signals.

5.2.10. Preparation of J774A.1 macrophages for STEM

5.2.10.1. Sample preparation

Treatment conditions were kept similar to the previously described conditions. Cells also glutaraldehyde fixed for 30 minutes and washed. Contrast enhancement was done using the reduced osmium tetroxide thiocarbohydrazide osmium tetroxide (rOTO) technique. Contrast enhancement was performed for 90 minutes in reduced osmium (1.5% ferricyanide and 1% osmium tetroxide) following 3 washing steps and an incubation of 20 minutes using 0.5% thiocarbohydrazide (TCH). Subsequently to the TCH incubation the samples were washed again in triplicate and stain in 1% osmium tetroxide for 90 minutes followed by a washing step. Samples were then dehydrated in an ethanol series 35 %, 50 %, 70 %, 80 %, 90 % (v/v). As Final dehydration step, the samples were 3 times incubated in absolute ethanol. Gradually the ethanol was replaced by a graded series of epoxy resin/ethanol mixtures with the last steps being pure resin, which is finally polymerized in an oven at 45 °C (modified from [37]). After 24 hours the temperature increased to 60 °C for 48 hours. Sample were fractured into suitable sized pieces. These pieces were glued on epoxy resin stubs and pre trimmed using Teflon coated razorblades (Graticules Optics Ltd, Tonbridge, Kent, United Kingdom). Ultrathin sections of 70 nm were cut from the block face via ultramicrotomy using a Powertome (Boeckeler Instruments Inc, Tucson, Arizona, United states of America) equipped with a diamond knife (Diatome AG, Nidau, Switzerland). Ultrathin sections were collected on formvar coated slot grids and placed into the Electron microscope. Micrographs were taken by brightfield STEM imaging at 30 kV using a Helios G4 CX FIB-SEM microscope (former FEI Company now Thermo Fisher Scientific Inc, Eindhoven, Netherlands).

Control samples included untreated cells, lalistat 2 and chloroquine treated cells and cells treated with commercially available 10 nm gold nanoparticles (AURION Immuno Gold Reagents & Accessories, Wageningen, The Netherlands), diluted 1:10 from stock (gold content in stock approximately 0.0125%).

5.2.10.2. Post staining

On grid staining was performed using uranyl acetate (Electron microscopy sciences, 1560 Industry Road Hatfield, Pennsylvania, USA) 2% solution for 25 minutes following 7 minutes 3% lead citrate.

5.3. Results

5.3.1. Screening for suitable osmiophilic excipients.

All excipients screened could successfully be emulsified using PVA 13000. In most cases the formation of electron dense black precipitates was observed except for medium chain triglycerides (MCT) which showed no reactivity and could not further be analyzed. Within the SEM (Figure 40) almost all samples analyzed in the screening showed electron dense spherical structures with intense contrast (Figure 40 A-G) except for the Span 80 and oleic acid based samples (Figure 40 H, I). Interestingly the oleic acid based samples showed electron denser precipitates on the surface.

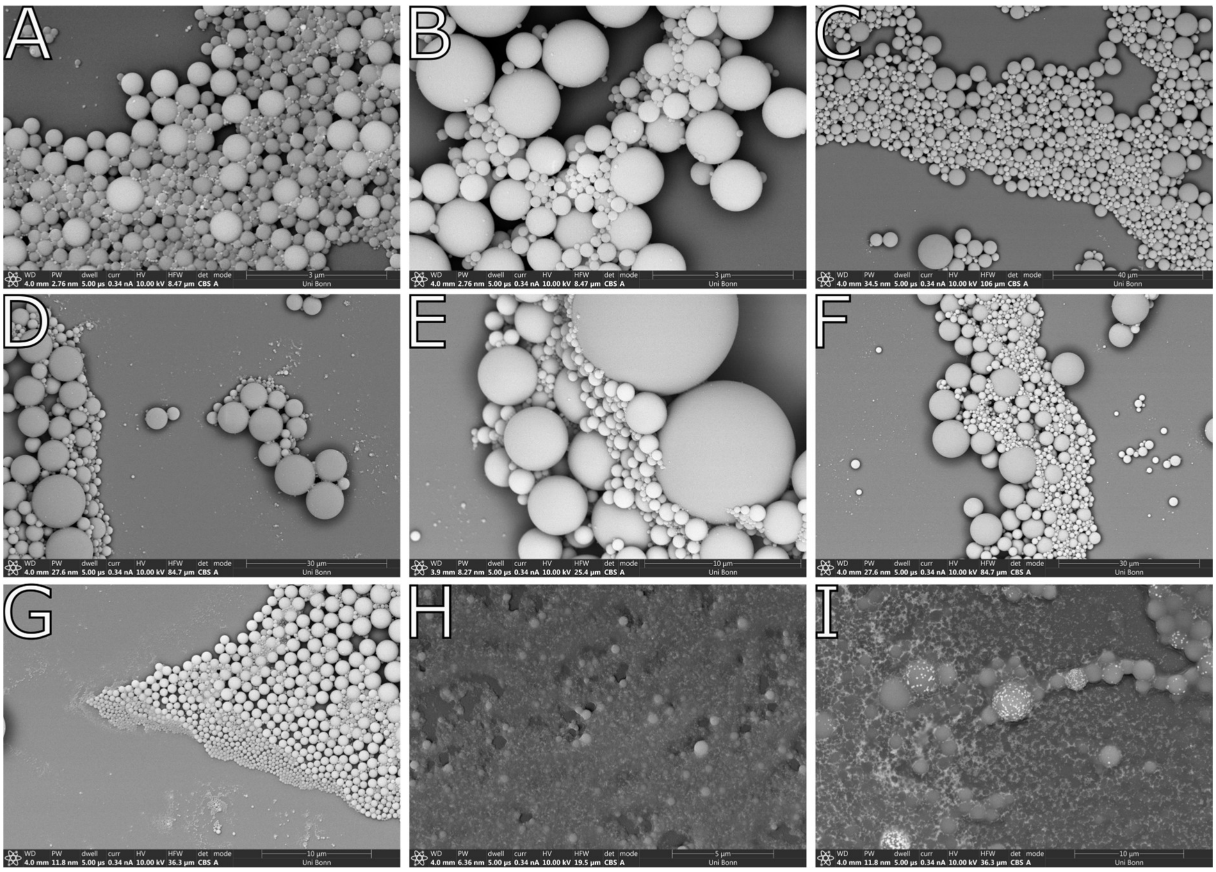

Figure 40: Osmification of unsaturated lipidic excipients.
Micrographs were obtained by SEM imaging using BSE. Theimage sectionsdisplay labrafil M2125 (A), K85EE omega-3-acid ethyl esters (B) squalene (C), olive oil Ph.Eur. grade (D), super refined corn oil (E), super refined cottonseed oil (F), Span 85 Ph.Eur. grade (G) Span 80 Ph.Eur. grade (H) and super refined oleic acid (I). (#)

In addition, the aforementioned mono-, di- and triglycerides of linoleic acid [Maisine CC™], omega-3 ethyl esters [Incromex E 7010™] and omega-3 triglycerides [Incromex TG 4030™] (Figure 41 B-D) were analyzed. The excipients could successfully be emulsified using polyvinyl alcohol 13000. The particle size distributions measured before osmification (Figure 41 A) were in the range of the particles shown in the micrographs (Figure 41 B-D). These excipients maintained their spherical shape as well during osmification. Resulting from screenings, the linoleic acid and Ω-3 based excipients are used for further experiments and formulation development.

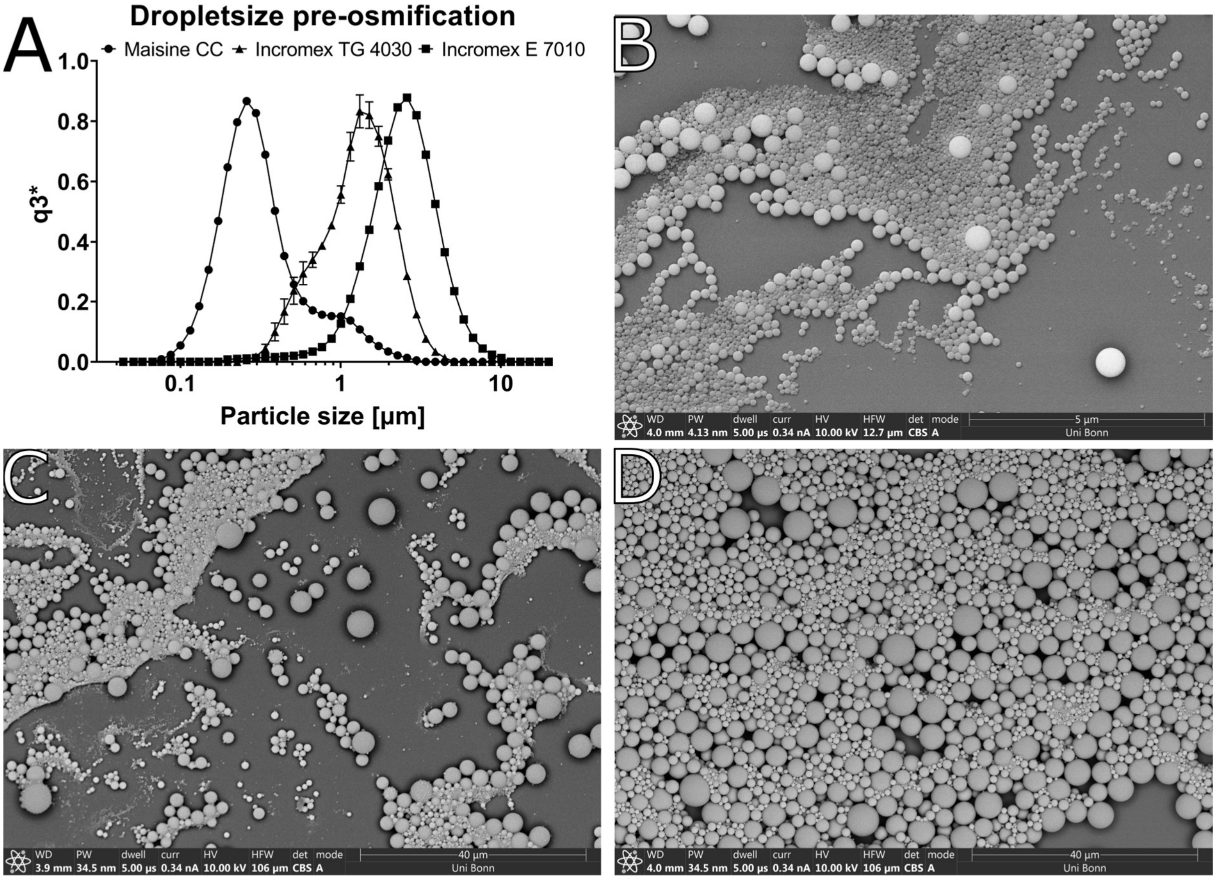

Figure 41: Particle size distribution of linoleic and Ω-3 based excipients pre osmification and SEM micrographs post osmification.
Image section A shows the droplet size distribution of the three oils before osmification, measured by laser diffraction. The following sections show Maisine CC™ (B), Incromex TG 4030™ (C) and Incromex E 7010™ (D) emulsion after osmification as SEM images. Data are presented as mean ± SD (n=3) (#)

5.3.2. LNC formulation development

The linoleic acid and Ω-3 based excipients were chosen for further investigation and their ability to form LNCs. Higher concentrations were investigated for potential upscaling enabling higher particle concentrations or respective potential drug loading. The emulsions were successfully prepared over a wide range of lipid concentrations as well as surfactant ratios (Figure 42, 43 44). Formulations were analyzed for their respective particle size distributions by laser diffraction aiming for distributions below 1 µm.

Maisine was able to form LNCs even at 15% weight fractions (Figure 42 A-D). Emulsion preparation was not always possible due to gelling, especially for high lipid contents paired with high surfactant ratios (Figure 42 C, D). This resulted in particle distribution with larger particles, as particles formed after dilution. The screening aimed to find the first formulation with true nanometer distribution in each weight fraction. With the formulations having the first nanometer distribution being 5%-Maisine+2% PS80, 10%-Maisine + 5% PS80 and 15% Maisine + 10% PS80. For the 20% fraction it was not possible to reach a pure nanoparticle fraction.

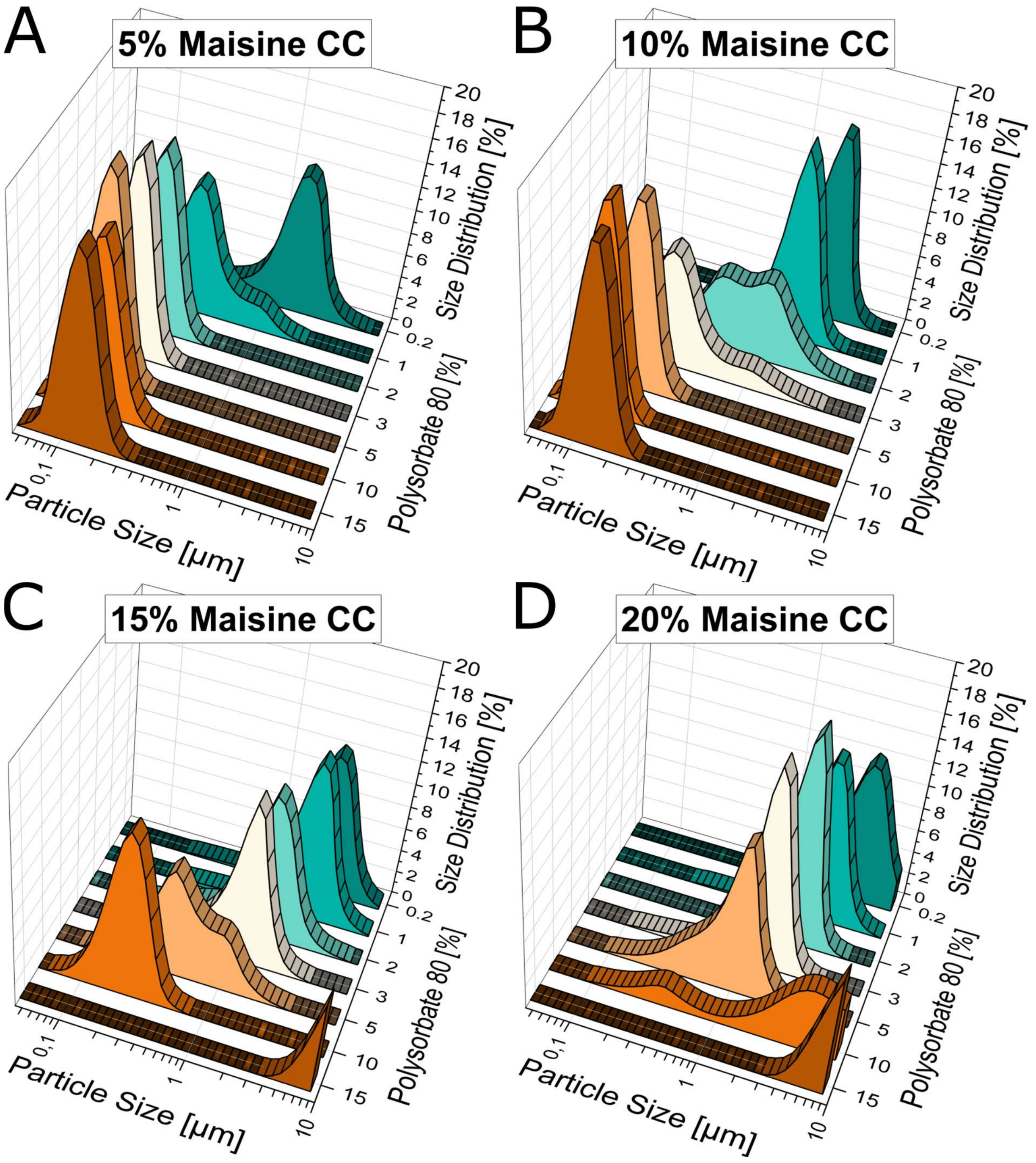

Figure 42: Particle size based formulation screening of Maisine CC based LNCs using polysorbate 80 as surfactant.
Shown are wall plot diagrams of particle size distributions obtained by liquid cell laser diffraction after ultrasound emulsification. Formulations with lipids consisting of mono-, di- and triesters of linoleic acid (Maisine CC) were prepared at concentrations of 5% (A), 10% (B), 15% (C) and 20% (D) using different polysorbate concentrations. The data is given as mean values (n=3).

Similar results were obtained with emulsions prepared using the omega-3 triglycerides. Omega 3 triglyceride based oils showed no gelling, thus leading to reduced particle size with increased PS-80 content. In this case the formulations which reached nanometer sized distribution were similar to the Maisine CC ones (Figure 43 A-D).

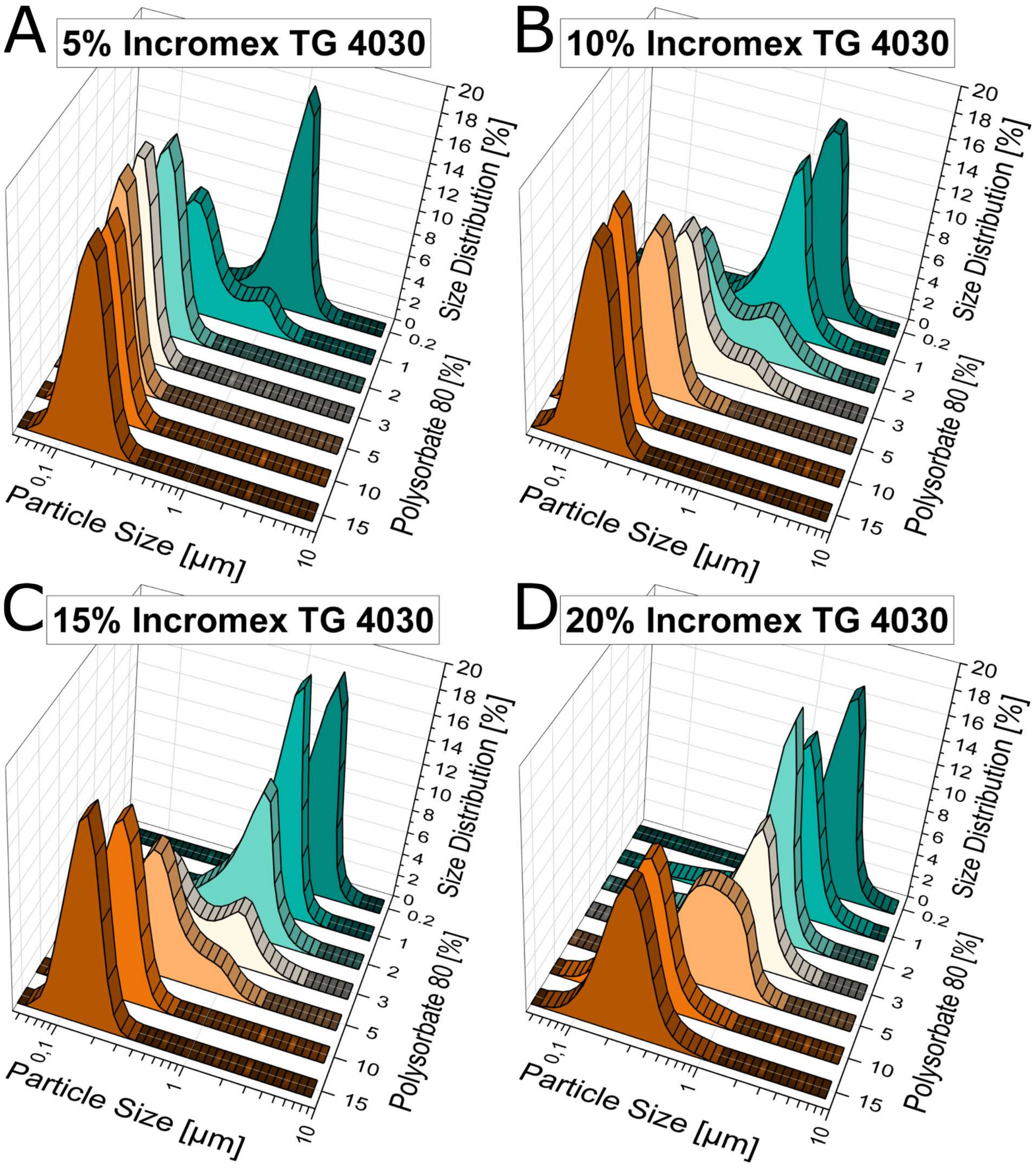

Figure 43: Particle size based formulation screening of Incromex TG 4030 based LNCs using polysorbate 80 as surfactant.
Shown are wall plot diagrams of particle size distributions obtained by liquid cell laser diffraction after ultrasound emulsification. Formulations with lipids consisting of Ω-3 triglycerides (Incromex TG 4030) were prepared at concentrations of 5% (A), 10% (B), 15% (C) and 20% (D) using different polysorbate concentrations. The data is given as mean values (n=3).

Again, similar results compared to the other obtained particle size distributions could be obtained for the compositions screened involving the omega-3 ethyl esters. Here all weight fractions of inner phase were able to achieve a nanometer distribution depending on the amount of PS80 used. The formulations reached the first nanometer sized distribution at 5%-Incromex-E 7010+3% PS80, 10%- Incromex-E 7010 + 5% PS80 and 15% Incromex-E 7010 + 10% PS80 and 20% Incromex-E 7010 + 15% PS80 (Figure 44 A-D).

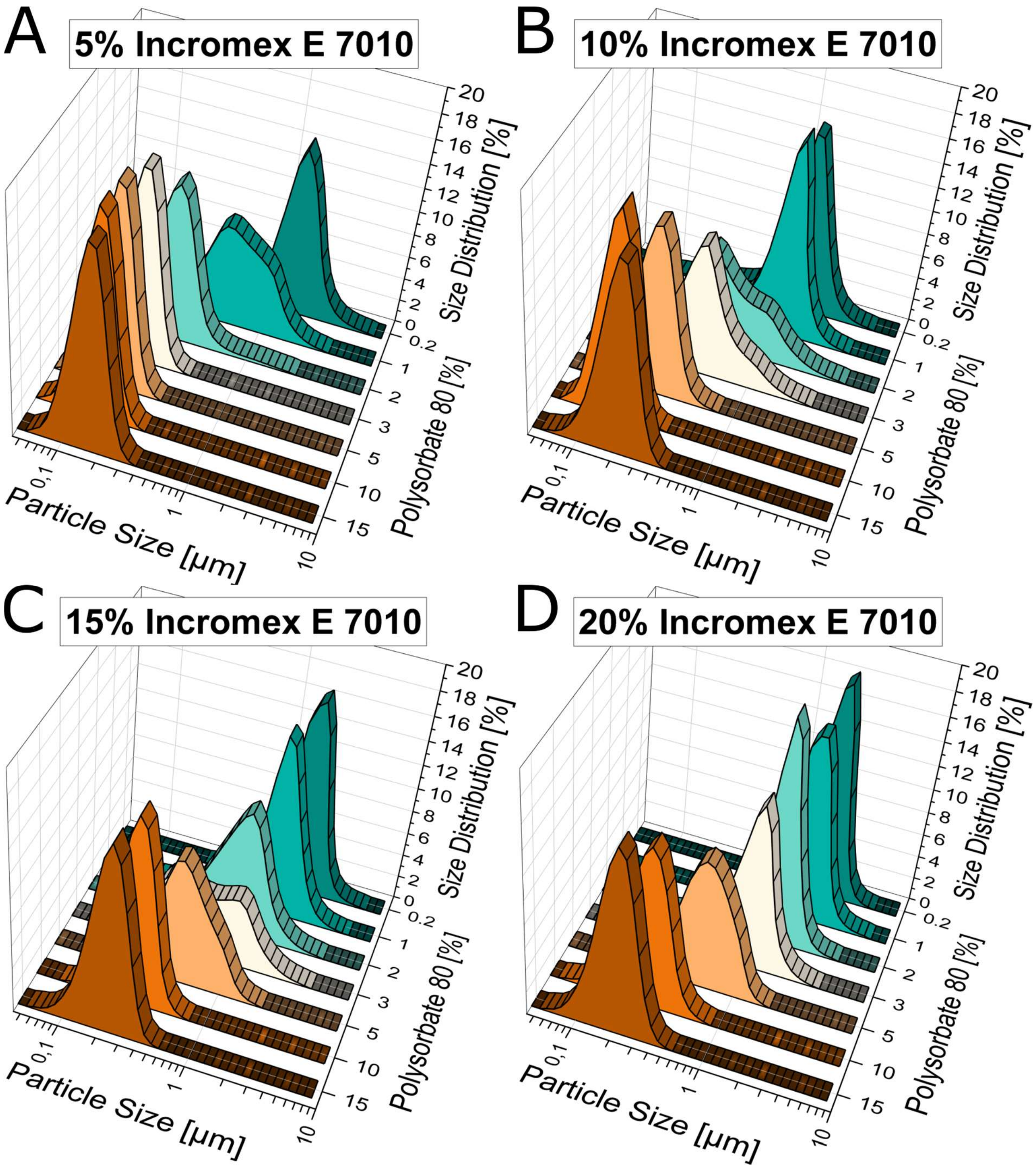

Figure 44: Particle size based formulation screening of Incromex E 7010 based LNCs using polysorbate 80 as surfactant.
Shown are wall plot diagrams of particle size distributions obtained by liquid cell laser diffraction after ultrasound emulsification. Formulations with lipids consisting of Ω-3 ethyl esters (Incromex E 7010) were prepared at concentrations of 5% (A), 10% (B), 15% (C) and 20% (D) using different polysorbate concentrations. The data is given as mean values (n=3).

From this screening, the emulsions with 5% lipid content were selected for further experiments. The properties and corresponding abbreviations of the formulations are summarized below (Table 10). These abbreviations will henceforth be used throughout the text to reference the respective compositions. Further particle size analysis was performed using DLS, as it offers better resolution within the nanometer range. DLS measurements revealed nanoparticle distributions within comparable size ranges (Figure 45 D). Overall, the particle obtained by DLS sizes were smaller compared to those determined by laser diffraction. Additionally, the lipid nano carriers were further analyzed for their particle size after osmification by SEM (Figure 45).

Table 10: LNC composition and particle sizes

Composition	*Abbreviation*	*Median (Laser Diff.) [nm]*	*Z-Average [nm]*	*Median (DLS) [nm]*
5% Maisine CC™ 2% PS80	Lino-LNC	154±1	151±1	112±4
5% Incromex TG4030™ 2% PS80	Ω3TG-LNC	152±0	120±3	81±9
5% Incromex E 7010™ 3% PS80	Ω3EE-LNC	144±0	126±3	96±7

The SEM micrographs showed particles of Lino-LNC (Figure 45 A), Ω3TG-LNC (Figure 45 B) and Ω3EE-LNC (Figure 45 C) within the size range measured by laser diffraction as well as DLS (Figure 45 D).

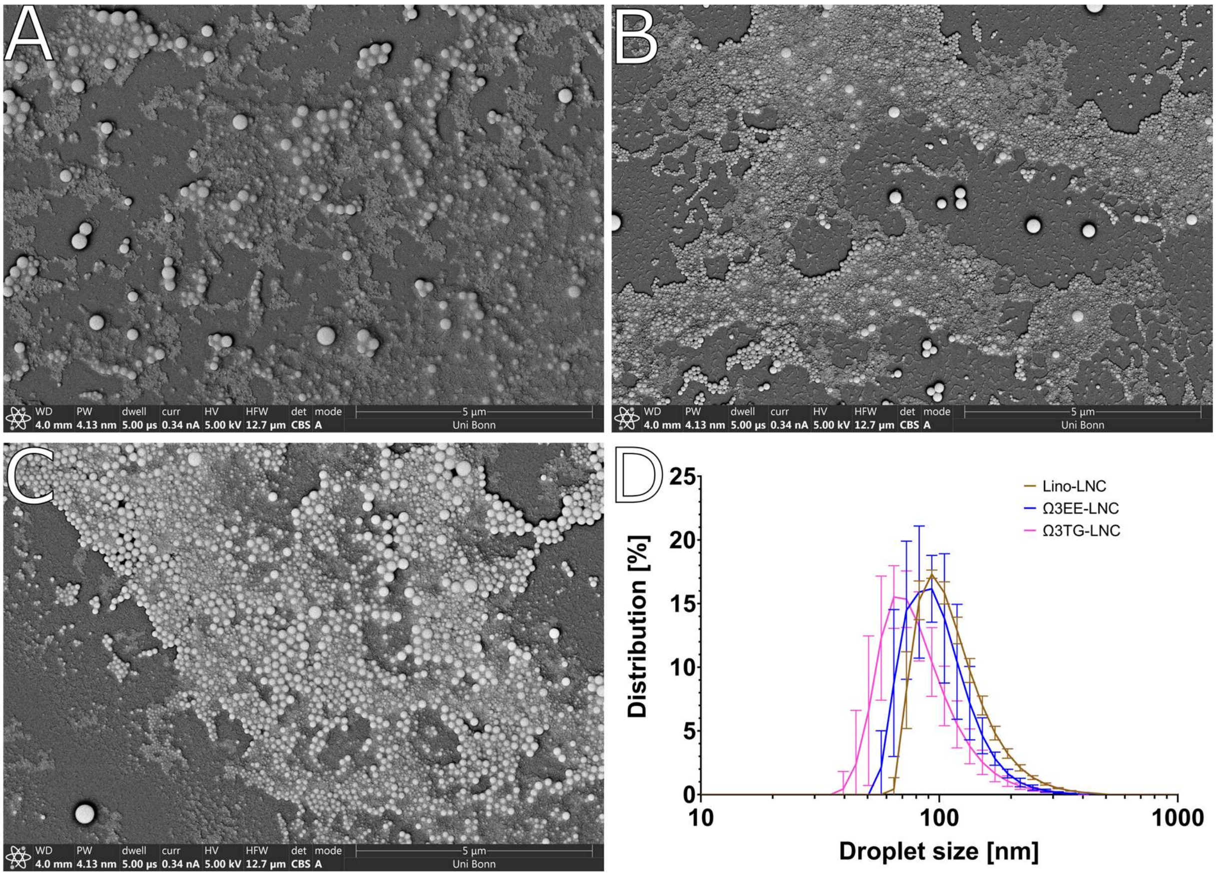

Figure 45 BSE-Micrographs of osmified LNC´s and respective particle size distribution measured by DLS.

With Micrograph (A) being Lino LNC, Ω3TG-LNC (B) and Ω3EE-LNC being (C) and image section D being the DLS volumetric particle size distribution. Data are presented as mean ± SD (n=10) (#)

5.3.3. Uptake studies under native conditions

The carriers characterized above (Table 10) were used to treat the murine macrophage cell-line J774A.1. Before the imaging by EM the influence of the LNCs on the viability of the J774A.1 cells was determined by MTT-assay. Consequently, a loss of viability was seen with increased concentration. The IC 50 values obtained were 267.4 µg/ml (95% CI [218.5 µg/ml, 319.1 µg/ml]) for Lino-LNC, 26.7 µg/ml (95% CI [23.42 µg/ml, 29.44 µg/ml]) for Ω3TG-LNC and 41.72 µg/ml (95% CI [30.46 µg/ml, 47.32 µg/ml]) for Ω3EE-LNC (Figure 46 A-C). The Lino-LNC had the lowest negative influence on cellular.

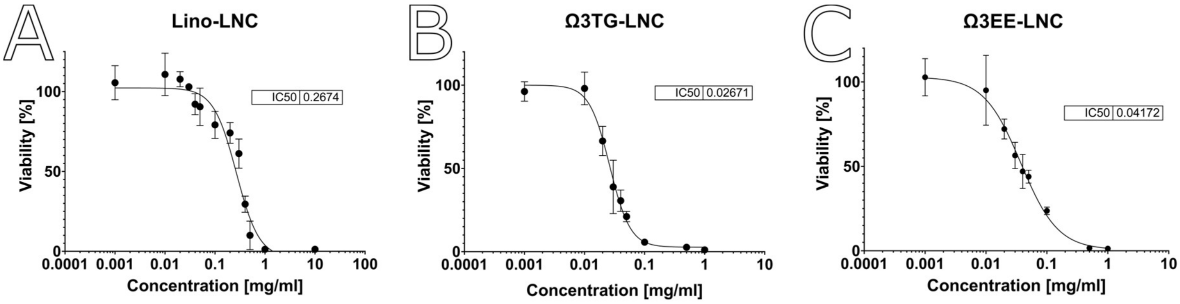

Figure 46: Viability of J774A.1 cells after 24 hours of LNC incubation.
Sections A-C display the concentration dependent influence of the LNCs on viability determined by MTT-assay on J774A.1 cells after 24 hours of incubation. The presented image sections display the viability influence of Lino LNCs (A), Ω3TG-LNCs (B) and Ω3EE-LNCs (C) using various concentrations. Data are presented as mean ± SD (n=4). (#)

Besides by EM imaging the LNC uptake was also investigated by CLSM (Figure 47 A, B). Both micrographs show a cell with nuclei in blue and the DiI label in orange. Orange accumulations range from sub-micron to around 5 µm in size. No accumulation of DiI related signal in a relevant amount is visible from surface attached Lino-LNC.

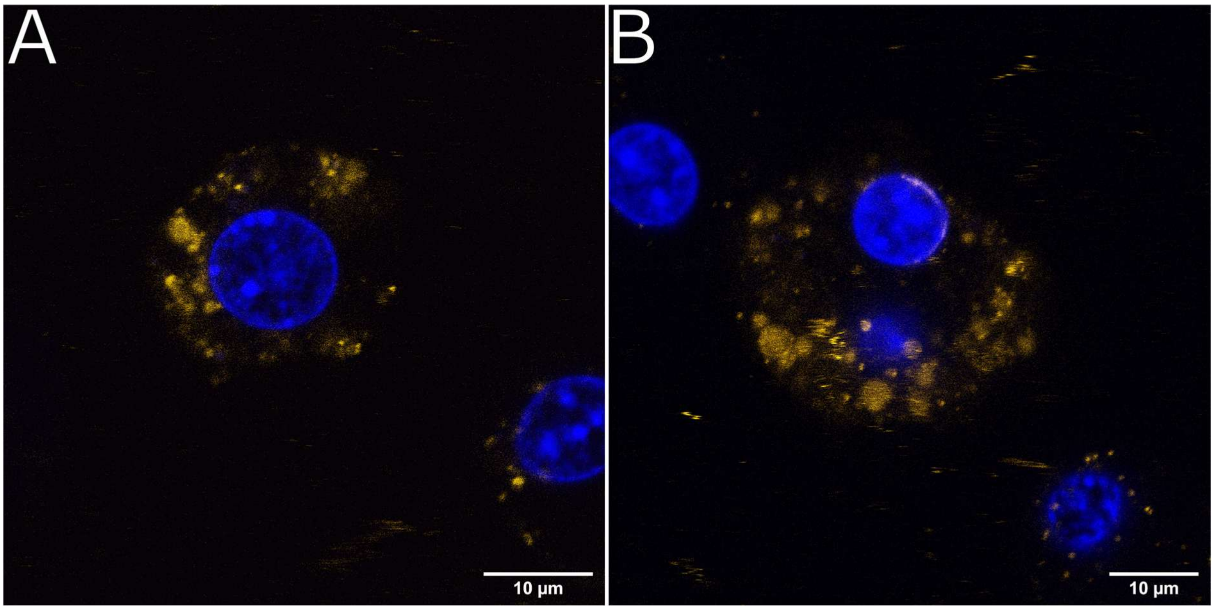

Figure 47: CLSM Micrographs of Lino-LNC treated J774A.1
The orange signal (A, B) shows the uptake of the DiI-labeled Lino-LNCs. The cell nuclei are shown in blue. Micrographs were obtained after 1 hour of incubation using 0.1 mg/ml of DiI labeled Lino-LNCs. (#)

Before imaging treated cells, untreated control samples were imaged (Figure 48 A-F). Macrophages showed three naive morphologies elongated and stretched cells (Figure 48 D), roundish (Figure 48

C) and occasionally very large and flat cells (Figure 48 E). All cells show extensive amounts of surface structures such as microvilli and membrane ruffles with occasional macropinocytotic cups. Elongated cells show lamellipodia with filopodia sprouting from it.

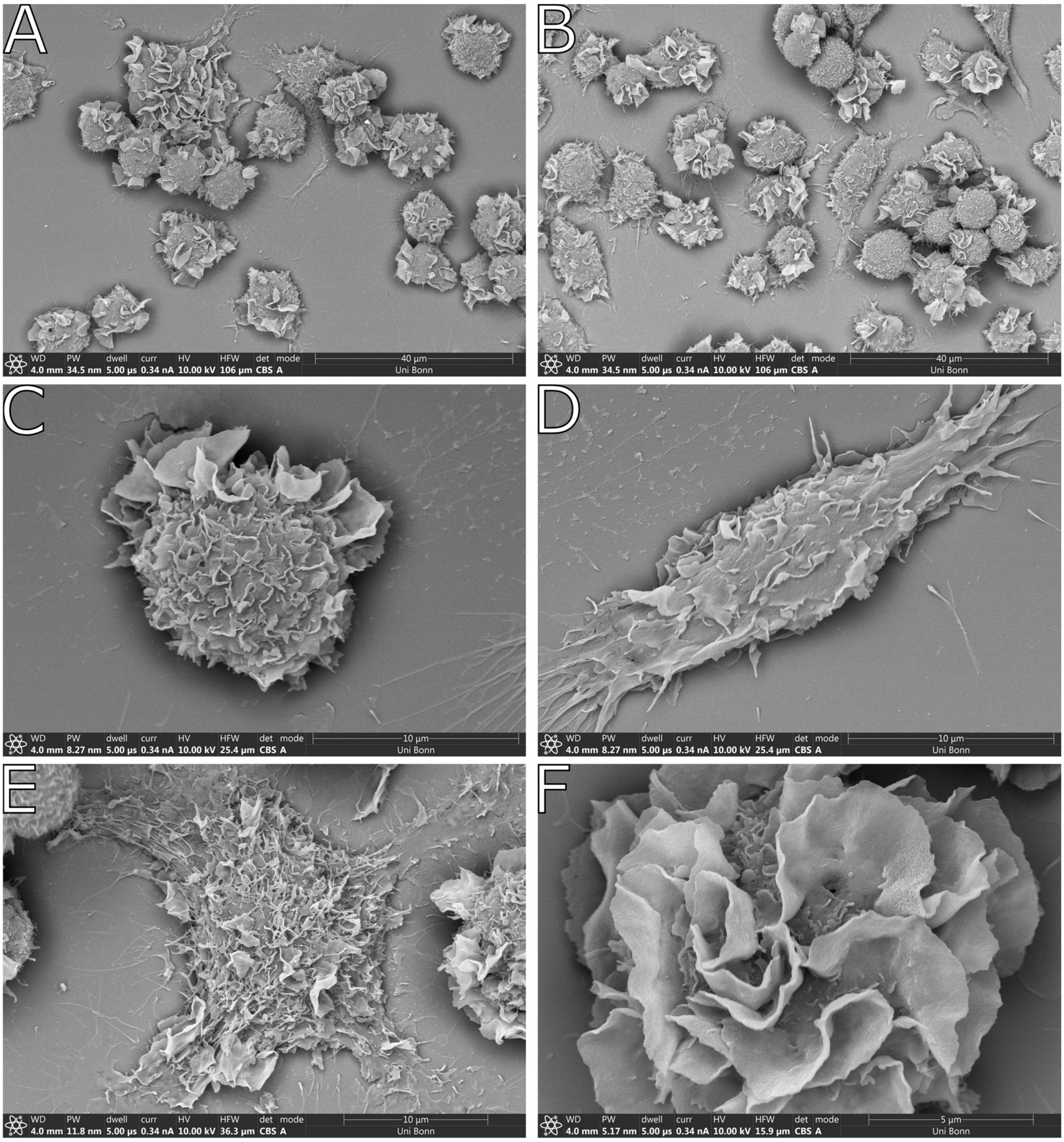

Figure 48: Overview of the cell morphology of the untreated J774A.1 cell line.
Sections A and B show small areas of adherent cells. The micrographs C-E show the three morphological types of the cell line, from round (C) to elongated (D) to large and flat (E). The elongated cells in particular can extend over distances of 40 µm. Most cells show clear signs of membrane ruffling (F). (#)

Morphological investigations of LNC treated cells by the HMDS technique showed cells in round or elongated shapes (Figure 49 A-F). Cellular surfaces were covered in protrusions and membrane ruffles. The elongated features such as lamellipodia from which filopodia spread were present as well. Cells showed membrane ruffles as well as formation of macropinocytotic cups (Figure. 49 B, E, F) indicating signs of macropinocytosis. Overall structural characteristics were comparable with untreated controls, except for accumulation of bright electron dense subsurface features. These subsurface features were very well visible in the lamellipodia but not limited to such structures. All treatments led to the appearance of bright structures after 24 hours of incubation, regardless of the prepared LNCs. Due to the higher dose, the Lino-LNCs (Figure 49 A, B) showed a higher enrichment and the Ω3TG-LNCs (Figure 49 C, D) showed the lowest amount. The cellular origin of the bright accumulations could not be further addressed using the HMDS technique.

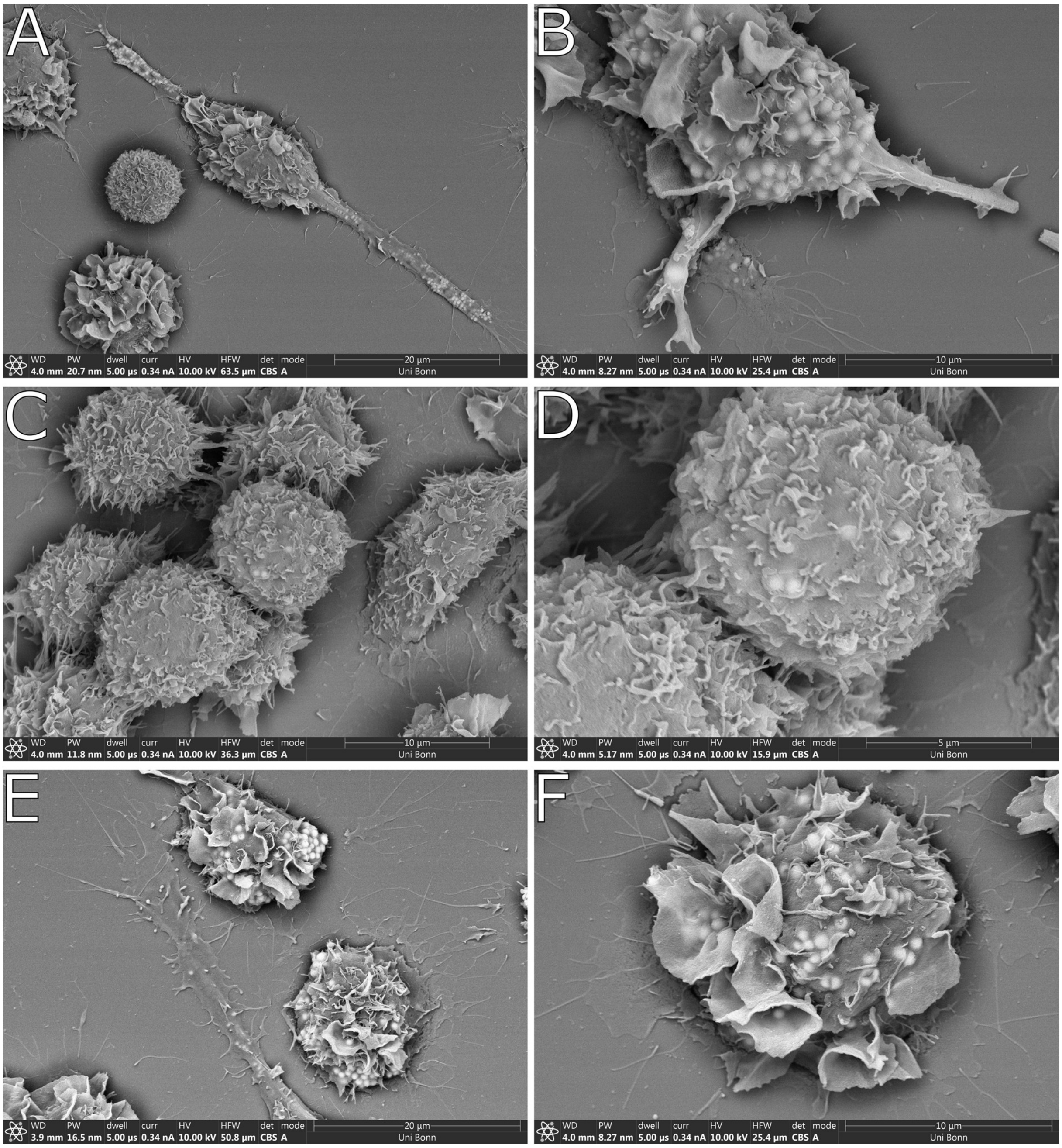

Figure 49: HMDS dried J774A.1 cells after 24 hours of LNC incubation
The micrographs display BSE images obtained from SEM imaging. Image sections (A, B) display Lino-LNC treated cells, sections (C, D) display Ω3TG-LNC treated cells and sections (E, F) display Ω3EE-LNC treated cells. Cells were treated with 0.1 mg/ml in case of Lino-LNC and 0.01 mg/ml in case of the Ω3-based excipients. All treated cells exhibit some degree of electron-dense material accumulation (indicated by arrows) in the BSE micrographs. Apart from the bright structures marked by the arrows, cell morphology remains unaffected. Both untreated and treated cells display extensive membrane ruffling, as well as the presence of lamellipodia and filopodia. Lamellipodia are elongated cellular structures very present in (C, D, G), from which the thread like filopodia sprout. (#)

Uptake of Lino LNCs was also successfully investigated at earlier timepoints e.g. 15, 30, 60 and 120 minutes (Figure 50 A-D). Overall, cellular morphology was comparable to earlier investigations and the untreated cells (Figure 48/49). The first visible bright structures were detected after 30 minutes which grew more pronounced at later timepoints. After 120 min bright accumulations are well visible. Using this approach Ω3TG-LNC and Ω3EE-LNC´s were also investigated with general comparable results.

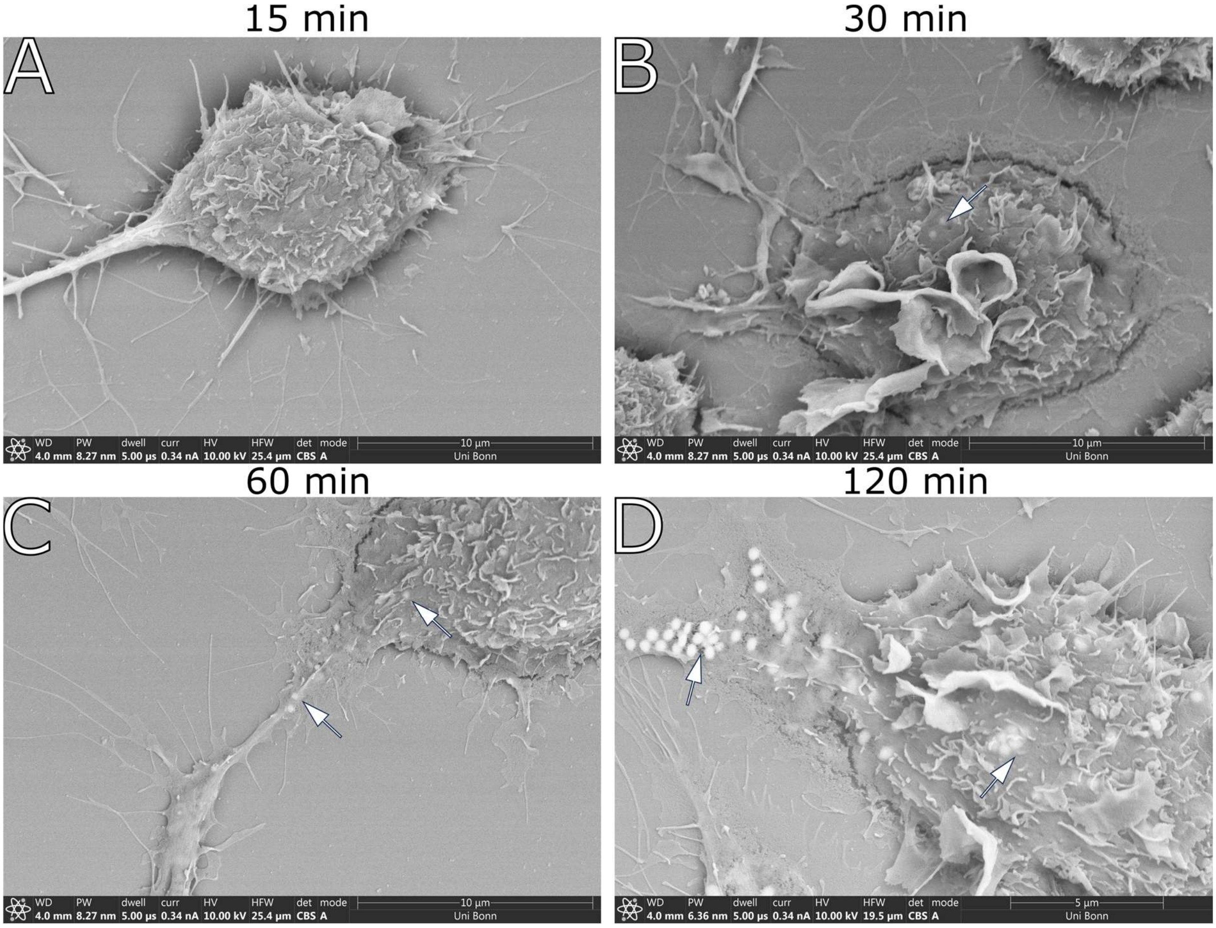

Figure 50 SEM micrographs of J774A.1 cells after treatment with Lino-LNC observed at different incubation times.
After 15 minutes of incubation, there are no discernible differences between the treated cells and the control group (A). However, after 30 minutes (B), subtle electron dense structures under the surface (indicated by arrows) become visible. These features become clearer after 60 minutes (C) and are even more pronounced after 120 minutes of incubation (D). (#)

The largest differences was found when imaging the Ω3TG-LNC interactions as here seldomly adherend structures of bright electron dense nature could be visible. These features were visible occasionally attached to the surface but also attached to lamellipodia as well as filopodia (Figure 51). These structures differed greatly in electron density compared to the spherical structures found endogenously in the J774A.1 cell line (Figure 52), which are addressed later. The occurrence of electron dense subsurface accumulations was also observed after 30 minutes. Observations on Ω3EE-LNC treated cells were comparable to the Lino LNC treated samples. In these samples, the first visible electron dense accumulation were already visible after 15 minutes of incubation.

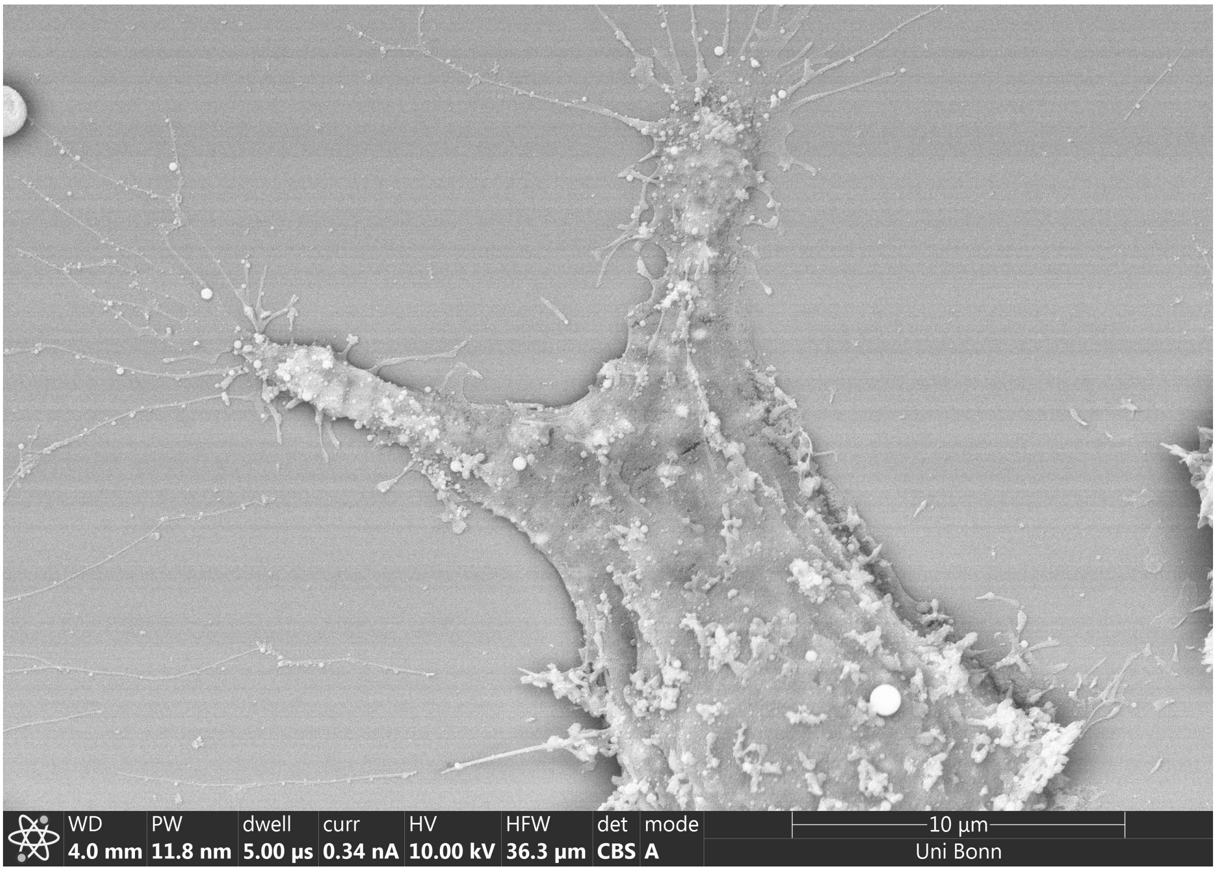

Figure 51: SEM micrographs of J774A.1 cells after treatment with Ω3TG-LNCs. *SEM micrographs of J774A.1 cells after treatment with Ω3TG-LNCs obtained after HDMS drying. (#)*

Especially when cells are imaged using secondary electrons, many spherical structures were visible which were attached to the cellular surface or located at the vicinity of cells (Figure 52 A, B). However, these structures were far less visible when BSE was used for imaging and were found in both treated and untreated cells. These structural features fit within the size range of many typical carriers used as nanotherapeutics. STEM imaging of untreated cells compared to cells treated with Lino-LNCs show a structural difference between the two collectives. Particles found within the untreated control were surrounded by a lipid bilayer containing material with heterogenic electron density (Figure 52 D,E,F [Ex]) whereas particles found in treated samples had two structural species (Figure 52 E). One of which belonged to the previously described particle species [Ex], while the other consisted of a homogeneous, electron-dense, dark, amorphous core with surrounding black precipitates (Figure 52 C,E). The latter mentioned particle collective matches the anticipated structure of the Lino-LNC (Figure 52 [LNC]). Lino-LNC should be consistent with the structure of nanoemulsion droplets, lipid surrounded by surfactant, thus particles showing this structure were considered primary particles from the LNC formulation. Particles endogenous present in control and treated samples match the theoretical ultrastructure of exosomes (Ex) and thus were identified as such.

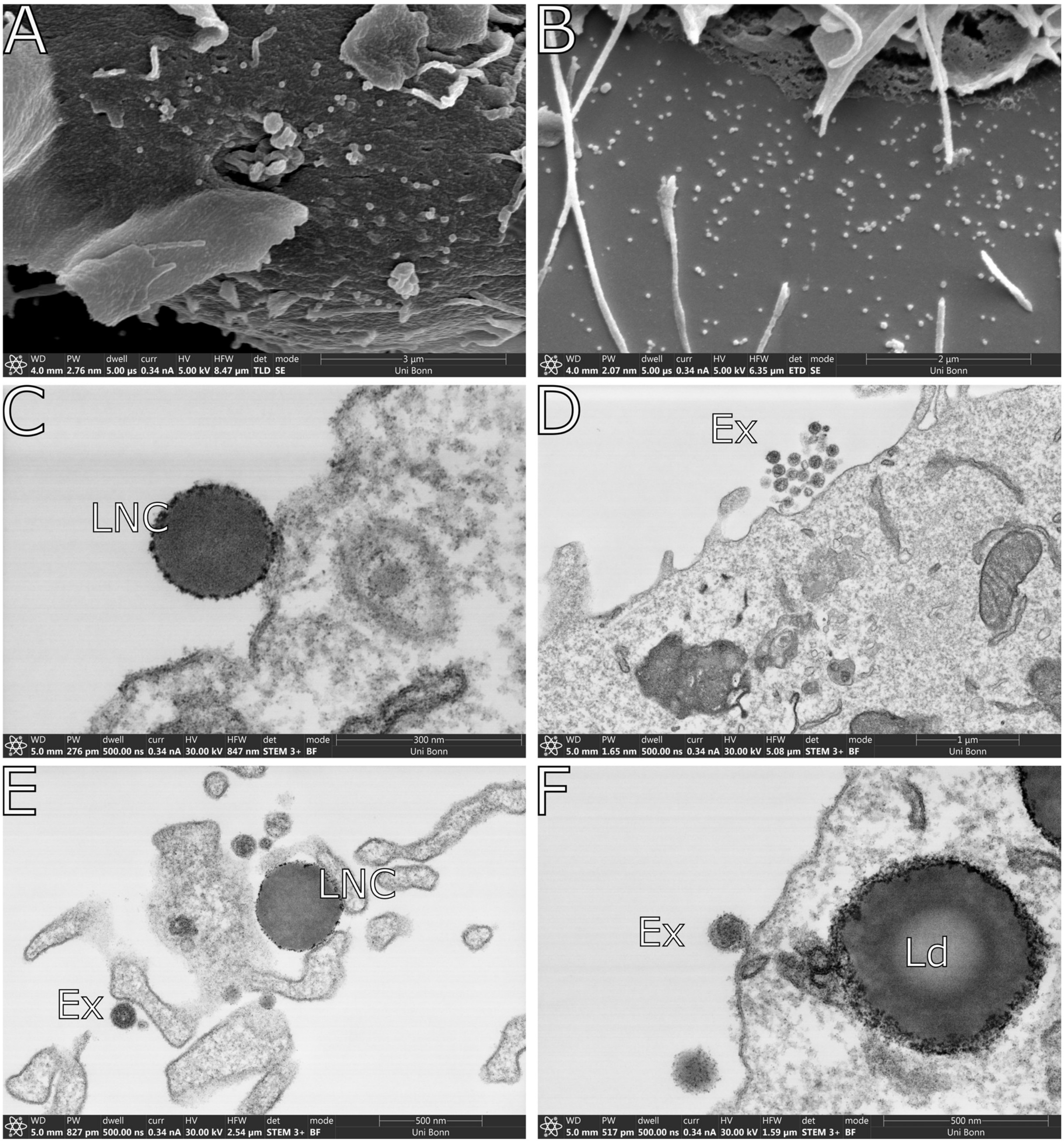

Figure 52: Comparison of surface-adherent endogenous and treatment-related structures.
SEM images of untreated J774A.1 cells obtained by SE imaging, showing endogenous spherical structures adhering to the cell surface (A) and spherical particles adhering to the glass surface (B). Ultrastructural studies by STEM of Lino-LNC treated cells prepared by rOTO staining show particles adhering to the surface (C, E). The endogenous spherical particles (Ex) are found in the untreated control (D) as well as in LNC treated samples alongside the LNCs (C, E, F). (#)

Abbreviations: Exosomes (Ex), Lipid droplet (Ld), Lipid nanocarrier (LNC)

As a control untreated J774A.1 cells were rOTO stained and imaged by STEM to address the cellular ultrastructure without treatments (Figure 53 A-F). Cells displayed many endolysosomes (Ly) characterized by their electron dense structure and heterogenic contents (Figure 53 A-E). The large vacuoles were most likely formed by macropinocytosis. Vacuoles (V) contained small amounts of greyish particulate content but else were as electron lucent as the surrounding resin (Figure 53 C, F). The cellular nucleus (N) takes up a relatively large portion (Figure 53 A, C, D, E) and is surrounded by a lipid double membrane with occasional nanosized pores e.g. nucleopores.

Cell nuclei can show deep invaginations with organelles occasionally present in such an invagination. Golgi apparatus (G) is also located within the vicinity of the nucleus (Figure 53 A). Multivesicular bodies (MvB) contained many spherical or membranous structures (Figure 53 E). Except for the structures, the lumen is electron lucent. Occasionally autophagosomes or phagophores (Pp) were visible (Figure 53 F). The endoplasmic reticulum is found throughout the cell as well as mitochondria (M).

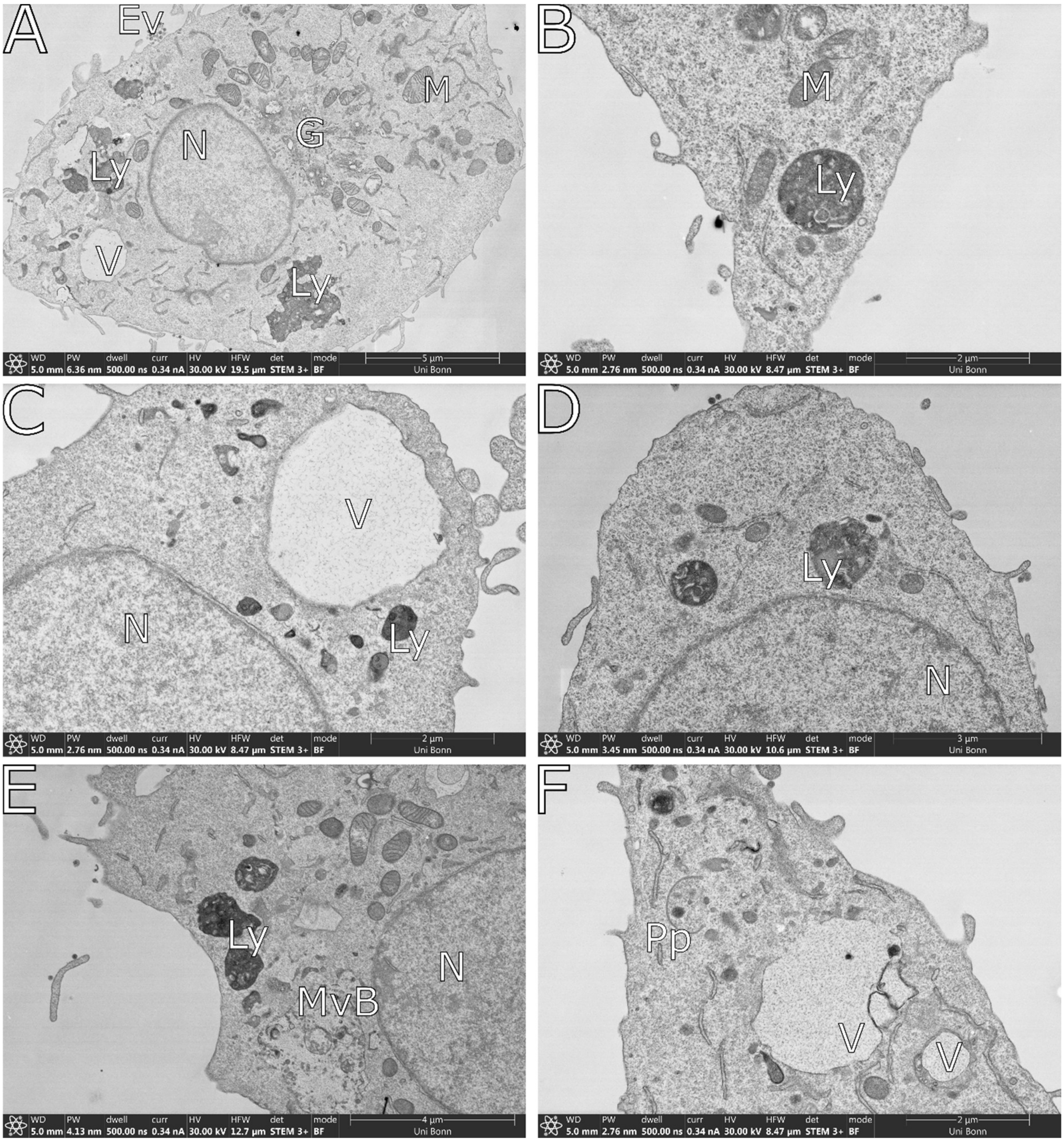

Figure 53: STEM images of various cells and cell regions representative of the untreated J774A.1 ultrastructure.
Micrographs were obtained from untreated rOTO-stained J774A.1 cells by brightfield STEM. Key structures identified include nuclei, the Golgi network, mitochondria, (endo)-lysosomes, multivesicular bodies/late endosomes, vacuoles likely formed by macropinocytosis, and phagophores. (#)

Abbreviations: Golgi complex (G), Lysosome (Ly), Mitochondria (M), Multivesicular bodies/Late endosomes (Mvb), Nucleus (N), Vacuole (V)

To determine which organelles are generally involved within the uptake of nanoparticles in the J774A.1 cell line, cells were incubated with commercially available 10 nm gold nanoparticles. (Figure 54 A-D). The nanoparticles visible as black dots in the brightfield STEM images accumulate especially within lysosomes (Ly) (Fig. 54 A, C, D) but were also found within multivesicular bodies (Mvb) (Fig. 54 A, B) and sometimes within endosomal vesicles (Ev).

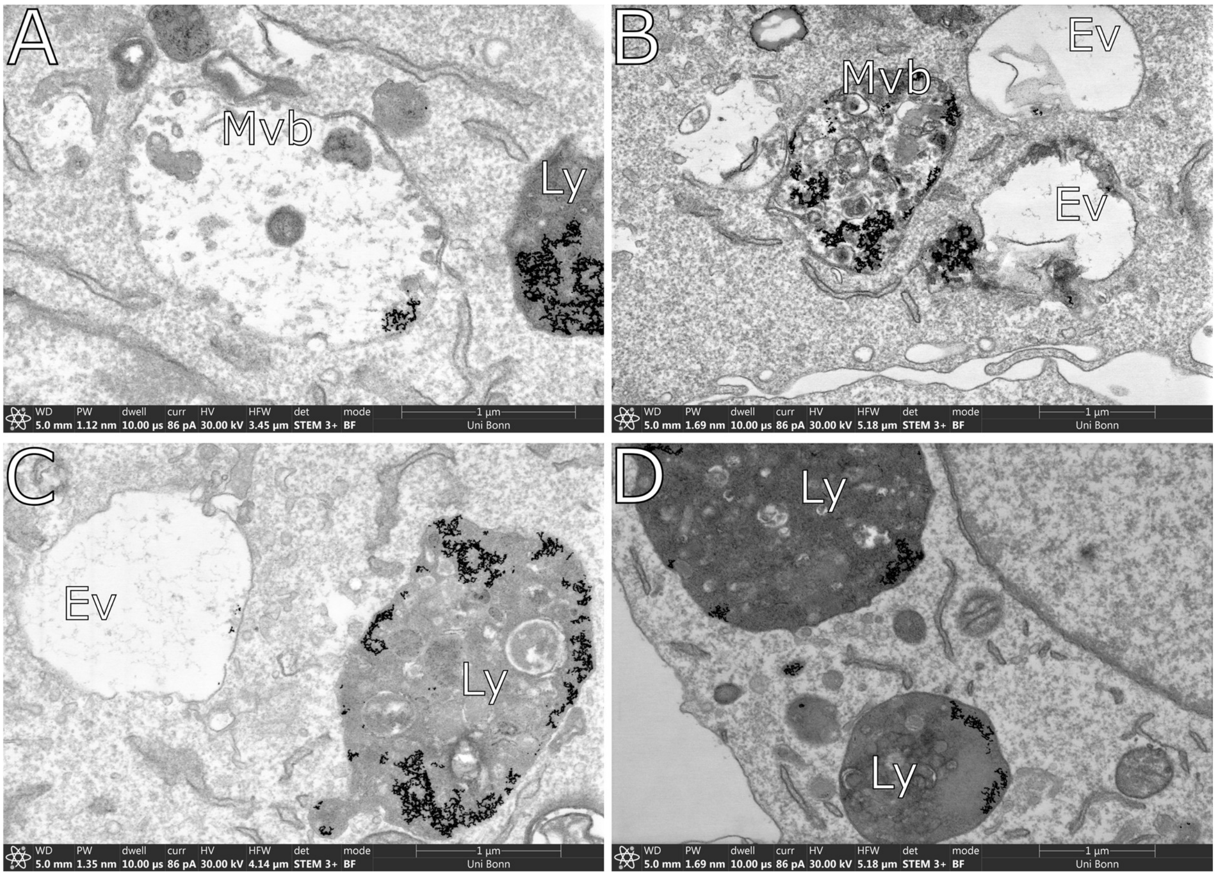

Figure 54: Micrographs of gold nanoparticles in J774A.1 cells.
The uptake of gold nanoparticles after 24 hours was imaged after rOTO staining by STEM. Gold nanoparticles, appearing as black electron-dense dots, were predominantly localized in lysosomes (A, C, D) and multivesicular bodies (A, B). Small amounts of gold nanoparticles could also be found within endosomal vesicles (B, C). (#)

Abbreviations: Endosomal vesicles (Ev), Lysosome (Ly), Multivesicular bodies/Late endosomes (Mvb),

STEM imaging of J774A.1 macrophages treated with Lino-LNC provided results consistent with those of the CLSM and HMDS uptake experiments (Figure 55 A-H). Micrographs acquired by STEM imaging allowed analysis of cellular ultrastructure after rOTO staining. The electron-dense accumulations observed after exposure to 0.1 mg/mL Lino-LNC were identified as lipid droplets and lysosomes. Notably, these lipid droplets were not present in untreated control cells. Early lipid droplets were occasionally observed after 15 minutes of incubation, albeit only to a small extent (Figure 55 B, asterisk), with the frequency of occurrence increasing after 30 minutes (Figure 55 C, D). Lipid droplets were frequently observed in the vicinity of the endoplasmic reticulum. In rare cases, intracellular LNC particles, which appear as spherical structures with an electron-dense core, were easily recognizable. These particles were located in endosomal vesicles or vacuoles characterized by an electron-lucent lumen, indicating recent internalization (Figure 55 A, G, H). A multivesicular body observed after 30 minutes of incubation (Figure 55 C) contained no structures clearly associated with LNCs.

When the lipid droplets reached a certain size, as observed after 30 minutes, they exhibited a recognizable “core-shell” structure. Depending on the section plane, only the darker, shell-like area surrounding the lipid droplets could be visible. This core-shell structure was absent in samples prepared with a simple reduced osmium tetroxide stain (Figure 56). After 60 minutes of LNC incubation, the lipid droplets were clearly visible and present in every cell examined. The accumulation of lipid droplets increased with increasing incubation time, as evidenced by the more pronounced presence at 60 minutes (Figure 55 E, F) and after 24 hours (Figure 55 G, H). After 24 hours of incubation, the overall structural characteristics of the cells remained comparable, although most lipid droplets had reached a diameter of about 1 µm.

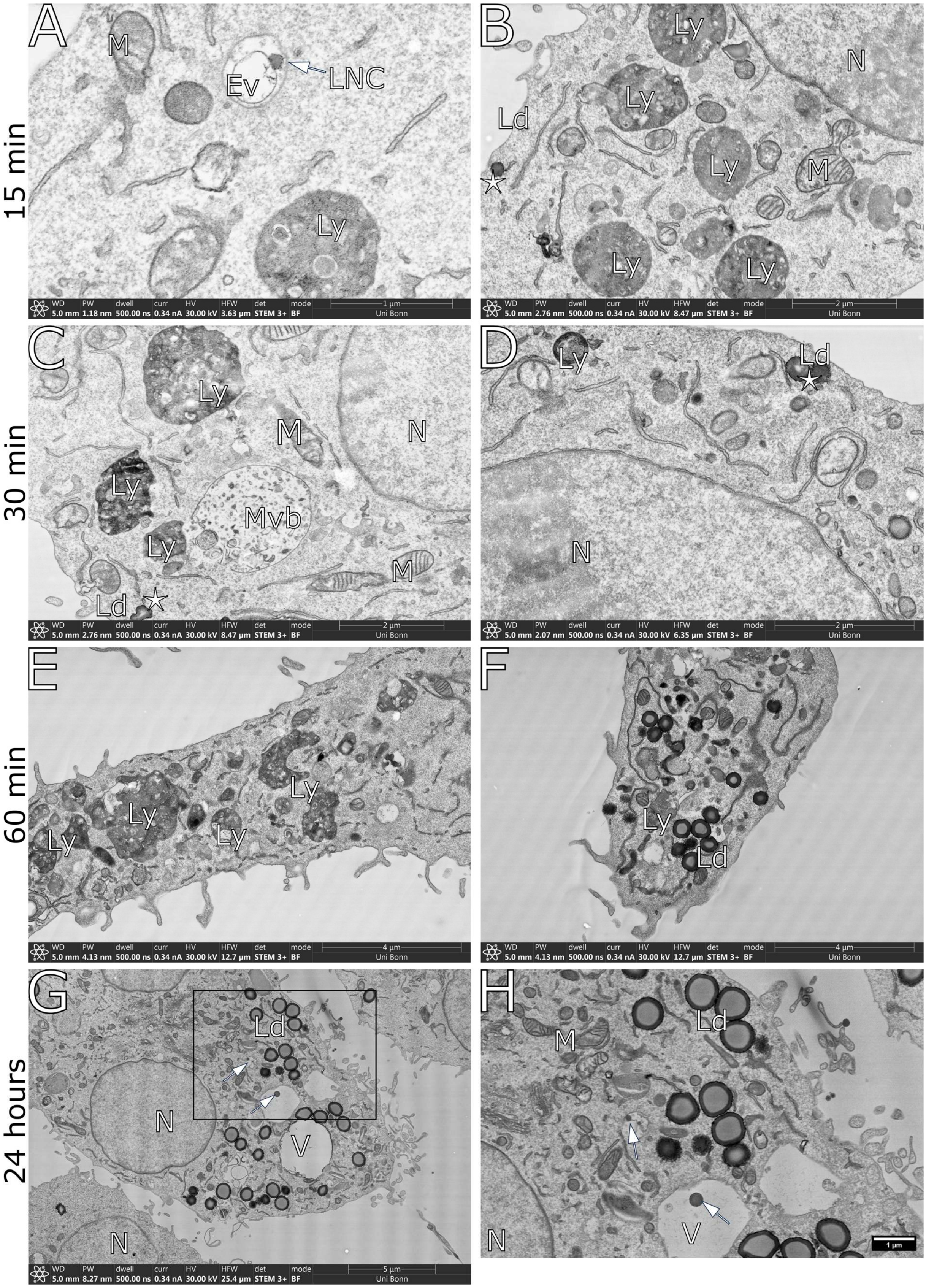

Figure 55: Micrographs of J774A.1 cells treated with Lino- LNC imaged by STEM at different incubation timepoints.

J774A.1 macrophage cells were imaged by STEM after incubation with 0.1 mg/ml Lino LNC and rOTO staining. Micrographs depict changes of the cellular ultrastructure after 15 min (A, B), 30 min (C, D), 60 min (E, F) as well as after 24 hours of incubation (G, H). LNCs (Arrows) are depicted as dark round spherical particles located within electron lucent vesicles (A, G,H). Lipid droplets *can be seen as early as 15 minutes (B, C, D, F G, H). The lipid droplets depicted at 15 and 30 minutes are additionally marked by asterisks. The depicted cell after 24 hours represents a typical cell except for the presence of the rarely observed LNC particles. A selected area within the micrograph is magnified in section H, providing a closer view of the ultrastructural features and LNC particles. (#)*

Abbreviations: Endosomal vesicles (Ev), Lipid droplet (Ld), Lipid nanocarrier (LNC), Lysosome (Ly), Mitochondria (M), Multivesicular bodies/Late endosomes (Mvb), Nucleus (N), Vacuole (V)

The lipid droplet appearing as a core shell structure is absent in samples prepared by a single staining of reduced osmium tetroxide (1% osmium tetroxide with 1,5% ferricyanide + uranyl acetate and lead citrate post staining) (Figure 56 A). This core shell structure resulting after rOTO staining is also not influenced by on-grid staining using uranyl acetate and lead citrate (Figure 56 B). Additionally, an increase in incubation time of thiocarbohydrazide did not change the lipid droplet structure but resulted in impaired staining quality (data not shown).

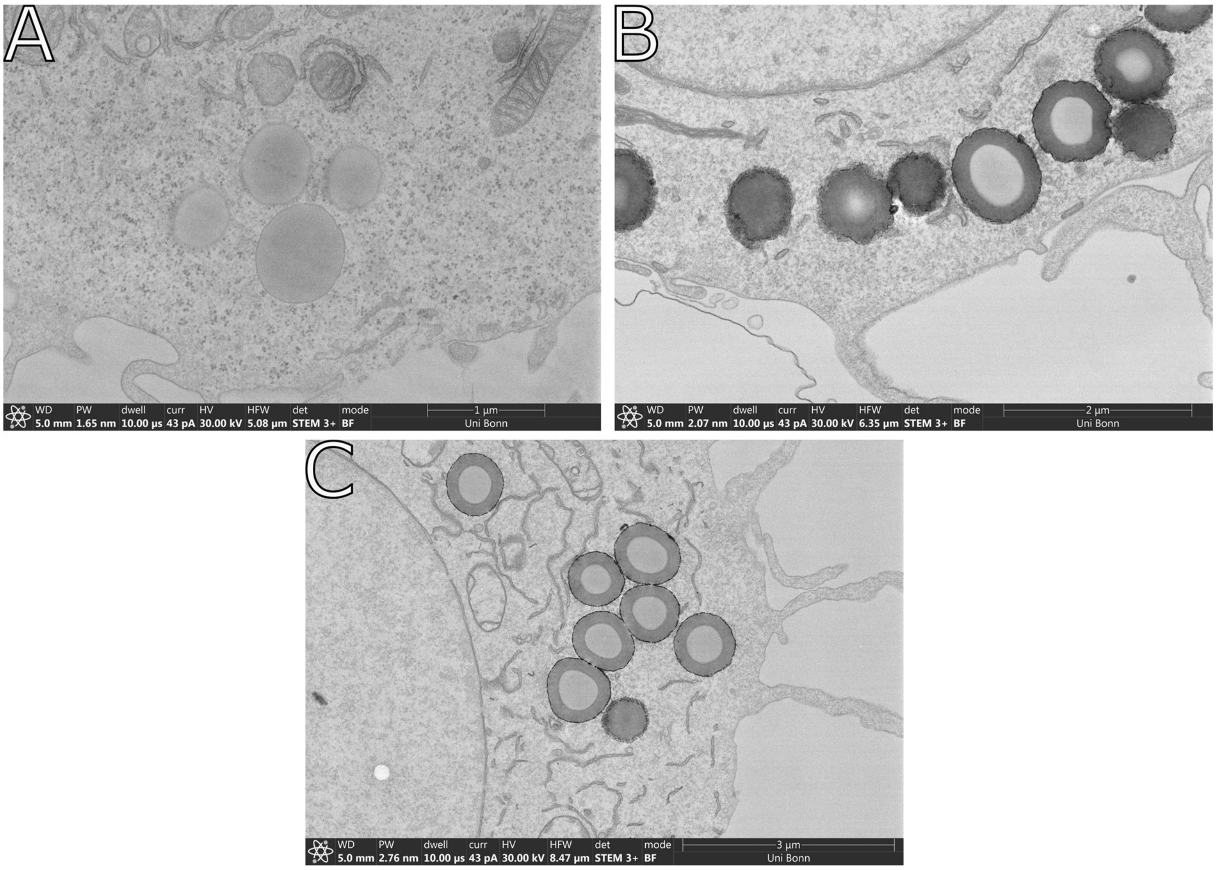

Figure 56: Lipid droplet structure after rO staining or rOTO staining
Lipid droplets in J774A.1 cells after Lino-LNC treatment stained with reduced osmium tetroxide, followed by post-staining on the grid, show a homogeneous grayish structure (A). Lipid droplets stained with rOTO show an apparent core-shell structure (B, C). The inclusion of staining on the grid did not change the observed morphology (B). (#)

After 24 h of incubation with Lino-LNC all cells contain numerous Lipid droplets throughout the cell (Figure 57).

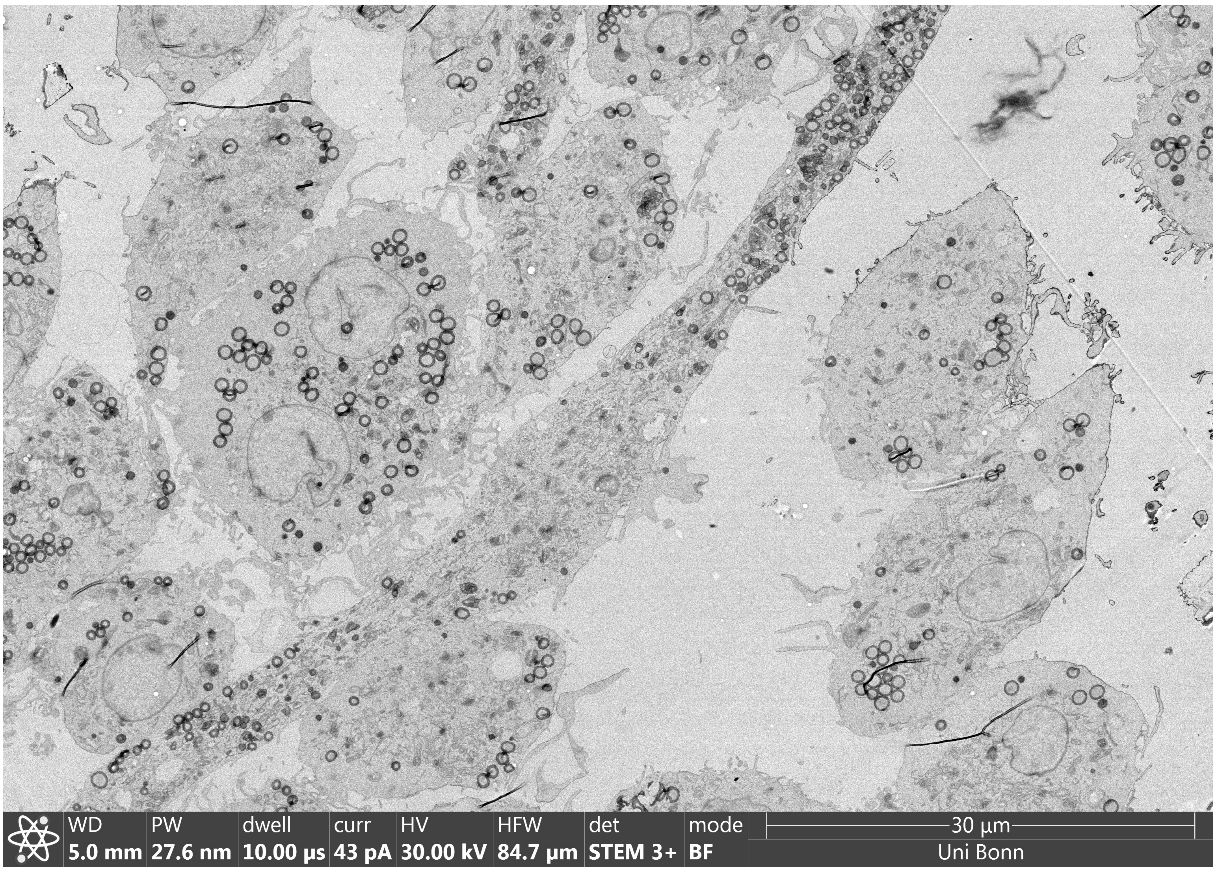

Figure 57: Overview of Lino-LNC treated cells after 24 hours
Overview of J774A.1 macrophage cells after 24 hours of 0.1 mg/ml Lino-LNC incubation. Cells were imaged by STEM after incubation with 0.1 mg/ml Lino LNC and rOTO staining. Accumulations of lipid droplets are visible throughout all cells. (#)

5.3.4. Uptake studies under influence of lalistat 2 and chloroquine

In addition, uptake studies were performed under modified conditions with the lysosomotropic agents chloroquine and lalistat 2. Before these agents were used as pretreatments in imaging experiments, their effects on J774A.1 viability, both alone and in combination, were evaluated using an MTT assay. Chloroquine had an IC50 value of 40.45 µmol/L (Figure 58 A). Lalistat 2 had no significant effect on viability at the usual concentrations of 10 or 20 µmol/L, but a reduction in viability was observed at 100 µmol/L (Figure 58 B). Co-treatment with Lino-LNCs in combination with chloroquine or lalistat 2 resulted in a significant decrease in viability compared to treatment with Lino-LNCs alone (Figure 58 C).

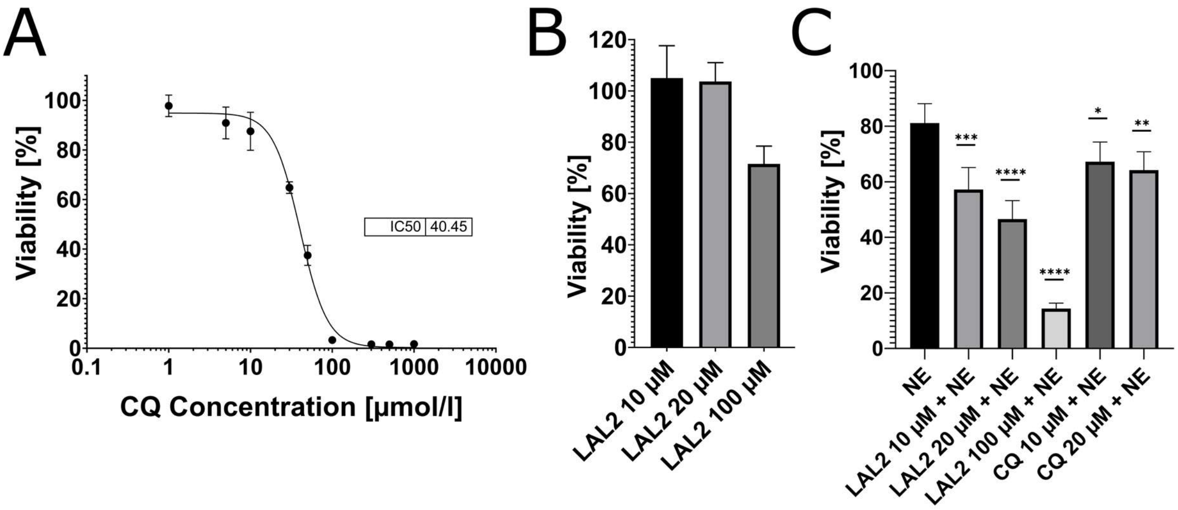

Figure 58 Effect of lysosomotropic agents with and without Lino-LNC treatment on the viability of J774A.1 cells as determined by the MTT assay.
Viability curve showing the effect of chloroquine (CQ) after 24 hours of incubation (A). Comparison of viability between Lalistat 2 (LAL2) and the untreated control after 24 hours (B). Diagram showing the effect of 0.1 mg/mL Lino-LNC on cell viability after pretreatment with LAL2 and CQ after 24 hours. Viability was calculated relative to the untreated control, which was set to 100 % (C). Data are presented as mean ± SD (n=4), with significance levels as follows: * $p < 0.05$, ** $p < 0.01$, *** $p < 0.001$, **** $p < 0.0001$, *calculated with one-way ANOVA. (#)*

Lalistat 2 treatment served as a control (Figure 59 A, B) and was compared to the combination of lalistat 2 and LNC co-treatment (Figure 59 C-F). Changes in lysosomal structure were evident in the lalistat 2 treated control, with the accumulation of electron-lucent structures ranging from less than 100 nm to 10 nm in size. The lysosomal lumen exhibited an electron-dense amorphous structure. Other cellular structures (Figure 59 A, B) appeared similar to the previously imaged controls (Figure 53)

Upon treatment with lalistat 2 and incubation with Lino-LNC for 24 hours, lipid droplets (Ld) were observed in the treated cells (Figure 59 C-F). These lipid droplets were primarily located within the cell plasma, with larger droplets seen inside vesicular structures. Some of these vesicles contained a single lipid membrane, while others had multiple membranes. The organelles with a single lipid membrane contained typical lysosomal electron-dense material, identifying them as lysosomes. Other membrane-bound structures (indicated with asterisks) were not clearly identifiable. Some of these structures had double lipid membranes, while others were enclosed by a single membrane but contained several membranous structures. Occasionally their lumen displayed lysosomal characteristics. In addition, smaller spherical structures, around 100 nm in size, were visible within these vesicles, resembling LNC particles (Figure 59 D, E). Additionally, smaller spherical structures, approximately 100 nm in size, were observed within these vesicles, resembling LNC particles (Figure 59 D, E). Some particles displayed the anticipated structure seen in previous images, while others exhibited an electron-lucent core. The smaller lipidic structures in the lalistat 2-treated control appeared less electron-dense (Figure 59 A) compared to those treated with Lino-LNC (Figure 59 E).

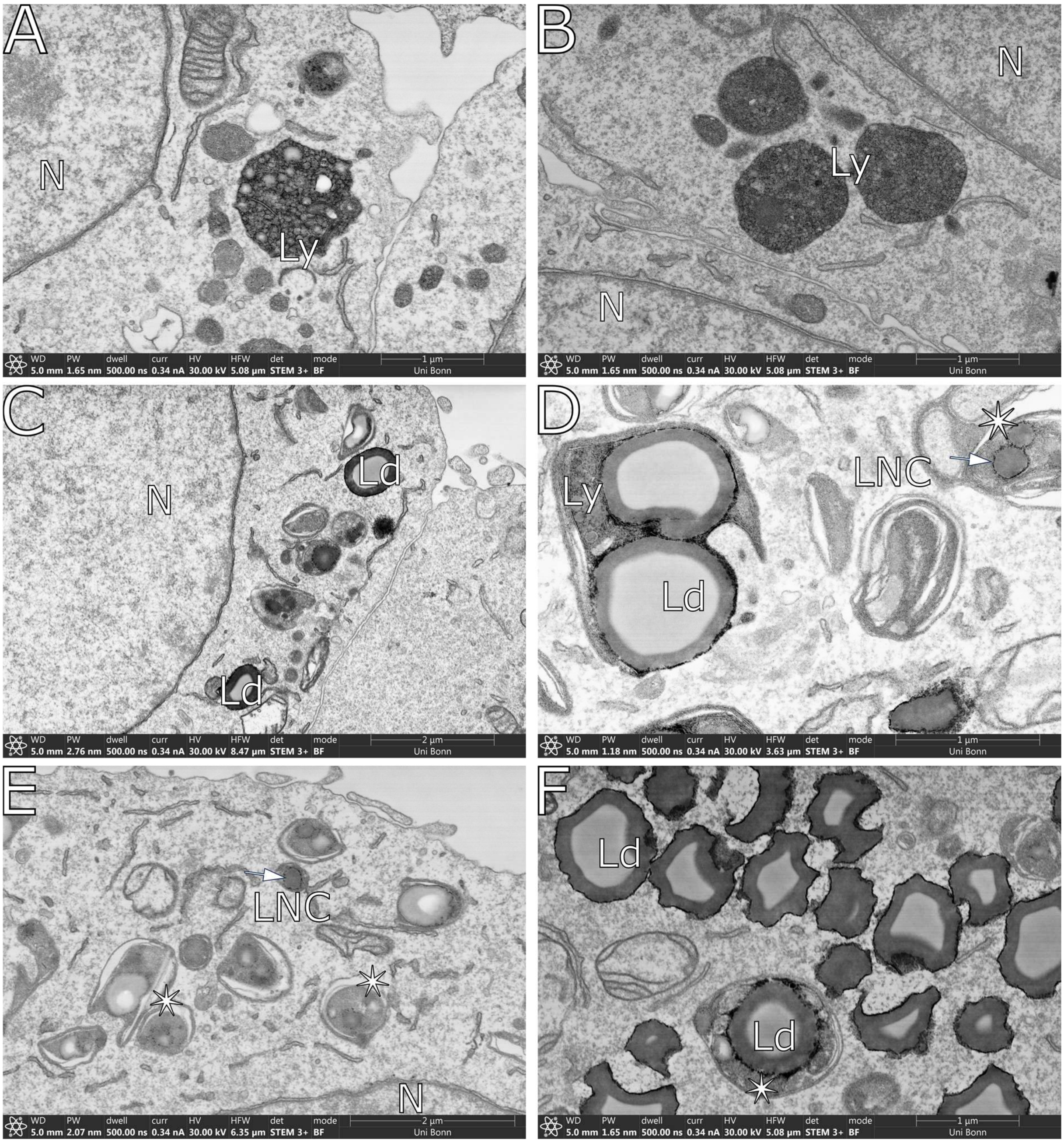

Figure 59: Ultrastructure of lalistat 2 treated cells with and without co-incubation.
Micrographs of rOTO-stained J774A.1 cells were obtained using STEM imaging after 24 hours of incubation with either 10 µM lalistat 2 (A, B) or a combination of 10 µM lalistat 2 and 0.1 mg/ml Lino-LNCs (C–F).The structure and content of lysosomes in cells treated with lalistat 2 alone (A, B) reveal electron-lucent lipid accumulations even in the absence of nanocarriers. Lino-LNC treated cells show lipid droplets distributed throughout the cytoplasm (C, F) and within membrane enclosed vesicles. (C-F). Single membrane enclosed vesicles are lysosomes (Ly). Double lipid membrane enclosed vesicles suggest vesicles of autophagic origin (asterisks) formed by fusion processes. (#)

Abbreviations: Lipid droplet (Ld), Lipid nanocarrier (LNC), Lysosome (Ly), Nucleus (N)

Treatment with chloroquine for 24 hours led to lysosomal enlargement and notable changes within the lysosomal lumen. The lumen contained numerous spherical structures along with electron-lucent material of lipidic origin (Figure 60 A, B). These alterations were solely attributed to chloroquine treatment and were unaffected by co-treatment with Lino-LNCs. Additionally, chloroquine treatment did not suppress lipid droplet formation following Lino-LNC administration

(Figure 60 C). Lipid droplets were present in all treated cells; however, no large micrometer-sized lipid droplet organelles were detected within multivesicular bodies or lysosomes, unlike the observations made under lalistat 2 co-treatment.

Combined treatment with chloroquine and Lino-LNCs resulted in a significant accumulation of LNCs within endosomal vesicles (Figure 60 E), multivesicular bodies (Figure 60 D), and lysosomes (Figure 60 D–F). This accumulation was not observed in samples pretreated with lalistat 2 or subjected to standard LNC treatment. In the control group, lipid accumulations within lysosomes (Figure 60 B) appeared electron-lucent, whereas lysosomes in LNC-treated cells were either uniformly electron-dense (Figure 60 E) or contained structures featuring an electron-dense shell surrounding an electron-lucent core (Figure 60 D). The uniform electron-dense structures were clearly linked to the treatment, as they exhibited similar structure, size, and contrast, and were exclusively found in treated cells. LNC particles displaying a lucent core exhibited a contrast similar to LNC particles, except for the lucent region. These structures were only observed in samples treated with both chloroquine and LNCs. Moreover, these structures were morphologically and in terms of contrast, distinct from the lipid accumulations observed in control samples treated with chloroquine alone.

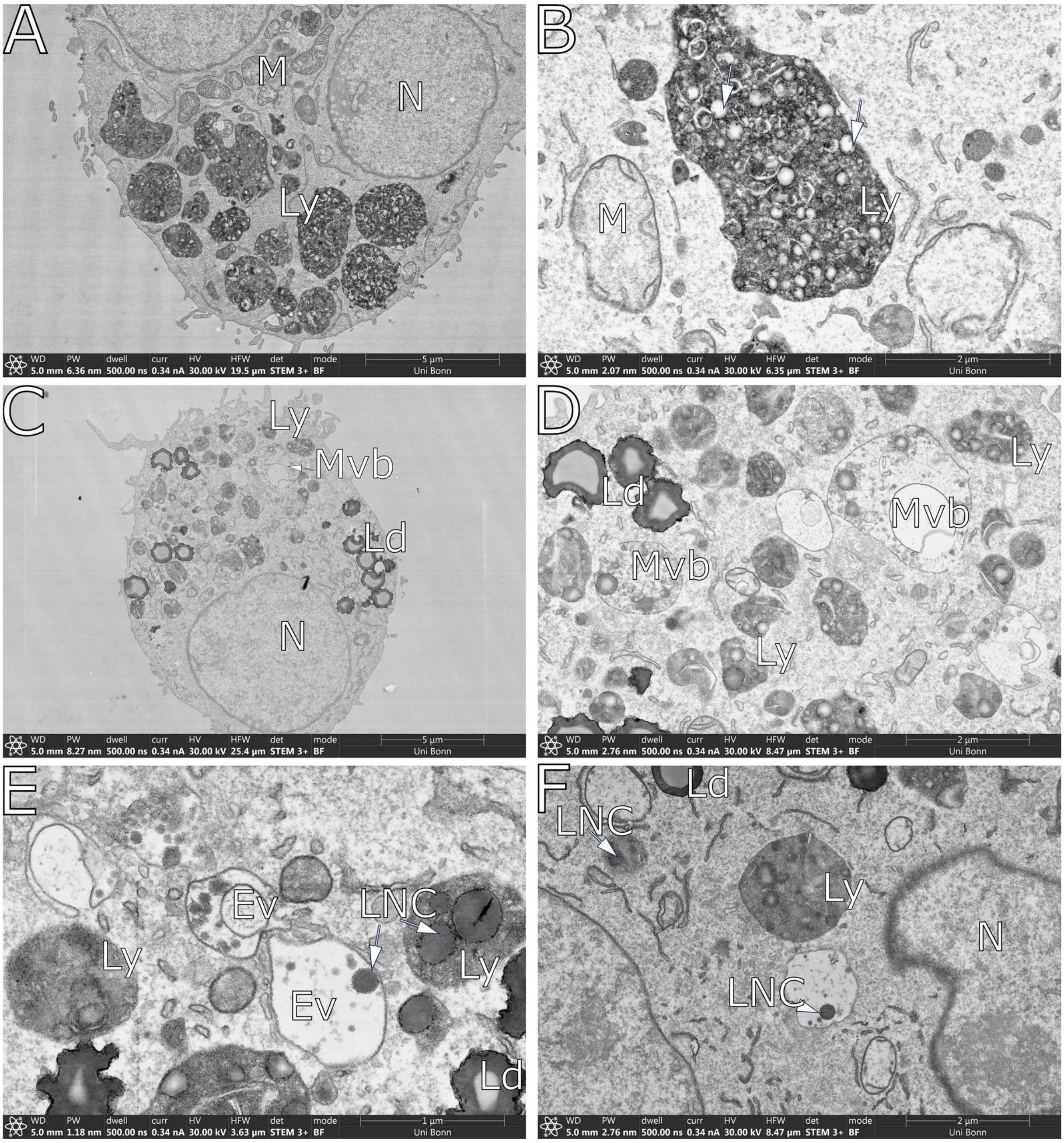

Figure 60: STEM micrographs of chloroquine-treated J774A.1 cells incubated with Lino-LNC.

Micrographs of rOTO-stained J774.A1 cells were obtained using STEM imaging after 24 hours of incubation with either 20 µM chloroquine (A, B) or a combination of 20 µM chloroquine and 0.1 mg/ml Lino-LNCs (C–F). Chloroquine-treated controls (A, B) show highly enlarged lysosomes with electron-dense amorphous contents and electron-lucent spherical lipid structures. Overview of a representative microscope image of a cell (C). The black square indicates the area of the higher magnification image seen in (D). Besides, lipid droplets and various structures of the endolysosomal system are shown, containing spherical structures of lipidic origin with varying electron density (D). These structures are distributed within lysosomal structures as well as multivesicular bodies. Some LNCs show a “core-shell” structure whereas some show a homogeneous amorphous electron dense structure (E, F). Arrows indicate LNC particles. (#)

Abbreviations: Endosomal vesicles (Ev), Lipid droplet (Ld), Lipid nanocarrier (LNC), Lysosome (Ly), Mitochondria (M), Multivesicular bodies/Late endosomes (Mvb), Nucleus (N).

5.4. Discussion

It could be demonstrated that emulsion droplets at the nanometer and micrometer scale, composed of osmiophilic excipients, retained their shape and size after reacting with osmium tetroxide. This reaction transforms emulsion droplets into stable spherical particles, resistant to the electron beam and the high vacuum within the SEM chamber. It appeared that at least one carbon double bond is necessary for the reaction, as no black reaction product was observed when medium-chain triglycerides (MCT) were incubated with osmium tetroxide (data not shown). This outcome was expected, given that MCTs lack any functional group suitable for reaction with osmium tetroxide such as carbon double bonds. Osmification of emulsion droplets for SEM imaging has previously been reported for propofol-containing emulsions derived from soybean oil [182].
The studies conducted on the interaction between LNCs and cellular surfaces were successfully performed using the HMDS sample preparation technique for SEM imaging, suggesting a broader applicability of osmiophilic excipients or materials to study nanoparticle uptake. However, the HMDS technique is limited as it cannot resolve the exact cellular origin of subsurface signals. For example, it cannot distinguish between a single particle, agglomerated particles, a newly formed organelle, or particles within organelles. Nonetheless, it is effective for imaging cellular surfaces and overall morphology. SEM analysis of HMDS-dried cells consistently showed membrane ruffling and macropinocytosis, as expected from the macrophage cell line J774A.1 [70,72,183]. This suggests macropinocytosis is a primary pathway for the cellular uptake of LNCs in these cells, as surface attachment and subsequent endocytosis of LNC droplets were seldom observed. Given that macropinocytosis is an endocytic pathway independent of receptor binding, it is a plausible mechanism in this context. This is further supported by the properties of polysorbate 80, a PEGylated surfactant, as PEGylation is an established strategy to mitigate protein binding. Nevertheless, PEGylation is not capable to fully negate protein attachment, thus other uptake routes cannot be fully excluded [184].

In addition to providing detailed images of cellular morphology, SEM imaging also revealed detectable accumulations of osmiophilic material after 15 to 30 minutes after incubation (Figure 50). These accumulations are likely due to LNC uptake, as they were absent in untreated control cells (Figure 48). Furthermore, the presence of these accumulations in cellular protrusions suggests that such structures may play a role in nanoparticle uptake, as lamellipodia have been previously implicated in the uptake of bacteria [185]. Another possible explanation is that the protrusions, being thin and widely spread, are more accessible to the electron beam, particularly at higher acceleration voltages, leading to enhanced visibility.

Identification of the LNC-particles is challenging as the cells can release spherical particles themselves. The J774A.1 cell line, like many other cells and cell lines, is capable of producing extracellular vesicles, e.g. exosomes [186], ectosomes and microvesicles [187]. Exosomes, in particular, are similar in size [188] and structure to many nanotherapeutics, making them difficult to distinguish. However, the ultrastructure of exosomes differs from the expected structure of LNCs. Exosomes consist of a lipid bilayer containing heterogeneous cargo, resulting in variable contrast in electron microscopy [189,190]. In contrast, Lino-LNCs are composed of only two components: a lipid core surrounded by surfactant. Therefore, these structures were identified as LNC particles. Identification was based on their presence only in treated samples and their expected structure.

Endogenous vesicles were found in both control and treated samples (Figure 52). This distinction is further supported by the fact that LNCs were observed both outside the cell and within organelles belonging to the endolysosomal system. Such organelles e.g. endosomal vesicles, macropinosomes, multivesicular bodies, late endosomes, or lysosomes, were also found to be involved in the uptake of the gold nanoparticles (Figure 54).

STEM imaging enabled the visualization of cellular ultrastructure and was performed on Lino-LNC-treated cells. The observed cellular accumulations were identified as lipid droplets and lysosomes. Lipid droplets are organelles that serve cellular lipid storage and lipid detoxification in response to high nutrient concentrations [191]. Their formation/existence in a drug delivery context was also reported amongst others by electron microscopy after treating cell lines with liposomes, ethosomes [192,193] or after parental nutrition [194].

The presence of lipid droplets suggests that ingested LNC droplets were fully digested, esterified, and transformed into lipid droplets for storage. Their biogenesis involves the complete esterification of glycerol and fatty acids into triacylglycerides within the endoplasmic reticulum [195,196], explaining the numerous contact points between lipid droplets and the endoplasmic reticulum. The "core-shell" structure observed in the imaged lipid droplets (Figure 55) is likely an artifact caused by the rOTO staining method, as this structure is not visible with the reduced osmium (rO) staining technique (Figure 56). This artifact is probably due to incomplete diffusion of thiocarbohydrazide into the lipid droplets. Extending the incubation time with thiocarbohydrazide to 90 minutes did not result in any structural changes (data not shown). This “core-shell” structure of lipid droplets has been observed in other applications of the technique [197,198]. Generally, the contrast of lipid droplets after osmium tetroxide staining increases with the amount of incorporated unsaturated lipids. A further study showed that if preexisting cholesterol enriched lipid droplets additionally incorporate docosahexaenoic acid, they exhibit a heterogeneous structure. This structure is characterized by electron-lucent and electron-dense areas [199,200]. This demonstrates how differences in lipid composition can be visualized and might explain the differences in contrast seen from some of the Lino-LNC particles which is discussed later in detail.

As LNCs enter the cell via the endolysosomal pathway, presumably through macropinocytosis, their cargo is degraded, as indicated by the formation of lipid droplets. The lipid droplets are larger than any particle found in the primary formulations. Without lysosomotropic agents, it was not possible to detect significant amounts of intact LNC particles within the cells, likely due to their rapid degradation (Figure 55). This is supported by the appearance of lipid droplets after 15 to 30 minutes of incubation with Lino-LNC, a time frame that coincides with the maturation time of macropinosomes, which is characterized by a reduction in vesicle size and gradual acidification via V-ATPase activity [75,201]. The final step of the degradation pathway would be either maturation in late endosomes/multivesicular bodies as an intermediate before fusion with a lysosome or outright lysosomal fusion [202,203]. The only lipase in the lysosomal lumen known to degrade triacylglycerides and cholesterol esters is lysosomal acid lipase, a hydrolase with a pH optimum at lysosomal pH [204,205] Therefore, altering lysosomal pH or inhibiting this enzyme should affect its function. To test this, cells were pretreated with lysosomotropic agents such as lalistat 2 and chloroquine.

Lalistat 2, an inhibitor of the lysosomal acid lipase, was unable to block lipid droplet formation, indicating that other cellular lipases might be involved in the degradation of Lino-LNCs within the endolysosomal system. The commonly used concentration range of 10 to 100 µmol/L for lalistat 2 should have been sufficient to inhibit lysosomal acid lipase [206,207], as its IC50 is reported to be 152 nM [208,209]. However, recent studies suggested that concentrations above 1 µmol/L may also affect other lipases [26], which could explain the significant loss of cell viability observed when cells were treated with 100 µmol/L of lalistat 2 and LNCs. The off-target effects may impair the cell's ability to detoxify lipids by other means, particularly over a 24-hour period. Treatment with lalistat 2 led to the accumulation of lipid droplets within lysosomes, likely due to lipophagy. The presence of large lipid droplets, up to 1000 nm in size, inside lysosomes without degradation suggests that lysosomal acid lipase was effectively inhibited. Some of the observed structures exhibit both lysosomal and autophagic characteristics, with contents similar to lysosomes but a poorly defined outer membrane. It is possible that lipid droplets enter lysosomes via lipophagy and remain there due to an inability to be degraded. Additionally, lalistat 2 treatment caused the accumulation of various spherical lipidic structures within lysosomes, which displayed heterogeneous features. Many lipid structures within endosomal vesicles co-incubated with Lino-LNCs had similar contrast to LNCs but contained electron-lucent core material, making their exact nature difficult to determine (Figure 59).

Chloroquine is known to affect lysosomal pH and to accumulate in acidic cellular organelles through ion trapping due to its weak basic properties. This accumulation leads to several effects, such as lysosomal swelling, inhibition of autophagolysosome formation, disruption of lysosomal degradation, and an increase in lysosomal pH [108,114,115]. Since chloroquine affects all acidifying organelles, these effects are not exclusive to lysosomes.

In this work, treatment of J774A.1 cells with 20 µmol/L of chloroquine significantly increased lysosome size and led to the accumulation of endogenous lipids (Figure 60). This suggests not only a change in lysosome size but also alterations in luminal content, likely due to disrupted digestive function. When chloroquine-pretreated J774A.1 cells were incubated with Lino-LNCs, several ultrastructural changes were observed. Although chloroquine did not block lipid droplet formation, no "full-size" lipid droplets were detected in autophagosomes, multivesicular bodies, or lysosomal structures, indicating that the cell does not engage in lipophagy due to lipid imbalance, as seen with lalistat 2 treatment.

However, many LNC-sized spheres were present in endosomal vesicles, multivesicular bodies, and lysosomes. Notably, the presence of these spheres within endosomal vesicles was not observed at this magnitude under lalistat 2 treatment. Among the lipidic structures, some resembled those found outside the cells, while others displayed additional electron-lucent areas. In the later stages of the endo-lysosomal pathway, such as in multivesicular bodies and lysosomes, the structures exhibited increased heterogeneity. This could be attributed to enzymatic degradation of the LNCs or the mixing of LNC lipids with endogenous lipids accumulating in the organelles, as electron-lucent lipids also accumulated in the lysosomes of control cells treated with chloroquine or lalistat 2. Since most lysosomal enzymes function optimally at acidic pH, a potential rise in lysosomal pH caused by chloroquine could lead to reduced enzyme activity, as demonstrated for phagosomal enzymes treated with chloroquine [90]. Degradation may also occur in the multivesicular bodies, where lipidic vesicles or LNCs with inhomogeneous morphology are present. This is supported by the fact that lipid droplets still formed when lipase activity was inhibited by lalistat 2. It is also known that protein degradation by cathepsins can occur at the late endosomal/multivesicular body stage, or even at the early endosomal stage [87,90]. A similar observation was described by Andrian et al. [119]. They found an increased number PEG-PLGA nanoparticles together with an increased relative fluorescence using correlative light and electron microscopy.

Based on the localization of the lipid structures, we conclude that the homogeneous LNC droplets were recently taken up or only exposed to degradative enzymes with limited activity. In contrast, the inhomogeneous spherical lipid structures were either exposed to degradative enzymes or mixed with endogenous, less osmiophilic lipids. These lipids lead to reduced contrast due to weaker reactions with osmium tetroxide. Similar to the earlier mentioned finding regarding lipid distributions within Lipid droplets. This reduction in degradation leads to accumulation of particles within endosomal vesicles and lysosomes.

The proposed mechanism of uptake and internalization for the LNC particles is displayed below (Figure 61) and the trafficking is briefly summarized. Particles are internalized via endocytosis pathways and routed through early endosomes toward late endosomes/multivesicular bodies. These organelles contain endogenously occurring particles, such as exosomes, as well as endocytosed material. They also serve as a connection point between the autophagy machinery and the endolysosomal system. Late endosomes/multivesicular bodies can either exocytosis their cargo or pass it further along the endolysosomal system.

The next step involves acquiring lysosomal characteristics, either through fusion with lysosomes or "kiss-and-run" processes, forming endolysosomes. This is where chloroquine exerts its effects. Chloroquine accumulates in acidifying organelles, interferes with fusion processes, and reduces lysosomal flux. It has been reported that chloroquine can inhibit enzyme activities and alter pH, but these mechanisms are still under investigation. Lalistat 2 is relatively specific to lysosomal acid lipase and inhibits this enzyme in a concentration-dependent manner. However, none of the inhibitors completely block degradation, as lipid droplets still form.

For lipid droplets to occur the LNCs need to be digested and hydrolyzed. How fatty acids released by hydrolysis in the lysosome reach the endoplasmic reticulum is currently unknown [102] as well as the exact process of lipid droplet formation within the endoplasmic reticulum [196].

In the case of the lalistat 2 treated cells, large lipid droplets within lysosomal structures may occur due to lipophagy. Lipophagy is a form of macroautophagic where lipo-phagosomes are formed by enclosing a lipid droplet in an autophagosome which explains the membrane structures and the large lipid droplets. Autophagosomes or lipophagosomes can either fuse with late endosomes bevor fusion with lysosomes or fuse directly with lysosomes. Both processes end in the formation of autophagolysosomes.

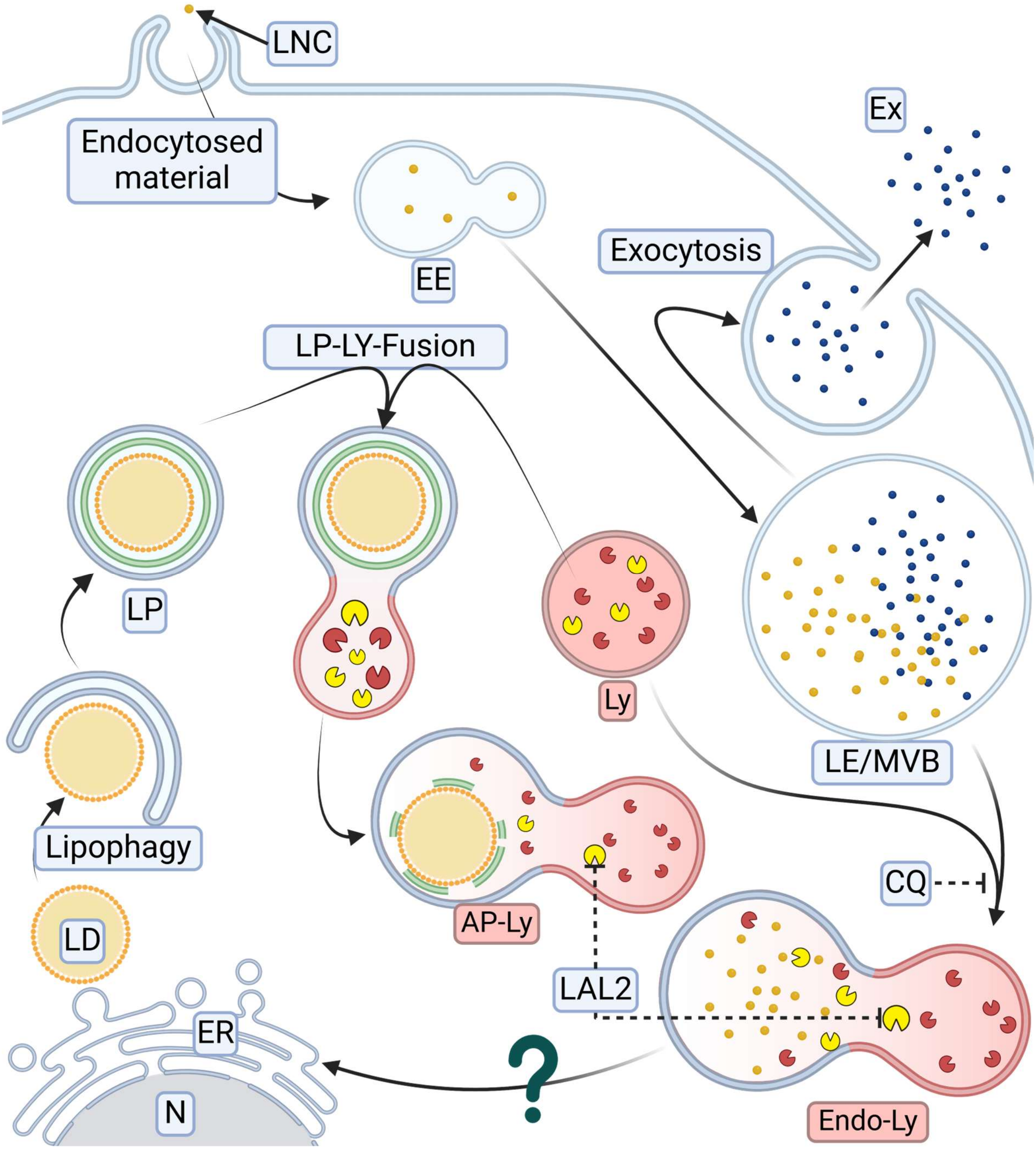

Figure 61: Presumed trafficking routes and digestion mechanisms
Schematic representation of LNC uptake routes and trafficking routes after internalization.

Abbreviations: Autophagolysosome (AP-LY), Chloroquine (CQ), Early endosomes (EE), Endolysosomes (Endo-Ly), Exosomes (Ex), Lalistat 2 (LAL2), Lipid droplets (LD), Late endosomes/Multivesicular bodies (LE/MVB), Lipid Nano carrier (LNC), Lipophagosome (LP), Lysosome (Ly)

5.5. Concluding remarks

This work demonstrated the cells' ability to rapidly degrade LNCs based on mono-, di-, and triacylglycerols. Their biodegradability enabled a more detailed examination of the effects of lysosomotropic substances on degradation processes within the endolysosomal system. These findings suggest that lysosomal acid lipase is likely not the only enzyme involved in degrading lipid excipients in this pathway. Furthermore, the experiments indicated that significant structural degradation of simple LNCs may occur within the endolysosomal system before they reach the lysosome. Increased use of EM imaging of treated biological samples is recommended to enhance our understanding of the ultrastructural changes and fate of internalized nanomedicines, addressing the existing gap in drug delivery research. This approach should be adopted regardless of the potential visibility of nanoparticles within the electron microscope, as structural changes in organelles can still be observed.

6. General Conclusion

This work successfully displayed the use of contrasting agents for identification of excipients or materials of interest via electron microscopy. Especially suitable for various approaches seems the use of osmium tetroxide. Nevertheless, ruthenium tetroxide vapor could demonstrate its suitability as well.

The preliminary experiments using ruthenium tetroxide vapor led to interesting observations, but the exact nature of the depicted structures could not always be elucidated. Especially promising in the field of pharmaceutics seems the use case for characterizing blends of polymers. This is not surprising as this is also a standard technique within polymer science [28,31,32,131,210]. Nevertheless, this technique has not been applied to pharmaceutical coatings and thus could lead to interesting observations especially regarding controlled release coatings composed of immiscible polymer blends. The results of the investigation of the drug distribution in the polymers appear to be very promising, but as orthogonal imaging techniques with sufficient resolution were not available. Thus, many of the structures imaged could not be characterized further. Since the samples were imaged in bulk by SEM relatively high electron densities and energies were needed to generate adequate contrast in the BSE micrographs resulting in many cases in beam damage of the polymer films.

Resulting from this, the biggest drawback of the technique is the high surface sensitivity [211]. Investigations are best performed on completely flat samples or ultra-thin sections obtained by ultramicrotomy. Thus, ruthenium tetroxide staining is best used on flat samples, particularly ultrathin sections, suitable for (S)-TEM. This is also the established method used by polymer scientist in the past [30–32,46,212]. Such flat samples can be prepared by ultramicrotomy, especially for imaging of ultra-thin sections [213]. If SEM imaging is to be applied in conjunction with ruthenium tetroxide vapor staining on samples, such as extruded ASD´s, only diamond knife polished sample regions should be imaged due to the beforementioned problems regarding topology. An alternative approach to producing perfectly flat cross-sections, which may be suitable for such imaging approaches, is broad ion beam (BIB) milling. While this technique is rarely employed in soft matter material science or pharmaceutics, earlier experiments suggest its potential applicability [214–217].

Such samples, including ultrathin sections or polished cross-sections of bulk materials, are also suitable for other imaging techniques capable of achieving comparable results. Since ruthenium tetroxide vapor stains chemically distinct phases, alternative imaging techniques can differentiate these phases without the need for contrast enhancement. Modern high end TEM techniques such as 4D-STEM, Cryo-EM or EDS can image nanosized compositional differences [218]. Other nanoscale imaging techniques for chemical analysis are atomic force microscopy (AFM) based techniques such as AFM-Raman or AFM IR [219,220]. These techniques can also only be used on flat samples achieving comparable results. Nevertheless, contrast enhancement with ruthenium tetroxide can be beneficial, even though other techniques are available. These alternative methods often necessitate expensive high-end instruments and highly trained personnel, which may limit their accessibility whereas the ruthenium tetroxide staining requires “only” an applicable electron microscope and a ultramicrotome suitable for polymer ultramicrotomy [213].

Ruthenium tetroxides high reactivity makes it an interesting contrasting agent for the uses mentioned above but ruthenium tetroxide vapor staining is not beneficial for FIB-SEM. Since ruthenium tetroxide is not penetrating deep into the sample, contrast enhancement by ruthenium is not suitable for FIB-SEM imaging approaches. Osmium tetroxide on the other hand lacks some of the reactivity but can penetrate deep into a sample and is thus a suitable contrasting agent for various electron microscopy approaches.

Osmium tetroxide vapor staining proved to be successful for the applications assessed within this thesis. The vapor effectively stained large sample volumes ranging from micrometer sized silica carriers to full sized tablets of several millimeters in size. As mentioned earlier, substances of amorphous nature are prone to react with substances such as ruthenium tetroxide or osmium tetroxide [39]. The contrast enhancement of the oils incorporated into porous silica carriers was expected, as lipids are the standard material contrasted by osmium tetroxide due to the containing carbon double bonds.

For further development of osmium tetroxide vapor staining as a tool in pharmaceutics a more profound understanding of the osmiophilicity of excipients is necessary. This is particularly important as pharmaceutical formulations or drug delivery systems seldomly contain just two or three substances but are rather multi component systems. Nevertheless, it could be shown that all lipidic excipients containing at least one carbon double bond readily react with osmium tetroxide and that this reaction product can be imaged by SEM, FIB-SEM and micro-CT. The potential of possible materials which can be stained is expected to be fairly large as carbon double bonds are a common structural feature of many API. Furthermore, since carbon–carbon double bonds are not the only functional groups known to react with osmium tetroxide, many substances could exhibit a certain osmiophilicity [34].

Osmium tetroxide staining is also easier to interpret for samples without complex topographical features, so the requirements for optimal sample morphology discussed in the section on ruthenium tetroxide also apply to osmium tetroxide vapor staining. Since the vapor stains a sample throughout the entire structure, the vapor staining is suitable for FIB-SEM investigations. In recent years, FIB-SEM has gained attention for providing unprecedented structural information in various drug delivery systems. Successful applications of FIB-SEM include controlled-release microspheres, spray-dried particles, implants, tablet coatings, and the tablets themselves [7,155,221–223]. Contrast enhancement by osmium tetroxide applied together with FIB-SEM could lead to easy identification of materials of interest if they possess osmiophilic properties.

In addition to its use as a contrast agent in electron microscopy, this work has also shown that osmium tetroxide can improve contrast for micro-CT imaging. Since micro-CT imaging is a nondestructive and noninvasive technique it is also possible to image the same sample before and after osmification. Osmium tetroxide vapor staining has shown potential as a tool to enhance conventional or advanced electron microscopical investigations as well as CT imaging techniques.

Identification of osmiophilic excipients is not only possible within DDS but within cells and tissues as well. This thesis could show that osmiophilic excipients can be used to identify the particles applied to biological system. In the case investigated, the formulated LNCs were readily biodegradable by the J774A.1 cell line. This, and the ability of the cell to release extracellular vesicles introduced challenges in the investigation. Nevertheless, it was possible to identify LNC particles within the cell, as their ultrastructure differed from the structure of the exosomes. However, the endolysosomal system had to be disrupted by lalistat 2 or chloroquine to observe significant amounts of particles. In particular, the observations made under chloroquine co-treatment are consistent with a recent study [119].

The contrast intensity of the LNCs was anticipated to be better distinguishable from surrounding cellular structures. It appears that for improved distinguishability, the presence of more than two unsaturated carbon–carbon double bonds is favorable. The Lino-LNCs were chosen due to their lower influence of cell viability as the ones composed of Ω-3-fatty-acids. It could have been beneficial to further investigate the cells treated with Ω-3 fatty acid based LNCs at earlier time points as the influence on cell viability would have been lower. It is likely that the contrast enhancement of drug delivery vehicles within biological systems will not be as pronounced as that of commonly used inorganic particles, such as gold nanoparticles. Therefore, it will often be difficult to distinguish whether the imaged structure is associated with the primary particle of the drug carrier or an endogenous structure.

A possible solution to this issue is the use of correlative light and electron microscopy (CLEM) [119,120,224]. This technique overlays fluorescence images of labeled drug delivery systems and cellular constituents with electron microscopy images from the same regions. CLEM adds an additional layer of information and allows for structural identification not only by ultrastructure but also by fluorescence. Although this is a highly advanced method, it allows for more precise localization and identification of particles. However, for the effective use and establishment of such techniques, optimized contrasting and sample preparation protocols must be developed to facilitate the visualization of drug delivery systems.

Electron microscopical techniques should be more frequently applied within the context of cellular drug delivery to fill the knowledge gap. The techniques should be applied regardless of particle visibility as ultrastructural changes induced by the treatments might still be visible.

The research conducted in this thesis will help future investigations by providing a sound foundation for using osmium tetroxide as a staining agent in the investigation of lipid-based nanoparticles using electron microscopy.

7. References

[1] G. Knott, C. Genoud, Is EM dead?, Journal of Cell Science 126 (2013) 4545–4552. https://doi.org/10.1242/jcs.124123.

[2] K.C.A. Smith, O.C. Wells, D. McMullan, The fiftieth anniversary of the first applications of the scanning electron microscope in materials research, Physics Procedia 1 (2008) 3–12. https://doi.org/10.1016/j.phpro.2008.07.073.

[3] E. Betzig, S.W. Hell, W.E. Moerner, The Nobel Prize in Chemistry 2014, (n.d.) 1.

[4] J. Dubochet, J. Frank, R. Henderson, The Nobel Prize in Chemistry 2017, (n.d.) 1.

[5] R.A. Carlton, Pharmaceutical Microscopy, Springer New York, New York, NY, 2011. https://doi.org/10.1007/978-1-4419-8831-7.

[6] Arzneibuch, (n.d.). https://arzneibuch.de/arzneibuch/arzneibuch/start.xav?lang=de#__arzneibuch__%2F%2F*%5B%40attr_id%3D%27eab_numtext-2.09.52.00%27%5D__1711119996341 (accessed March 22, 2024).

[7] T. Faber, J.T. McConville, A. Lamprecht, Focused ion beam-scanning electron microscopy provides novel insights of drug delivery phenomena, Journal of Controlled Release 366 (2024) 312–327. https://doi.org/10.1016/j.jconrel.2023.12.048.

[8] C.G. Galbraith, J.A. Galbraith, Super-resolution microscopy at a glance, J Cell Sci 124 (2011) 1607–1611. https://doi.org/10.1242/jcs.080085.

[9] G.H. Michler, ed., Transmission Electron Microscopy: Fundamentals of Methods and Instrumentation, in: Electron Microscopy of Polymers, Springer, Berlin, Heidelberg, 2008: pp. 15–51. https://doi.org/10.1007/978-3-540-36352-1_3.

[10] thermionic-emission gun | Glossary | JEOL Ltd., Thermionic-Emission Gun | Glossary | JEOL Ltd. (n.d.). https://www.jeol.com/ (accessed March 25, 2024).

[11] field-emission electron gun, FE electron gun | Glossary | JEOL Ltd., Field-Emission Electron Gun, FE Electron Gun | Glossary | JEOL Ltd. (n.d.). https://www.jeol.com/ (accessed March 25, 2024).

[12] Schottky-emission electron gun, SE electron gun | Glossary | JEOL Ltd., Schottky-Emission Electron Gun, SE Electron Gun | Glossary | JEOL Ltd. (n.d.). https://www.jeol.com/ (accessed March 25, 2024).

[13] W. Zhou, R.P. Apkarian, Z.L. Wang, D. Joy, Fundamentals of Scanning Electron Microscopy, (n.d.).

[14] D.C. Joy, J.B. Pawley, High-resolution scanning electron microscopy, Ultramicroscopy 47 (1992) 80–100. https://doi.org/10.1016/0304-3991(92)90186-N.

[15] G.H. Michler, ed., Scanning Electron Microscopy (SEM), in: Electron Microscopy of Polymers, Springer, Berlin, Heidelberg, 2008: pp. 87–120. https://doi.org/10.1007/978-3-540-36352-1_5.

[16] G.H. Michler, ed., Transmission Electron Microscopy: Conventional and Special Investigations of Polymers, in: Electron Microscopy of Polymers, Springer, Berlin, Heidelberg, 2008: pp. 53–85. https://doi.org/10.1007/978-3-540-36352-1_4.

[17] Stokroos, Kalicharan, Van Der Want, Jongebloed, A comparative study of thin coatings of Au/Pd, Pt and Cr produced by magnetron sputtering for FE-SEM, Journal of Microscopy 189 (1998) 79–89. https://doi.org/10.1046/j.1365-2818.1998.00282.x.

[18] R. Bhattacharya, S. Saha, O. Kostina, L. Muravnik, A. Mitra, Replacing critical point drying with a low-cost chemical drying provides comparable surface image quality of glandular trichomes from leaves of Millingtonia hortensis L. f. in scanning electron micrograph, Applied Microscopy 50 (2020) 15. https://doi.org/10.1186/s42649-020-00035-6.

[19] A. Katsen-Globa, N. Puetz, M.M. Gepp, J.C. Neubauer, H. Zimmermann, Study of SEM preparation artefacts with correlative microscopy: Cell shrinkage of adherent cells by HMDS-drying: Cell shrinkage during HMDS-drying, Scanning 38 (2016) 625–633. https://doi.org/10.1002/sca.21310.

[20] J. Orloff, M. Utlaut, L. Swanson, High Resolution Focused Ion Beams: FIB and its Applications, Springer US, Boston, MA, 2003. https://doi.org/10.1007/978-1-4615-0765-9.

[21] M.S. Joens, C. Huynh, J.M. Kasuboski, D. Ferranti, Y.J. Sigal, F. Zeitvogel, M. Obst, C.J. Burkhardt, K.P. Curran, S.H. Chalasani, L.A. Stern, B. Goetze, J.A.J. Fitzpatrick, Helium Ion Microscopy (HIM) for the imaging of biological samples at sub-nanometer resolution, Sci Rep 3 (2013) 3514. https://doi.org/10.1038/srep03514.

[22] X. Zhong, C.A. Wade, P.J. Withers, X. Zhou, C. Cai, S.J. Haigh, M.G. Burke, Comparing Xe+pFIB and Ga+FIB for TEM sample preparation of Al alloys: Minimising FIB-induced artefacts, Journal of Microscopy 282 (2021) 101–112. https://doi.org/10.1111/jmi.12983.

[23] K.A. Telari, B.R. Rogers, H. Fang, L. Shen, R.A. Weller, D.N. Braski, Characterization of platinum films deposited by focused ion beam-assisted chemical vapor deposition, J. Vac. Sci. Technol. B 20 (2002) 590. https://doi.org/10.1116/1.1458958.

[24] Y. Kubota, J. Sohn, Y. Kawaguchi, Large Volume Electron Microscopy and Neural Microcircuit Analysis, Front. Neural Circuits 12 (2018) 98. https://doi.org/10.3389/fncir.2018.00098.

[25] J. Kuo, ed., Electron microscopy: methods and protocols, Third edition, Humana Press, New York, 2014.

[26] I. Wacker, E. Hummel, S. Burgold, R. Schröder, eds., Volume Microscopy: Multiscale Imaging with Photons, Electrons, and Ions, Springer US, New York, NY, 2020. https://doi.org/10.1007/978-1-0716-0691-9.

[27] N.L. Schieber, P. Machado, S.M. Markert, C. Stigloher, Y. Schwab, A.M. Steyer, Chapter 4 - Minimal resin embedding of multicellular specimens for targeted FIB-SEM imaging, in: T. Müller-Reichert, P. Verkade (Eds.), Methods in Cell Biology, Academic Press, 2017: pp. 69–83. https://doi.org/10.1016/bs.mcb.2017.03.005.

[28] G.M. Brown, J.H. Butler, New method for the characterization of domain morphology of polymer blends using ruthenium tetroxide staining and low voltage scanning electron microscopy (LVSEM), Polymer 38 (1997) 3937–3945. https://doi.org/10.1016/S0032-3861(96)00962-7.

[29] P.E. Froehling, A.J. Pijpers, Ruthenium tetroxide as a staining agent for transmission electron microscopy of polyamide-polyether blends and block copolymers, J. Polym. Sci. B Polym. Phys. 25 (1987) 947–952. https://doi.org/10.1002/polb.1987.090250417.

[30] H. Janik, E. Walch, R.J. Gaymans, Ruthenium tetroxide staining of polybutylene terephthalate (PBT) and polyisobutylene-b-PBT segmented block copolymers, Polymer 33 (1992) 3522–3524. https://doi.org/10.1016/0032-3861(92)91114-H.

[31] Y. Wang, N. Coombs, A. Turak, Z.-H. Lu, I. Manners, M.A. Winnik, Interfacial Staining of a Phase-Separated Block Copolymer with Ruthenium Tetroxide, Macromolecules 40 (2007) 1594–1597. https://doi.org/10.1021/ma061914u.

[32] R. Vitali, E. Montani, Ruthenium tetroxide as a staining agent for unsaturated and saturated polymers, Polymer 21 (1980) 1220–1222. https://doi.org/10.1016/0032-3861(80)90091-9.

[33] M.A. (Eric) Hayat, Fixation for Electron Microscopy, Elsevier, 2012.

[34] G.F. Bahr, Osmium tetroxide and ruthenium tetroxide and their reactions with biologically important substances: Electron stains III, Experimental Cell Research 7 (1954) 457–479. https://doi.org/10.1016/S0014-4827(54)80091-7.

[35] A.M. Seligman, H.L. Wasserkrug, J.S. Hanker, A NEW STAINING METHOD (OTO) FOR ENHANCING CONTRAST OF LIPID-CONTAINING MEMBRANES AND DROPLETS IN OSMIUM TETROXIDE-FIXED TISSUE WITH OSMIOPHILIC THIOCARBOHYDRAZIDE (TCH), Journal of Cell Biology 30 (1966) 424–432. https://doi.org/10.1083/jcb.30.2.424.

[36] C. Genoud, B. Titze, A. Graff-Meyer, R.W. Friedrich, Fast Homogeneous En Bloc Staining of Large Tissue Samples for Volume Electron Microscopy, Front. Neuroanat. 12 (2018) 76. https://doi.org/10.3389/fnana.2018.00076.

[37] J.C. Tapia, N. Kasthuri, K.J. Hayworth, R. Schalek, J.W. Lichtman, S.J. Smith, J. Buchanan, High-contrast en bloc staining of neuronal tissue for field emission scanning electron microscopy, Nat Protoc 7 (2012) 193–206. https://doi.org/10.1038/nprot.2011.439.

[38] E. Kim, J. Lee, S. Noh, O. Kwon, J.Y. Mun, Double staining method for array tomography using scanning electron microscopy, Applied Microscopy 50 (2020) 14. https://doi.org/10.1186/s42649-020-00033-8.

[39] G.H. Michler, ed., Contrast Enhancement, in: Electron Microscopy of Polymers, Springer, Berlin, Heidelberg, 2008: pp. 241–260. https://doi.org/10.1007/978-3-540-36352-1_14.

[40] J.S. Trent, J.I. Scheinbeim, P.R. Couchman, Ruthenium tetraoxide staining of polymers for electron microscopy, Macromolecules 16 (1983) 589–598. https://doi.org/10.1021/ma00238a021.

[41] K. KATO, Osmium Tetroxide Fixation of Rubber Latices, Journal of Electron Microscopy 14 (1965) 219–220. https://doi.org/10.1093/oxfordjournals.jmicro.a049487.

[42] P. Barland, M. Rojkind, Negative Staining with Osmium Tetroxide Vapour, Nature 212 (1966) 84–85. https://doi.org/10.1038/212084b0.

[43] LCSS: OSMIUM TETROXIDE, (n.d.). https://web.stanford.edu/dept/EHS/cgi-bin/lcst/lcss/lcss64.html (accessed August 12, 2024).

[44] SPI-Chem Ruthenium Tetroxide Staining Kit | 02592-AA | SPI Supplies, (n.d.). https://www.2spi.com/item/02592-aa/ (accessed September 20, 2024).

[45] Q. Guo, ed., Polymer morphology: principles, characterization, and processing, John Wiley & Sons, Hoboken, New Jersey, 2016.

[46] H. Sano, T. Usami, H. Nakagawa, Lamellar morphologies of melt-crystallized polyethylene, isotactic polypropylene and ethylene-propylene copolymers by the RuO4 staining technique, Polymer 27 (1986) 1497–1504. https://doi.org/10.1016/0032-3861(86)90094-7.

[47] X. Geng, M.X. Zhai, T. Sun, G. Meyers, Morphology Observation of Latex Particles with Scanning Transmission Electron Microscopy by a Hydroxyethyl Cellulose Embedding Combined with RuO4 Staining Method, Microscopy and Microanalysis 19 (2013) 319–326. https://doi.org/10.1017/S1431927612014377.

[48] S. Velamoor, A. Mitchell, M. Bostina, D. Harland, Processing hair follicles for transmission electron microscopy, Experimental Dermatology 31 (2022) 110–121. https://doi.org/10.1111/exd.14439.

[49] S. Velamoor, M. Richena, A. Mitchell, S. Lequeux, M. Bostina, D. Harland, High-pressure freezing followed by freeze substitution of a complex and variable density miniorgan: the wool follicle, Journal of Microscopy 278 (2020) 18–28. https://doi.org/10.1111/jmi.12875.

[50] S. Reipert, I. Fischer, G. Wiche, High-pressure freezing of epithelial cells on sapphire coverslips, Journal of Microscopy 213 (2004) 81–85. https://doi.org/10.1111/j.1365-2818.2004.01260.x.

[51] L. Graham, J.M. Orenstein, Processing tissue and cells for transmission electron microscopy in diagnostic pathology and research, Nat Protoc 2 (2007) 2439–2450. https://doi.org/10.1038/nprot.2007.304.

[52] H.H. Edwards, Y.Y. Yeh, B.I. Tarnowski, G.R. Schonbaum, Acetonitrile as a substitute for ethanol/propylene oxide in tissue processing for transmission electron microscopy: comparison of fine structure and lipid solubility in mouse liver, kidney, and intestine, Microsc Res Tech 21 (1992) 39–50. https://doi.org/10.1002/jemt.1070210106.

[53] H.P. Ting-Beall, D.V. Zhelev, R.M. Hochmuth, Comparison of different drying procedures for scanning electron microscopy using human leukocytes, Microscopy Research and Technique 32 (1995) 357–361. https://doi.org/10.1002/jemt.1070320409.

[54] C. Barré, D. O'Neil, V.M. Bricelj, PREPARATION OF LARGE BIVALVE SPECIMENS FOR SCANNING ELECTRON MICROSCOPY USING HEXAMETHYLDISILAZANE (HMDS), Journal of Shellfish Research 25 (2006) 639–641. https://doi.org/10.2983/0730-8000(2006)25[639:POLBSF]2.0.CO;2.

[55] W.F. Chissoe, E.L. Vezey, J.J. Skvarla, Hexamethyldisilazane as a Drying Agent for Pollen Scanning Electron Microscopy, Biotechnic & Histochemistry 69 (1994) 192–198. https://doi.org/10.3109/10520299409106286.

[56] F. Braet, R. De Zanger, E. Wisse, Drying cells for SEM, AFM and TEM by hexamethyldisilazane: a study on hepatic endothelial cells, Journal of Microscopy 186 (1997) 84–87. https://doi.org/10.1046/j.1365-2818.1997.1940755.x.

[57] C. Kizilyaprak, G. Longo, J. Daraspe, B.M. Humbel, Investigation of resins suitable for the preparation of biological sample for 3-D electron microscopy, Journal of Structural Biology 189 (2015) 135–146. https://doi.org/10.1016/j.jsb.2014.10.009.

[58] P. Borghgraef, A. Kremer, M. De Bruyne, C.J. Guérin, S. Lippens, Resin comparison for serial block face scanning volume electron microscopy, Methods Cell Biol 177 (2023) 33–54. https://doi.org/10.1016/bs.mcb.2023.01.011.

[59] A. Khademhosseini, K.Y. Suh, J.M. Yang, G. Eng, J. Yeh, S. Levenberg, R. Langer, Layer-by-layer deposition of hyaluronic acid and poly-l-lysine for patterned cell co-cultures, Biomaterials 25 (2004) 3583–3592. https://doi.org/10.1016/j.biomaterials.2003.10.033.

[60] C.A. Scarff, M.J.G. Fuller, R.F. Thompson, M.G. Iadaza, Variations on Negative Stain Electron Microscopy Methods: Tools for Tackling Challenging Systems, JoVE (2018) 57199. https://doi.org/10.3791/57199.

[61] N.D. Donahue, H. Acar, S. Wilhelm, Concepts of nanoparticle cellular uptake, intracellular trafficking, and kinetics in nanomedicine, Advanced Drug Delivery Reviews 143 (2019) 68–96. https://doi.org/10.1016/j.addr.2019.04.008.

[62] J.J. Rennick, A.P.R. Johnston, R.G. Parton, Key principles and methods for studying the endocytosis of biological and nanoparticle therapeutics, Nat. Nanotechnol. 16 (2021) 266–276. https://doi.org/10.1038/s41565-021-00858-8.

[63] H. Damke, T. Baba, A.M. van der Bliek, S.L. Schmid, Clathrin-independent pinocytosis is induced in cells overexpressing a temperature-sensitive mutant of dynamin., Journal of Cell Biology 131 (1995) 69–80. https://doi.org/10.1083/jcb.131.1.69.

[64] E. Boucrot, A.P.A. Ferreira, L. Almeida-Souza, S. Debard, Y. Vallis, G. Howard, L. Bertot, N. Sauvonnet, H.T. McMahon, Endophilin marks and controls a clathrin-independent endocytic pathway, Nature 517 (2015) 460–465. https://doi.org/10.1038/nature14067.

[65] J.-H. Tao-Cheng, Stimulation-induced differential redistributions of clathrin and clathrin-coated vesicles in axons compared to soma/dendrites, Molecular Brain 13 (2020) 141. https://doi.org/10.1186/s13041-020-00683-5.

[66] M.T. Howes, M. Kirkham, J. Riches, K. Cortese, P.J. Walser, F. Simpson, M.M. Hill, A. Jones, R. Lundmark, M.R. Lindsay, D.J. Hernandez-Deviez, G. Hadzic, A. McCluskey, R. Bashir, L. Liu, P. Pilch, H. McMahon, P.J. Robinson, J.F. Hancock, S. Mayor, R.G. Parton, Clathrin-independent carriers form a high capacity endocytic sorting system at the leading edge of migrating cells, Journal of Cell Biology 190 (2010) 675–691. https://doi.org/10.1083/jcb.201002119.

[67] G.J. Cannon, J.A. Swanson, The macrophage capacity for phagocytosis, Journal of Cell Science 101 (1992) 907–913. https://doi.org/10.1242/jcs.101.4.907.

[68] N.D. Condon, J.M. Heddleston, T.-L. Chew, L. Luo, P.S. McPherson, M.S. Ioannou, L. Hodgson, J.L. Stow, A.A. Wall, Macropinosome formation by tent pole ruffling in macrophages, Journal of Cell Biology 217 (2018) 3873–3885. https://doi.org/10.1083/jcb.201804137.
[69] J.A. Swanson, C. Watts, Macropinocytosis, Trends in Cell Biology 5 (1995) 424–428. https://doi.org/10.1016/S0962-8924(00)89101-1.
[70] X.P. Lin, J.D. Mintern, P.A. Gleeson, Macropinocytosis in Different Cell Types: Similarities and Differences, Membranes (Basel) 10 (2020) 177. https://doi.org/10.3390/membranes10080177.
[71] M.C. Kerr, R.D. Teasdale, Defining Macropinocytosis, Traffic 10 (2009) 364–371. https://doi.org/10.1111/j.1600-0854.2009.00878.x.
[72] N. Means, C.K. Elechalawar, W.R. Chen, R. Bhattacharya, P. Mukherjee, Revealing macropinocytosis using nanoparticles, Mol Aspects Med 83 (2022) 100993. https://doi.org/10.1016/j.mam.2021.100993.
[73] M. Zeziulia, S. Blin, F.W. Schmitt, M. Lehmann, T.J. Jentsch, Proton-gated anion transport governs macropinosome shrinkage, Nat Cell Biol 24 (2022) 885–895. https://doi.org/10.1038/s41556-022-00912-0.
[74] W.H. Toh, J. Louber, I.S. Mahmoud, J. Chia, G.T. Bass, S.K. Dower, A.M. Verhagen, P.A. Gleeson, FcRn mediates fast recycling of endocytosed albumin and IgG from early macropinosomes in primary macrophages, Journal of Cell Science 133 (2019) jcs235416. https://doi.org/10.1242/jcs.235416.
[75] C.M. Buckley, J.S. King, Drinking problems: mechanisms of macropinosome formation and maturation, The FEBS Journal 284 (2017) 3778–3790. https://doi.org/10.1111/febs.14115.
[76] N.J. Yang, M.J. Hinner, Getting Across the Cell Membrane: An Overview for Small Molecules, Peptides, and Proteins, Methods Mol Biol 1266 (2015) 29–53. https://doi.org/10.1007/978-1-4939-2272-7_3.
[77] J. Tu, A.C.H. Yu, Ultrasound-Mediated Drug Delivery: Sonoporation Mechanisms, Biophysics, and Critical Factors, BME Front 2022 (n.d.) 9807347. https://doi.org/10.34133/2022/9807347.
[78] Y. Chen, S. Aslanoglou, T. Murayama, G. Gervinskas, L.I. Fitzgerald, S. Sriram, J. Tian, A.P.R. Johnston, Y. Morikawa, K. Suu, R. Elnathan, N.H. Voelcker, Silicon-Nanotube-Mediated Intracellular Delivery Enables Ex Vivo Gene Editing, Advanced Materials 32 (2020) 2000036. https://doi.org/10.1002/adma.202000036.
[79] S. Kube, N. Hersch, E. Naumovska, T. Gensch, J. Hendriks, A. Franzen, L. Landvogt, J.-P. Siebrasse, U. Kubitscheck, B. Hoffmann, R. Merkel, A. Csiszár, Fusogenic Liposomes as Nanocarriers for the Delivery of Intracellular Proteins, Langmuir 33 (2017) 1051–1059. https://doi.org/10.1021/acs.langmuir.6b04304.
[80] M. Farid, T. Faber, D. Dietrich, A. Lamprecht, Cell membrane fusing liposomes for cytoplasmic delivery in brain endothelial cells, Colloids and Surfaces B: Biointerfaces 194 (2020) 111193. https://doi.org/10.1016/j.colsurfb.2020.111193.
[81] N. Naslavsky, S. Caplan, The enigmatic endosome – sorting the ins and outs of endocytic trafficking, Journal of Cell Science 131 (2018) jcs216499. https://doi.org/10.1242/jcs.216499.
[82] M. Nagano, J.Y. Toshima, D.E. Siekhaus, J. Toshima, Rab5-mediated endosome formation is regulated at the trans-Golgi network, Commun Biol 2 (2019) 1–12. https://doi.org/10.1038/s42003-019-0670-5.
[83] H. Stenmark, Rab GTPases as coordinators of vesicle traffic, Nat Rev Mol Cell Biol 10 (2009) 513–525. https://doi.org/10.1038/nrm2728.
[84] Y. Homma, S. Hiragi, M. Fukuda, Rab family of small GTPases: an updated view on their regulation and functions, FEBS J 288 (2021) 36–55. https://doi.org/10.1111/febs.15453.
[85] P.G. Woodman, Biogenesis of the Sorting Endosome: The Role of Rab5, Traffic 1 (2000) 695–701. https://doi.org/10.1034/j.1600-0854.2000.010902.x.
[86] B. Sönnichsen, S. De Renzis, E. Nielsen, J. Rietdorf, M. Zerial, Distinct Membrane Domains on Endosomes in the Recycling Pathway Visualized by Multicolor Imaging of Rab4, Rab5, and Rab11, Journal of Cell Biology 149 (2000) 901–914. https://doi.org/10.1083/jcb.149.4.901.
[87] T.E. Tjelle, A. Brech, L.K. Juvet, G. Griffiths, T. Berg, Isolation and characterization of early endosomes, late endosomes and terminal lysosomes: their role in protein degradation, J Cell Sci 109 (Pt 12) (1996) 2905–2914. https://doi.org/10.1242/jcs.109.12.2905.
[88] D. Brömme, P.R. Bonneau, P. Lachance, B. Wiederanders, H. Kirschke, C. Peters, D.Y. Thomas, A.C. Storer, T. Vernet, Functional expression of human cathepsin S in Saccharomyces cerevisiae. Purification and characterization of the recombinant enzyme, J Biol Chem 268 (1993) 4832–4838.

[89] T. Ludwig, G. Griffiths, B. Hoflack, Distribution of newly synthesized lysosomal enzymes in the endocytic pathway of normal rat kidney cells., The Journal of Cell Biology 115 (1991) 1561–1572. https://doi.org/10.1083/jcb.115.6.1561.

[90] V. Claus, A. Jahraus, T. Tjelle, T. Berg, H. Kirschke, H. Faulstich, G. Griffiths, Lysosomal Enzyme Trafficking between Phagosomes, Endosomes, and Lysosomes in J774 Macrophages: ENRICHMENT OF CATHEPSIN H IN EARLY ENDOSOMES*, Journal of Biological Chemistry 273 (1998) 9842–9851. https://doi.org/10.1074/jbc.273.16.9842.

[91] C. Wang, T. Zhao, Y. Li, G. Huang, M.A. White, J. Gao, Investigation of Endosome and Lysosome Biology by Ultra pH-Sensitive Nanoprobes, Adv Drug Deliv Rev 113 (2017) 87–96. https://doi.org/10.1016/j.addr.2016.08.014.

[92] J. Klumperman, G. Raposo, The Complex Ultrastructure of the Endolysosomal System, Cold Spring Harb Perspect Biol 6 (2014) a016857. https://doi.org/10.1101/cshperspect.a016857.

[93] J. Huotari, A. Helenius, Endosome maturation, EMBO J 30 (2011) 3481–3500. https://doi.org/10.1038/emboj.2011.286.

[94] N. Matsumoto, M. Sekiya, G.-H. Sun-Wada, Y. Wada, M. Nakanishi-Matsui, The lysosomal V-ATPase a3 subunit is involved in localization of Mon1-Ccz1, the GEF for Rab7, to secretory lysosomes in osteoclasts, Sci Rep 12 (2022) 8455. https://doi.org/10.1038/s41598-022-12397-w.

[95] R.C. Piper, D.J. Katzmann, Biogenesis and Function of Multivesicular Bodies, Annu Rev Cell Dev Biol 23 (2007) 519–547. https://doi.org/10.1146/annurev.cellbio.23.090506.123319.

[96] D.J. Klionsky, E.-L. Eskelinen, V. Deretic, Autophagosomes, phagosomes, autolysosomes, phagolysosomes, autophagolysosomes... Wait, I'm confused, Autophagy 10 (2014) 549–551. https://doi.org/10.4161/auto.28448.

[97] E.-L. Eskelinen, To be or not to be? Examples of incorrect identification of autophagic compartments in conventional transmission electron microscopy of mammalian cells, Autophagy 4 (2008) 257–260. https://doi.org/10.4161/auto.5179.

[98] M. Pavelka, J. Roth, Functional Ultrastructure: Atlas of Tissue Biology and Pathology, Springer Vienna, Vienna, 2015. https://doi.org/10.1007/978-3-7091-1830-6.

[99] E.-L. Eskelinen, Roles of LAMP-1 and LAMP-2 in lysosome biogenesis and autophagy, Molecular Aspects of Medicine 27 (2006) 495–502. https://doi.org/10.1016/j.mam.2006.08.005.

[100] M.F. Coutinho, M.J. Prata, S. Alves, Mannose-6-phosphate pathway: A review on its role in lysosomal function and dysfunction, Molecular Genetics and Metabolism 105 (2012) 542–550. https://doi.org/10.1016/j.ymgme.2011.12.012.

[101] S. Laiouar, N. Berns, A. Brech, V. Riechmann, RabX1 Organizes a Late Endosomal Compartment that Forms Tubular Connections to Lysosomes Consistent with a "Kiss and Run" Mechanism, Current Biology 30 (2020) 1177-1188.e5. https://doi.org/10.1016/j.cub.2020.01.048.

[102] T. Kolter, K. Sandhoff, Lysosomal degradation of membrane lipids, FEBS Letters 584 (2010) 1700–1712. https://doi.org/10.1016/j.febslet.2009.10.021.

[103] H. Schulze, T. Kolter, K. Sandhoff, Principles of lysosomal membrane degradation: Cellular topology and biochemistry of lysosomal lipid degradation, Biochimica et Biophysica Acta (BBA) - Molecular Cell Research 1793 (2009) 674–683. https://doi.org/10.1016/j.bbamcr.2008.09.020.

[104] S. Rudnik, M. Damme, The lysosomal membrane—export of metabolites and beyond, The FEBS Journal 288 (2021) 4168–4182. https://doi.org/10.1111/febs.15602.

[105] D. Bulfon, J. Breithofer, G.F. Grabner, N. Fawzy, A. Pirchheim, H. Wolinski, D. Kolb, L. Hartig, M. Tischitz, C. Zitta, G. Bramerdorfer, A. Lass, U. Taschler, D. Kratky, P. Greimel, R. Zimmermann, Functionally overlapping intra- and extralysosomal pathways promote bis(monoacylglycero)phosphate synthesis in mammalian cells, Nat Commun 15 (2024) 9937. https://doi.org/10.1038/s41467-024-54213-1.

[106] N.A. Bright, L.J. Davis, J.P. Luzio, Endolysosomes Are the Principal Intracellular Sites of Acid Hydrolase Activity, Curr Biol 26 (2016) 2233–2245. https://doi.org/10.1016/j.cub.2016.06.046.

[107] S. Pisonero-Vaquero, D.L. Medina, Lysosomotropic Drugs: Pharmacological Tools to Study Lysosomal Function, Current Drug Metabolism 18 (n.d.) 1147–1158.

[108] C. De Duve, T. De Barsy, B. Poole, A. Trouet, P. Tulkens, F. Van Hoof, Lysosomotropic agents, Biochemical Pharmacology 23 (1974) 2495–2531. https://doi.org/10.1016/0006-2952(74)90174-9.

[109] J. Gilleron, W. Querbes, A. Zeigerer, A. Borodovsky, G. Marsico, U. Schubert, K. Manygoats, S. Seifert, C. Andree, M. Stöter, H. Epstein-Barash, L. Zhang, V. Koteliansky, K. Fitzgerald, E. Fava, M. Bickle, Y. Kalaidzidis, A. Akinc, M. Maier, M. Zerial, Image-based analysis of lipid nanoparticle–mediated siRNA delivery, intracellular trafficking and endosomal escape, Nat Biotechnol 31 (2013) 638–646. https://doi.org/10.1038/nbt.2612.

[110] M. Maugeri, M. Nawaz, A. Papadimitriou, A. Angerfors, A. Camponeschi, M. Na, M. Hölttä, P. Skantze, S. Johansson, M. Sundqvist, J. Lindquist, T. Kjellman, I.-L. Mårtensson, T. Jin, P. Sunnerhagen, S. Östman, L. Lindfors, H. Valadi, Linkage between endosomal escape of LNP-mRNA and loading into EVs for transport to other cells, Nat Commun 10 (2019) 4333. https://doi.org/10.1038/s41467-019-12275-6.

[111] R.V. Benjaminsen, M.A. Mattebjerg, J.R. Henriksen, S.M. Moghimi, T.L. Andresen, The Possible "Proton Sponge " Effect of Polyethylenimine (PEI) Does Not Include Change in Lysosomal pH, Mol Ther 21 (2013) 149–157. https://doi.org/10.1038/mt.2012.185.

[112] L.M.P. Vermeulen, S.C. De Smedt, K. Remaut, K. Braeckmans, The proton sponge hypothesis: Fable or fact?, European Journal of Pharmaceutics and Biopharmaceutics 129 (2018) 184–190. https://doi.org/10.1016/j.ejpb.2018.05.034.

[113] N. Gong, W. Zhong, M.-G. Alameh, X. Han, L. Xue, R. El-Mayta, G. Zhao, A.E. Vaughan, Z. Qin, F. Xu, A.G. Hamilton, D. Kim, J. Xu, J. Kim, X. Teng, J. Li, X.-J. Liang, D. Weissman, W. Guo, M.J. Mitchell, Tumour-derived small extracellular vesicles act as a barrier to therapeutic nanoparticle delivery, Nat. Mater. (2024) 1–12. https://doi.org/10.1038/s41563-024-01961-6.

[114] C. Lübow, J. Bockstiegel, G. Weindl, Lysosomotropic drugs enhance pro-inflammatory responses to IL-1β in macrophages by inhibiting internalization of the IL-1 receptor, Biochemical Pharmacology 175 (2020) 113864. https://doi.org/10.1016/j.bcp.2020.113864.

[115] M. Mauthe, I. Orhon, C. Rocchi, X. Zhou, M. Luhr, K.-J. Hijlkema, R.P. Coppes, N. Engedal, M. Mari, F. Reggiori, Chloroquine inhibits autophagic flux by decreasing autophagosome-lysosome fusion, Autophagy 14 (2018) 1435–1455. https://doi.org/10.1080/15548627.2018.1474314.

[116] C. Mauvezin, P. Nagy, G. Juhász, T.P. Neufeld, Autophagosome–lysosome fusion is independent of V-ATPase-mediated acidification, Nat Commun 6 (2015) 7007. https://doi.org/10.1038/ncomms8007.

[117] K. Ciftci, R.J. Levy, Enhanced plasmid DNA transfection with lysosomotropic agents in cultured fibroblasts, Int J Pharm 218 (2001) 81–92. https://doi.org/10.1016/s0378-5173(01)00623-8.

[118] A. Parodi, M. Evangelopoulos, N. Arrighetti, A. Cevenini, M. Livingston, S.Z. Khaled, B.S. Brown, I.K. Yazdi, F. Paradiso, J.N. Campa-Carranza, A. De Vita, F. Taraballi, E. Tasciotti, Endosomal Escape of Polymer-Coated Silica Nanoparticles in Endothelial Cells, Small 16 (2020) 1907693. https://doi.org/10.1002/smll.201907693.

[119] T. Andrian, Y. Muela, L. Delgado, L. Albertazzi, S. Pujals, A super-resolution and transmission electron microscopy correlative approach to study intracellular trafficking of nanoparticles, Nanoscale 15 (2023) 14615–14627. https://doi.org/10.1039/D3NR02838K.

[120] T. Andrian, P. Delcanale, S. Pujals, L. Albertazzi, Correlating Super-Resolution Microscopy and Transmission Electron Microscopy Reveals Multiparametric Heterogeneity in Nanoparticles, Nano Lett 21 (2021) 5360–5368. https://doi.org/10.1021/acs.nanolett.1c01666.

[121] C. Fager, S. Barman, M. Röding, A. Olsson, N. Lorén, C. von Corswant, D. Bolin, H. Rootzén, E. Olsson, 3D high spatial resolution visualisation and quantification of interconnectivity in polymer films, International Journal of Pharmaceutics 587 (2020) 119622. https://doi.org/10.1016/j.ijpharm.2020.119622.

[122] F. Siepmann, J. Siepmann, M. Walther, R.J. MacRae, R. Bodmeier, Polymer blends for controlled release coatings, Journal of Controlled Release 125 (2008) 1–15. https://doi.org/10.1016/j.jconrel.2007.09.012.

[123] J.A. Baird, L.S. Taylor, Evaluation of amorphous solid dispersion properties using thermal analysis techniques, Advanced Drug Delivery Reviews 64 (2012) 396–421. https://doi.org/10.1016/j.addr.2011.07.009.

[124] A. Singh, G. Van den Mooter, Spray drying formulation of amorphous solid dispersions, Advanced Drug Delivery Reviews 100 (2016) 27–50. https://doi.org/10.1016/j.addr.2015.12.010.

[125] M. Monschke, K.G. Wagner, Amorphous solid dispersions of weak bases with pH-dependent soluble polymers to overcome limited bioavailability due to gastric pH variability – An in-vitro approach, International Journal of Pharmaceutics 564 (2019) 162–170. https://doi.org/10.1016/j.ijpharm.2019.04.034.

[126] M. Neuwirth, S.K. Kappes, M.U. Hartig, K.G. Wagner, Amorphous Solid Dispersions Layered onto Pellets—An Alternative to Spray Drying?, Pharmaceutics 15 (2023) 764. https://doi.org/10.3390/pharmaceutics15030764.

[127] S.J. Dengale, H. Grohganz, T. Rades, K. Löbmann, Recent advances in co-amorphous drug formulations, Advanced Drug Delivery Reviews 100 (2016) 116–125. https://doi.org/10.1016/j.addr.2015.12.009.

[128] H.S. Purohit, G.G.Z. Zhang, Y. Gao, Detecting Crystallinity in Amorphous Solid Dispersions Using Dissolution Testing: Considerations on Properties of Drug Substance, Drug Product, and Selection of Dissolution Media, Journal of Pharmaceutical Sciences 112 (2023) 290–303. https://doi.org/10.1016/j.xphs.2022.10.020.

[129] B.R. Adhikari, K.C. Gordon, S.C. Das, Solid state of inhalable high dose powders, Advanced Drug Delivery Reviews 189 (2022) 114468. https://doi.org/10.1016/j.addr.2022.114468.

[130] M. S'ari, H. Blade, S. Cosgrove, R. Drummond-Brydson, N. Hondow, L.P. Hughes, A. Brown, Characterization of Amorphous Solid Dispersions and Identification of Low Levels of Crystallinity by Transmission Electron Microscopy, Mol. Pharmaceutics 18 (2021) 1905–1919. https://doi.org/10.1021/acs.molpharmaceut.0c00918.

[131] H.G. Haubruge, A.M. Jonas, R. Legras, Staining of poly(ethylene terephthalate) by ruthenium tetroxide, Polymer 44 (2003) 3229–3234. https://doi.org/10.1016/S0032-3861(03)00255-6.

[132] G.H. Michler, ed., Block Copolymers, in: Electron Microscopy of Polymers, Springer, Berlin, Heidelberg, 2008: pp. 373–392. https://doi.org/10.1007/978-3-540-36352-1_20.

[133] D. Borah, T. Ghoshal, M.T. Shaw, A. Chaudhari, N. Petkov, A.P. Bell, J.D. Holmes, M.A. Morris, The Morphology of Ordered Block Copolymer Patterns as Probed by High Resolution Imaging, Nanomaterials and Nanotechnology 4 (2014) 25. https://doi.org/10.5772/59098.

[134] Z. Yang, K. Nollenberger, J. Albers, D. Craig, S. Qi, Microstructure of an Immiscible Polymer Blend and Its Stabilization Effect on Amorphous Solid Dispersions, Mol. Pharmaceutics 10 (2013) 2767–2780. https://doi.org/10.1021/mp400209w.

[135] G.H. Michler, ed., Polymer Blends, in: Electron Microscopy of Polymers, Springer, Berlin, Heidelberg, 2008: pp. 329–349. https://doi.org/10.1007/978-3-540-36352-1_18.

[136] M.A. Parker, D. Vesely, Contrast enhancement and polymer identification in the electron microscope by the formation and staining of unsaturated double bonds, Microscopy Research and Technique 24 (1993) 333–339. https://doi.org/10.1002/jemt.1070240406.

[137] B. Van Eerdenbrugh, M. Lo, K. Kjoller, C. Marcott, L.S. Taylor, Nanoscale Mid-Infrared Imaging of Phase Separation in a Drug–Polymer Blend, Journal of Pharmaceutical Sciences 101 (2012) 2066–2073. https://doi.org/10.1002/jps.23099.

[138] T. Kilpeläinen, K. Pajula, T. Ervasti, E. Uurasjärvi, A. Koistinen, O. Korhonen, Raman imaging of amorphous-amorphous phase separation in small molecule co-amorphous systems, European Journal of Pharmaceutics and Biopharmaceutics 155 (2020) 49–54. https://doi.org/10.1016/j.ejpb.2020.08.007.

[139] J. Zhang, D. Khanal, M.M. Banaszak Holl, Applications of AFM-IR for drug delivery vector characterization: infrared, thermal, and mechanical characterization at the nanoscale, Adv Drug Deliv Rev 192 (2023) 114646. https://doi.org/10.1016/j.addr.2022.114646.

[140] N. Prine, Z. Cao, S. Zhang, T. Li, C. Do, K. Hong, C. Cardinal, T.L. Thornell, S.E. Morgan, X. Gu, Enabling quantitative analysis of complex polymer blends by infrared nanospectroscopy and isotopic deuteration, Nanoscale 15 (2023) 7365–7373. https://doi.org/10.1039/D3NR00886J.

[141] A.C.V.D. dos Santos, B. Lendl, G. Ramer, Systematic analysis and nanoscale chemical imaging of polymers using photothermal-induced resonance (AFM-IR) infrared spectroscopy, Polymer Testing 106 (2022) 107443. https://doi.org/10.1016/j.polymertesting.2021.107443.

[142] D.E. Newbury*, N.W.M. Ritchie, Is Scanning Electron Microscopy/Energy Dispersive X-ray Spectrometry (SEM/EDS) Quantitative?, Scanning 35 (2013) 141–168. https://doi.org/10.1002/sca.21041.

[143] R. Pirie, H.A. Stanway-Gordon, H.L. Stewart, K.L. Wilson, S. Patton, J. Tyerman, D.J. Cole, K. Fowler, M.J. Waring, An analysis of the physicochemical properties of oral drugs from 2000 to 2022, RSC Med. Chem. 15 (2024) 3125–3132. https://doi.org/10.1039/D4MD00160E.

[144] A.M. Vargason, A.C. Anselmo, S. Mitragotri, The evolution of commercial drug delivery technologies, Nat Biomed Eng 5 (2021) 951–967. https://doi.org/10.1038/s41551-021-00698-w.

[145] D. Hwang, J.D. Ramsey, A.V. Kabanov, Polymeric Micelles for the Delivery of Poorly Soluble Drugs: from Nanoformulation to Clinical Approval, Adv Drug Deliv Rev 156 (2020) 80–118. https://doi.org/10.1016/j.addr.2020.09.009.

[146] W.-R. Ke, R.Y.K. Chang, H.-K. Chan, Engineering the right formulation for enhanced drug delivery, Advanced Drug Delivery Reviews 191 (2022) 114561. https://doi.org/10.1016/j.addr.2022.114561.

[147] A.J. Hickey, Emerging trends in inhaled drug delivery, Advanced Drug Delivery Reviews 157 (2020) 63–70. https://doi.org/10.1016/j.addr.2020.07.006.

[148] M. Sohail Arshad, S. Zafar, B. Yousef, Y. Alyassin, R. Ali, A. AlAsiri, M.-W. Chang, Z. Ahmad, A. Ali Elkordy, A. Faheem, K. Pitt, A review of emerging technologies enabling improved

solid oral dosage form manufacturing and processing, Advanced Drug Delivery Reviews 178 (2021) 113840. https://doi.org/10.1016/j.addr.2021.113840.

[149] H. Giesche, Mercury Porosimetry: A General (Practical) Overview, Particle & Particle Systems Characterization 23 (2006) 9–19. https://doi.org/10.1002/ppsc.200601009.

[150] S. Barman, C. Fager, M. Röding, N. Lorén, C. von Corswant, E. Olsson, D. Bolin, H. Rootzén, New Characterization Measures of Pore Shape and Connectivity Applied to Coatings used for Controlled Drug Release, Journal of Pharmaceutical Sciences (2021) S0022354921001040. https://doi.org/10.1016/j.xphs.2021.02.024.

[151] V. Klang, C. Valenta, N.B. Matsko, Electron microscopy of pharmaceutical systems, Micron 44 (2013) 45–74. https://doi.org/10.1016/j.micron.2012.07.008.

[152] S. Zhang, G. Byrne, Characterization of transport mechanisms for controlled release polymer membranes using focused ion beam scanning electron microscopy image-based modelling, Journal of Drug Delivery Science and Technology 61 (2021) 102136. https://doi.org/10.1016/j.jddst.2020.102136.

[153] H. Xi, A. Zhu, G.R. Klinzing, L. Zhou, S. Zhang, A.J. Gmitter, K. Ploeger, P. Sundararajan, M. Mahjour, W. Xu, Characterization of Spray Dried Particles Through Microstructural Imaging, Journal of Pharmaceutical Sciences (2020). https://doi.org/10.1016/j.xphs.2020.07.032.

[154] A.G. Clark, R. Wang, Y. Qin, Y. Wang, A. Zhu, J. Lomeo, Q. Bao, D.J. Burgess, J. Chen, B. Qin, Y. Zou, S. Zhang, Assessing microstructural critical quality attributes in PLGA microspheres by FIB-SEM analytics, Journal of Controlled Release 349 (2022) 580–591. https://doi.org/10.1016/j.jconrel.2022.06.066.

[155] A.G. Clark, R. Wang, J. Lomeo, Y. Wang, A. Zhu, M. Shen, Q. Bao, D.J. Burgess, B. Qin, S. Zhang, Investigating structural attributes of drug encapsulated microspheres with quantitative X-ray imaging, Journal of Controlled Release 358 (2023) 626–635. https://doi.org/10.1016/j.jconrel.2023.05.019.

[156] Y. Hua, P. Laserstein, M. Helmstaedter, Large-volume en-bloc staining for electron microscopy-based connectomics, Nat Commun 6 (2015) 7923. https://doi.org/10.1038/ncomms8923.

[157] K. McDonald, Osmium ferricyanide fixation improves microfilament preservation and membrane visualization in a variety of animal cell types, Journal of Ultrastructure Research 86 (1984) 107–118. https://doi.org/10.1016/S0022-5320(84)80051-9.

[158] J. Brostin, Compositional imaging of polymers using a field emission scanning electron microscope with a microchannel plate backscattered electron detector, Scanning 17 (2006) 327–329. https://doi.org/10.1002/sca.4950170511.

[159] M. Arai, G.-I. Uramoto, M. Asano, K. Uematsu, K. Uesugi, A. Takeuchi, Y. Morono, R. Wagai, An improved method to identify osmium-stained organic matter within soil aggregate structure by electron microscopy and synchrotron X-ray micro-computed tomography, Soil and Tillage Research 191 (2019) 275–281. https://doi.org/10.1016/j.still.2019.04.010.

[160] D. Docter, M. Timmerman, Y. Dawood, J. Hagoort, N. Lobe, E. van Heurn, R. Gorter, K. Jacobs, G. Pyka, G. Kerckhofs, M.J.B. van den Hoff, B. de Bakker, Scaling up contrast-enhanced micro-CT imaging: Optimizing contrast and acquisition for large ex-vivo human samples, Forensic Imaging 37 (2024) 200596. https://doi.org/10.1016/j.fri.2024.200596.

[161] T. van den Boogert, M. van Hoof, S. Handschuh, R. Glueckert, N. Guinand, J.-P. Guyot, H. Kingma, A. Perez-Fornos, B. Seppen, L. Johnson Chacko, A. Schrott-Fischer, R. van de Berg, Optimization of 3D-Visualization of Micro-Anatomical Structures of the Human Inner Ear in Osmium Tetroxide Contrast Enhanced Micro-CT Scans, Front. Neuroanat. 12 (2018). https://doi.org/10.3389/fnana.2018.00041.

[162] T. Huo, C. Tao, M. Zhang, Q. Liu, B. Lin, Z. Liu, J. Zhang, M. Zhang, H. Yang, J. Wu, X. Sun, Q. Zhang, H. Song, Preparation and comparison of tacrolimus-loaded solid dispersion and self-microemulsifying drug delivery system by in vitro/in vivo evaluation, European Journal of Pharmaceutical Sciences 114 (2018) 74–83. https://doi.org/10.1016/j.ejps.2017.12.002.

[163] M. Farzan, R. Roth, G. Québatte, J. Schoelkopf, J. Huwyler, M. Puchkov, Loading of Porous Functionalized Calcium Carbonate Microparticles: Distribution Analysis with Focused Ion Beam Electron Microscopy and Mercury Porosimetry, Pharmaceutics 11 (2019) 32. https://doi.org/10.3390/pharmaceutics11010032.

[164] J. Appelhaus, K.E. Steffens, K.G. Wagner, Effect of Liquid Load Level and Binder Type on the Tabletability of Mesoporous Silica Based Liquisolids, AAPS PharmSciTech 25 (2024) 246. https://doi.org/10.1208/s12249-024-02958-9.

[165] S.G. Gumaste, S.A. Pawlak, D.M. Dalrymple, C.J. Nider, L.D. Trombetta, A.T.M. Serajuddin, Development of Solid SEDDS, IV: Effect of Adsorbed Lipid and Surfactant on Tableting Properties and Surface Structures of Different Silicates, Pharm Res 30 (2013) 3170–3185. https://doi.org/10.1007/s11095-013-1114-4.

[166] A.O. Beringhs, B.C. Minatovicz, G.G.Z. Zhang, B. Chaudhuri, X. Lu, Impact of Porous Excipients on the Manufacturability and Product Performance of Solid Self-Emulsifying Drug Delivery Systems, AAPS PharmSciTech 19 (2018) 3298–3310. https://doi.org/10.1208/s12249-018-1178-x.

[167] M. Farzan, G. Québatte, K. Strittmatter, F.M. Hilty, J. Schoelkopf, J. Huwyler, M. Puchkov, Spontaneous In Situ Formation of Liposomes from Inert Porous Microparticles for Oral Drug Delivery, Pharmaceutics 12 (2020) 777. https://doi.org/10.3390/pharmaceutics12080777.

[168] J. Quodbach, P. Kleinebudde, A critical review on tablet disintegration, Pharmaceutical Development and Technology 21 (2016) 763–774. https://doi.org/10.3109/10837450.2015.1045618.

[169] P. Kanaujia, W.K. Ng, R.B.H. Tan, Solid self-emulsifying drug delivery system (S-SEDDS) for improved dissolution rate of fenofibrate, Journal of Microencapsulation 31 (2014) 293–298. https://doi.org/10.3109/02652048.2013.843601.

[170] A. du Plessis, C. Broeckhoven, A. Guelpa, S.G. le Roux, Laboratory x-ray micro-computed tomography: a user guideline for biological samples, GigaScience 6 (2017) gix027. https://doi.org/10.1093/gigascience/gix027.

[171] E.L. Scheller, N. Troiano, J.N. Vanhoutan, M.A. Bouxsein, J.A. Fretz, Y. Xi, T. Nelson, G. Katz, R. Berry, C.D. Church, C.R. Doucette, M.S. Rodeheffer, O.A. Macdougald, C.J. Rosen, M.C. Horowitz, Use of osmium tetroxide staining with microcomputerized tomography to visualize and quantify bone marrow adipose tissue in vivo, Methods Enzymol 537 (2014) 123–139. https://doi.org/10.1016/B978-0-12-411619-1.00007-0.

[172] X. Hou, T. Zaks, R. Langer, Y. Dong, Lipid nanoparticles for mRNA delivery, Nat Rev Mater 6 (2021) 1078–1094. https://doi.org/10.1038/s41578-021-00358-0.

[173] S. Behzadi, V. Serpooshan, W. Tao, M.A. Hamaly, M.Y. Alkawareek, E.C. Dreaden, D. Brown, A.M. Alkilany, O.C. Farokhzad, M. Mahmoudi, Cellular Uptake of Nanoparticles: Journey Inside the Cell, Chem Soc Rev 46 (2017) 4218–4244. https://doi.org/10.1039/c6cs00636a.

[174] H. Hadji, K. Bouchemal, Effect of micro- and nanoparticle shape on biological processes, Journal of Controlled Release 342 (2022) 93–110. https://doi.org/10.1016/j.jconrel.2021.12.032.

[175] J.S. Lengyel, J.L. Milne, S. Subramaniam, Electron Tomography in Nanoparticle Imaging and Analysis, Nanomedicine 3 (2008) 125–131. https://doi.org/10.2217/17435889.3.1.125.

[176] P. Liu, G. Chen, J. Zhang, A Review of Liposomes as a Drug Delivery System: Current Status of Approved Products, Regulatory Environments, and Future Perspectives, Molecules 27 (2022) 1372. https://doi.org/10.3390/molecules27041372.

[177] R. Tenchov, R. Bird, A.E. Curtze, Q. Zhou, Lipid Nanoparticles─From Liposomes to mRNA Vaccine Delivery, a Landscape of Research Diversity and Advancement, ACS Nano 15 (2021) 16982–17015. https://doi.org/10.1021/acsnano.1c04996.

[178] M.A. Beach, U. Nayanathara, Y. Gao, C. Zhang, Y. Xiong, Y. Wang, G.K. Such, Polymeric Nanoparticles for Drug Delivery, Chem. Rev. 124 (2024) 5505–5616. https://doi.org/10.1021/acs.chemrev.3c00705.

[179] R. Liang, M. Wei, D.G. Evans, X. Duan, Inorganic nanomaterials for bioimaging, targeted drug delivery and therapeutics, Chem. Commun. 50 (2014) 14071–14081. https://doi.org/10.1039/C4CC03118K.

[180] T.L. Riss, R.A. Moravec, A.L. Niles, S. Duellman, H.A. Benink, T.J. Worzella, L. Minor, Cell Viability Assays, in: S. Markossian, A. Grossman, K. Brimacombe, M. Arkin, D. Auld, C. Austin, J. Baell, T.D.Y. Chung, N.P. Coussens, J.L. Dahlin, V. Devanarayan, T.L. Foley, M. Glicksman, J.V. Haas, M.D. Hall, S. Hoare, J. Inglese, P.W. Iversen, S.C. Kales, M. Lal-Nag, Z. Li, J. McGee, O. McManus, T. Riss, P. Saradjian, G.S. Sittampalam, M. Tarselli, O.J. Trask, Y. Wang, J.R. Weidner, M.J. Wildey, K. Wilson, M. Xia, X. Xu (Eds.), Assay Guidance Manual, Eli Lilly & Company and the National Center for Advancing Translational Sciences, Bethesda (MD), 2004. http://www.ncbi.nlm.nih.gov/books/NBK144065/ (accessed September 16, 2022).

[181] S. Vahdati, A. Lamprecht, Membrane-Fusing Vehicles for Re-Sensitizing Transporter-Mediated Multiple-Drug Resistance in Cancer, Pharmaceutics 16 (2024) 493. https://doi.org/10.3390/pharmaceutics16040493.

[182] Y. Masaki, M. Tanaka, T. Nishikawa, Physicochemical Compatibility of Propofol-Lidocaine Mixture:, Anesthesia & Analgesia 97 (2003) 1646–1651. https://doi.org/10.1213/01.ANE.0000087802.50796.FB.

[183] R. Weissleder, M. Nahrendorf, M.J. Pittet, Imaging macrophages with nanoparticles, Nature Mater 13 (2014) 125–138. https://doi.org/10.1038/nmat3780.

[184] D. Pozzi, V. Colapicchioni, G. Caracciolo, S. Piovesana, A.L. Capriotti, S. Palchetti, S. De Grossi, A. Riccioli, H. Amenitsch, A. Laganà, Effect of polyethyleneglycol (PEG) chain length on the bio–nano-interactions between PEGylated lipid nanoparticles and biological fluids:

from nanostructure to uptake in cancer cells, Nanoscale 6 (2014) 2782. https://doi.org/10.1039/c3nr05559k.

[185] J. Möller, T. Lühmann, M. Chabria, H. Hall, V. Vogel, Macrophages lift off surface-bound bacteria using a filopodium-lamellipodium hook-and-shovel mechanism, Sci Rep 3 (2013) 2884. https://doi.org/10.1038/srep02884.

[186] M. García-Martínez, L. Vázquez-Flores, V.D. Álvarez-Jiménez, J. Castañeda-Casimiro, M. Ibáñez-Hernández, L.E. Sánchez-Torres, J. Barrios-Payán, D. Mata-Espinosa, S. Estrada-Parra, R. Chacón-Salinas, J. Serafín-López, I. Wong-Baeza, R. Hernández-Pando, I. Estrada-García, Extracellular vesicles released by J774A.1 macrophages reduce the bacterial load in macrophages and in an experimental mouse model of tuberculosis, Int J Nanomedicine 14 (2019) 6707–6719. https://doi.org/10.2147/IJN.S203507.

[187] L.M. Thomas, R.D. Salter, Activation of Macrophages by P2X7-Induced Microvesicles from Myeloid Cells Is Mediated by Phospholipids and Is Partially Dependent on TLR4, The Journal of Immunology 185 (2010) 3740–3749. https://doi.org/10.4049/jimmunol.1001231.

[188] G. van Niel, G. D'Angelo, G. Raposo, Shedding light on the cell biology of extracellular vesicles, Nat Rev Mol Cell Biol 19 (2018) 213–228. https://doi.org/10.1038/nrm.2017.125.

[189] H. Choi, J.Y. Mun, Structural Analysis of Exosomes Using Different Types of Electron Microscopy, Applied Microscopy 47 (2017) 171–175. https://doi.org/10.9729/AM.2017.47.3.171.

[190] D. Bella, M. Antonietta, Overview and Update on Extracellular Vesicles: Considerations on Exosomes and Their Application in Modern Medicine, Biology 11 (2022) 804. https://doi.org/10.3390/biology11060804.

[191] J.A. Olzmann, P. Carvalho, Dynamics and functions of lipid droplets, Nat Rev Mol Cell Biol 20 (2019) 137–155. https://doi.org/10.1038/s41580-018-0085-z.

[192] M. Costanzo, L. Scolaro, G. Berlier, A. Marengo, S. Grecchi, C. Zancanaro, M. Malatesta, S. Arpicco, Cell uptake and intracellular fate of phospholipidic manganese-based nanoparticles, International Journal of Pharmaceutics 508 (2016) 83–91. https://doi.org/10.1016/j.ijpharm.2016.05.019.

[193] M. Costanzo, E. Esposito, M. Sguizzato, M.A. Lacavalla, M. Drechsler, G. Valacchi, C. Zancanaro, M. Malatesta, Formulative Study and Intracellular Fate Evaluation of Ethosomes and Transethosomes for Vitamin D3 Delivery, Int J Mol Sci 22 (2021) 5341. https://doi.org/10.3390/ijms22105341.

[194] U.J.G.M. van Haelst, R.C.A. Sengers, Effects of parenteral nutrition with lipids on the human liver, Virchows Arch. B Cell Path. 22 (1976) 323–332. https://doi.org/10.1007/BF02889226.

[195] A. Zadoorian, X. Du, H. Yang, Lipid droplet biogenesis and functions in health and disease, Nat Rev Endocrinol 19 (2023) 443–459. https://doi.org/10.1038/s41574-023-00845-0.

[196] T.C. Walther, J. Chung, R.V. Farese, Lipid Droplet Biogenesis, Annu Rev Cell Dev Biol 33 (2017) 491–510. https://doi.org/10.1146/annurev-cellbio-100616-060608.

[197] M.C. Willingham, A.V. Rutherford, The use of osmium-thiocarbohydrazide-osmium (OTO) and ferrocyanide-reduced osmium methods to enhance membrane contrast and preservation in cultured cells., J Histochem Cytochem. 32 (1984) 455–460. https://doi.org/10.1177/32.4.6323574.

[198] A. Crabtree, K. Neikirk, J. Pinette, A. Whiteside, B. Shao, J. McKenzie, Z. Vue, L. Vang, H. Le, M. Dermici, T. Ahmad, T.C. Owens, A. Oliver, F. Zeleke, H.K. Beasley, E.G. Lopez, E. Scudese, T. Rodman, K. Kabugi, A. Koh, S. Navarro, J. Lam, B. Kirk, M. Mungai, M. Sweetwyne, H.-J. Koh, E. Zaganjor, S.M. Damo, J.A. Gaddy, A. Kirabo, S.A. Murray, A. Cooper, C. Williams, M.R. McReynolds, A.G. Marshall, A. Hinton, Quantitative Assessment of Morphological Changes in Lipid Droplets and Lipid-Mito Interactions with Aging in Brown Adipose, bioRxiv (2024) 2023.09.23.559135. https://doi.org/10.1101/2023.09.23.559135.

[199] T. Fujimoto, R.G. Parton, Not Just Fat: The Structure and Function of the Lipid Droplet, Cold Spring Harb Perspect Biol 3 (2011) a004838. https://doi.org/10.1101/cshperspect.a004838.

[200] J. Cheng, A. Fujita, Y. Ohsaki, M. Suzuki, Y. Shinohara, T. Fujimoto, Quantitative electron microscopy shows uniform incorporation of triglycerides into existing lipid droplets, Histochem Cell Biol 132 (2009) 281–291. https://doi.org/10.1007/s00418-009-0615-z.

[201] C.M. Buckley, N. Gopaldass, C. Bosmani, S.A. Johnston, T. Soldati, R.H. Insall, J.S. King, WASH drives early recycling from macropinosomes and phagosomes to maintain surface phagocytic receptors, Proc Natl Acad Sci U S A 113 (2016) E5906–E5915. https://doi.org/10.1073/pnas.1524532113.

[202] H.S. Kruth, N.L. Jones, W. Huang, B. Zhao, I. Ishii, J. Chang, C.A. Combs, D. Malide, W.-Y. Zhang, Macropinocytosis Is the Endocytic Pathway That Mediates Macrophage Foam Cell

Formation with Native Low Density Lipoprotein *, Journal of Biological Chemistry 280 (2005) 2352–2360. https://doi.org/10.1074/jbc.M407167200.

[203] A. Bayati, E. Banks, C. Han, W. Luo, W.E. Reintsch, C.E. Zorca, I. Shlaifer, E. Del Cid Pellitero, B. Vanderperre, H.M. McBride, E.A. Fon, T.M. Durcan, P.S. McPherson, Rapid macropinocytic transfer of α-synuclein to lysosomes, Cell Reports 40 (2022) 111102. https://doi.org/10.1016/j.celrep.2022.111102.

[204] S. Masi, N. Chennamaneni, F. Turecek, C.R. Scott, M.H. Gelb, A Specific Substrate for the Assay of Lysosomal Acid Lipase, Clin Chem 64 (2018) 690–696. https://doi.org/10.1373/clinchem.2017.282251.

[205] K.J. Besler, V. Blanchard, G.A. Francis, Lysosomal acid lipase deficiency: A rare inherited dyslipidemia but potential ubiquitous factor in the development of atherosclerosis and fatty liver disease, Front Genet 13 (2022) 1013266. https://doi.org/10.3389/fgene.2022.1013266.

[206] M. Tuohetahuntila, M.R. Molenaar, B. Spee, J.F. Brouwers, R. Wubbolts, M. Houweling, C. Yan, H. Du, B.C. VanderVen, A.B. Vaandrager, J.B. Helms, Lysosome-mediated degradation of a distinct pool of lipid droplets during hepatic stellate cell activation, J Biol Chem 292 (2017) 12436–12448. https://doi.org/10.1074/jbc.M117.778472.

[207] S. Schlager, N. Vujic, M. Korbelius, M. Duta-Mare, J. Dorow, C. Leopold, S. Rainer, M. Wegscheider, H. Reicher, U. Ceglarek, W. Sattler, B. Radovic, D. Kratky, Lysosomal lipid hydrolysis provides substrates for lipid mediator synthesis in murine macrophages, Oncotarget 8 (2017) 40037–40051. https://doi.org/10.18632/oncotarget.16673.

[208] A.I. Rosenbaum, C.C. Cosner, C.J. Mariani, F.R. Maxfield, O. Wiest, P. Helquist, Thiadiazole Carbamates: Potent Inhibitors of Lysosomal Acid Lipase and Potential Niemann–Pick Type C Disease Therapeutics, J. Med. Chem. 53 (2010) 5281–5289. https://doi.org/10.1021/jm100499s.

[209] I. Bradić, K.B. Kuentzel, S. Honeder, G.F. Grabner, N. Vujić, R. Zimmermann, R. Birner-Gruenberger, D. Kratky, Off-target effects of the lysosomal acid lipase inhibitors Lalistat-1 and Lalistat-2 on neutral lipid hydrolases, Molecular Metabolism 61 (2022) 101510. https://doi.org/10.1016/j.molmet.2022.101510.

[210] J.X. Li, W.L. Cheung, RuO4 staining and lamellar structure of α- and β-PP, Journal of Applied Polymer Science 72 (1999) 1529–1538. https://doi.org/10.1002/(SICI)1097-4628(19990620)72:12<1529::AID-APP4>3.0.CO;2-U.

[211] B. Ohlsson, B. Törnell, The use of RuO4 in studies of polymer blends by scanning electron microscopy, Journal of Applied Polymer Science 41 (1990) 1189–1196. https://doi.org/10.1002/app.1990.070410528.

[212] B.K. Wilson, R.K. Prud'homme, Nanoparticle size distribution quantification from transmission electron microscopy (TEM) of ruthenium tetroxide stained polymeric nanoparticles, Journal of Colloid and Interface Science 604 (2021) 208–220. https://doi.org/10.1016/j.jcis.2021.04.081.

[213] J. Vastenhout, H. Gnaegi, Ultramicrotomy of Polymers Using an Oscillating Diamond Knife; Improving Polymer Morphology, Microscopy and Microanalysis 8 (2002) 324–325. https://doi.org/10.1017/S1431927602100560.

[214] J. Klaver, G. Desbois, J.L. Urai, R. Littke, BIB-SEM study of the pore space morphology in early mature Posidonia Shale from the Hils area, Germany, International Journal of Coal Geology 103 (2012) 12–25. https://doi.org/10.1016/j.coal.2012.06.012.

[215] J. Klaver, G. Desbois, R. Littke, J.L. Urai, BIB-SEM pore characterization of mature and post mature Posidonia Shale samples from the Hils area, Germany, International Journal of Coal Geology 158 (2016) 78–89. https://doi.org/10.1016/j.coal.2016.03.003.

[216] Y. Ma, J. Liang, J. Zheng, Y. Wang, M. Ashraf, C. Srinivasan, Significance of Cryogenic Broad Ion Beam Milling in Evaluating Microstructures of PLGA-based Drug Products, Microscopy and Microanalysis 27 (2021) 90–91. https://doi.org/10.1017/S1431927621000945.

[217] D. Francis, S. Mouftah, R. Steffen, A. Beduneau, Y. Pellequer, A. Lamprecht, Ion milling coupled field emission scanning electron microscopy reveals current misunderstanding of morphology of polymeric nanoparticles, European Journal of Pharmaceutics and Biopharmaceutics 89 (2015) 56–61. https://doi.org/10.1016/j.ejpb.2014.11.008.

[218] R. Pal, A.K. Sikder, K. Saito, A.M. Funston, J.R. Bellare, Electron energy loss spectroscopy for polymers: a review, Polym. Chem. 8 (2017) 6927–6937. https://doi.org/10.1039/C7PY01459G.

[219] A. Dazzi, C.B. Prater, AFM-IR: Technology and Applications in Nanoscale Infrared Spectroscopy and Chemical Imaging, Chem. Rev. 117 (2017) 5146–5173. https://doi.org/10.1021/acs.chemrev.6b00448.

[220] P. Nguyen-Tri, P. Ghassemi, P. Carriere, S. Nanda, A.A. Assadi, D.D. Nguyen, Recent Applications of Advanced Atomic Force Microscopy in Polymer Science: A Review, Polymers (Basel) 12 (2020) 1142. https://doi.org/10.3390/polym12051142.

[221] C. Janich, A. Friedmann, J. Martins de Souza e Silva, C. Santos de Oliveira, L.E. de Souza, D. Rujescu, C. Hildebrandt, M. Beck-Broichsitter, C.E.H. Schmelzer, K. Mäder, Risperidone-

Loaded PLGA–Lipid Particles with Improved Release Kinetics: Manufacturing and Detailed Characterization by Electron Microscopy and Nano-CT, Pharmaceutics 11 (2019) 665. https://doi.org/10.3390/pharmaceutics11120665.

[222] S. Zhang, D. Wu, L. Zhou, Characterization of Controlled Release Microspheres Using FIB-SEM and Image-Based Release Prediction, AAPS PharmSciTech 21 (2020) 194. https://doi.org/10.1208/s12249-020-01741-w.

[223] Z. Liu, L. Li, S. Zhang, J. Lomeo, A. Zhu, J. Chen, S. Barrett, A. Koynov, S. Forster, P. Wuelfing, W. Xu, Correlative Image-Based Release Prediction and 3D Microstructure Characterization for a Long Acting Parenteral Implant, Pharm Res (2021). https://doi.org/10.1007/s11095-021-03145-2.

[224] N. de Souza, Super-resolution CLEM, Nat Methods 12 (2015) 37–37. https://doi.org/10.1038/nmeth.3239.

8. Publikationsliste

8.1. Publikationen

Focused ion beam-scanning electron microscopy provides novel insights of drug delivery phenomena

T. Faber, J.T. McConville, A. Lamprecht, Journal of Controlled Release 366 (2024) 312–327. https://doi.org/10.1016/j.jconrel.2023.12.048.

Nanosphere-shaped ammonio methacrylate copolymers: converting a pharmaceutical inactive ingredient to efficient therapeutics for experimental colitis

B. Moulari, M.A.S. Boushehri, J.-P.P. de Barros, T. Faber, A. Béduneau, L. Lagrost, Y. Pellequer, A. Lamprecht, Nanoscale 12 (2020) 9590–9602. https://doi.org/10.1039/D0NR00465K.

Cell membrane fusing liposomes for cytoplasmic delivery in brain endothelial cells

M. Farid, T. Faber, D. Dietrich, A. Lamprecht, Colloids and Surfaces B: Biointerfaces 194 (2020) 111193. https://doi.org/10.1016/j.colsurfb.2020.111193.

Effects of carrier agents on powder properties, stability of carotenoids, and encapsulation efficiency of goldenberry (Physalis peruviana L.) powder produced by co-current spray drying

L. Etzbach, M. Meinert, T. Faber, C. Klein, A. Schieber, F. Weber, Current Research in Food Science 3 (2020) 73–81. https://doi.org/10.1016/j.crfs.2020.03.002.

In vitro and in vivo assessment of hydroxypropyl cellulose as functional additive for enabling formulations containing itraconazole

R.D. Bachmaier, M. Monschke, T. Faber, A.K. Krome, Y. Pellequer, E. Stoyanov, A. Lamprecht, K.G. Wagner, International Journal of Pharmaceutics: X 3 (2021) 100076. https://doi.org/10.1016/j.ijpx.2021.100076.

Improving Transungual Permeation Study Design by Increased Bovine Hoof Membrane Thickness and Subsequent Infection

S. Kappes, T. Faber, L. Nelleßen, T. Yesilkaya, U. Bock, A. Lamprecht, , Pharmaceutics 13 (2021) 2098. https://doi.org/10.3390/pharmaceutics13122098.

Itraconazole Nanosuspensions via Dual Centrifugation Media Milling: Impact of Formulation and Process Parameters on Particle Size and Solid-State Conversion as Well as Storage Stability

A.-C. Willmann, K. Berkenfeld, T. Faber, H. Wachtel, G. Boeck, K.G. Wagner, Pharmaceutics 14 (2022) 1528. https://doi.org/10.3390/pharmaceutics14081528.

8.2. Poster

Visualization of an ophthalmic emulsion - An Ex Vivo imaging study
K. Viemeister, T. Faber, A. Manuelli, C. Guérin, A. Lamprecht
DDF 2023, Berlin

9. Angaben zur erhaltenen Hilfe

Ich habe Hilfen erhalten bei den Anwendungsgrundlagen des von mir genutzten Helios G4 CX FIB-SEM Mikroskops welche durch 3 Schulungen des Unternehmens FEI/ThermoFisher vermittelt wurden. Teilweise sind die dort vermittelten Inhalte und Methoden insbesondere bei den FIB-SEM-milling Einstellungen in meinen Methoden übernommen worden.

Die Ultramikrotomie zur Herstellung der Ultradünnschnitte für die STEM-Messungen wurden durchgeführt von Pia Stausberg in der Mikroskopie Core Facility der Medizinischen Fakultät Bonn als Auftragsarbeiten. Des Weiteren wurden von Ihr die On-Grid Post-Kontrastierungen mit Uranacetat und Bleicitrat durchgeführt. Die dafür verwendeten Geräte wurden von der Deutschen Forschungsgesellschaft mit der Projektnummer 388171357 bereitgestellt.

Bei der Herstellung und der Vermessung der Tabletten habe ich Hilfe von Maike Werner erhalten, welche ich im Zuge Ihres Mastermoduls betreut habe. Ebenfalls habe ich beratende Unterstützung von Dr. Christina Steffens in diesem Zusammenhang erhalten.

Desweitern sind die µ-CT Messungen nicht von mir Persönlich durchgeführt wurden, sondern von Prof. Alexander Blanke im Institut für Organismische Biologie der Universität Bonn.

Die Abbildungen 1 bis 16 und Abbildung 61 sind mittels der Biorender Software erstellt worden, welche vom Pharmazeutischen Institut der Universität Bonn in Form von Lizenzen erworben wurde. Diese Software nutzt vorgefertigte Standardmotive. Diese Abbildungen sind mittels dieser Motive entstanden und sind nicht von mir einzeln entworfen worden.